

**FLUCTUATIONS AND CORRELATIONS  
IN NUCLEUS-NUCLEUS COLLISIONS  
WITHIN TRANSPORT APPROCHES**

Dissertation  
zur Erlangung des Doktorgrades  
der Naturwissenschaften

vorgelegt beim Fachbereich Physik  
der Johann Wolfgang Goethe–Universität  
in Frankfurt am Main

von  
Volodymyr P. Konchakovski  
aus Korosten, Ukraine

Frankfurt am Main  
2009

(D30)

vom Fachbereich Physik der  
Johann Wolfgang Goethe–Universität, Frankfurt am Main,  
als Dissertation angenommen.

Dekan: Prof. Dr. Dirk-Hermann Rischke

Gutachter: PD Dr. Elena Bratkovskaya

Datum der Disputation: 1 .10.2009

# Zusammenfassung

Wie aus der Quantenstatistik wohl bekannt ist, können Fluktuationen physikalischer Observable wertvolle Hinweise auf kritische Punkte im Phasendiagramm liefern. Diese Betrachtungen gelten auch für das Phasendiagramm hadronischer Materie, welches gegenwärtig von verschiedenen Arbeitsgruppen in theoretischer und experimenteller Hinsicht erforscht wird. Die vorliegende Arbeit ist eine systematische Analyse von Fluktuationen und Korrelationen in relativistischen Schwerionenstößen auf der Basis des HSD Transportmodells, welches eine mikroskopische Beschreibung dieser Reaktionen liefert. Der Vorteil solcher mikroskopischer Simulationen liegt darin, daß die komplizierten experimentellen Triggerbedingungen für jede einzelne Schwerionenreaktion implementiert werden können. Auf diese Weise können experimentelle Zentralitäts-Bestimmungen für Eventklassen explizit in die Analyse integriert werden. Der Vergleich mit differenziellen experimentellen Daten gibt sodann Aufschluß über die Frage, inwieweit gemessene Signale auf einen Phasenübergang bzw. kritischen Punkt hinweisen. Des Weiteren liefern die mikroskopischen Phasenraumsimulationen – unter Ausschluß von spezifischen Cuts – wertvolle Hinweise darauf, welche Observablen durch mikrokanonische, kanonische oder großkanonische Gesamtheiten beschrieben werden können.

Nach einer detaillierten Ableitung und Beschreibung des HSD Transportmodells in Kapitel 2 wurde in Kapitel 3 zunächst die Abhängigkeit der Fluktuationen in den Teilchenmultiplizitäten von der Zentralität der Reaktionen untersucht. Dabei wurden verschiedene Ansätze zur Definition der Zentralität in diesen Reaktionen verwendet, die den jeweiligen experimentellen Randbedingungen genügen. Bei SPS Energien wurden Gesamtheiten mit fester Anzahl von Projektil-Partizipanten,  $N_P^{proj}$ , ausgewählt während bei den PHENIX Experimenten am RHIC Gesamtheiten mit unterschiedlicher Phasenraumbesetzung bei Midrapidität ausgewählt wurden. Eine Abnahme der Teilchenfluktuationen mit

der Zentralität der Reaktion konnte in beiden Energiebereichen festgestellt werden.

In Kapitel 4 konnte weiterhin gezeigt werden, daß Fluktuationen in der Zahl der Target-Partizipanten großen Einfluß auf die Fluktuationen in der Baryonenzahl haben. Dieses kommt dadurch zustande, daß durch den experimentellen Trigger auf feste Zahl  $N_P^{proj}$  zwar die Anzahl der Projektil-Partizipanten festgelegt wird, jedoch keine Einschränkung in der Anzahl der Target-Partizipanten erfolgt. Letztere fluktuiert daher signifikant um  $N_P^{proj}$ . Als Folge zeigen die gemessenen Fluktuationen in der Zahl der geladenen Teilchen eine explizite Abhängigkeit von der Rapidität  $y$ . Diese Abhängigkeit kann wiederum benutzt werden, um die Durchdringung der longitudinalen Flüsse von Projektil- und Target-Hadronen im Vergleich mit dem Experiment zu bestimmen. In der Tat zeigen die HSD Rechnungen eine nur geringe Mischung von Target- und Projektil-Hadronen im Vergleich mit den Daten der NA49 Kollaboration, was auf – in HSD nicht enthaltene – partonische Freiheitsgrade hinweist. Andererseits zeigen die HSD Rechnungen für die Ladungsfluktuation  $\Delta\Phi$  eine gute Übereinstimmung mit den NA49 Daten, was bedeutet, daß diese Observable durch Wechselwirkungen in der späten hadronischen Phase dominiert wird und daher wenig Information über eine frühe partonische Phase liefert.

Bei RHIC Energien wurden die Fluktuationen in der Teilchenmultiplizität für Au+Au bei  $\sqrt{s} = 200$  GeV berechnet und mit den vorläufigen Daten der PHENIX Kollaboration konfrontiert. In der Tat wird eine qualitative und quantitative Übereinstimmung zwischen den Rechnungen und Daten gefunden, was darauf hindeutet, daß die Zentralitätsabhängigkeit der gegenwärtigen Daten der PHENIX Kollaboration vorwiegend auf Fluktuationen in der Zahl der Partizipanten zurückzuführen ist.

Die Anregungsfunktion der Fluktuationen in der Teilchenmultiplizität wurde in Kapitel 5 untersucht und mit Resultaten des statistischen Modells verglichen. Während HSD ein Anwachsen der skalierten Fluktuationen mit der Kollisionsenergie liefert, zeigt das statistische Modell ein konstantes Verhältnis bei hohen Energien. So ist der Unterschied zwischen HSD Vorhersagen und dem statistischen Modell bereits ein Faktor 10 bei der RHIC Energie  $\sqrt{s} = 200$  GeV. Jedoch liefert ein direkter Vergleich mit experimentellen Daten für sehr zentrale Reaktionen von Pb+Pb bei 160 A GeV keine signifikanten Differenzen zwischen beiden Modellen. Dieses ist darauf zurückzuführen, daß bei SPS Energien die Unter-

schiede ohnehin nur klein sind und durch die geringe experimentelle Akzeptanz weiter reduziert werden. Daher sind neue Messungen bei höheren Energien mit deutlich verbesserter Akzeptanz erforderlich, um zwischen den Modellen experimentell eine Präferenz festzulegen.

Die geplanten Experimente der NA61 Kollaboration bei SPS Energien von 20 - 158 A GeV wurden in Kapitel 6 untersucht, einerseits in Hinsicht auf die Abhängigkeit der Fluktuationen von der Kollisionsenergie, andererseits in Abhängigkeit von der Systemgröße und Zentralität. Zu diesem Zweck wurden C+C, S+S, In+In und Pb+Pb Reaktionen bei 10, 20, 30, 40, 80 und 158 A GeV mit hoher Statistik berechnet. Insbesondere der Einfluß von Fluktuationen in der Zahl der Partizipanten stellte sich erneut als dominant heraus. Um diesen ‘geometrischen’ Effekt zu minimieren, sollte man nur sehr zentrale Stöße betrachten. Jedoch ist zu beachten, daß für ‘leichte Systeme’ wie C+C und S+S selbst die Festlegung ‘sehr zentraler Stöße’ modellabhängig bleibt. Die HSD Rechnungen zeigten eine monotone Abhängigkeit der Fluktuationen von der Einschußenergie und Systemgröße auch bei sehr zentralen Reaktionen. Da in diesen Transportrechnungen keine expliziten partonischen Freiheitsgrade enthalten sind, bedeutet dieses Ergebnis für das Experiment, daß nicht-monotone Fluktuationen (in sehr zentralen Eventklassen) ein Anzeichen für das Auftreten eines kritischen Punktes sein könnten.

Weitere kritische Observablen sind Verhältnisse von Hadronen zueinander wie  $K/\pi$ ,  $p/\pi$ ,  $\Lambda/p$  etc., die nicht zu sehr von Volumenfluktuationen beeinflußt werden. Insbesondere Fluktuationen in diesen Teilchenverhältnissen wie  $K/\pi$  wurden lange Zeit als vielversprechende Observable betrachtet. Eine entsprechende systematische Analyse wurde in Kapitel 7 vorgestellt für Schwerionenkollisionen von den unteren SPS Energien bis zu den höchsten Energien bei RHIC. Neben den HSD Rechnungen wurden statische Modellrechnungen für mikrokanonische, kanonische und großkanonische Gesamtheiten herangezogen, um insbesondere den Einfluß von Erhaltungsgrößen auf diese Observablen zu studieren. Es ergaben sich signifikante Unterschiede zwischen dem HSD Transportmodell und den statistischen Ansätzen in den verschiedenen Varianten für die skalierten Varianzen  $\omega_A$  und Korrelationsparameter  $\rho_{AB}$ . Bei SPS Energien zeigten die HSD Rechnungen eine weitgehende Übereinstimmung mit mikrokanonischen und kanonischen Rechnungen, was auf die dominante Rolle von Resonanzzerfällen und Erhaltungssätzen hinweist. Dagegen ergaben sich deutliche Unterschiede für die skalierten Vari-

enzen und Korrelationsparameter  $\rho_{AB}$  bei RHIC Energien, die in erster Linie auf die Nichtgleichgewichts-Dynamik der HSD Transportrechnungen zurückzuführen sind. Dieses bedeutet andererseits, daß die Observablen gut geeignet sein sollten, das Maß an Äquilibration in Reaktionen bei RHIC experimentell festzulegen. Des Weiteren zeigte sich, daß die dynamischen Korrelationen, charakterisiert durch die Variable  $\sigma_{dyn}$  sehr stark von Niederenergieeigenschaften des Modells abhängen, so daß von experimenteller Seite hier keine eindeutigen Schlußfolgerungen gezogen werden können.

Es ist hervorzuheben, daß die HSD Rechnungen die gemessene Anregungsfunktion in den Fluktuationen des  $K/\pi$  Verhältnisse bei SPS Energien sehr gut beschreibt, was bisherigen Modellen nicht gelang. In diesem Zusammenhang ist darauf hinzuweisen, daß Akzeptanz-Cuts und die spezielle Wahl der Zentralitäts-Definition keinen signifikanten Einfluß auf diese Observable haben. Bei RHIC Energien dagegen wurde eine starke Abhängigkeit dieser Observablen von Akzeptanz-Cuts festgestellt.

Als weitere charakterische Observable werden Korrelationen in der Rapiditätsverteilung von Hadronen angesehen. Ein Vergleich der STAR Daten für solche ‘Forward-Backward’ Korrelationen mit den HSD Rechnungen zeigt eine qualitative Übereinstimmung. Im Gegensatz zu mittleren Multiplizitäten in verschiedenen Rapiditätsbereichen sind die ‘Forward-Backward’ Korrelationen jedoch sehr sensitiv auf die Wahl der Eventklassen; eine geometrische Bestimmung über den Stoßparameter und eine über eine Referenz-Teilchenmultiplizität ergeben hier stark unterschiedliche Resultate. Allerdings kann man diese Korrelationen zusätzlich als Funktion der Ensemble-Größe untersuchen wie auch Intervallgröße für die betrachteten Rapiditätsintervalle. Die Studien haben gezeigt, daß mit kleinen Intervallgrößen die induzierten geometrischen Korrelationen kleiner werden und zu einer weniger ausgeprägten Abhängigkeit von der Zentralität führen sollten.

Die systematischen Analysen dieser Arbeit, einerseits mit mikroskopischen Transportmodellen, andererseits mit statistischen Modellen für verschiedene Gesamtheiten, haben gezeigt, daß die experimentelle Bestimmung des kritischen Punktes im hadronischen Phasendiagramm ein sehr komplexes Unterfangen ist. Bisher wenig beachtete Parameter wie Fluktuationen in der Zahl der Partizipanten haben sich als entscheidend für die gegenwärtigen Messungen herausgestellt. Doch konnten in dieser Arbeit Wege aufgezeigt werden, mit denen

‘geometrische Effekte’ klarer von physikalischen Korrelationen zu trennen sind. Die nächsten Generationen von Experimenten am SPS (NA61) sowie am RHIC (STAR, PHENIX) – sollten ein tieferes Verständnis der dynamischen Fluktuationen erlauben. Auch für die zukünftigen Experimente der CBM Kollaboration bei FAIR sollten die Resultate dieser Arbeit von Bedeutung sein.

# Contents

<b>Zusammenfassung</b>	<b>3</b>
<b>Contents</b>	<b>8</b>
<b>1 Introduction</b>	<b>11</b>
1.1 Relativistic Heavy-Ion Collisions . . . . .	11
1.2 The Phase Diagram of Strongly Interacting Matter . . . . .	12
1.3 Signatures of the critical point and onset of deconfinement . . . . .	14
1.4 LQCD results on susceptibilities . . . . .	16
1.5 Fluctuations and Correlations in High Energy Collisions . . . . .	18
<b>2 The Hadron-String-Dynamics Transport Approach</b>	<b>20</b>
2.1 Off-shell relativistic transport . . . . .	20
2.1.1 The Kadanoff-Baym equations . . . . .	20
2.1.2 Off-shell relativistic transport theory . . . . .	25
2.1.3 Generalized transport equation . . . . .	29
2.1.4 Transport in the Botermans-Malfliet scheme . . . . .	31
2.1.5 Generalized testparticle representation . . . . .	33
2.1.6 Collision terms . . . . .	34
2.2 The covariant transport approach HSD . . . . .	36
2.2.1 Scalar and vector potentials in HSD . . . . .	38
2.2.2 Hadronic degrees of freedom . . . . .	41
2.2.3 Hadron-hadron interactions . . . . .	42
2.2.4 The LUND String model . . . . .	42
2.2.5 Numerical realization of the HSD model . . . . .	46



<b>3</b>	<b>Multiplicity Fluctuations in Nucleus-Nucleus Collisions</b>	<b>49</b>
3.1	Scaled Variance . . . . .	49
3.2	Multiplicity Fluctuations in Pb+Pb Collisions at 158 AGeV . . .	50
3.2.1	Fluctuations in the number of participants . . . . .	50
3.2.2	HSD and UrQMD results in comparison to the NA49 Data	53
3.2.3	Multiplicity fluctuations in the wounded nucleon model .	55
3.2.4	Transparency, Mixing, and Reflection models . . . . .	60
3.2.5	Fluctuations in the projectile and target hemispheres . . .	63
3.2.6	Fluctuations in different rapidity intervals . . . . .	69
3.3	Multiplicity Fluctuations in Au+Au Collisions at RHIC . . . . .	71
3.4	Summary of Chapter 3 . . . . .	74
<b>4</b>	<b>Baryon Number and Electric Charge Fluctuations in Pb+Pb Collisions at SPS energies</b>	<b>77</b>
4.1	Net Baryon Number Fluctuations . . . . .	77
4.2	Net Electric Charge Fluctuations . . . . .	83
4.3	Fluctuations in Most Central Collisions . . . . .	87
4.4	Electric charge fluctuations: comparison to the data . . . . .	90
4.5	Summary of Chapter 4 . . . . .	93
<b>5</b>	<b>Excitation Function of the Multiplicity Fluctuations in Central Nucleus-Nucleus Collisions</b>	<b>94</b>
5.1	p+p collisions . . . . .	95
5.2	N+N collisions . . . . .	96
5.3	Central A+A collisions . . . . .	97
5.4	Comparison to the data . . . . .	99
5.5	Summary of Chapter 5 . . . . .	101
<b>6</b>	<b>Multiplicity Fluctuations in Nucleus-Nucleus Collisions: Dependence on Energy and Atomic Number</b>	<b>103</b>
6.1	Multiplicity fluctuations in proton-proton collisions . . . . .	105
6.2	Participant number fluctuations . . . . .	106
6.3	Multiplicity fluctuations at zero impact parameter . . . . .	108
6.3.1	Centrality Selection in A+A Collisions by Impact Parameter	108
6.3.2	HSD and UrQMD Results for the Multiplicity Fluctuations for b=0 . . . . .	110

6.3.3	Comparison to the Independent Source Model . . . . .	111
6.4	Multiplicity fluctuations in 1% most central collisions . . . . .	114
6.5	Summary of Chapter 6 . . . . .	119
<b>7</b>	<b>Ratio Fluctuations in Nucleus-Nucleus Collisions: Statistical and Transport Models</b>	<b>124</b>
7.1	Measures of Particle Ratio Fluctuations . . . . .	126
7.1.1	Notations and Approximations . . . . .	126
7.1.2	Mixed Events Procedure . . . . .	128
7.2	Fluctuations of Ratios in Statistical Models . . . . .	130
7.2.1	Quantum Statistics and Resonance Decays . . . . .	130
7.2.2	Global Conservation Laws . . . . .	132
7.3	Statistical and HSD model results . . . . .	134
7.3.1	Results for $\omega_A$ and $\rho_{AB}$ . . . . .	135
7.3.2	$\sigma$ , $\sigma_{mix}$ , and $\sigma_{dyn}$ for $K/\pi$ ratio fluctuations . . . . .	141
7.3.3	Volume Fluctuations . . . . .	143
7.4	Excitation function for the ratio fluctuations: Comparison with data	144
7.5	Summary of Chapter 7 . . . . .	147
<b>8</b>	<b>Forward-backward correlations in nucleus-nucleus collisions: baseline contributions from geometrical fluctuations</b>	<b>149</b>
8.1	Definition of Observables . . . . .	150
8.2	Glauber Monte Carlo Model . . . . .	151
8.3	HSD Transport Model Simulations . . . . .	154
8.4	Summary of Chapter 8 . . . . .	158
<b>9</b>	<b>Summary and Discussion</b>	<b>160</b>
	<b>Appendix A: String Model</b>	<b>165</b>
	<b>Bibliography</b>	<b>174</b>
	<b>Acknowledgments</b>	<b>185</b>
	<b>Curriculum Vitae</b>	<b>186</b>

# Chapter 1

## Introduction

### 1.1 Relativistic Heavy-Ion Collisions

Hot and dense nuclear matter can be generated in the laboratory in a wide range of temperatures and densities by colliding atomic nuclei at high energies. In the collision zone, the matter is heated and compressed for a very short period of time. If the energy pumped into the formed fireball is sufficiently large the quark-gluon substructure of nucleons comes into play. At moderate temperatures, nucleons are excited to short-lived states (baryonic resonances) which decay by the emission of mesons. At higher temperatures, also baryon-antibaryon pairs are created. This mixture of baryons, antibaryons and mesons, all strongly interacting particles, is generally called hadronic matter, or baryonic matter if baryons prevail. At even higher temperatures or densities the hadrons melt, and the constituents, the quarks and gluons, form a new phase, the Quark-Gluon Plasma (QGP). High-energy heavy-ion collision experiments provide the unique possibility to create and investigate these extreme states of matter.

The study of nuclear matter under extremely high baryon density and temperature – where according to lattice quantum chromodynamics (QCD) [1, 2, 3] the hadronic matter transforms to a Quark-Gluon Plasma – is the aim of a variety of experiments at current and future facilities: NA38, NA49, NA50, NA60 and NA61/SHINE at the Super-Proton-Synchrotron (SPS) [4, 5, 6, 7, 8]; PHENIX, STAR, PHOBOS and BRAHMS at the Relativistic-Heavy-Ion-Collider (RHIC) [9, 10, 11, 12]; ALICE at the Large-Hadron-Collider (LHC) [13]; CBM and PANDA at the Facility for Antiproton and Ion Research (FAIR) [14]; MPD

at the Nuclotron-based Ion Collider Facility (NICA) [15].

Relativistic nucleus-nucleus collisions have been studied so far at beam energies from 0.1 to 2 A·GeV at the SIS (SchwerIonen-Synchrotron), from 2 to 11.6 A·GeV at the AGS (Alternating Gradient Synchrotron) and from 20 to 160 A·GeV at the SPS [16, 17]. While part of these programs are closed now, the heavy-ion research has been extended at RHIC with Au+Au collisions at invariant energies  $\sqrt{s}$  from  $\sim 20$  to 200 GeV (equivalent energies in a fixed target experiment: 0.2 to 21.3 A·TeV). In the near future, further insight into the physics of matter at even more extreme conditions will be gained at the LHC, which will reach center-of-mass energies of the few TeV scale. Apart from LHC, the SPS successor SHINE will operate at CERN in order to scan the 10A-158A·GeV energy range with light and intermediate mass nuclei [8]. At FAIR, which is expected to start operation in 2015, collisions of gold nuclei from 5 A·GeV up to 35 A·GeV will be studied. At NICA it is planned to start the experimental program of colliding *Au* and/or *U* ions as well as polarized light nuclei at energies up to of 5 A·GeV in 2013 (an upgrade to  $\sqrt{s} = 9$  GeV is foreseen [18]).

At very high beam energies – as available at RHIC and LHC – the research programs concentrate on the study of the properties of deconfined QCD matter at very high temperatures and almost zero net baryon densities, whereas at moderate beam energies (SPS, FAIR and NICA) experiments focus on the search for structures in the QCD phase diagram such as the critical endpoint, the predicted first order phase transition between hadronic and partonic matter, and the chiral phase transition. The critical endpoint and the first order phase transition are expected to occur at finite baryon chemical potential and moderate temperatures. In the following we continue with the QCD phase diagram.

## 1.2 The Phase Diagram of Strongly Interacting Matter

Particle yields or ratios measured at different beam energies and analyzed with the statistical model provide sets of thermal parameters, temperature ( $T$ ) and baryo-chemical potential ( $\mu_b$ ), which establish a "line of chemical freeze-out" [19, 20, 21]. The results of the fits to experimental data are shown in a phase diagram of hadronic and quark-gluon matter in Fig. 1.1 [22] with full circles.

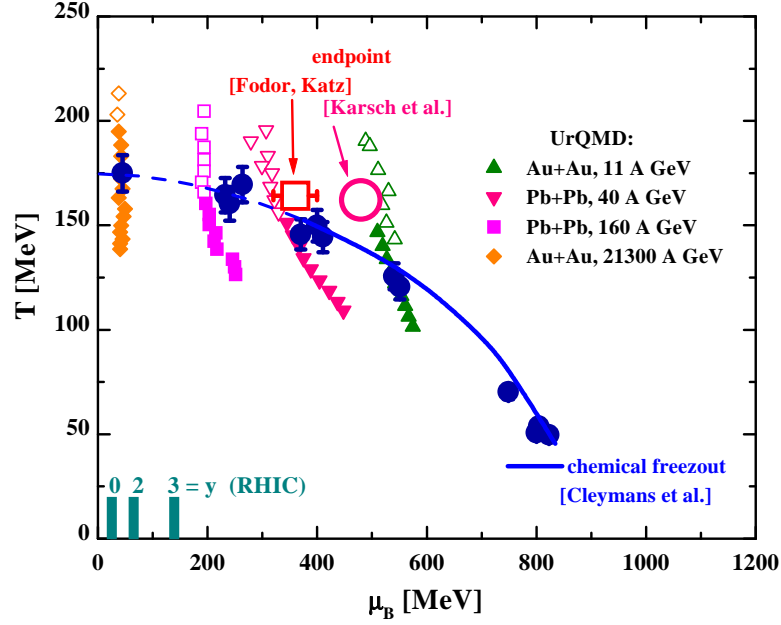


Figure 1.1: The phase diagram with the critical end point at  $\mu_B \approx 400$  MeV,  $T \approx 160$  MeV as predicted by Lattice QCD. In addition, the time evolution in the  $T - \mu$ -plane of a central cell in UrQMD calculations [27, 28] is depicted for different bombarding energies. Note, that the calculations indicate that bombarding energies  $E_{LAB} \leq 40$  A·GeV are needed to probe a first order phase transition. At RHIC (see insert at the  $\mu_B$  scale) this point is accessible in the fragmentation region only (taken from Ref. [29]).

Lattice QCD results [1, 23, 24] (cf. Fig. 1.1) show a crossing, but no first order phase transition to the QGP for vanishing or small chemical potentials  $\mu_B$ , i.e. at the conditions accessible at central rapidities at RHIC full energies. A first order phase transition does occur according to the QCD lattice calculations [1, 23, 24] only at high baryochemical potentials or densities, i.e. at SIS-300 and lower SPS energies and in the fragmentation region of RHIC,  $y \approx 4 - 5$  [25, 26]. The critical baryochemical potential is predicted [1, 23, 24] to be  $\mu_B^c \approx 400 \pm 50$  MeV and the critical temperature  $T_c \approx 150 - 160$  MeV.

A comparison of the thermodynamic parameters  $T$  and  $\mu_B$  extracted from the UrQMD-transport model in the central overlap regime of Au+Au collisions [29] with the QCD predictions is shown in Fig. 1.1, where the full dots with error bars denote the 'experimental' chemical freeze-out parameters – determined from fits to the experimental yields – taken from Ref. [21]. The triangular and quadratic symbols (time-ordered in vertical sequence) stand for temperatures

$T$  and chemical potentials  $\mu_B$  extracted from UrQMD transport calculations in central Au+Au (Pb+Pb) collisions at RHIC (21.3 A·TeV), 160, 40 and 11 A·GeV [27, 28] as a function of the reaction time (separated by 1 fm/c steps from top to bottom). The open symbols denote nonequilibrium configurations and correspond to  $T$  parameters extracted from the transverse momentum distributions, whereas the full symbols denote configurations in approximate pressure equilibrium in longitudinal and transverse direction.

During the nonequilibrium phase (open symbols) the transport calculations show much higher temperatures (or energy densities) than the 'experimental' chemical freeze-out configurations at all bombarding energies ( $\geq 11$  A·GeV). These numbers are also higher than the critical point (circle) of (2+1) flavor - Lattice QCD calculations by the Bielefeld-Swansea-Collaboration [24] (large open circle) and by the Wuppertal-Budapest-Collaboration [1, 23] (the star shows earlier results from [1, 23]). The energy density at  $(\mu_c, T_c)$  is in the order of  $\approx 1$  GeV/fm<sup>3</sup> (or slightly below). At RHIC energies a cross-over is expected at midrapidity, when stepping down in temperature during the expansion phase of the 'hot fireball'. This situation changes at lower SPS (and top AGS) as well as at the future GSI SIS-300 energies: sufficiently large chemical potentials  $\mu_B$  should allow for a first order phase transition [30] (to the right of the critical point in the  $(T, \mu_B)$  plane). The transport calculations show high temperatures (high energy densities) in the very early phase of the collisions, only. Here, hadronic interactions are weak due to formation time effects and yield little pressure. Diquark, quark and gluon interactions should cure this problem.

### 1.3 Signatures of the critical point and onset of deconfinement

The challenge is to identify signatures of the partonic phase, of the coexistence phase, or of the critical point which survive hadronization. It is obvious that those observables, which are generated in the early phase of the collision and interact weakly with other particles during the evolution of the fireball, are the most promising candidates in this respect.

One of the observables, which develop early, is the elliptic flow as it is related to the anisotropic fireball shape in coordinate space. An important question is

whether the hadron elliptic flow still remembers its partonic origin, as it is suggested by the data obtained at RHIC: the observed elliptic flow is extremely large and its strength scales with the number of constituent quarks, independent of the quark flavor content. Will this strength and its scaling break down below a certain beam energy? The answer to this question requires a beam energy scan of the elliptic flow of pions, kaons,  $\phi$ -mesons,  $D$ -mesons, charmonium, as well as for nucleons, and (multi-) strange hyperons (including the antiparticles). Particularly sensitive probes of the partonic phase are  $\phi$ -mesons and particles containing charm quarks because of their small hadronic cross sections. The experimental challenge is to measure all these particles up to high transverse momenta. This would also allow to search for the disappearance of the suppression of high energetic particles at a given beam energy as a signature for the phase transition.

The microscopic properties of QCD matter vary with temperature and density. The structure of hot and dense hadronic matter as created in energetic heavy-ion collisions is strongly related to the spectral properties of the hadrons and their interactions in the medium. Therefore, the investigation of hadronic excitations will shed light on the conditions inside the fireball. The in-medium properties of strange and charmed hadrons are not directly measurable, but might be extracted from their abundance, phase-space distributions, and flow pattern. Using electromagnetic radiation as a probe, one can study the in-medium modifications of light vector mesons. The dilepton observable accumulates information on the entire collision history, and, thus, provides a undistorted insight into the hot and dense phase [31].

The dissociation of charmonium due to Debye-screening in the QGP has been proposed as a signature for the deconfined phase [32]. Lattice QCD calculations predict different dissociation temperatures for the various charmonium states. As a consequence, the observation of sequential melting of  $\psi'$  and  $J/\psi$  mesons might serve as an indication for the onset of deconfinement [33].

Another sensitive probe of the structure of strongly interacting matter are the charm diffusion coefficients which differ for the QGP as compared to the hadronic phase [34]. These coefficients will affect significantly both the nuclear suppression factor and the elliptic flow of  $D$  mesons in a consistent way. Moreover, the relative yields of hadrons containing charm quarks ( $D^+$ ,  $D^-$ ,  $D^0$ ,  $D_s$ ,  $J/\psi$ ,  $\psi'$ ,  $\Lambda_c$ ) may allow to distinguish whether the early phase is partonic or hadronic [35]. Possible in-medium effects on the  $D$  meson are expected to modify the observed charmonia

ratio  $\psi'/(J/\psi)$ .

Particle correlations - in particular strange particle correlations - might serve as an indication for a phase coexistence which is expected to cause clustering or clumping of particles in the spinodal region. Nonstatistical fluctuations of charges, particle abundances or mean transverse momenta measured event-by-event have been proposed as a signature for critical opalescence which might occur at the critical endpoint.

## 1.4 LQCD results on susceptibilities

The concepts of fluctuations and correlations have a well defined physical interpretation for a system in thermal equilibrium. In this case fluctuations and correlations are related to the second cumulants of the partition function. These cumulants, or susceptibilities, can also be expressed in terms of integrals of equal-time correlation functions, which in turn characterize the (space-like) static responses of the system. In the case of heavy-ion collisions other, non-statistical, effects may contribute to the measured correlations. For example, the dynamical evolution of the system may be too fast for long range correlations to build up.

As already mentioned, the study of fluctuations is essential for the characterization of phase transitions. In case of a second order phase transition, the fluctuations of the order parameter diverge with a critical exponent specific to the universality class of the transition [36]. Furthermore, the system size dependences of the fluctuations can be used to distinguish between cross-over transitions and first or second order phase transitions using finite size scaling arguments.

A strongly interacting system in thermal equilibrium can be studied in the framework of Lattice QCD (LQCD) (see e.g. [37] for a review). Here we will just use the results from LQCD as input to discuss the relevant physics

A system in thermal equilibrium (for a grand-canonical ensemble) is characterized by its partition function

$$Z = \text{Tr} \left[ \exp \left( -\frac{H - \sum_i \mu_i Q_i}{T} \right) \right] \quad (1.1)$$

where  $H$  is the Hamiltonian of the system, and  $Q_i$  and  $\mu_i$  denote the conserved charges and the corresponding chemical potentials, respectively. In case of three flavor QCD these are strangeness, baryon-number, and electric charge, or, equiv-



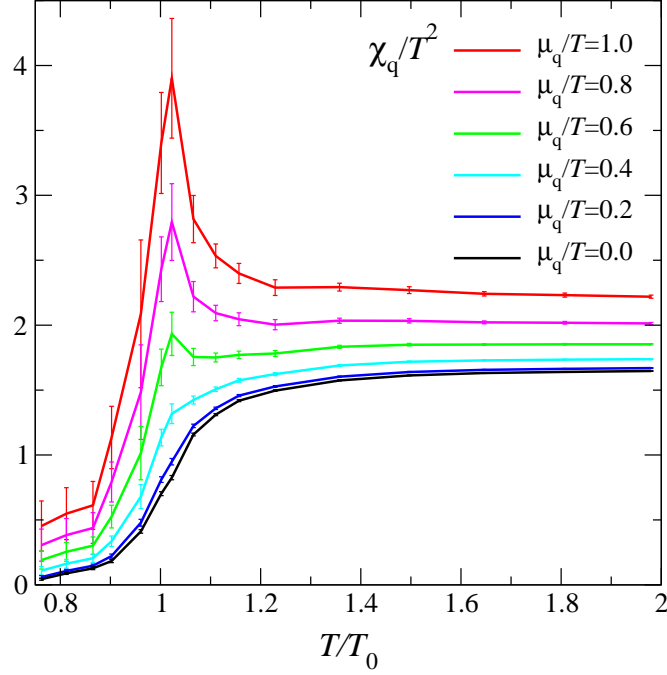


Figure 1.2:  $\chi_q/T^2$  as a function of  $T/T_0$  for various  $\mu_q/T$  according to Ref. [38].

alently, the three quark flavors up, down, and strange. The mean values and the (co-)variances are then expressed in terms of derivatives of the partition function with respect to the appropriate chemical potentials,

$$\begin{aligned} \langle Q_i \rangle &= T \frac{\partial}{\partial \mu_i} \log(Z) \\ \langle \delta Q_i \delta Q_j \rangle &= T^2 \frac{\partial^2}{\partial \mu_i \partial \mu_j} \log(Z) \equiv VT \chi_{i,j} \end{aligned} \quad (1.2)$$

with  $\delta Q_i = Q_i - \langle Q_i \rangle$ . Here we have introduced the susceptibilities

$$\chi_{i,j} = \frac{T}{V} \frac{\partial^2}{\partial \mu_i \partial \mu_j} \log(Z) \quad (1.3)$$

which are generally quoted as a measure of the (co-)variances. The diagonal susceptibilities,  $\chi_{i,i}$ , are a measure for the fluctuations of the system, whereas the off-diagonal susceptibilities,  $\chi_{i,j}$  ( $i \neq j$ ), characterize the correlations between the conserved charges  $Q_i$  and  $Q_j$ .

Quark number ( $q$ ) susceptibility is defined as follows [38]:

$$\frac{\chi_q}{T^2} = \left( \frac{\partial}{\partial(\mu_u/T)} + \frac{\partial}{\partial(\mu_d/T)} \right) \frac{n_u + n_d}{T^3}, \quad (1.4)$$

Eq. 1.4 has been used in Fig. 1.2 to plot the dimensionless quark number susceptibility  $\chi_q/T^2$  as a function of  $T/T_0$  for various  $\mu_q/T$ . The peak, which develops in  $\chi_q$  as  $\mu_q$  increases, is a sign that fluctuations in the baryon density are growing as the critical endpoint in the  $(\mu, T)$  plane is approached.

## 1.5 Fluctuations and Correlations in High Energy Collisions

Fluctuations and correlations are important characteristics of any physical system. They provide essential information about the effective degrees of freedom and their possible quasi-particle nature. In addition, the susceptibilities, which characterize the correlations and fluctuations, determine the response of the system to small external forces.

In general, one can distinguish between several classes of fluctuations. On the most fundamental level there are quantum fluctuations, which arise if the specific observable does not commute with the Hamiltonian of the system under consideration. These fluctuations probably play less a role for the physics of heavy-ion collisions. Second, there are “dynamical” fluctuations and correlations reflecting the underlying dynamics of the system. Examples are density fluctuations, which are controlled by the compressibility of the system. Finally, there are “trivial” fluctuations induced by the measurement process itself, such as finite number statistics, etc. These need to be understood, controlled and subtracted in order to access the dynamical fluctuations which tell us about the properties of the system.

A prominent example, where the measurement of correlations has led to a scientific breakthrough, are the fluctuations of the cosmic microwave background radiation, first carried out by the COBE satellite [39] and later refined by WMAP [40]. In the case of the cosmic microwave background the fluctuations are on the level of  $10^{-4}$  with respect to the thermal distribution. In addition, a large dipole correlation, due to the motion of the earth through the heatbath of the

microwave background, has been seen and needed to be subtracted before the more interesting correlations, due to the big bang, could be revealed.

Increased fluctuations of various observables are expected at the onset of deconfinement, near the critical point or when the system passes the first order phase transition line during expansion.

It is predicted [41] that the onset of deconfinement should lead to a non-monotonous behaviour in the energy dependence of multiplicity fluctuations, the so-called “shark fin”. Furthermore, an increase of multiplicity fluctuations near the critical point of strongly interacting matter is expected [42].

In a very simplified picture, due to fluctuations the system can either be in a quark-gluon plasma phase or not when the mean temperature of the fireball is close to the transition temperature. Even if the collision energy is fixed, the temperature in that picture fluctuates and can therefore be in some collisions sufficient for the creation of QGP and in some not.

For a first order phase transition it is expected that a mixed phase of hadrons and QGP is formed at the temperature of the phase transition. For a large range of energy densities the temperature stays constant while more matter is transformed to QGP (“latent heat”). Therefore, at a fixed collision energy, one does not expect two different classes of events, but the events should only differ in the amount of QGP created at the early stage of the collision.

It is therefore not sufficient to look just for two different classes of events; a more sophisticated analysis of fluctuations is needed. The commonly used fluctuation observables are the event-by-event fluctuations of particle ratios, the electrical charge, the mean transverse momentum and the particle multiplicity.

The centrality (Chapter 3), energy (Chapter 5) and system size dependence (Chapter 6) of event-by-event fluctuations in the particle multiplicity in heavy-ion collisions are studied in this thesis. Our main tool is the Hadron-String-Dynamics (HSD) transport approach (Chapter 2). Electric charge and baryonic number are also objects of consideration in Chapter 4. Fluctuations of the  $K/\pi$  number ratio are presented in Chapter 7 and compared with statistical model results. STAR results on forward-backward multiplicity correlations are discussed in Chapter 8. A summary in Chapter 9 concludes the thesis, while specific details are presented in the Appendixes.

## Chapter 2

# The Hadron-String-Dynamics Transport Approach

### 2.1 Off-shell relativistic transport

The description of strongly interacting quantum fields - as encountered in relativistic nucleus-nucleus collisions - is based on two-particle irreducible (2PI) approaches that allow for a consistent treatment of quantum systems out-of-equilibrium as well as in thermal equilibrium. Especially the powerful method of the ‘Schwinger-Keldysh’ [43, 44, 45, 46] or ‘closed time path’ (CTP) (non-equilibrium) real-time Greens functions has been shown to provide an appropriate basis for the formulation of the complex problems in the various areas of nonequilibrium quantum many-body physics. Within this framework one can derive valid approximations - depending, of course, on the problem under consideration - by preserving overall consistency relations. Originally, the resulting causal Dyson-Schwinger equation of motion for the one-particle Greens functions (or two-point functions), i.e. the Kadanoff-Baym (KB) equations [47], have served as the underlying scheme for deriving various transport phenomena and generalized transport equations. A brief derivation of such transport schemes is presented in the following (closely in line with the review [48]).

#### 2.1.1 The Kadanoff-Baym equations

As mentioned above a natural starting point for non-equilibrium quantum theory is provided by the closed-time-path (CTP) method. Here all quantities

are given on a special real-time contour with the time argument running from  $-\infty$  to  $\infty$  on the chronological branch (+) and returning from  $\infty$  to  $-\infty$  on the antichronological branch (-). In cases of systems prepared at a time  $t_0$  this value is (instead of  $-\infty$ ) the start and end point of the real-time contour (cf. Fig. 2.1). In particular the path ordered Green functions (in case of real scalar fields  $\phi(x)$  which provide a representative example) are defined as

$$\begin{aligned} G(x, y) &= \langle T^P \{ \phi(x) \phi(y) \} \rangle \\ &= \Theta^P(x_0 - y_0) \langle \phi(x) \phi(y) \rangle + \Theta^P(y_0 - x_0) \langle \phi(y) \phi(x) \rangle \end{aligned} \quad (2.1)$$

where the operator  $T^P$  orders the field operators according to the position of their arguments on the real-time path as expressed by the path step-functions  $\Theta^P$ . The expectation value in Eq. 2.1 is taken with respect to some initial density matrix  $\rho_0$ , which is constant in time, while the operators in the Heisenberg picture contain the entire time dependence of the non-equilibrium system, i.e.  $O(t) = \exp(iH(t - t_0)) O \exp(-iH(t - t_0))$ .

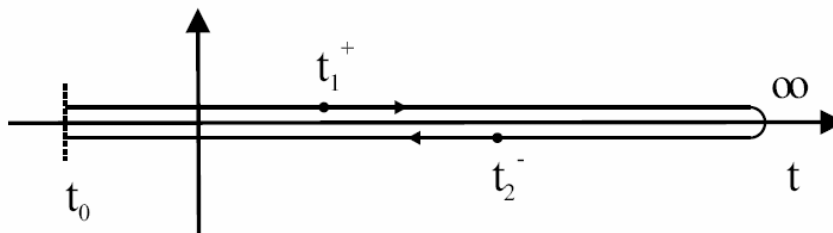


Figure 2.1: The closed time contour in the Schwinger-Keldysh formalism. The figure is taken from Ref. [48].

Self-consistent equations of motion for these Green functions can be obtained with help of the two-particle irreducible (2PI) effective action  $\Gamma[G]$ . It is given by the Legendre transform of the generating functional of the connected Green functions  $W$  as

$$\Gamma[G] = \Gamma^\circ + \frac{i}{2} [ \ln(1 - \odot_p G_o \odot_p \Sigma) + \odot_p G \odot_p \Sigma ] + \Phi[G] \quad (2.2)$$

in case of vanishing vacuum expectation value  $\langle 0 | \phi(x) | 0 \rangle = 0$ . In Eq. 2.2  $\Gamma^\circ$  depends only on free Green functions and is treated as a constant, while the symbols  $\odot_p$  represent convolution integrals over the closed time path in Fig. 2.1.

The functional  $\Phi$  is the sum of all closed  $2PI$  diagrams built up by *full propagators*  $G$ ; it determines the *self-energies* by functional variation as

$$\Sigma(x, y) = 2i \frac{\delta\Phi}{\delta G(y, x)}. \quad (2.3)$$

From the effective action  $\Gamma(G)$  the *equations of motion for the Green function* are determined by the stationarity condition

$$\delta\Gamma/\delta G = 0. \quad (2.4)$$

In line with the position of the coordinates on the contour there exist four different two-point functions (in case of scalar boson fields  $\phi$  as an example)

$$\begin{aligned} i G^c(x, y) &= i G^{++}(x, y) = \langle T^c \{ \phi(x) \phi(y) \} \rangle, \\ i G^<(x, y) &= i G^{+-}(x, y) = \langle \{ \phi(y) \phi(x) \} \rangle, \\ i G^>(x, y) &= i G^{-+}(x, y) = \langle \{ \phi(x) \phi(y) \} \rangle, \\ i G^a(x, y) &= i G^{--}(x, y) = \langle T^a \{ \phi(x) \phi(y) \} \rangle. \end{aligned} \quad (2.5)$$

Here  $T^c$  ( $T^a$ ) represent the (anti-)time-ordering operators in case of both arguments lying on the (anti-)chronological branch of the real-time contour. These four functions are not independent of each other. In particular the non-continuous functions  $G^c$  and  $G^a$  are built up by the Wightman functions  $G^>$  and  $G^<$  and the usual  $\Theta$ -functions in the time coordinates.

By using the stationarity condition for the action [Eq. 2.4](#) and resolving the time structure of the path ordered quantities one obtains the Kadanoff-Baym equations for the time evolution of the Wightman functions [\[49, 50\]](#):

$$\begin{aligned}
- [\partial_\mu^x \partial_x^\mu + m^2] G^{\lesseqgtr}(x, y) &= \Sigma^\delta(x) G^{\lesseqgtr}(x, y) \\
&+ \int_{t_0}^{x_0} dz_0 \int d^d z [\Sigma^>(x, z) - \Sigma^<(x, z)] G^{\lesseqgtr}(z, y) \\
&- \int_{t_0}^{y_0} dz_0 \int d^d z \Sigma^{\lesseqgtr}(x, z) [G^>(z, y) - G^<(z, y)] , \\
- [\partial_\mu^y \partial_y^\mu + m^2] G^{\lesseqgtr}(x, y) &= \Sigma^\delta(y) G^{\lesseqgtr}(x, y) \\
&+ \int_{t_0}^{x_0} dz_0 \int d^d z [G^>(x, z) - G^<(x, z)] \Sigma^{\lesseqgtr}(z, y) \\
&- \int_{t_0}^{y_0} dz_0 \int d^d z G^{\lesseqgtr}(x, z) [\Sigma^>(z, y) - \Sigma^<(z, y)] ,
\end{aligned} \tag{2.6}$$

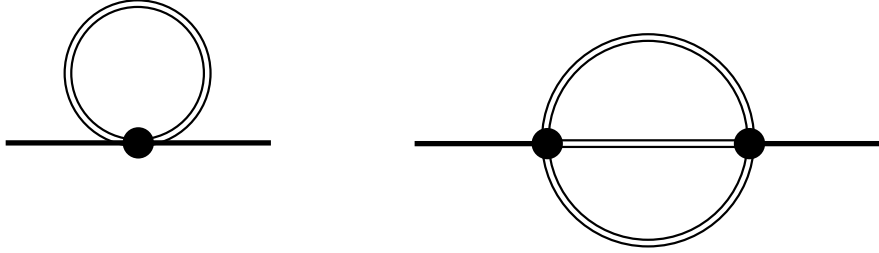


Figure 2.2: Self-energies of the Kadanoff-Baym equation in case of the scalar  $\Phi^4$ -theory: tadpole self-energy (l.h.s.) and sunset self-energy (r.h.s.). Since the lines represent full Green functions the self-energies are self-consistent with the external coordinates indicated by full dots. The figure is taken from Ref. [48].

As an example let us consider again the case of the scalar  $\Phi^4$ -theory. Within the 3-loop approximation for the 2PI effective action one gets two different self-energies: In leading order of the coupling constant only the tadpole diagram (l.h.s. of Fig. 2.2) contributes and leads to the generation of an effective mass for the field quanta. This self-energy (in coordinate space) is given by

$$\Sigma^\delta(x) = \frac{\lambda}{2} i G^<(x, x) , \tag{2.7}$$

and is local in space and time. In next order in the coupling constant (i.e.  $\lambda^2$ )

the non-local sunset self-energy (r.h.s. of Fig. 2.2) enters the time evolution as

$$\begin{aligned}\Sigma^{\lessgtr}(x, y) &= -\frac{\lambda^2}{6} G^{\lessgtr}(x, y) G^{\lessgtr}(x, y) G^{\gtrless}(y, x) \\ \longrightarrow \Sigma^{\lessgtr}(x, y) &= -\frac{\lambda^2}{6} \left[ G^{\lessgtr}(x, y) \right]^3.\end{aligned}\quad (2.8)$$

Thus the Kadanoff-Baym Eq. 2.6 (in  $\Phi^4$ -theory) includes the influence of a mean-field on the particle propagation – generated by the tadpole diagram – as well as scattering processes as inherent in the sunset diagram.

The Kadanoff-Baym equation describes the full quantum nonequilibrium time evolution on the two-point level for a system prepared at an initial time  $t_0$ , i.e. when higher order correlations are discarded. The causal structure of this initial value problem is obvious since the time integrations are performed over the past up to the actual time  $x_0$  (or  $y_0$ , respectively) and do not extend to the future.

Furthermore, also linear combinations of the Green functions in single-time representation are of interest and shed further light on the spectral properties of the system. The retarded Green function  $G^R$  and the advanced Green function  $G^A$  are given as

$$\begin{aligned}G^R(x_1, x_2) &= \Theta(t_1 - t_2) [ G^>(x_1, x_2) - G^<(x_1, x_2) ] \\ &= \Theta(t_1 - t_2) \langle [ \phi(x_1), \phi(x_2) ]_- \rangle \\ &= G^c(x_1, x_2) - G^<(x_1, x_2) = G^>(x_1, x_2) - G^a(x_1, x_2),\end{aligned}\quad (2.9)$$

$$\begin{aligned}G^A(x_1, x_2) &= -\Theta(t_2 - t_1) [ G^>(x_1, x_2) - G^<(x_1, x_2) ] \\ &= -\Theta(t_2 - t_1) \langle [ \phi(x_1), \phi(x_2) ]_- \rangle \\ &= G^c(x_1, x_2) - G^>(x_1, x_2) = G^<(x_1, x_2) - G^a(x_1, x_2).\end{aligned}\quad (2.10)$$

These Green functions contain exclusively spectral but no statistical information of the system. Their time evolution is determined by Dyson-Schwinger equations



and given by (cf. Ref. [50])

$$- [\partial_\mu^{x_1} \partial_\mu^{x_1} + m^2 + \Sigma^\delta(x_1)] G^R(x_1, x_2) \quad (2.11)$$

$$= \delta^{(d+1)}(x_1 - x_2) + \int d^{d+1} z \Sigma^R(x_1, z) G^R(z, x_2) ,$$

$$- [\partial_\mu^{x_1} \partial_\mu^{x_1} + m^2 + \Sigma^\delta(x_1)] G^A(x_1, x_2) \quad (2.12)$$

$$= \delta^{(d+1)}(x_1 - x_2) + \int d^{d+1} z \Sigma^A(x_1, z) G^A(z, x_2) ,$$

where the retarded and advanced self-energies  $\Sigma^R, \Sigma^A$  are defined via  $\Sigma^>, \Sigma^<$  similar to the Green functions. Thus the retarded (advanced) Green functions are determined by retarded (advanced) quantities, only.

The framework specified above now allows for a general derivation of covariant transport approaches.

### 2.1.2 Off-shell relativistic transport theory

The derivation of generalized transport equations starts by rewriting the Kadanoff-Baym equation for the Wightman functions in coordinate space ( $x_1 = (t_1, \vec{x}_1), x_2 = (t_2, \vec{x}_2)$ ) Eq. 2.6 as

$$[\partial_{x_1}^\mu \partial_\mu^{x_1} + m^2 + \Sigma^\delta(x_1)] i G^{\lessgtr}(x_1, x_2) = i I_1^{\lessgtr}(x_1, x_2) . \quad (2.13)$$

The collision terms on the r.h.s. of Eq. 2.13 are given in  $D = d + 1$  space-time dimensions by convolution integrals over coordinate space self-energies and Green functions:

$$\begin{aligned} I_1^{\lessgtr}(x_1, x_2) = & - \int_{t_0}^{t_1} d^D z [\Sigma^>(x_1, z) - \Sigma^<(x_1, z)] G^{\lessgtr}(z, x_2) \\ & + \int_{t_0}^{t_2} d^D z \Sigma^{\lessgtr}(x_1, z) [G^>(z, x_2) - G^<(z, x_2)] . \end{aligned} \quad (2.14)$$

In the general case of an arbitrary (scalar) quantum field theory  $\Sigma^\delta$  is the local (non-dissipative) part of the path self-energy while  $\Sigma^{\lessgtr}$  resemble the non-local collisional self-energy contributions. In the representation Eq. 2.14 the integration boundaries are exclusively given for the time coordinates, while the integration

over the spatial coordinates extends over the whole spatial volume from  $-\infty$  to  $+\infty$  in  $d$  dimensions.

Since transport theories are formulated in phase-space one now changes to the Wigner representation via Fourier transformation with respect to the rapidly varying ('intrinsic') relative coordinate  $\Delta x = x_1 - x_2$  and treats the system evolution in terms of the ('macroscopic') mean space-time coordinate  $x = (x_1 + x_2)/2$  and the four-momentum  $p = (p_0, \vec{p})$ . The functions in Wigner space (indicated by a 'bar') are obtained as

$$\bar{F}(p, x) = \int_{-\infty}^{\infty} d^D \Delta x e^{+i \Delta x_\mu p^\mu} F(x_1 = x + \Delta x/2, x_2 = x - \Delta x/2) . \quad (2.15)$$

For the formulation of transport theory in the Wigner representation one has to focus not only on the transformation properties of ordinary two-point functions as given in [Eq. 2.15](#), but also of convolution integrals as appearing in [Eq. 2.14](#).

A convolution integral in  $D$  dimensions (for arbitrary functions  $F, G$ ),

$$H(x_1, x_2) = \int_{-\infty}^{\infty} d^D z F(x_1, z) G(z, x_2) \quad (2.16)$$

transforms as

$$\begin{aligned} \bar{H}(p, x) &= \int_{-\infty}^{\infty} d^D \Delta x e^{+i \Delta x_\mu p^\mu} H(x_1, x_2) \quad (2.17) \\ &= \int_{-\infty}^{\infty} d^D \Delta x e^{+i \Delta x_\mu p^\mu} \int_{-\infty}^{\infty} d^D z F(x_1, z) G(z, x_2) \\ &= e^{+i \frac{1}{2} (\partial_p^\mu \cdot \partial_{x'}^\mu - \partial_x^\mu \cdot \partial_{p'}^\mu)} \left[ \bar{F}(p, x) \bar{G}(p', x') \right] \Big|_{x'=x, p'=p} . \end{aligned}$$

In accordance with the standard assumption of transport theory one assumes that all functions only smoothly evolve in the mean space-time coordinates and thus one restricts to first order derivatives. All terms proportional to second or higher order derivatives in the mean space-time coordinates (also mixed ones) will be dropped. Thus the Wigner transformed convolution integrals ([Eq. 2.16](#)) are given in *first order gradient approximation* by,

$$\bar{H}(p, x) = \bar{F}(p, x) \bar{G}(p, x) + i \frac{1}{2} \{ \bar{F}(p, x) , \bar{G}(p, x) \} + \mathcal{O}(\partial_x^2) , \quad (2.18)$$

using the relativistic generalization of the Poisson bracket

$$\{\bar{F}(p, x), \bar{G}(p, x)\} = \partial_\mu^p \bar{F}(p, x) \cdot \partial_x^\mu \bar{G}(p, x) - \partial_x^\mu \bar{F}(p, x) \cdot \partial_\mu^p \bar{G}(p, x). \quad (2.19)$$

In order to obtain the dynamics for the spectral functions within the approximate scheme one starts with the Dyson-Schwinger equations for the retarded and advanced Green functions in coordinate space (Eq. 2.11, Eq. 2.12). The further procedure consists in the following steps: First one has to

i) transform the above equations into the Wigner representation and apply the first order gradient approximation. In this limit the convolution integrals yield the product terms and the general Poisson bracket of the self-energies and the Green functions  $\{\Sigma^{R/A}, G^{R/A}\}$ . Furtheron, both equations are represented in terms of real quantities by the decomposition of the retarded and advanced Green functions and self-energies as

$$\begin{aligned} \bar{G}^{R/A} &= Re \bar{G}^R \pm i Im \bar{G}^R = Re \bar{G}^R \mp i \bar{A}/2, & \bar{A} &= \mp 2 Im \bar{G}^{R/A}, \\ \bar{\Sigma}^{R/A} &= Re \bar{\Sigma}^R \pm i Im \bar{\Sigma}^R = Re \bar{\Sigma}^R \mp i \bar{\Gamma}/2, & \bar{\Gamma} &= \mp 2 Im \bar{\Sigma}^{R/A}. \end{aligned} \quad (2.20)$$

In Wigner space the real parts of the retarded and advanced Green functions and self-energies are equal, while the imaginary parts have opposite sign and are proportional to the spectral function  $\bar{A}$  and the width  $\bar{\Gamma}$ , respectively. The next step consists in

ii) the separation of the real part and the imaginary part of the two equations for the retarded and advanced Green functions that have to be fulfilled independently. Thus one obtains four real-valued equations for the self-consistent retarded and advanced Green functions. In the last step

iii) one gets simple relations by linear combination of these equations, i.e. by adding/subtracting the relevant equations.

This finally leads to two algebraic relations for the spectral function  $\bar{A}$  and the real part of the retarded Green function  $Re \bar{G}^R$  in terms of the width  $\bar{\Gamma}$  and

the real part of the retarded self-energy  $Re \bar{\Sigma}^R$  as [51, 52]:

$$[ p_0^2 - \vec{p}^2 - m^2 - \bar{\Sigma}^\delta + Re \bar{\Sigma}^R ] Re \bar{G}^R = 1 + \frac{1}{4} \bar{\Gamma} \bar{A}, \quad (2.21)$$

$$[ p_0^2 - \vec{p}^2 - m^2 - \bar{\Sigma}^\delta + Re \bar{\Sigma}^R ] \bar{A} = \bar{\Gamma} Re \bar{G}^R. \quad (2.22)$$

Note that all terms with first order gradients have disappeared in Eq. 2.21 and Eq. 2.22. A first consequence of Eq. 2.22 is a direct relation between the real and the imaginary parts of the retarded/advanced Green function, which reads (for  $\bar{\Gamma} \neq 0$ ):

$$Re \bar{G}^R = \frac{p_0^2 - \vec{p}^2 - m^2 - \bar{\Sigma}^\delta - Re \bar{\Sigma}^R}{\bar{\Gamma}} \bar{A}. \quad (2.23)$$

Inserting Eq. 2.23 in Eq. 2.21 one ends up with the following result for the spectral function and the real part of the retarded Green function

$$\bar{A} = \frac{\bar{\Gamma}}{[ p_0^2 - \vec{p}^2 - m^2 - \bar{\Sigma}^\delta - Re \bar{\Sigma}^R ]^2 + \bar{\Gamma}^2/4} = \frac{\bar{\Gamma}}{\bar{M}^2 + \bar{\Gamma}^2/4}, \quad (2.24)$$

$$Re \bar{G}^R = \frac{[ p_0^2 - \vec{p}^2 - m^2 - \bar{\Sigma}^\delta - Re \bar{\Sigma}^R ]}{[ p_0^2 - \vec{p}^2 - m^2 - \bar{\Sigma}^\delta - Re \bar{\Sigma}^R ]^2 + \bar{\Gamma}^2/4} = \frac{\bar{M}}{\bar{M}^2 + \bar{\Gamma}^2/4}, \quad (2.25)$$

where the mass-function  $\bar{M}(p, x)$  in Wigner space has been introduced as:

$$\bar{M}(p, x) = p_0^2 - \vec{p}^2 - m^2 - \bar{\Sigma}^\delta(x) - Re \bar{\Sigma}^R(p, x). \quad (2.26)$$

The spectral function (Eq. 2.24) shows a typical Breit-Wigner shape with energy- and momentum-dependent self-energy terms. Although the above equations are purely algebraic solutions and contain no derivative terms, they are valid up to the first order in the gradients!

In addition, subtraction of the real parts and adding up the imaginary parts lead to the time evolution equations

$$p^\mu \partial_\mu^x \bar{A} = \frac{1}{2} \{ \bar{\Sigma}^\delta + Re \bar{\Sigma}^R, \bar{A} \} + \frac{1}{2} \{ \bar{\Gamma}, Re \bar{G}^R \}, \quad (2.27)$$

$$p^\mu \partial_\mu^x Re \bar{G}^R = \frac{1}{2} \{ \bar{\Sigma}^\delta + Re \bar{\Sigma}^R, Re \bar{G}^R \} - \frac{1}{8} \{ \bar{\Gamma}, \bar{A} \}. \quad (2.28)$$

The Poisson bracket containing the mass-function  $\bar{M}$  leads to the well-known

drift operator  $p^\mu \partial_\mu^x \bar{F}$  (for an arbitrary function  $\bar{F}$ ), i.e.

$$\begin{aligned} \{ \bar{M}, \bar{F} \} &= \{ p_0^2 - \vec{p}^2 - m^2 - \bar{\Sigma}^\delta - Re \bar{\Sigma}^R, \bar{F} \} \\ &= 2 p^\mu \partial_\mu^x \bar{F} - \{ \bar{\Sigma}^\delta + Re \bar{\Sigma}^R, \bar{F} \}, \end{aligned} \quad (2.29)$$

such that the first order [Eq. 2.27](#) and [Eq. 2.28](#) can be written in a more compact form as

$$\{ \bar{M}, \bar{A} \} = \{ \bar{\Gamma}, Re \bar{G}^R \}, \quad (2.30)$$

$$\{ \bar{M}, Re \bar{G}^R \} = -\frac{1}{4} \{ \bar{\Gamma}, \bar{A} \}. \quad (2.31)$$

When inserting [Eq. 2.24](#) and [Eq. 2.25](#) one finds that these first order time evolution equations are *solved* by the algebraic expressions. In this case the following relations hold:

$$\{ \bar{M}, \bar{A} \} = \{ \bar{\Gamma}, Re \bar{G}^R \} = \{ \bar{M}, \bar{\Gamma} \} \frac{\bar{M}^2 - \bar{\Gamma}^2/4}{[\bar{M}^2 + \bar{\Gamma}^2/4]^2}, \quad (2.32)$$

$$\{ \bar{M}, Re \bar{G}^R \} = -\frac{1}{4} \{ \bar{\Gamma}, \bar{A} \} = \{ \bar{M}, \bar{\Gamma} \} \frac{\bar{M} \bar{\Gamma}/2}{[\bar{M}^2 + \bar{\Gamma}^2/4]^2}. \quad (2.33)$$

Thus one has derived the proper structure of the spectral function ([Eq. 2.24](#)) within the first-order gradient (or semiclassical) approximation. Together with the explicit form for the real part of the retarded Green function ([Eq. 2.25](#)) the dynamics of the spectral properties now are fixed in a consistent manner (up to first order in the gradients).

### 2.1.3 Generalized transport equation

As a next step one rewrites the memory terms in the collision integrals ([Eq. 2.14](#)) such that the time integrations extend from  $-\infty$  to  $+\infty$ . In this respect one considers the initial time  $t_0 = -\infty$  whereas the upper time boundaries

$t_1, t_2$  are taken into account by  $\Theta$ -functions, i.e.

$$\begin{aligned} I_1^{\lessgtr}(x_1, x_2) &= - \int_{-\infty}^{\infty} d^D x' \Theta(t_1 - t') [\Sigma^>(x_1, x') - \Sigma^<(x_1, x')] G^{\lessgtr}(x', x_2) \quad (2.34) \\ &+ \int_{-\infty}^{\infty} d^D x' \Sigma^{\lessgtr}(x_1, x') \Theta(t_2 - t') [G^>(x', x_2) - G^<(x', x_2)] \\ &= - \int_{-\infty}^{\infty} d^D x' \Sigma^R(x_1, x') G^{\lessgtr}(x', x_2) + \Sigma^{\lessgtr}(x_1, x') G^A(x', x_2) . \end{aligned}$$

One now performs the analogous steps as invoked before for the retarded and advanced Dyson-Schwinger equations. One starts with a first order gradient expansion of the Wigner transformed Kadanoff-Baym equation using [Eq. 2.34](#) for the memory integrals. Again the real and the imaginary parts in the resulting equation are separated and have to be satisfied independently. At the end of this procedure one obtains a generalized transport equation [[47](#), [53](#), [54](#), [51](#), [52](#), [55](#), [56](#), [57](#), [58](#)]:

$$\underbrace{2p^\mu \partial_\mu^x i \bar{G}^{\lessgtr} - \{\bar{\Sigma}^\delta + Re \bar{\Sigma}^R, i\bar{G}^{\lessgtr}\}}_{\{\bar{M}, i \bar{G}^{\lessgtr}\}} - \{i \bar{\Sigma}^{\lessgtr}, Re \bar{G}^R\} = i \bar{\Sigma}^< i\bar{G}^> - i \bar{\Sigma}^> i \bar{G}^< \quad (2.35)$$

$$\{i \bar{\Sigma}^{\lessgtr}, Re \bar{G}^R\} = i \bar{\Sigma}^< i\bar{G}^> - i \bar{\Sigma}^> i \bar{G}^<$$

as well as a generalized mass-shell equation

$$\underbrace{[p^2 - m^2 - \bar{\Sigma}^\delta - Re \bar{\Sigma}^R]}_{\bar{M}} i\bar{G}^{\lessgtr} = i\bar{\Sigma}^{\lessgtr} Re \bar{G}^R + \frac{1}{4} \{i\bar{\Sigma}^>, i\bar{G}^<\} - \frac{1}{4} \{i\bar{\Sigma}^<, i\bar{G}^>\} \quad (2.36)$$

with the mass-function  $\bar{M}$  specified in [Eq. 2.26](#). Since the Green function  $G^{\lessgtr}(x_1, x_2)$  consists of an antisymmetric real part and a symmetric imaginary part with respect to the relative coordinate  $x_1 - x_2$ , the Wigner transform of this function is purely imaginary. It is thus convenient to represent the Wightman functions in Wigner space by the real-valued quantities  $i\bar{G}^{\lessgtr}(p, x)$ . Since the collisional self-energies obey the same symmetry relations in coordinate space and in phase-space, they will be kept also as  $i\bar{\Sigma}^{\lessgtr}(p, x)$  furtheron.

In the transport equation ([Eq. 2.35](#)) one recognizes on the l.h.s. the drift term  $p^\mu \partial_\mu^x i\bar{G}^{\lessgtr}$ , as well as the Vlasov term with the local self-energy  $\bar{\Sigma}^\delta$  and the real part of the retarded self-energy  $Re \bar{\Sigma}^R$ . On the other hand the r.h.s.

represents the collision term with its typical ‘gain and loss’ structure. The loss term  $i\bar{\Sigma}^> i\bar{G}^<$  (proportional to the Green function itself) describes the scattering out of a respective phase-space cell whereas the gain term  $i\bar{\Sigma}^< i\bar{G}^>$  takes into account scatterings into the actual cell.

The last term on the l.h.s. of Eq. 2.35  $\{ i\bar{\Sigma}^{\lessgtr}, Re \bar{G}^R \}$  (so called ‘backflow’ term) is very *peculiar* since it does not contain directly the distribution function  $i\bar{G}^<$ . This second Poisson bracket vanishes in the quasiparticle approximation and thus does not appear in the on-shell Boltzmann limit. As demonstrated in detail in Refs. [47, 51, 52, 55, 56, 57, 58] the second Poisson bracket  $\{ i\bar{\Sigma}^{\lessgtr}, Re \bar{G}^R \}$  governs the evolution of the off-shell dynamics for nonequilibrium systems.

Although the generalized transport equation (Eq. 2.35) and the generalized mass-shell equation (Eq. 2.36) have been derived from the same Kadanoff-Baym equation in a first order gradient expansion, both equations are not exactly equivalent [54, 51, 58]. Instead, they deviate from each other by contributions of second gradient order, which are hidden in the term  $\{ i\bar{\Sigma}^{\lessgtr}, Re \bar{G}^R \}$  (see below).

#### 2.1.4 Transport in the Botermans-Malfliet scheme

Furthermore, one recognizes by subtraction of the  $i\bar{G}^>$  and  $i\bar{G}^<$  mass-shell and transport equations, that the dynamics of the spectral function  $\bar{A} = i\bar{G}^> - i\bar{G}^<$  is determined in the same way as derived from the retarded and advanced Dyson-Schwinger equations (Eq. 2.24 and Eq. 2.30). The inconsistency between the two equations Eq. 2.35 and Eq. 2.36 vanishes since the differences are contained in the collisional contributions on the r.h.s. of Eq. 2.35.

In order to evaluate the  $\{ i\bar{\Sigma}^<, Re \bar{G}^R \}$ -term on the l.h.s. of Eq. 2.35 and to explore the differences between the KB- and BM-form of the transport equations (see below) it is useful to introduce distribution functions for the Green functions and self-energies as

$$\begin{aligned} i\bar{G}^<(p, x) &= \bar{N}(p, x) \bar{A}(p, x), & i\bar{G}^>(p, x) &= [1 + \bar{N}(p, x)] \bar{A}(p, x), \\ i\bar{\Sigma}^<(p, x) &= \bar{N}^\Sigma(p, x) \bar{\Gamma}(p, x), & i\bar{\Sigma}^>(p, x) &= [1 + \bar{N}^\Sigma(p, x)] \bar{\Gamma}(p, x). \end{aligned} \quad (2.37)$$

In equilibrium the distribution function with respect to the Green functions  $\bar{N}$  and the self-energies  $\bar{N}^\Sigma$  are given as Bose functions in the energy  $p_0$  at given temperature (in case of a bosonic theory); they thus are equal in equilibrium

but in general might differ out-of-equilibrium. Following the argumentation of Botermans and Malfliet [54] the distribution functions  $\bar{N}$  and  $\bar{N}^\Sigma$  in Eq. 2.37 should be identical within the second term of the l.h.s. of Eq. 2.35 in order to obtain a consistent first order gradient expansion (without hidden higher order gradient terms). In order to demonstrate their argument let's write

$$i\bar{\Sigma}^< = \bar{\Gamma} \bar{N}^\Sigma = \bar{\Gamma} \bar{N} + \bar{K} . \quad (2.38)$$

The 'correction' term

$$\bar{K} = \bar{\Gamma} ( \bar{N}^\Sigma - \bar{N} ) = ( i\bar{\Sigma}^< i\bar{G}^> - i\bar{\Sigma}^> i\bar{G}^< ) \bar{A}^{-1} , \quad (2.39)$$

is proportional to the collision term of the generalized transport equation (Eq. 2.35), which itself is already of first order in the gradients. Thus, whenever a distribution function  $\bar{N}^\Sigma$  appears within a Poisson bracket, the difference term  $(\bar{N}^\Sigma - \bar{N})$  becomes of second order in the gradients and should be omitted for consistency. As a consequence  $\bar{N}^\Sigma$  can be replaced by  $\bar{N}$  and thus, the self-energy in the Poisson bracket term  $\{i\bar{\Sigma}^<, Re \bar{G}^R\}$  is

$$i\bar{\Sigma}^< = i\bar{G}^< \cdot \bar{\Gamma} / \bar{A} = \bar{N} \bar{\Gamma} . \quad (2.40)$$

The generalized transport equation (Eq. 2.35) then can be written in short-hand notation

$$\frac{1}{2} \bar{A} \bar{\Gamma} \left[ \{ \bar{M} , i\bar{G}^< \} - \frac{1}{\bar{\Gamma}} \{ \bar{\Gamma} , \bar{M} \cdot i\bar{G}^< \} \right] = i\bar{\Sigma}^< i\bar{G}^> - i\bar{\Sigma}^> i\bar{G}^< \quad (2.41)$$

with the mass-function  $\bar{M}$  (Eq. 2.26). The transport equation (Eq. 2.41) within the Botermans-Malfliet (BM) form resolves the discrepancy between the generalized mass-shell equation (Eq. 2.36) and the generalized transport equation in its original Kadanoff-Baym (KB) form (Eq. 2.35). In fact, as shown in Ref. [48] numerical solutions of both transport schemes (KB and BM) are very close to each other (at least for the strongly interacting  $\Phi^4$ -theory).



### 2.1.5 Generalized testparticle representation

The generalized transport equation (Eq. 2.41) allows to extend the traditional on-shell transport approaches for which efficient numerical recipes have been set up [59, 60, 61, 62, 63, 64, 65, 66, 67, 68, 69, 70, 71, 72, 73] (and Refs. therein). In order to obtain a practical solution to the transport equation (Eq. 2.41) one introduces a testparticle ansatz for the Green function  $G^<$ , more specifically for the real and positive semidefinite quantity

$$F(X, P) = \bar{N}(X, P) \bar{A}(X, P) = i G^<(X, P) \quad (2.42)$$

$$\sim \sum_{i=1}^N \delta^3(\vec{X} - \vec{X}_i(t)) \delta^3(\vec{P} - \vec{P}_i(t)) \delta(P_0 - \varepsilon_i(t)).$$

In the most general case (where the self energies depend on four-momentum  $P$ , time  $t$  and the spatial coordinates  $\vec{X}$ ) the equations of motion for the testparticles read [52]

$$\frac{d\vec{X}_i}{dt} = \frac{1}{1 - C_{(i)}} \frac{1}{2\varepsilon_i} \left[ 2\vec{P}_i + \vec{\nabla}_{P_i} \text{Re}\Sigma_{(i)}^R + \frac{\varepsilon_i^2 - \vec{P}_i^2 - M_0^2 - \text{Re}\Sigma_{(i)}^R}{\Gamma_{(i)}} \vec{\nabla}_{P_i} \Gamma_{(i)} \right] \quad (2.43)$$

$$\frac{d\vec{P}_i}{dt} = - \frac{1}{1 - C_{(i)}} \frac{1}{2\varepsilon_i} \left[ \vec{\nabla}_{X_i} \text{Re}\Sigma_{(i)}^R + \frac{\varepsilon_i^2 - \vec{P}_i^2 - M_0^2 - \text{Re}\Sigma_{(i)}^R}{\Gamma_{(i)}} \vec{\nabla}_{X_i} \Gamma_{(i)} \right], \quad (2.44)$$

$$\frac{d\varepsilon_i}{dt} = \frac{1}{1 - C_{(i)}} \frac{1}{2\varepsilon_i} \left[ \frac{\partial \text{Re}\Sigma_{(i)}^R}{\partial t} + \frac{\varepsilon_i^2 - \vec{P}_i^2 - M_0^2 - \text{Re}\Sigma_{(i)}^R}{\Gamma_{(i)}} \frac{\partial \Gamma_{(i)}}{\partial t} \right], \quad (2.45)$$

where the notation  $F_{(i)}$  implies that the function is taken at the coordinates of the testparticle, i.e.  $F_{(i)} \equiv F(t, \vec{X}_i(t), \vec{P}_i(t), \varepsilon_i(t))$ .

In Eq. 2.43 - Eq. 2.45 a common multiplication factor  $(1 - C_{(i)})^{-1}$  appears, which contains the energy derivatives of the retarded self energy

$$C_{(i)} = \frac{1}{2\varepsilon_i} \left[ \frac{\partial}{\partial \varepsilon_i} \text{Re}\Sigma_{(i)}^R + \frac{\varepsilon_i^2 - \vec{P}_i^2 - M_0^2 - \text{Re}\Sigma_{(i)}^R}{\Gamma_{(i)}} \frac{\partial}{\partial \varepsilon_i} \Gamma_{(i)} \right]. \quad (2.46)$$

It yields a shift of the system time  $t$  to the 'eigentime' of particle  $i$  defined by  $\tilde{t}_i = t/(1 - C_{(i)})$ . As one immediately verifies, the derivatives with respect to the 'eigentime', i.e.  $d\vec{X}_i/d\tilde{t}_i$ ,  $d\vec{P}_i/d\tilde{t}_i$  and  $d\varepsilon_i/d\tilde{t}_i$  then emerge without this

renormalization factor for each testparticle  $i$  when neglecting higher order time derivatives in line with the semiclassical approximation scheme.

Some limiting cases should be mentioned explicitly: In case of a momentum-independent 'width'  $\Gamma(X)$  one takes  $M^2 = P^2 - Re\Sigma^R$  as an independent variable instead of  $P_0$ , which then fixes the energy (for given  $\vec{P}$  and  $M^2$ ) to

$$P_0^2 = \vec{P}^2 + M^2 + Re\Sigma_{X\vec{P}M^2}^R . \quad (2.47)$$

Eq. 2.45 then turns to ( $\Delta M_i^2 = M_i^2 - M_0^2$ )

$$\frac{d\Delta M_i^2}{dt} = \frac{\Delta M_i^2}{\Gamma_{(i)}} \frac{d\Gamma_{(i)}}{dt} \leftrightarrow \frac{d}{dt} \ln \left( \frac{\Delta M_i^2}{\Gamma_{(i)}} \right) = 0 \quad (2.48)$$

for the time evolution of the test-particle  $i$  in the invariant mass squared. In case of  $\Gamma = const$  the familiar equations of motion for testparticles in on-shell transport approaches are regained.

### 2.1.6 Collision terms

The collision term of the Kadanoff-Baym equation can only be worked out in more detail by giving explicit approximations for  $\Sigma^<$  and  $\Sigma^>$ . A corresponding collision term can be formulated in full analogy to Refs. [61, 74], e.g. from Dirac-Brueckner theory following detailed balance as (omitting the bars for the phase-space representation, i.e.  $\bar{A} = A$ ,  $\bar{N} = N$ ,  $\bar{\Gamma} = \Gamma$  etc.)

$$\begin{aligned} I_{coll}(X, \vec{P}, M^2) &= Tr_2 Tr_3 Tr_4 A(X, \vec{P}, M^2) A(X, \vec{P}_2, M_2^2) A(X, \vec{P}_3, M_3^2) A(X, \vec{P}_4, M_4^2) \\ &|T((\vec{P}, M^2) + (\vec{P}_2, M_2^2) \rightarrow (\vec{P}_3, M_3^2) + (\vec{P}_4, M_4^2))|_{\mathcal{A}, \mathcal{S}}^2 \delta^{(4)}(P + P_2 - P_3 - P_4) \\ &\left[ N_{X\vec{P}_3M_3^2} N_{X\vec{P}_4M_4^2} \bar{f}_{X\vec{P}M^2} \bar{f}_{X\vec{P}_2M_2^2} - N_{X\vec{P}M^2} N_{X\vec{P}_2M_2^2} \bar{f}_{X\vec{P}_3M_3^2} \bar{f}_{X\vec{P}_4M_4^2} \right] \end{aligned} \quad (2.49)$$

with

$$\bar{f}_{X\vec{P}M^2} = 1 + \eta N_{X\vec{P}M^2} \quad (2.50)$$

and  $\eta = \pm 1$  for bosons/fermions, respectively. The indices  $\mathcal{A}, \mathcal{S}$  stand for the antisymmetric/symmetric matrix element of the in-medium scattering amplitude  $T$  in case of fermions/bosons. In Eq. 2.49 the trace over particles 2,3,4 reads

explicitly for fermions

$$Tr_2 = \sum_{\sigma_2, \tau_2} \frac{1}{(2\pi)^4} \int d^3 P_2 \frac{dM_2^2}{2\sqrt{\vec{P}_2^2 + M_2^2}}, \quad (2.51)$$

where  $\sigma_2, \tau_2$  denote the spin and isospin of particle 2. In case of bosons one has

$$Tr_2 = \sum_{\sigma_2, \tau_2} \frac{1}{(2\pi)^4} \int d^3 P_2 \frac{dP_{0,2}^2}{2}, \quad (2.52)$$

since here the spectral function  $A_B$  is normalized as

$$\int \frac{dP_0^2}{4\pi} A_B(X, P) = 1 \quad (2.53)$$

whereas for fermions one obtains

$$\int \frac{dP_0}{2\pi} A_F(X, P) = 1. \quad (2.54)$$

Neglecting the 'gain-term' in [Eq. 2.49](#) one recognizes that the collisional width of the particle in the rest frame is given by

$$\begin{aligned} \Gamma_{coll}(X, \vec{P}, M^2) = & \quad (2.55) \\ & Tr_2 Tr_3 Tr_4 |T((\vec{P}, M^2) + (\vec{P}_2, M_2^2) \rightarrow (\vec{P}_3, M_3^2) + (\vec{P}_4, M_4^2))|_{\mathcal{A}, \mathcal{S}}^2 \\ & A(X, \vec{P}_2, M_2^2) A(X, \vec{P}_3, M_3^2) A(X, \vec{P}_4, M_4^2) \\ & \delta^4(P + P_2 - P_3 - P_4) N_{X\vec{P}_2 M_2^2} \bar{f}_{X\vec{P}_3 M_3^2} \bar{f}_{X\vec{P}_4 M_4^2}, \end{aligned}$$

where – as in [Eq. 2.49](#) – local on-shell scattering processes are assumed for the transitions  $P + P_2 \rightarrow P_3 + P_4$ . The extension of [Eq. 2.49](#) to inelastic scattering processes (e.g.  $NN \rightarrow N\Delta$ ) or ( $\pi N \rightarrow \Delta$  etc.) is straightforward when exchanging the elastic transition amplitude  $T$  by the corresponding inelastic one and taking care of Pauli-blocking or Bose-enhancement for the particles in the final state.

For particles of infinite life time in vacuum – such as protons – the collisional width ([Eq. 2.55](#)) has to be identified with twice the imaginary part of the self energy. Thus the transport approach determines the particle spectral function

dynamically via [Eq. 2.55](#) for all hadrons if the in-medium transition amplitudes  $T$  are known in their full off-shell dependence. Since this information is not available for configurations of hot and dense matter, which is still the major subject of future development, a couple of assumptions and numerical approximation schemes have to be invoked in actual applications as in the HSD transport approach to be employed in the investigations within this work.

## 2.2 The covariant transport approach HSD

Whereas nucleus-nucleus collisions at top SPS or RHIC energies are dominated by the mesons dynamics this no longer holds for nucleus-nucleus collisions at lower energies and especially for proton-nucleus or pion-nucleus reactions. In the latter cases the dynamics of the hadronic fermions (nucleons and their elementary excitations) are more important and require a slightly different dynamical treatment since the fermion degrees follow a Dirac equation instead of a Klein-Gordon equation. Especially when considering a nucleus close to its groundstate only nucleon degrees of freedom play a role since time-like bosonic states cannot be excited. Accordingly, the general off-shell dynamics outlined in [section 2.1](#) has to be reformulated for the case of fermions, too.

The general connection between bosonic and fermionic degrees of freedom is given by the mass-function ([Eq. 2.26](#)). For the bosons  $B$  the mass function is

$$M_B(p, x) = p_0^2 - \vec{p}^2 - m^2 - \text{Re}\Sigma(p, x) \quad (2.56)$$

where the (local and nonlocal) selfenergies are included in  $\text{Re}\Sigma(p, x)$ . In case of fermions the Lorentz covariant mass-function ([Eq. 2.56](#)) has to be modified, i.e. one has to split in explicit contributions due to scalar and vector interactions, separately. This leads to the mass-function for fermions  $F$

$$M_F(p, x) = \Pi_0^2 - \vec{\Pi}^2 - m_h^{*2}, \quad (2.57)$$

with the effective mass and four-momentum given by

$$m_h^*(x, p) = m_h + U_h^S(x, p) \quad (2.58)$$

$$\Pi^\mu(x, p) = p^\mu - U_h^\mu(x, p).$$

In Eq. 2.58  $U_h^S(x, p)$  and  $U_h^\mu(x, p)$  denote the real part of the scalar and vector hadron self-energies, respectively, and  $m_h$  stands for the bare (vacuum) mass of baryon  $h$ . The quantities  $U_h^S(x, p)$  and  $U_h^\mu(x, p)$  will be specified below.

With the replacement Eq. 2.57 the fermion off-shell dynamics can be defined in full analogy to the mesonic sector in subsection 2.2.5. Since the explicit and formulae play no relevant role in the present study, which essentially addresses high energy nucleus-nucleus collisions at top SPS and RHIC energies, an explicit representation of the latter equations is omitted here.

Inserting Eq. 2.57 in the generalized transport equation (Eq. 2.35 or Eq. 2.41), the covariant off-shell transport theory emerges, that has been denoted as **Hadron-String-Dynamics** (HSD) [73, 61]. It is formally written as a coupled set of transport equations for the phase-space distributions  $N_h(x, p)$  ( $x = (t, \vec{r})$ ,  $p = (\varepsilon, \vec{p})$ ) of fermion  $h$  [73, 75, 61] with a spectral function  $A_h(x, p)$  (using  $i\bar{G}_h^<(x, p) = N_h(x, p)A_h(x, p)$ ), i.e.

$$\begin{aligned} & \{(\Pi_\mu - \Pi_\nu \partial_\mu^p U_h^\nu - m_h^* \partial_\mu^p U_h^S) \partial_x^\mu + (\Pi_\nu \partial_\mu^x U_h^\nu + m_h^* \partial_\mu^x U_h^S) \partial_p^\mu\} N_h(x, p) A_h(x, p) \\ & - \{i\Sigma^<, Re G^R\} = \sum_{h_2 h_3 h_4} Tr_2 Tr_3 Tr_4 [T^\dagger T]_{12 \rightarrow 34} \delta^4(\Pi + \Pi_2 - \Pi_3 - \Pi_4) \quad (2.59) \\ & \quad \times A_h(x, p) A_{h_2}(x, p_2) A_{h_3}(x, p_3) A_{h_4}(x, p_4) \\ & \quad \times \{N_{h_3}(x, p_3) N_{h_4}(x, p_4) \bar{f}_h(x, p) \bar{f}_{h_2}(x, p_2) - N_h(x, p) N_{h_2}(x, p_2) \bar{f}_{h_3}(x, p_3) \bar{f}_{h_4}(x, p_4)\}. \end{aligned}$$

Here  $\partial_\mu^x \equiv (\partial_t, \vec{\nabla}_r)$  and  $\partial_\mu^p \equiv (\partial_\varepsilon, \vec{\nabla}_p)$ , ( $\mu = 0, 1, 2, 3$ ). The backflow term in Eq. 2.59 is given by

$$\begin{aligned} -\{i\Sigma^<, Re G^R\} &= \partial_p^\mu \left( \frac{M_h(x, p)}{M_h(x, p)^2 + \Gamma_h(x, p)^2/4} \right) \partial_\mu^x (N_h(x, p) \Gamma_h(x, p)) \quad (2.60) \\ & - \partial_\mu^x \left( \frac{M_h(x, p)}{M_h(x, p)^2 + \Gamma_h(x, p)^2/4} \right) \partial_p^\mu (N_h(x, p) \Gamma_h(x, p)). \end{aligned}$$

It stands for the off-shell evolution which vanishes in the on-shell limit, when the spectral function  $A_h(x, p)$  does not change its shape during the propagation through the medium, i.e.  $\vec{\nabla}_r \Gamma(x, p) = 0$  and  $\vec{\nabla}_p \Gamma(x, p) = 0$ .

In Eq. 2.59  $[T^\dagger T]_{12 \rightarrow 34}$  is the 'transition rate' for the process  $1 + 2 \rightarrow 3 + 4$  (which is taken to be on-shell in the default HSD approach). In the cms of the

colliding particles the transition rate is given by

$$[T^\dagger T]_{12 \rightarrow 34} \Rightarrow v_{12} \left. \frac{d\sigma}{d\Omega} \right|_{1+2 \rightarrow 3+4}, \quad (2.61)$$

where  $d\sigma/d\Omega$  is the differential cross section of the reaction and  $v_{12}$  the relative velocity of particles 1 and 2. Note, that a generalized collisional term for  $n \leftrightarrow m$  reactions is given in Ref. [76] and optionally included in HSD, which is, however, not used in the present study.

The hadron quasi-particle properties in Eq. 2.59 are defined via the mass-function (Eq. 2.57) with Eq. 2.58 while the phase-space factors

$$\bar{f}_h(x, p) = 1 \pm N_h(x, p) \quad (2.62)$$

are responsible for fermion Pauli-blocking or Bose enhancement, respectively, depending on the type of hadron in the final/initial channel. The transport approach (Eq. 2.59) is fully specified by  $U_h^S(x, p)$  and  $U_h^\mu(x, p)$ , which determine the mean-field propagation of the hadrons, and by the transition rates  $T^\dagger T$  in the collision term, that describe the scattering and hadron production/absorption rates. Note that the collisional width  $\Gamma_{coll}$  is given explicitly by Eq. 2.55. Accordingly, the coupled set of hadronic transport equations (Eq. 2.59) may be employed for a large variety of hadronic systems at relativistic (and nonrelativistic) energies.

### 2.2.1 Scalar and vector potentials in HSD

Apart from differential cross sections in the general transport equations the scalar and vector potentials  $U_h^S$  and  $U_h^\mu$  play an essential role for nuclear binding close to the groundstate as well as for proton-nucleus scattering where the optical potential modifies the proton wavelength while propagating through the nucleus. There are several ways to determine  $U_h^S$  and  $U_h^\mu$  in a relativistic framework: i) one may start with a covariant Ansatz for the in-medium nucleon-nucleon interaction and then fit the parameters to nuclear masses and excitation spectra; ii) independently one can address a many-body framework like Dirac-Brueckner theory for  $U_h^S$  and  $U_h^\mu$  and fit the numerical results by an analytic function in the baryon density  $\rho$  and the relative nucleon momentum  $\vec{p}$ . The strategy employed in HSD is based on both concepts simultaneously and involves extrapolations to

high nucleon densities and relative momenta  $\vec{p}$ .

The baryon density  $\rho$  here stands for

$$\rho = \sqrt{j_\mu j^\mu} \quad (2.63)$$

with  $j_\mu$  denoting the baryon four-current:

$$j_\mu(x) = \sum_h \text{Tr} p_\mu N_h(x, p) A_h(x, p), \quad (2.64)$$

where the sum runs over all baryons  $h$ . In the on-shell limit [Eq. 2.64](#) reads as

$$j_\mu(x) = \sum_h \int \frac{d^3p}{E} p_\mu N_h(x, p). \quad (2.65)$$

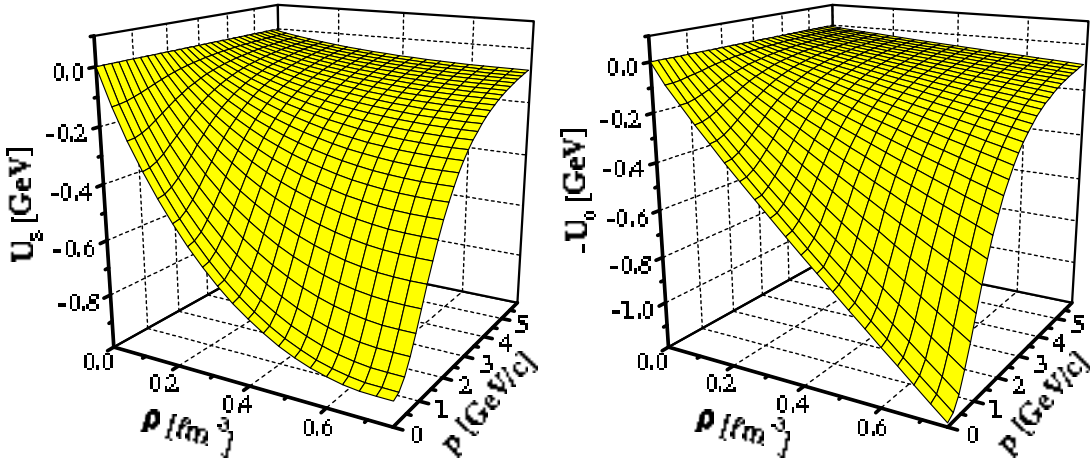


Figure 2.3: The nucleon scalar ( $U_S$ ) and negative vector potential ( $-U_0$ ) as a function of the nuclear density  $\rho$  and relative momentum  $p$  of the nucleon with respect to the nuclear matter rest frame as implemented in the HSD transport approach. The figure is taken from Ref. [\[77\]](#).

In Ref. [\[73\]](#) the scalar and vector mean-fields  $U_h^S$  and  $U_h^\mu$  have been determined in the mean-field limit from an effective hadronic Lagrangian density  $\mathcal{L}_H$  that has been fitted to the equation of state of nucleonic matter as resulting from the Nambu-Jona-Lasinio (NJL) model. Without going through the detailed arguments the nucleon scalar ( $U_S$ ) and negative vector potential ( $-U_0$ ) are shown in [Fig. 2.3](#) as a function of the baryon density  $\rho$  and relative momentum  $\vec{p}$  of the nucleon with respect to the nuclear matter rest frame. Whereas the vector potential

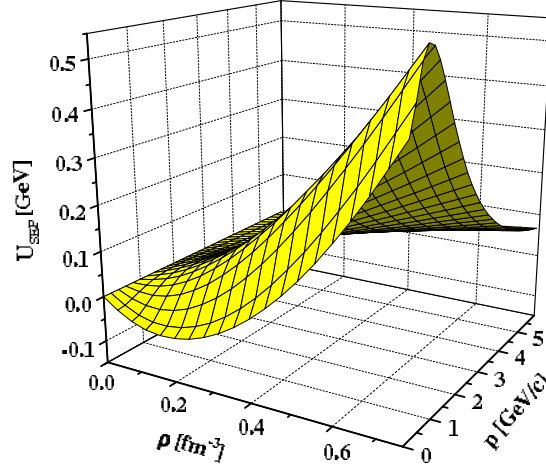


Figure 2.4: The potential  $U_{SEP}$  (5) – as resulting from the nucleon scalar ( $U_S$ ) and vector potential ( $U_0$ ) in Fig. 2.3 – as a function of the nuclear density  $\rho$  and relative momentum  $p$  of the nucleon with respect to the nuclear matter rest frame. The figure is taken from Ref. [77].

increases practically linearly with density (at low momentum  $\vec{p}$ ) the scalar potential saturates with density such that the nucleon effective mass  $m^* = m_0 + U_S$  almost drops to zero for  $\rho \geq 0.6 \text{ fm}^{-3}$ . Both potentials decrease rather fast in magnitude with momentum  $\vec{p}$  and practically vanish above a few GeV/c. Accordingly, these nucleon potentials play no decisive role in nucleus-nucleus collisions at very high energies.

In Fig. 2.4 the real part of the potential

$$U_{SEP} = U_0(\rho_0, \vec{p}) + \sqrt{\vec{p}^2 + (m_N + U_S)^2} - \sqrt{\vec{p}^2 + m_N^2} \quad (2.66)$$

is shown as a function of  $\rho$  and  $\vec{p}$ . Whereas one sees a net attraction for momenta  $|\vec{p}| \leq 0.5 \text{ GeV/c}$  up to densities of  $\approx 0.3 \text{ fm}^{-3}$ , the net potential becomes repulsive for higher momenta, reaches a maximum repulsion at  $|\vec{p}| \approx 1 \text{ GeV/c}$  and then drops again with  $|\vec{p}|$ . As stated in the review [61] at density  $\rho_0$  the potential  $U_{SEP}$  compares well with the potential from the experimental data analysis of Hama et al. [78] as well as Dirac-Brueckner computations from Ref. [79] up to a kinetic energy  $E_{kin}$  of 1 GeV [73]. Furthermore, Eq. 2.66 reduces to the familiar expression for the Schroedinger equivalent potential (Eq. (3.16) of Ref. [61]) in the low density limit, which has the familiar interpretation of a nonrelativistic potential.



### 2.2.2 Hadronic degrees of freedom

The HSD approach propagates explicitly on the baryonic side nucleons ( $p, n$ ),  $\Delta(1232)$ ,  $N^*(1440)$ ,  $N^*(1535)$ ,  $\Lambda$ ,  $\Sigma$  and  $\Sigma^*$  hyperons,  $\Xi$ 's,  $\Xi^*$ 's and  $\Omega$ 's as well as their antiparticles. The mesonic sector includes the pseudoscalar  $0^-$  and vector  $1^-$  SU(4)-16 plets states - cf. Fig. 2.5 - as well as the axialvector  $1^+$   $a_1$  meson, which plays a particular role in dilepton production but is of no specific relevance in this work.

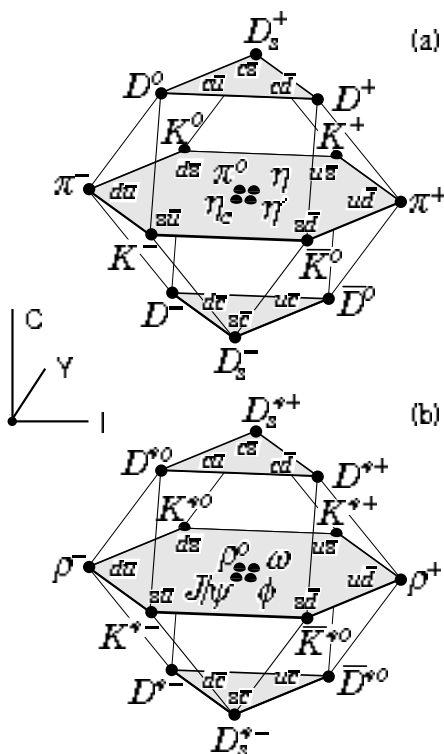


Figure 2.5: SU(4) diagram showing the 16-plets for pseudoscalar (a) and vector mesons (b) made of  $u, d, s$  and  $c$  quarks as a function of isospin  $I$ , charm  $C$  and hypercharge  $Y = S + B - C/3$ , where  $B$  is the baryon number. The figure is taken from [80].

In a first approximation it is assumed in HSD that all baryons (made out of light ( $u, d$ ) quarks) have the same scalar and vector self-energies as the nucleons while the hyperons pick up a factor  $2/3$  according to the light quark content and  $\Xi$ 's a factor of  $1/3$ , respectively. The multi-strange  $\Omega$ 's are propagated without potentials. Baryons of mass  $> 1.6$  GeV (or mesons of mass  $> 1.3$  GeV) are treated as 'strings' which have to be considered as color neutral continuum excitations of the hadrons.

As pre-hadronic degrees of freedom HSD includes 'effective' quarks (anti-quarks) and diquarks (antidiquarks) which interact with cross sections in accordance with the constituent quark model (cf. [subsection 2.2.3](#)).

### 2.2.3 Hadron-hadron interactions

Inelastic baryon–baryon  $BB \rightarrow X$  and meson-baryon  $mB \rightarrow X$  collisions with energies above  $\sqrt{s_{th}} \simeq 2.6$  GeV for  $BB$  and  $\sqrt{s_{th}} \simeq 2.3$  GeV for  $mB$  collisions are described by the FRITIOF string model [\[81, 82\]](#) (incorporating PYTHIA v 5.5 with JETSET v 7.3 for the production and fragmentation of jets [\[83\]](#)).

The low energy hadron–hadron collisions – baryon-baryon ( $BB$ ), meson-baryon ( $mB$ ) and meson-meson ( $mm$ ) - are modeled in line with experimental cross sections when available or based on different microscopic models. The backward reactions for 2-particle interaction  $2 \leftrightarrow 2$  and resonance formation and decay  $1 \leftrightarrow 2$  channels are calculated using detailed balance. A detailed description of all channels included in HSD as well as elementary cross sections in comparison with existing experimental data are given in the early Refs. [\[73, 84, 61\]](#). The updated version of the off-shell production cross section for the vector mesons ( $\rho, \omega, \phi$ ) (including different in-medium scenarios) as well as an updated  $\eta$ -production cross section in  $BB$  and  $mB$  collisions is given in Ref. [\[85\]](#).

It worth to point out that the low energy nucleon-nucleon and meson-nucleon cross sections fit well to the high energy parametrizations as shown in [Fig. 2.6](#) for  $\pi^+p$  (upper part) and  $pp$  (lower part) reactions together with the data from Ref. [\[80\]](#).

### 2.2.4 The LUND String model

In the HSD approach the high energy inelastic hadron-hadron collisions are described by the FRITIOF model [\[81, 82\]](#), where two incoming hadrons emerge the reaction as two excited color singlet states, i.e. 'strings'. According to the Lund model [\[81, 82\]](#) a 'string' is characterized by the leading constituent quarks of the incoming hadron and a tube of color flux is supposed to be formed connecting the rapidly receding string-ends. In the HSD approach baryonic ( $qq - q$ ) and mesonic ( $q - \bar{q}$ ) strings are considered with different flavors ( $q = u, d, s$ ). In the uniform color field of the strings virtual  $q\bar{q}$  or  $qq\bar{q}\bar{q}$  pairs are produced causing the tube to fission and thus to create mesons or baryon-antibaryon pairs.

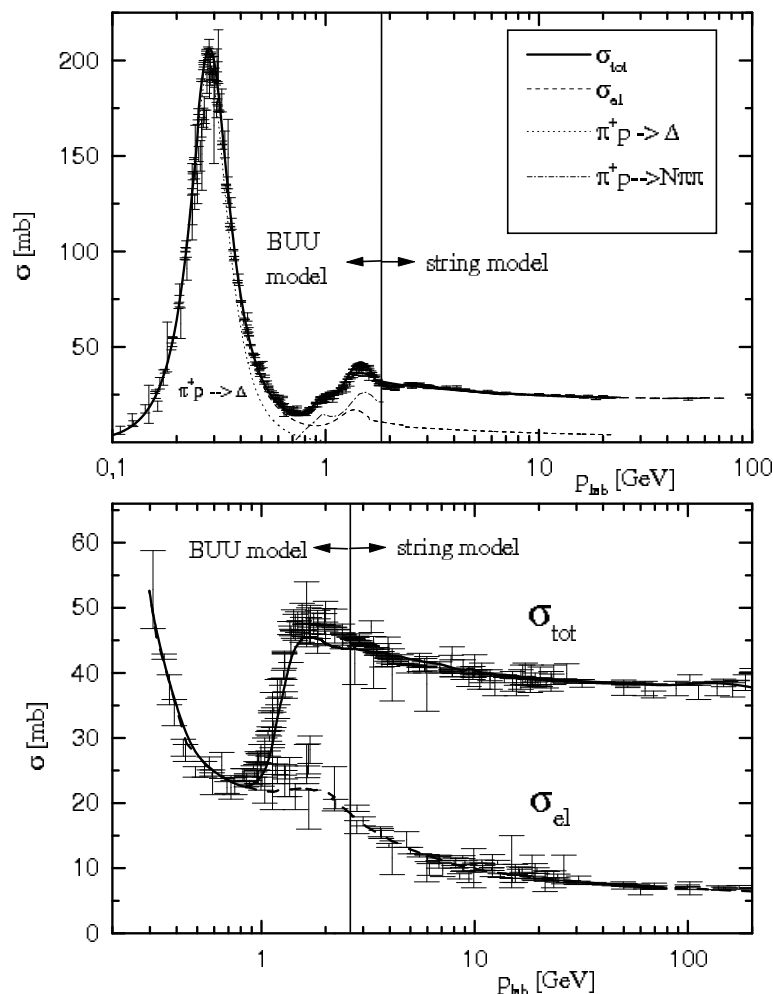


Figure 2.6: The total and elastic  $\pi^+$ -proton (upper part) and proton-proton (lower part) cross sections in comparison with the experimental data from Ref. [80]. The figure is taken from Ref. [84].

The production probability  $P$  of massive  $s\bar{s}$  or  $qq\bar{q}\bar{q}$  pairs is suppressed in comparison to light flavor production ( $u\bar{u}$ ,  $d\bar{d}$ ) according to the Schwinger formula [43]

$$\frac{P(s\bar{s})}{P(u\bar{u})} = \gamma_s = \exp\left(-\pi \frac{m_s^2 - m_q^2}{2\kappa}\right) \quad (2.67)$$

with  $\kappa \approx 1$  GeV/fm denoting the string tension. Thus in the Lund string picture the production of strangeness and baryon-antibaryon pairs is controlled by the constituent quark and diquark masses. Inserting the constituent quark masses  $m_u = 0.3$  GeV and  $m_s = 0.5$  GeV a value of  $\gamma_s \approx 0.3$  is obtained. While the

strangeness production in proton-proton collisions at SPS energies is reasonably well reproduced with this value, the strangeness yield for p + Be collisions at AGS energies is underestimated by roughly 30% (cf. [84]). For that reason the relative factors used in the HSD model are [84]

$$u : d : s : diquark = \begin{cases} 1 : 1 : 0.3 : 0.07 & \text{for } \sqrt{s} \geq 20 \text{ GeV} \\ 1 : 1 : 0.4 : 0.07 & \text{for } \sqrt{s} \leq 5 \text{ GeV} \end{cases} \quad (2.68)$$

with a linear transition of the strangeness suppression factor as a function of  $\sqrt{s}$  in between.

Additionally a fragmentation function  $f(x, m_t)$  has to be specified, which is the probability distribution for hadrons with transverse mass  $m_t = (p_t^2 + m^2)^{1/2}$  to acquire the energy-momentum fraction  $x$  from the fragmenting string,

$$f(x, m_t) \approx \frac{1}{x} (1-x)^a \exp(-bm_t^2/x), \quad (2.69)$$

with  $a = 0.23$  and  $b = 0.34 \text{ GeV}^{-2}$  [84].

Furthermore, the LUND model [81, 82] includes partonic diffractive scattering and mini-jet production as well [83]. The latter phenomena are not important at SPS energies and below, however, become appreciable at RHIC energies. In this respect the HSD approach dynamically also includes the hard partonic processes as far as quarks and antiquarks are involved. However, it does not employ hard gluon-gluon processes beyond the level of 'string phenomenology'. This has to be kept in mind with respect to the predictive power of the model at RHIC energies and beyond.

The medium modifications due to the hadron self-energies, furthermore, require to introduce some conserving approximations in the collision terms in line with the modified quasi-particle properties. Since these in-medium modifications – related to 'low momentum physics' – are not of primary interest in this study an explicit discussion here is discarded and referred to Refs. [73, 61].

The implementation of the string fragmentation model into a covariant transport theory implies to use a time scale for the particle production process, i. e. the formation time  $\tau_F$ . The formation time includes the formation of the string, the fission of the string due to  $q\bar{q}$  and  $qq\bar{q}\bar{q}$  production into small sub-strings and the time to form physical hadrons. It can be interpreted as the time needed for a

hadron to tunnel out of the vacuum and to form its internal wavefunction. The 'unformed' hadrons, i.e. those under formation time, are called 'pre-hadrons'.

In the HSD model the formation time is a single fixed parameter for all hadrons and is set to  $\tau_F = 0.8 \text{ fm}/c$  [73] in the rest frame of the new produced particle. In the center of mass of a string the hadronization starts after the formation time and proceeds to the stringends as illustrated in Fig. 2.7. The formation point of a new produced hadron with velocity  $\vec{\beta}$  in the string cms is given by

$$\vec{x} = \vec{x}_{coll} + \vec{\beta} \cdot \tau_F, \quad (2.70)$$

where  $\vec{x}_{coll}$  is the collision point of the two incoming hadrons.

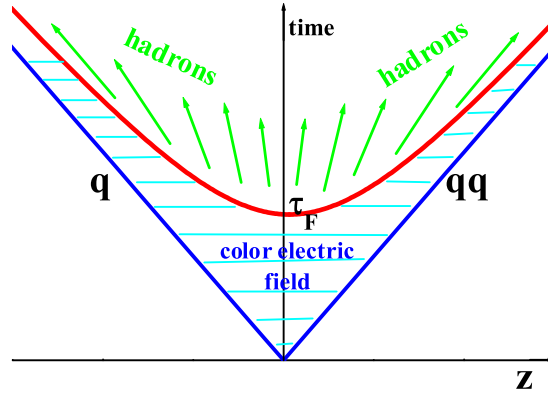


Figure 2.7: Dynamical evolution of a baryonic string; the fragmentation into hadrons starts after the formation time  $\tau_F$ . The figure is taken from [84].

Due to time dilatation and Lorentz  $\gamma$ -factors of  $\approx 2 - 6$  for the leading constituent quarks for AGS to SPS energies the formation time of the leading hadrons are long in comparison to the time between two consecutive collisions in heavy-ion reactions. Thus applying the concept of string fragmentation to heavy-ion collisions one has to specify the interaction of strings and their constituents with the surrounding hadrons. The cross section of the secondary interactions of the leading quarks/diquarks are reduced prior to the formation as

$$\begin{aligned} \sigma(q - B) &= 1/3 \sigma(B - B) \approx 10mb \\ \sigma(qq - B) &= 2/3 \sigma(B - B) \approx 20mb \\ \sigma(qq - q) &= 2/9 \sigma(B - B) \approx 6.6mb \end{aligned}$$

and so on. In order to treat this scheme within the FRITIOF string picture the  $q$  ( $qq$ ) is assumed to form a meson (baryon) together with its prospective quark partner inside the string. This procedure has to be seen as a heuristic approximation of the underlying soft partonic dynamics. Nevertheless, the global properties of heavy-ion collisions, the baryon stopping and pion production, can be described within this procedure over a wide energy range [61].

The interaction of the string field spanned between the constituent quarks with other hadrons is not taken into account. This is motivated by the fact, that most of the strings (in a given space-time volume) fragment within a small time interval. Thus the interaction of secondaries with the string field should be negligible in first order. Furthermore, since most of the strings are stretched longitudinally, no string-string interaction or a string fusion to color ropes as suggested in [86, 87, 88] is included in order to avoid new parameters.

Additionally to the formation time  $\tau_F = 0.8 \text{ fm}/c$  there is another criterium in HSD for the 'transition' of pre-hadrons to hadrons, i.e. an energy-density cut (in the local rest frame), which does not allow hadron formation when the energy density is above  $1 \text{ GeV}/\text{fm}^3$  which corresponds roughly to the critical energy density for a parton/hadron phase transition. Above this critical energy density explicit parton-parton interactions have to be considered which are not included in HSD, however, incorporated in an extended HSD version denoted by PHSD (Parton-Hadron-String-Dynamics) [48, 89].

### 2.2.5 Numerical realization of the HSD model

The set of coupled differential-integral equations (Eq. 2.59) is solved via a test-particle Ansatz (cf. Eq. 2.42) for the spectral phase-space densities:

$$\begin{aligned}
 F(\vec{r}, \vec{p}, M, t) &= N(\vec{r}, \vec{p}, M, t) \cdot A(\vec{r}, \vec{p}, M, t) \\
 &= \frac{1}{N} \sum_{i=1}^{N \cdot A} \delta(\vec{r} - \vec{r}_i(t)) \delta^3(\vec{p} - \vec{p}_i(t)) \delta(M - M_i(t))
 \end{aligned}
 \tag{2.71}$$

where  $\vec{r}_i$ ,  $\vec{p}_i$  and  $M_i$  denote the position, momentum and mass of the test particle  $i$  at time  $t$  and  $N$  is the number of test particles per physical particle. Furthermore,  $A$  denotes the number of hadrons at time  $t$ . Here the mass  $M_i(t)$  is used instead of the energy  $\varepsilon_i(t)$  employing Eq. 2.47.

In the HSD model the method of parallel ensembles is used, i.e. the test particles are divided into  $N$  different ensembles which do not influence each other. This is equivalent to simulating  $N$  independent nuclear reactions in parallel and averaging the observables over the ensembles in the end. For a test-particle number  $N \rightarrow \infty$  the test particles will give the time evolution of the spectral phase-space densities.

When initializing a nuclear reaction the test particles, that correspond to nucleons of the nucleus, are distributed in position space following a Woods-Saxon distribution:

$$\rho(r) = \frac{\rho_0}{1 + \exp\left(\frac{r-R}{a}\right)} \quad (2.72)$$

with the parameters  $a = 0.13$  fm and  $R = 1.124 \cdot A^{1/3}$  fm. Here  $\rho_0 = 0.168$  fm<sup>-3</sup> denotes the saturation density of nuclear matter.

For the initialization in momentum space the local Thomas-Fermi approximation is used: the nucleus remains close to its ground state and the phase-space density  $N$  can be approximated by the phase space density of (uncorrelated) cold nuclear matter

$$N(\vec{r}, \vec{p}) \sim \Theta(p_F(\vec{r}) - |\vec{p}|) \quad (2.73)$$

with the local Fermi momentum

$$p_F(\vec{r}) = \left( \frac{3\pi^2}{g} \rho(r) \right)^{1/3}. \quad (2.74)$$

The calculation is performed on a discretized dynamical grid in space-time  $(\Delta t, \Delta x, \Delta y, \Delta z)$ . The grid size  $\Delta z$  is chosen initially as  $\Delta z = 1/\gamma$  in order to optimize the computational performance; the time grid also is adjusted dynamically - i.e.  $\Delta t$  is getting sufficiently small during the high density phase and becomes larger during the expansion phase.

In each time step  $\Delta t$  the test particles are first assumed to move as non-interacting particles in the mean fields  $U_S$  and  $U^\mu$ . They follow the extended off-shell equations of motion (Eq. 2.43 - Eq. 2.45). However, between the time steps the particles may also interact. We do not assume any medium modification of the matrix elements  $\mathcal{M}$  that enter the collision term in Eq. 2.59. If one accounts

for the energy shift caused by the potentials  $U_S$  and  $U^\mu$ , the transition rates can be directly taken from the corresponding vacuum cross sections [61].

The collision criteria are chosen in line with the method by Kodama et al. [90]: Two particles collide in a time step  $\Delta t$  if the impact parameter  $b$ , i.e. the minimum separation in their center-of-momentum system, is smaller than

$$b \leq b_{max} = \sqrt{\frac{\sigma_{geom}}{\pi}}. \quad (2.75)$$

Furthermore, it is checked if both particles reach this minimal distance during the time step  $\Delta t$ . In Eq. 2.75  $\sigma_{geom}$  denotes the maximal cross section for the interaction of the two particles which is estimated using a simple geometrical picture. The further choice of individual channels  $i$ , which might be realized in this collision, is done by the Monte-Carlo method with a probability

$$P_i = \frac{\sigma_i}{\sigma_{geom}}. \quad (2.76)$$

An important feature of the HSD model is the decay of unstable particles with mass  $M$  and energy  $E$  during a time step  $\Delta t$ . The corresponding decay probability is given by

$$P_{dec} = 1 - \exp\left(-\frac{\Gamma_d(M)}{\gamma}\Delta t\right), \quad (2.77)$$

where  $\gamma = E/M$  is the Lorentz factor while  $\Gamma_d$  denotes the decay width of the particle in its rest frame. The final state of the decay products is again determined by Monte Carlo assuming the decay to be isotropic in the rest frame of the decaying particle since the spin degree of freedom is neglected. Due to the low densities of highly excited baryons Pauli blocking is only accounted for in collisions and decays that involve nucleons in the final state.



## Chapter 3

# Multiplicity Fluctuations in Nucleus-Nucleus Collisions

The first part of this chapter contains the result for study the particle number fluctuations in Pb+Pb collisions at 158 AGeV within HSD transport model [91]. The correspondent UrQMD results are shown for the comparison. This allows to check the robustness of the two approaches and derive physical consequences from the results of the HSD and UrQMD simulations. The results of transport models are compared also to the simplistic wounded nucleon model.

The results for the charged multiplicity fluctuations in Au+Au collisions at RHIC energy  $\sqrt{s} = 200\text{GeV}$  [92] are presented in the second part in comparison with data from PHENIX Collaboration [93, 94]. This study is based on the wounded nucleon model while employing the HSD transport model to define the centrality selection and to calculate the properties of hadron production sources.

### 3.1 Scaled Variance

Let us introduce some notations. We define the deviation  $\Delta N_A$  from the average number  $\langle N_A \rangle$  of the particle species  $A$  by  $N_A = \langle N_A \rangle + \Delta N_A$ . Then we define covariance for species  $A$  and  $B$ ,

$$\Delta(N_A, N_B) \equiv \langle \Delta N_A \Delta N_B \rangle = \langle N_A N_B \rangle - \langle N_A \rangle \langle N_B \rangle, \quad (3.1)$$

scaled variance

$$\omega_A \equiv \frac{\Delta(N_A, N_A)}{\langle N_A \rangle} = \frac{\langle (\Delta N_A)^2 \rangle}{\langle N_A \rangle} = \frac{\langle N_A^2 \rangle - \langle N_A \rangle^2}{\langle N_A \rangle}, \quad (3.2)$$

Note that  $\omega = 1$  for the Poisson multiplicity distribution,  $P(N) = \exp(-\bar{N})\bar{N}^N/N!$ .

## 3.2 Multiplicity Fluctuations in Pb+Pb Collisions at 158 AGeV

### 3.2.1 Fluctuations in the number of participants

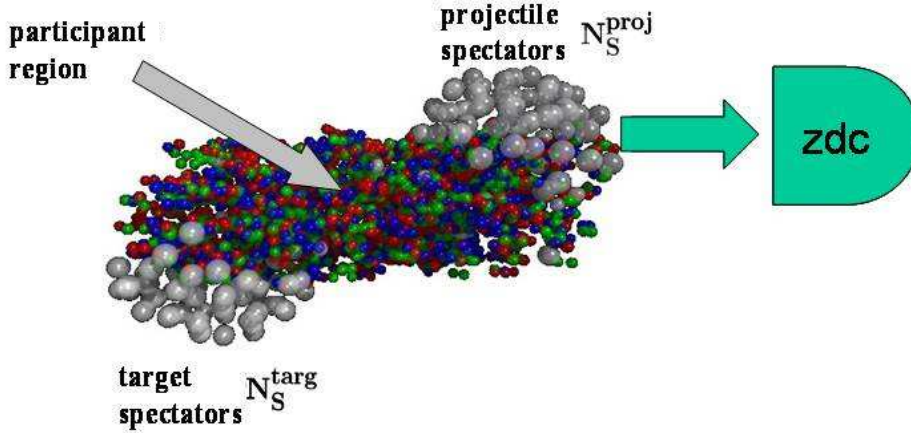


Figure 3.1: Non-central heavy ion collision. Spectators in the projectile and target are denoted as  $N_P^{proj}$  and  $N_P^{targ}$ . 'Participant region' indicates the region where the particle production occurs due to the interaction of participants from target and projectile. Note that in a fix target experiment it is possible to fix the number of projectile participant by detecting projectile spectators via Zero Degree Calorimeter (ZDC).

The multiplicity fluctuations are measured experimentally versus the number of participants. Fig. 3.1 demonstrates non-central Au+Au collision, where in each collision only a fraction of all  $2A$  nucleons interact. These are called participant nucleons and are denoted as  $N_P^{proj}$  and  $N_P^{targ}$  for the projectile and target nuclei, respectively. The correspondent nucleons, which do not interact, are called the projectile and target spectators,  $N_S^{proj} = A - N_P^{proj}$  and  $N_S^{targ} = A - N_P^{targ}$ .

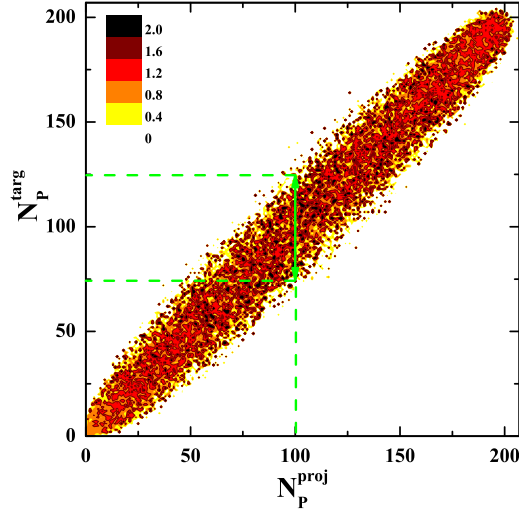


Figure 3.2: The HSD simulations of the participant (from projectile,  $N_P^{proj}$ , and target,  $N_P^{targ}$ ) distribution for Pb+Pb collision at  $158 AGeV$ . The dashed lines demonstrate that even for fixed  $N_P^{proj} = 100$ , number of target participants vary from 75 to 125.

The fluctuations in high energy A+A collisions are dominated by a geometrical variation of the impact parameter. However, even for the fixed impact parameter the number of participants,  $N_P \equiv N_P^{proj} + N_P^{targ}$ , fluctuates from event to event. This is due to the fluctuations of the initial states of the colliding nuclei and the probabilistic character of the interaction process. The fluctuations of  $N_P$  form usually a large and uninteresting background. In order to minimize its contribution the NA49 Collaboration has selected samples of collisions with a fixed numbers of projectile participants. This selection is possible due to a measurement of  $N_S^{proj}$  in each individual collision by a calorimeter which covers the projectile fragmentation domain. However, even in the samples with  $N_P^{proj} = const$  the number of target participants fluctuates considerably. Hence, an asymmetry between projectile and target participants is introduced, i.e.  $N_P^{proj}$  is constant by constraint, whereas  $N_P^{targ}$  fluctuates independently. As an example [Fig. 3.2](#) shows the HSD simulations of the distribution of projectile and target participants for Pb+Pb collision at  $158 AGeV$ . One can see that even for fixed  $N_P^{proj} = 100$ , number of target participants vary from 75 to 125.

In each sample with  $N_P^{proj} = const$  the number of target participants fluctuates around its mean value,  $\langle N_P^{targ} \rangle$  with the scaled variance  $\omega_P^{targ}$ . From an output

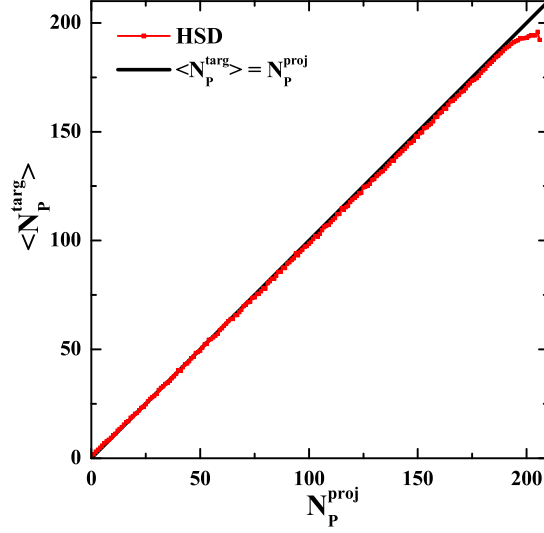


Figure 3.3: The HSD simulations in Pb+Pb collisions at 158 AGeV for the average value  $\langle N_P^{targ} \rangle$  as functions of  $N_P^{proj}$ .

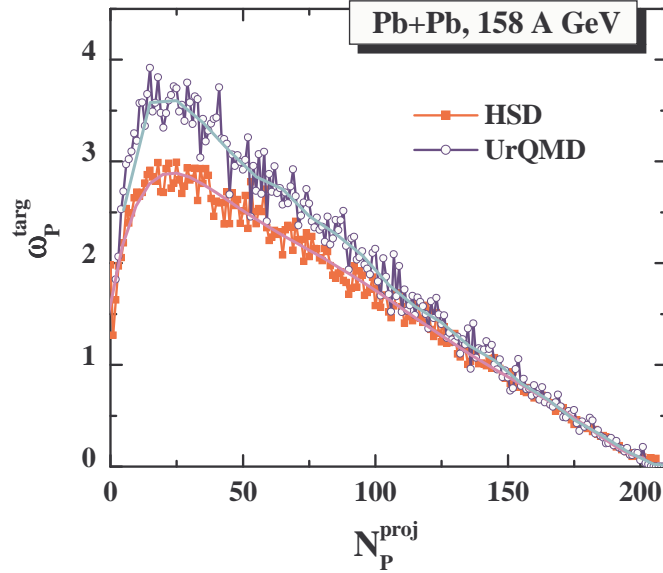


Figure 3.4: Scaled variance  $\omega_P^{targ}$  for the fluctuations of the number of target participants,  $N_P^{targ}$ . HSD and UrQMD simulations show similar behavior of  $\omega_P^{targ}$  as a function of  $N_P^{proj}$ .

of the HSD minimum bias simulations of Pb+Pb collisions at 158 AGeV the samples of events with fixed values of  $N_P^{proj}$  have been formed. Fig. 3.3 presents the HSD average value  $\langle N_P^{targ} \rangle$  as functions of  $N_P^{proj}$ . One finds  $\langle N_P^{targ} \rangle \simeq N_P^{proj}$ ; the deviations are only seen at very small ( $N_P^{proj} \approx 1$ ) and very large ( $N_P^{proj} \approx$

A) numbers of projectile participants. **Fig. 3.4** shows both HSD and UrQMD results for the scaled variances  $\omega_P^{targ}$  as functions of fixed number of  $N_P^{proj}$ . The fluctuations of  $N_P^{targ}$  are quite strong; the largest value of  $\omega_P^{targ} = 3 - 3.5$  occurs at  $N_P^{proj} = 20 - 30$ .

### 3.2.2 HSD and UrQMD results in comparison to the NA49 Data

The NA49 Collaboration has minimized the event by event fluctuations of the number of nucleon participants in measuring the multiplicity fluctuations by selecting the samples of collisions with a fixed number of projectile spectators,  $N_S^{proj} = const$ , and thus a fixed number of projectile participants,  $N_P^{proj} = A - N_S^{proj}$ . This selection is possible in fixed target experiments, where  $N_S^{proj}$  is measured by a Zero Degree Veto Calorimeter, which covers the projectile fragmentation domain (**Fig. 3.1**).

From an output of the HSD and UrQMD minimum bias simulations the samples of Pb+Pb events with fixed values of  $N_P^{proj}$  have been formed. **Fig. 3.5** presents the HSD and UrQMD results and compare them with the NA49 data for the scaled variances of negatively, positively, and all charged particles in Pb+Pb collisions at 158 AGeV. The average values,  $\langle N_i \rangle$  and the scaled variances  $\omega_i$  (see **Eq. 3.2**, here  $i = +, -, ch$ ) are calculated for the samples of collision events with fixed values of the projectile participants,  $N_P^{proj}$ .

The final particles in the HSD and UrQMD simulations are accepted at rapidities  $1.1 < y < 2.6$  ( $y$  corresponds to the particle rapidities in the Pb+Pb c.m.s. frame) in accord to the NA49 transverse momentum filter [95]. This is done to compare the HSD and UrQMD results with the NA49 data. The HSD and UrQMD simulations both show flat  $\omega_i$  values,  $\omega_- \approx \omega_+ \approx 1.2$ ,  $\omega_{ch} \approx 1.5$ , and exhibit almost no dependence on  $N_P^{proj}$ . The NA49 data, in contrast, exhibit an enhancement in  $\omega_i$  for  $N_P^{proj} \approx 50$ . The data show maximum values,  $\omega_- \approx \omega_+ \approx 2$  and  $\omega_{ch} \approx 3$ , and a rather strong dependence on  $N_P^{proj}$ .

**Fig. 3.5** also shows results of the HSD and UrQMD simulations for the full  $4\pi$  acceptance for final particles, and shows the NA49-like acceptance in the mirror rapidity interval,  $-2.6 < y < -1.1$  of the target hemisphere. HSD and UrQMD both result in large values of  $\omega_i$ , i.e. large fluctuations in the backward hemisphere: in the backward rapidity interval  $-2.6 < y < -1.1$  (target hemisphere)

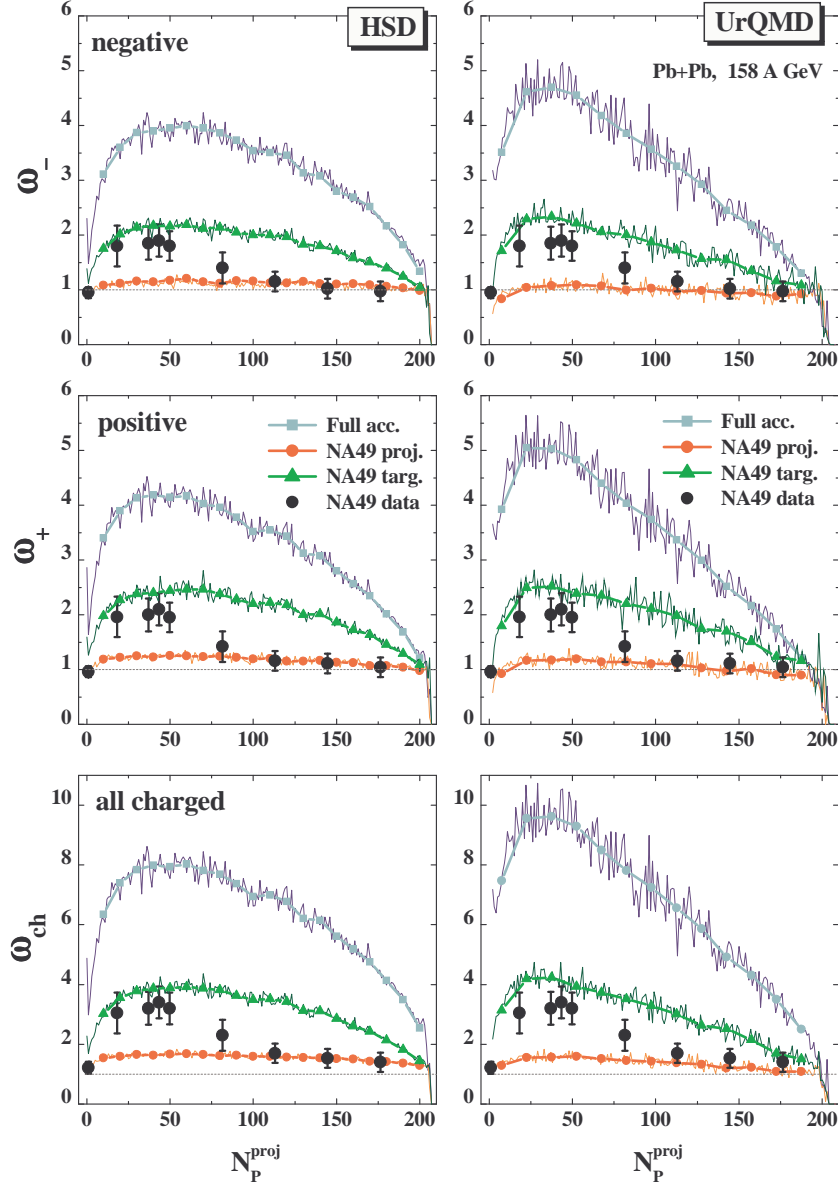


Figure 3.5: The results of the HSD (left) and UrQMD (right) simulations are shown for  $\omega_-$ ,  $\omega_+$ , and  $\omega_{ch}$  in Pb+Pb collisions at 158 AGeV as functions of  $N_P^{proj}$ . The black points are the NA49 data. The different lines correspond to the model simulations with the original NA49 acceptance,  $1.1 < y < 2.6$ , in the projectile hemisphere (lower lines), the NA49-like acceptance in the mirror rapidity interval,  $-2.6 < y < -1.1$ , in the target hemisphere (middle lines), and full  $4\pi$  acceptance (upper lines).

the fluctuations are much larger than those calculated in the forward rapidity interval  $1.1 < y < 2.6$  (projectile hemisphere, where the NA49 measurements

have been done). Even larger fluctuations follow from the HSD and UrQMD simulations for the full acceptance of final particles.

### 3.2.3 Multiplicity fluctuations in the wounded nucleon model

At fixed values of the numbers of participants  $N_P^{proj}$  and  $N_P^{targ}$  one can introduce the average multiplicity ( $i = -, +, ch$ ):

$$\overline{N}_i \equiv \sum_{N_i \geq 0} N_i W(N_i | N_P^{targ}, N_P^{proj}), \quad (3.3)$$

where  $W(N_i | N_P^{targ}, N_P^{proj})$  is the probability for producing  $N_i$  final hadrons at fixed  $N_P^{targ}$  and  $N_P^{proj}$ . In fact, only  $N_P^{proj}$  is fixed experimentally – hence, also in the HSD and UrQMD simulations presented in [Fig. 3.5](#). The value of  $N_P^{targ}$  fluctuates, and the average over the target participants is denoted as

$$\langle \dots \rangle \equiv \sum_{N_P^{targ} \geq 1}^A \dots W(N_P^{targ} | N_P^{proj}), \quad (3.4)$$

where  $W(N_P^{targ} | N_P^{proj})$  is the probability for a given value of  $N_P^{targ}$  in a sample of events with fixed number of the projectile participants,  $N_P^{proj}$ .

The total averaging procedure, performed at fixed number of projectile participants,  $N_P^{proj}$ , includes both the averaging [Eq. 3.3](#) and [Eq. 3.4](#), so that the total variance is:

$$\begin{aligned} Var(N_i) &\equiv \langle \overline{N}_i^2 \rangle - \langle \overline{N}_i \rangle^2 \\ &\equiv \langle \overline{N}_i^2 \rangle - \langle \overline{N}_i^2 \rangle + \langle \overline{N}_i^2 \rangle - \langle \overline{N}_i \rangle^2 \\ &= \omega_i^* \langle \overline{N}_i \rangle + \omega_P n_i \langle \overline{N}_i \rangle, \end{aligned} \quad (3.5)$$

where

$$\omega_i^* \equiv \frac{\overline{N}_i^2 - \overline{N}_i^2}{\overline{N}_i}, \quad \omega_P \equiv \frac{\langle N_P^2 \rangle - \langle N_P \rangle^2}{\langle N_P \rangle}, \quad n_i \equiv \frac{\langle \overline{N}_i \rangle}{\langle N_P \rangle}, \quad (3.6)$$

and  $N_P = N_P^{targ} + N_P^{proj}$ , is the total number of participants. At the last step in

Eq. 3.5 two assumptions have been made. First, it is assumed that  $\omega_i^*$  does not depend on  $N_P$  and can be thus taken out from the averaging,  $\langle \dots \rangle$ , in Eq. 3.4. The second assumption is that the average multiplicities  $\overline{N}_i$  are proportional to the number of participating nucleons, i.e.  $\overline{N}_i = N_P n_i$ , where  $n_i$  (defined in Eq. 3.6) is the average number of particles of  $i$ -th type per participant.

Finally, the scaled variances,  $\omega_i$ , can be presented as:

$$\omega_i \equiv \frac{\text{Var}(N_i)}{\langle \overline{N}_i \rangle} = \omega_i^* + \omega_P n_i. \quad (3.7)$$

The total number of participants fluctuates due to the fluctuations of  $N_P^{targ}$  (the values of  $N_P^{proj}$  are fixed experimentally, as well as in the HSD and UrQMD simulations). One calculates the average values,  $\langle N_P^{targ} \rangle \simeq N_P^{proj}$ , and scaled variances,  $\omega_P^{targ}$ , for the target participants in both the HSD and UrQMD models (see Fig. 3.4). The scaled variance  $\omega_P$  (Eq. 3.6) for the total number of participants is easily found,  $\omega_P = \omega_P^{targ}/2$ , as only a half of the total number,  $N_P$ , of participants, i.e.,  $N_P^{targ}$ , does fluctuate.

Putting everything together one gets:

$$\omega_i = \omega_i^* + \frac{1}{2} \omega_P^{targ} n_i. \quad (3.8)$$

The value of  $\omega_P^{targ}$  depends on  $N_P^{proj}$ , as shown by the HSD and UrQMD results in Fig. 3.4. The average particle number  $n_i$  of  $i$ -th type ( $i =$  positive, negative and all charged) per participant calculated within the HSD (solid lines) and UrQMD (dashed lines) models for full acceptance ( $4\pi$ ) are presented in Fig. 3.6. The squares correspond to the NA49 data (extrapolated to full acceptance [5]) for the average  $\pi + K^-$  multiplicity (which is an approximately 95% of all negatively charged hadrons) over the number of nucleon participants, using  $\pi \equiv (\pi^- + \pi^+)/2$ . As seen from Fig. 3.6, both transport models show a good agreement with each other as well as with the extrapolated  $4\pi$  NA49 data.  $n_i$  from Fig. 3.6 will be used for the further model calculations.

The Eq. 3.7 coincides with the result of the so called wounded nucleon model (WNM) <sup>1</sup>, i.e. a model which treats the A+A collision as a superposition of independent nucleon-nucleon (N+N) interactions. The same result (Eq. 3.7) can be

<sup>1</sup>Also known as 'participant model' or independent sources model (see e.g., [96])



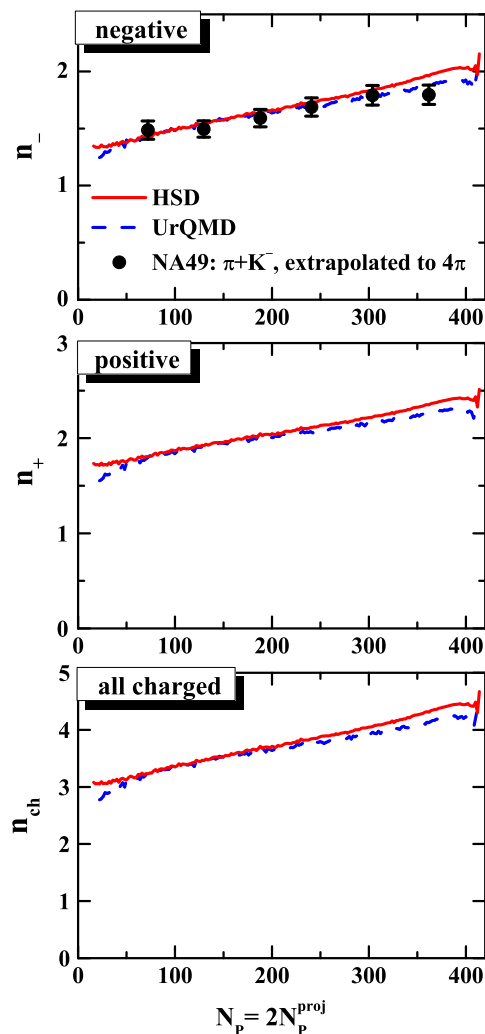


Figure 3.6: The average particle number of  $i$ -th type ( $i = \text{positive, negative and all charged}$ ) per participant calculated within the HSD (solid lines) and UrQMD (dashed lines) models for full acceptance ( $4\pi$ ). The squares correspond to the the NA49 data (extrapolated to full acceptance [5]) for the average  $\pi+K^-$  multiplicity over the number of nucleon participants, using  $\pi \equiv (\pi^- + \pi^+)/2$ .

obtained within a more general framework. One assumes that a part of the initial projectile and target energy is converted into hadron sources. The numbers of projectile and target related sources are taken to be proportional to the number of projectile and target participant nucleons, respectively. This results in Eq. 3.7. The physical meaning of the different sources depends on the model under consideration (e.g., wounded nucleons [97], strings and resonances [73, 61, 63, 64], or

the fluid cells at chemical freeze-out, in the hydrodynamical models). The Eq. 3.7 presents the final multiplicity fluctuations as a sum of two terms: the fluctuations from one source,  $\omega_i^*$ , and the contribution due to the fluctuations of the number of sources,  $\omega_{PN_i}$ .

In peripheral A+A collisions there are only few N+N collisions, and rescatterings are rare, so that the picture of independent N+N collisions looks reasonable. In this case, a hadron production source can be associated with a N+N collision and, therefore, the fluctuations from one source read:

$$\omega_i^* = \omega_i^{NN} = \frac{\alpha_{pp} \omega_i^{pp} \overline{N}_i^{pp} + \alpha_{pn} \omega_i^{pn} \overline{N}_i^{pn} + \alpha_{nn} \omega_i^{nn} \overline{N}_i^{nn}}{\alpha_{pp} \overline{N}_i^{pp} + \alpha_{pn} \overline{N}_i^{pn} + \alpha_{nn} \overline{N}_i^{nn}}, \quad (3.9)$$

where

$$\begin{aligned} \alpha_{pp} &= Z^2/A^2 = 0.155, \\ \alpha_{pn} &= 2Z(A-Z)/A^2 = 0.478, \\ \alpha_{nn} &= (A-Z)^2/A^2 = 0.367 \end{aligned} \quad (3.10)$$

are the probabilities of proton-proton, proton-neutron, and neutron-neutron collisions in Pb+Pb reactions ( $A=208$ ,  $Z=82$ ). The average multiplicities and scaled variances for elementary collisions calculated within the HSD simulations at 158 GeV are equal to:

$$\overline{N}_{ch}^{pp} = 6.2, \quad \overline{N}_{ch}^{pn} = 5.8, \quad \overline{N}_{ch}^{nn} = 5.4, \quad (3.11)$$

$$\omega_{ch}^{pp} = 2.1, \quad \omega_{ch}^{pn} = 2.4, \quad \omega_{ch}^{nn} = 2.9. \quad (3.12)$$

For negatively and positively charged hadrons, the average multiplicities and scaled variances in elementary reactions can be presented in terms of corresponding quantities for all charged particles:  $\overline{N}_{\pm} = 0.5(\overline{N}_{ch} \pm \gamma)$  and  $\omega_{\pm} = 0.5\omega_{ch}\overline{N}_{ch}/(\overline{N}_{ch} \pm \gamma)$ , with  $\gamma = 2, 1, 0$  for pp, pn and nn reactions, respectively.

This yields:

$$\begin{aligned}
\overline{N_-^{pp}} &= 2.1, & \overline{N_-^{pn}} &= 2.4, & \overline{N_-^{nn}} &= 2.7, \\
\overline{N_+^{pp}} &= 4.1, & \overline{N_+^{pn}} &= 3.4, & \overline{N_+^{nn}} &= 2.7, \\
\omega_-^{pp} &= 1.55, & \omega_-^{pn} &= 1.5, & \omega_-^{nn} &= 1.45, \\
\omega_+^{pp} &= 0.8, & \omega_+^{pn} &= 1.0, & \omega_+^{nn} &= 1.45.
\end{aligned} \tag{3.13}$$

Thus, using [Eq. 3.9](#) one finds the HSD results for  $\omega_i^*$  per N+N collision at 158 GeV:

$$\omega_{ch}^* = 2.5, \quad \omega_-^* = 1.5, \quad \omega_+^* = 1.1. \tag{3.14}$$

The above arguments of the WNM are not applicable for central A+A collisions, where a large degree of thermalization is expected. In the limit of  $N_P^{proj} = A$  one can take the values of  $\omega_i^*$  from the Pb+Pb data or model simulations. In this limit,  $\omega_P = \omega_P^{targ}/2 \approx 0$  (see [Fig. 3.4](#)), and thus  $\omega_i \approx \omega_i^*$ . It has been found that [Eq. 3.14](#) gives a reasonable description of  $\omega_i$  in the HSD simulations for central Pb+Pb collisions, too. Therefore, we will use [Eq. 3.8](#) and [Eq. 3.14](#) for all values of  $N_P^{proj}$ . A comparison of  $\omega_i$  calculated according to [Eq. 3.8](#) with the terms obtained from HSD simulations (in full  $4\pi$  acceptance) is presented in [Fig. 3.7](#).

The values of  $\omega_P^{targ}$  and  $n_i$  are calculated within the HSD model (see [Fig. 3.4](#) and [Fig. 3.6](#)), and for  $\omega_i^*$  we use [Eq. 3.14](#). As seen from [Fig. 3.7](#), there is a qualitative agreement between [Eq. 3.8](#) and the HSD simulations. The fluctuations of the total hadron multiplicities - generated by the HSD dynamics - are large (the  $\omega_i$  are essentially larger than 1). The main contributions to  $\omega_i$  come from the second terms in [Eq. 3.8](#), which are due to the fluctuations of  $N_P^{targ}$ . These fluctuations of the target nucleon participants presented in [Fig. 3.4](#) explain both, the large values of  $\omega_i$  and their strong dependence on  $N_P^{proj}$ . Therefore, [Eq. 3.8](#) takes into account two main ingredients of the multiplicity fluctuations in Pb+Pb collision: a fluctuation of the particle number created in a single N+N collision and a fluctuation in the number of nucleon participants. [Fig. 3.7](#) shows that the HSD dynamics produces even larger values of  $\omega_i$  than those calculated from [Eq. 3.8](#). A very similar picture occurs for the UrQMD model.

[Fig. 3.8](#) supports the previous findings. HSD events with fixed target partici-

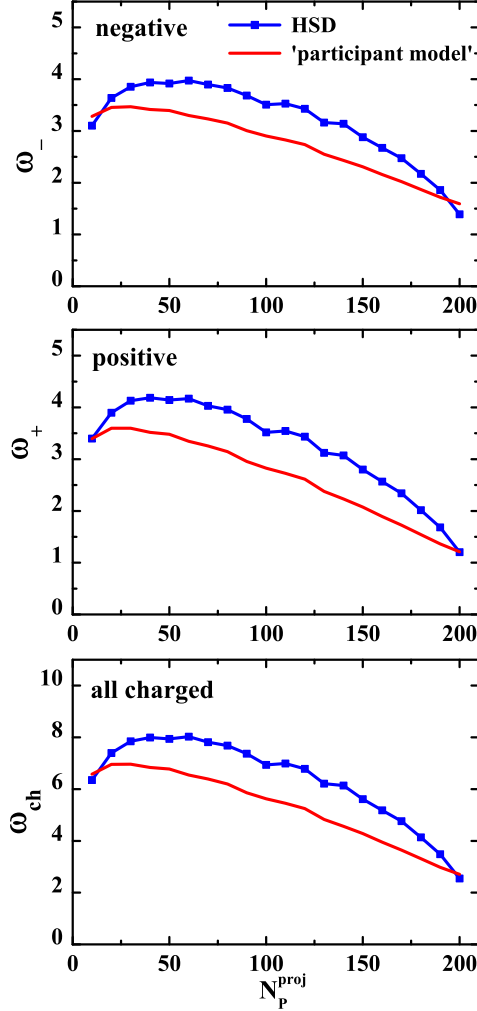


Figure 3.7: The boxes are the results of the HSD simulations for  $\omega_i$  in full  $4\pi$  acceptance as functions of  $N_P^{proj}$ . The solid lines correspond to  $\omega_i$  from Eq. 3.8 obtained in the WNM where  $\omega_i^*$  are taken from Eq. 3.14.

participant number,  $N_P^{targ} = N_P^{proj}$ , exhibit much smaller multiplicity fluctuations. This is due to the fact that terms proportional to  $\omega_P^{targ}$  in Eq. 3.8 do not contribute, and  $\omega_i$  become approximately equal to  $\omega_i^*$ .

### 3.2.4 Transparency, Mixing, and Reflection models

Different models of hadron production in relativistic A+A collisions can be divided into three limiting groups: transparency, mixing, and reflection models (see Ref. [98]). The first group assumes that the final longitudinal flows of the

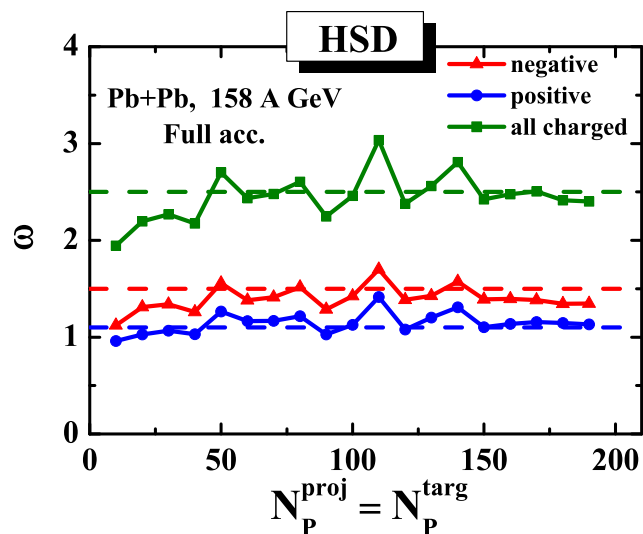


Figure 3.8: The circles, triangles, and boxes are the results of the HSD simulations for  $\omega_i$  in full  $4\pi$  acceptance with  $N_P^{\text{targ}} = N_P^{\text{proj}}$ . This condition yields  $\omega_P^{\text{targ}} = 0$ , and Eq. 3.8 is reduced to  $\omega_i = \omega_i^*$ . The dashed lines correspond to  $\omega_i^*$  taken from Eq. 3.14.

hadron production sources related to projectile and target participants follow in the directions of the projectile and target, respectively. One calls this group of models as transparency (T-)models. If the projectile and target flows of hadron production sources are mixed, these models are called as mixing (M-)models. Finally, one may assume that the initial flows are reflected in the collision process. The projectile related matter then flows in the direction of the target and the target related matter flows in the direction of the projectile. This class of models corresponds to the reflection (R-)models. The rapidity distributions resulting from the T-, M-, and R-models are sketched in Fig. 3.9 taken from Ref. [98].

An asymmetry between the projectile and target participants introduced by the experimental selection procedure in a fix target experiment can be used to distinguish between projectile related and target related final state flows of hadron production sources as suggested in Ref. [98]. One expects large fluctuations of hadron multiplicities in the domain of the target related flow and small fluctuations in the domain of the projectile related flow. When both flows are mixed, intermediate fluctuations are predicted. The different scenarios are presented in Fig. 3.9. The multiplicity fluctuations measured in the projectile momentum hemisphere clearly are larger than those measured in the target hemisphere in

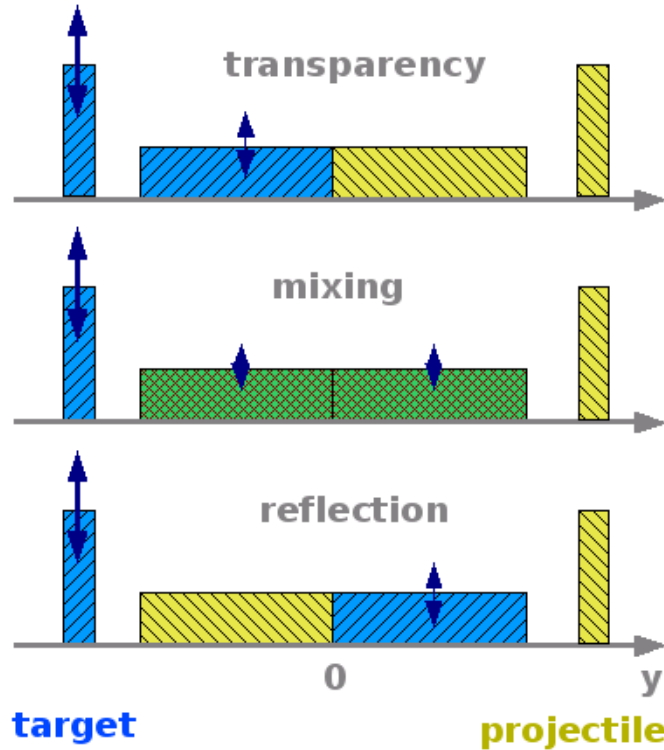


Figure 3.9: The sketch of the rapidity distributions of the baryon number or the particle production sources (horizontal rectangles) in nucleus-nucleus collisions resulting from the transparency, mixing and reflection models. The spectator nucleons are indicated by the vertical rectangles. In the collisions with a fixed number of projectile spectators only matter related to the target shows significant fluctuations (vertical arrows). See Ref. [98] for more details.

T-models. The opposite relation is predicted for R-models, whereas for M-models the fluctuations in the projectile and target hemispheres are expected to be the same.

Note that there are models which assume the mixing of hadron production sources, however, the transparency of baryon flows, e.g. three-fluid hydrodynamical model [99, 100]. R-models appear rather unrealistic and are included for completeness in the discussion.

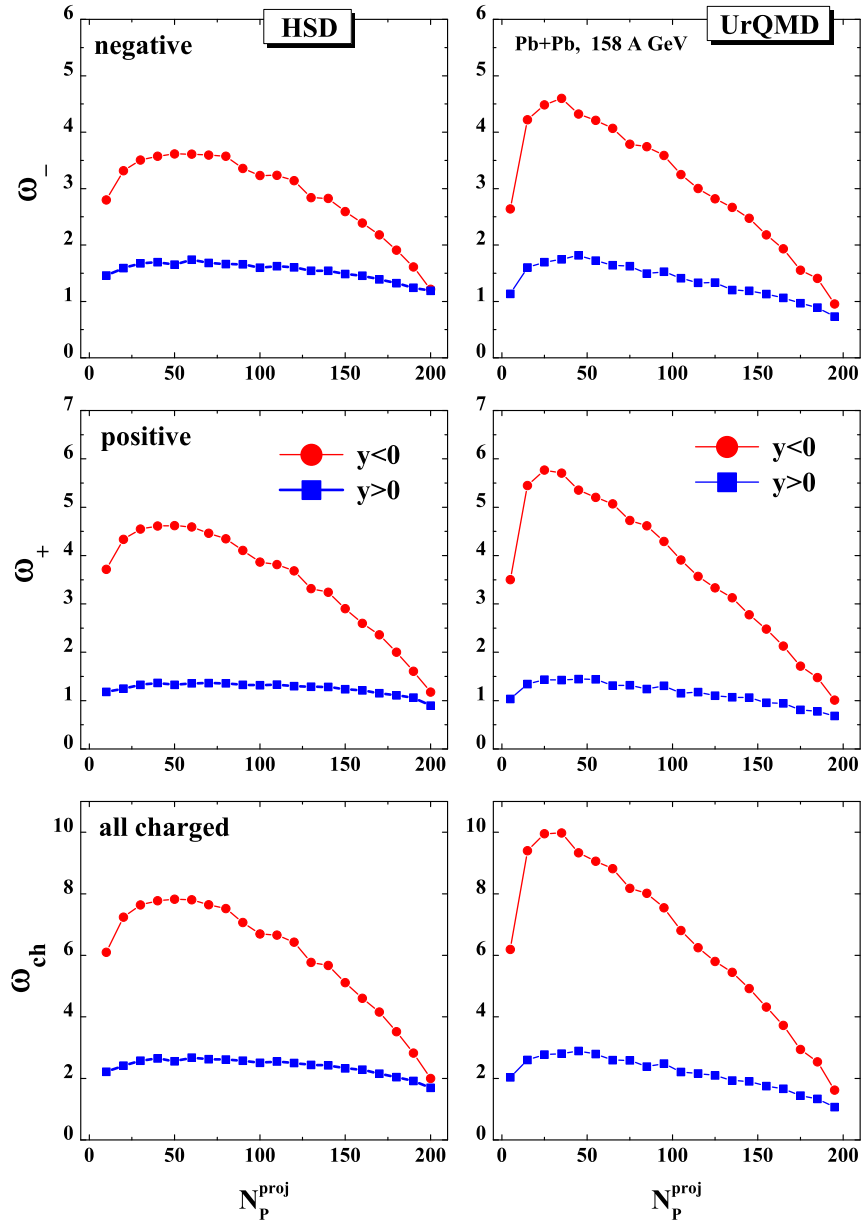


Figure 3.10: The scaled variances  $\omega_i$  for the projectile (boxes) and target (circles) hemispheres in the HSD (left) and UrQMD (right) simulations.

### 3.2.5 Fluctuations in the projectile and target hemispheres

Now the fluctuations of the particle multiplicities in the projectile ( $y > 0$ ) and target ( $y < 0$ ) hemispheres are considered. As one can see from Fig. 3.4, in

samples with  $N_P^{proj} = const$  the number of target participants,  $N_P^{targ}$ , fluctuates considerably. Of course, this event selection procedure introduces an asymmetry between projectile and target participants:  $N_P^{proj}$  is constant, whereas  $N_P^{targ}$  fluctuates. Then both simulations, HSD and UrQMD, give very different results for the particle number fluctuations in the projectile and target hemispheres. The particle number fluctuations in the target hemispheres are much stronger (see Fig. 3.10) than those in the projectile hemispheres. There is also a strong  $N_P^{proj}$ -dependence of  $\omega_i$  in the target hemisphere, which is almost absent for the  $\omega_i$  in the projectile hemisphere. This is due to the asymmetry between projectile and target participants. The target participants,  $N_P^{targ}$ , play a quite small role for the particle production in the projectile hemisphere. Thus, the fluctuations of  $N_P^{targ}$  have a small influence on the final multiplicity fluctuations in the projectile hemisphere, but they contribute very strongly to those in the target hemisphere.

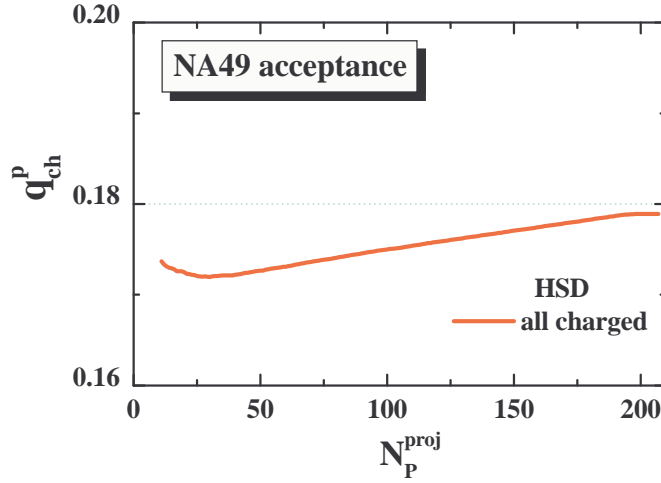


Figure 3.11: The ratio of charged multiplicity within the NA49 acceptance to that in the whole projectile hemisphere. Similar results are obtained for negative and positive hadron multiplicities.

In real experiments only a fraction of all final state particles is accepted. In the case of weak correlations between particles, the scaled variances in the limited acceptance can be calculated ([96, 101]) as  $\omega_i^{acc} = 1 - q_i + q_i \cdot \omega_i$ . Here the  $q_i$  are the probabilities that particles of type  $i$  are accepted. The  $q_i$  values can be calculated as the ratio of the average multiplicity of the  $i$ -th hadrons within the given experimental acceptance inside the projectile (target) hemisphere to the average multiplicity in the whole projectile (target) hemisphere. The HSD



values of  $q_i^p \approx 0.18$  are presented as functions of  $N_P^{proj}$  in **Fig. 3.11** in the NA49 acceptance (in the projectile hemisphere).

Under the above assumptions, the scaled variances of the multiplicity distributions in the projectile hemisphere,  $\omega_i^{proj}$ , and target hemisphere,  $\omega_i^{targ}$ , in the T-, M- and R-models read [98]:

$$\begin{aligned} \omega_i^{proj}(T) &= 1 - q_i^p + q_i^p \cdot \omega_i^* , \\ \omega_i^{targ}(T) &= 1 - q_i^t + q_i^t \cdot (\omega_i^* + \omega_P^{targ} n_i) , \end{aligned} \quad (3.15)$$

$$\omega_i^{proj}(M) = \omega_i^{targ}(M) = 1 - q_i^{p,t} + q_i^{p,t} \cdot (\omega_i^* + 0.5 \omega_P^{targ} n_i) , \quad (3.16)$$

$$\begin{aligned} \omega_i^{proj}(R) &= 1 - q_i^p + q_i^p \cdot (\omega_i^* + \omega_P^{targ} n_i) , \\ \omega_n^{targ}(R) &= 1 - q_i^t + q_i^t \cdot \omega_i^* . \end{aligned} \quad (3.17)$$

Here  $q_i^p$  and  $q_i^t$  are the acceptances in the projectile and target hemispheres, respectively.

Results presented in **Fig. 3.10** suggest that HSD and UrQMD are closer to T-models. Using **Eq. 3.15** the HSD simulations yield within the NA49 acceptance, and within the analogous acceptance in the mirror target rapidity interval,

$$\begin{aligned} \omega_-^{proj}(T) &\cong 1.09 , \quad \omega_+^{proj}(T) \cong 1.02 , \quad \omega_{ch}^{proj}(T) \cong 1.27 , \\ \omega_-^{targ}(T) &\cong 1.09 + 0.18 \cdot \omega_P^{targ} \cdot n_- , \\ \omega_+^{targ}(T) &\cong 1.02 + 0.18 \cdot \omega_P^{targ} \cdot n_+ , \\ \omega_{ch}^{targ}(T) &\cong 1.27 + 0.18 \cdot \omega_P^{targ} \cdot n_{ch} . \end{aligned} \quad (3.18)$$

Here, the values of  $q_i^p = q_i^t \approx 0.18$  are taken from the HSD calculations (**Fig. 3.11**), and the  $\omega_i^*$  from **Eq. 3.14** are used. The results of **Eq. 3.18** and **Eq. 3.19** agree well with the HSD simulations (**Fig. 3.12**) for large projectile participant number and retain the general trend also for more peripheral collisions. Similar results are obtained within the UrQMD simulations. Hence, both the HSD and UrQMD approach are closer to T-models of hadron production sources.

Using **Eq. 3.16** one can estimate  $\omega_i$  for the NA49 acceptance in M-models. It follows:

$$\omega_i^{proj}(M) = \omega_i^{targ}(M) = 0.82 + 0.18 \cdot (\omega_i^* + 0.5 \omega_P^{targ} n_i) . \quad (3.20)$$

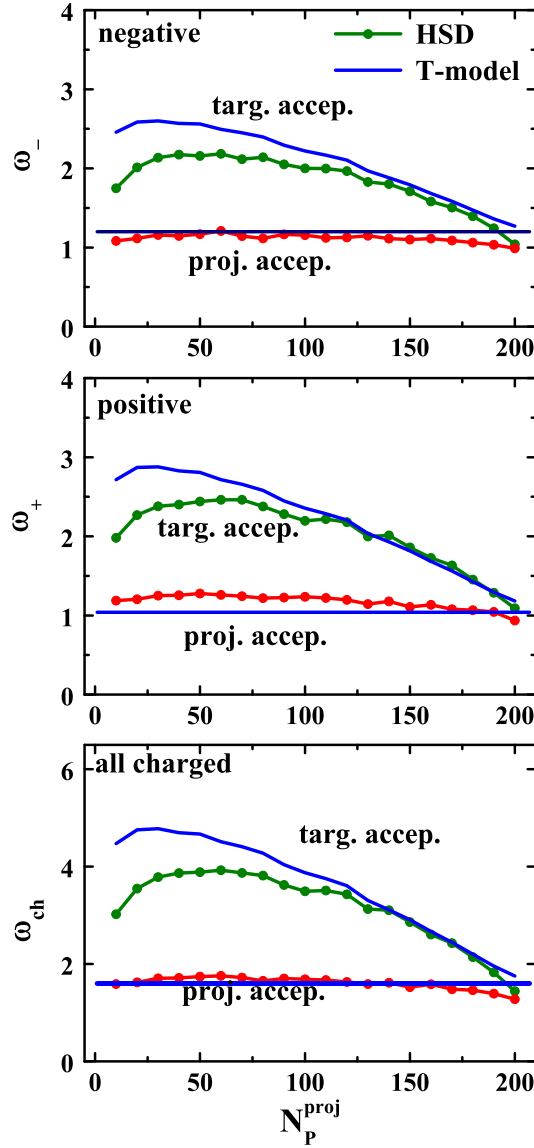


Figure 3.12: The HSD simulations in the NA49 acceptance in the projectile,  $1.1 < y < 2.6$ , and target,  $-2.6 < y < -1.1$ , hemispheres. The solid lines correspond to Eq. 3.18 and Eq. 3.19, which assume transparency of the longitudinal flows of the hadron production sources.

In Fig. 3.13 the results of Eq. 3.20 (with  $\omega_i^*$  (Eq. 3.14),  $\omega_P^{targ}$ , and  $n_i$  taken from the HSD simulations) are compared with the NA49 data. Eq. 3.20 for the M-model gives a much better agreement with the NA49 data than Eq. 3.18 for the T-model. The NA49 data suggest therefore a large degree of mixing in the longitudinal flow of the projectile- and target hadron production sources, in agreement

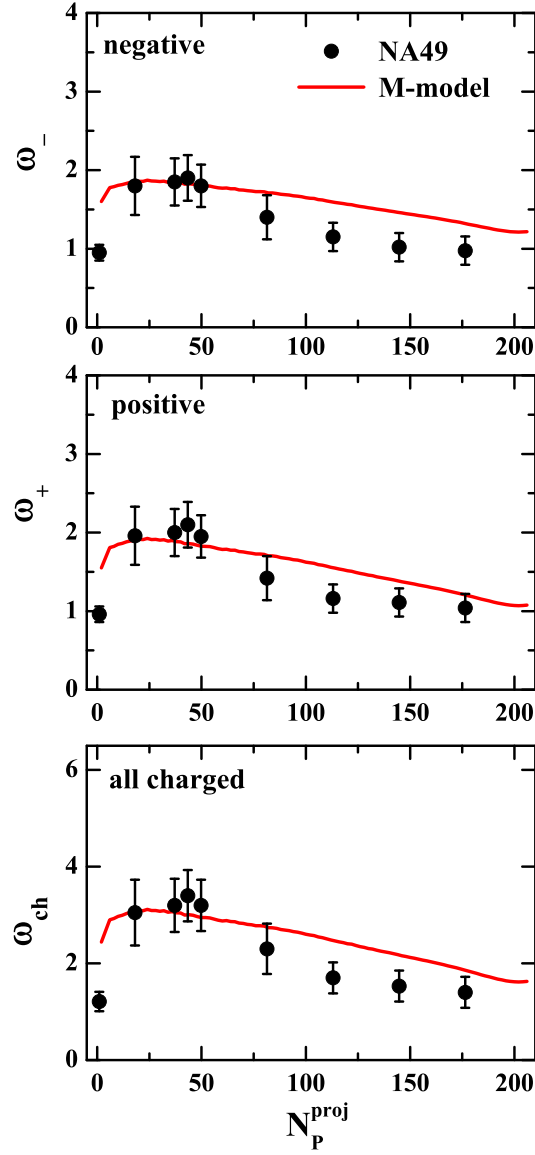


Figure 3.13: The solid lines correspond to Eq. 3.20 with  $\omega_i^*$  (Eq. 3.14),  $\omega_P^{\text{targ}}$ , and  $n_i$  taken from the HSD simulations; the points are the NA49 data.

with suggestions formulated in Ref. [98].

A selection of collisions with a fixed number of  $N_P^{\text{proj}}$  and fluctuating number of  $N_P^{\text{targ}}$  means that the projectile and target initial flows are marked in fluctuations [98] in the number of colliding nucleons. The projectile and target related matters in the final state of collisions can be then distinguished by an analysis of fluctuations of extensive quantities. In the case of non-identical nuclei (different

baryon number and/or proton to neutron ratios) one can trace flows of the conserved charges – baryon number and electric charge – by looking at their inclusive final state distributions [63, 102]. The analysis of the fluctuations can be applied also to collisions of identical nuclei. Furthermore, it gives a unique possibility to investigate the flows of particle production sources.

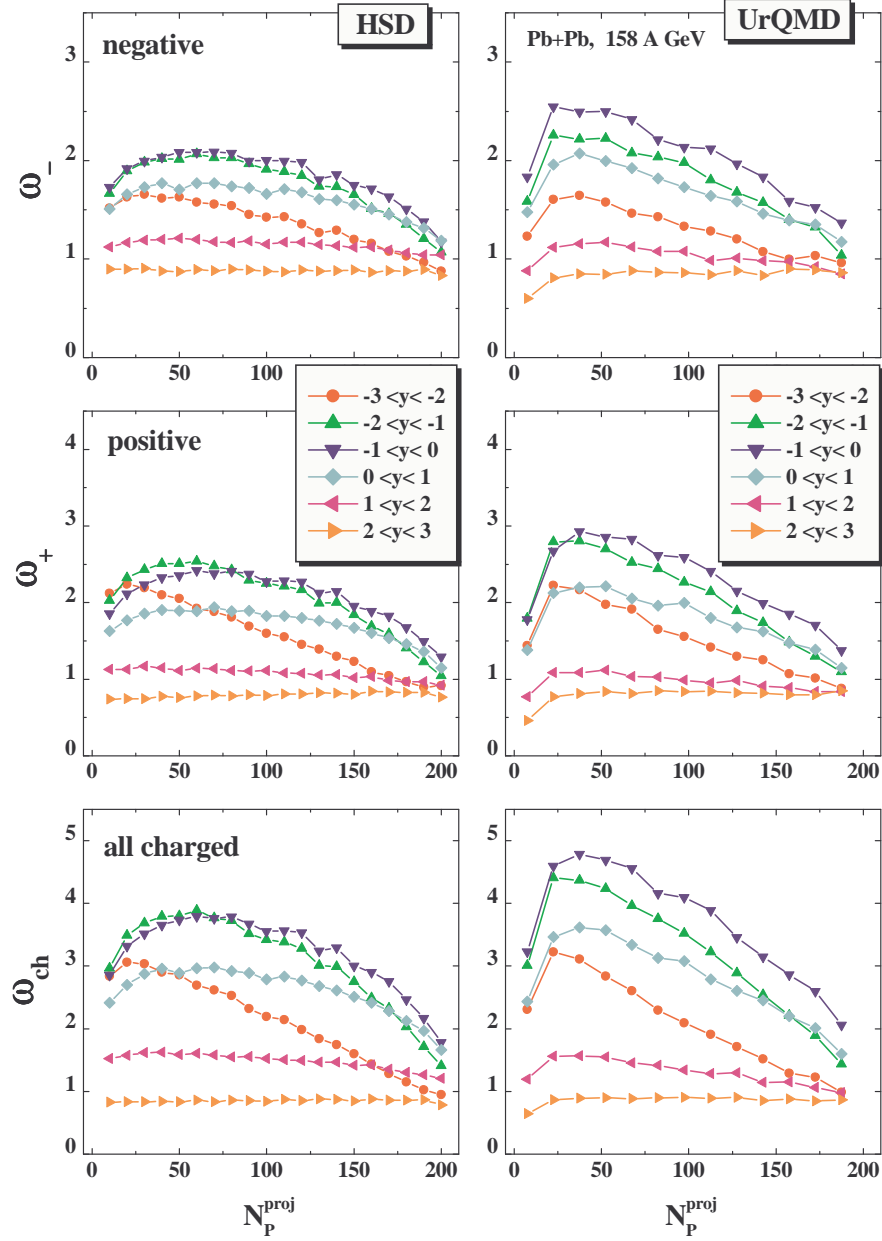


Figure 3.14: Particle number fluctuations ( $\omega_-$ ,  $\omega_+$ , and  $\omega_{ch}$ ) in the HSD (left) and UrQMD simulations (right) in different rapidity intervals in the projectile ( $y > 0$ ) and target hemispheres ( $y < 0$ ).

### 3.2.6 Fluctuations in different rapidity intervals

Fig. 3.14 shows the particle number fluctuations ( $\omega_-$ ,  $\omega_+$  and  $\omega_{ch}$ ) in the HSD and UrQMD simulations, given in different rapidity intervals of the projectile

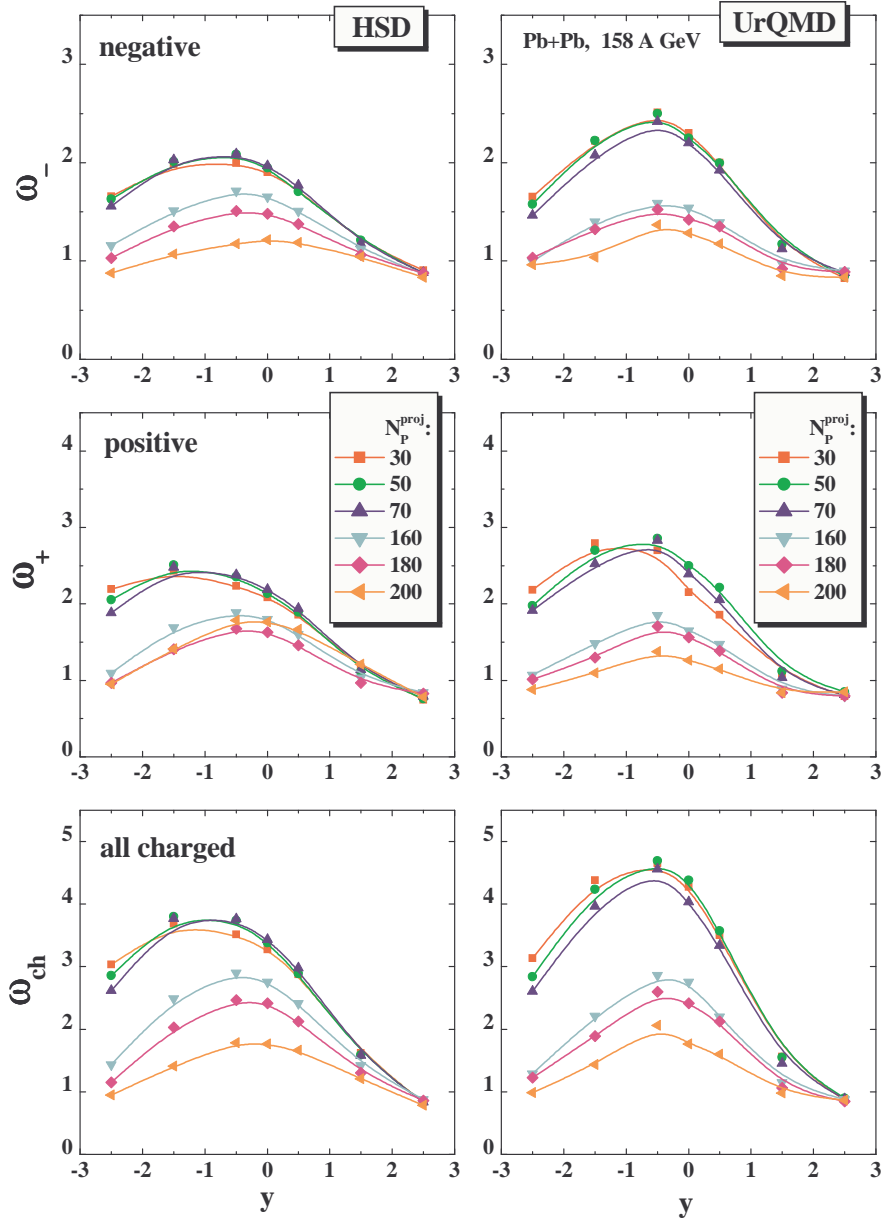


Figure 3.15: Particle number fluctuations ( $\omega_-$ ,  $\omega_+$ , and  $\omega_{ch}$ ) from the HSD (left) and UrQMD (right) approaches as a function of rapidity  $y$  for different number of projectile participants  $N_p^{part}$ .

( $y > 0$ ) and target ( $y < 0$ ) hemispheres. The same information is presented in Fig. 3.15, where  $\omega_-$ ,  $\omega_+$ , and  $\omega_{ch}$  are displayed explicitly as functions of rapidity for different  $N_p^{proj}$  values. It is clearly seen that the bias on a fixed number of projectile participants reduces strongly the particle fluctuations in the for-

ward hemisphere, in particular within the NA49 acceptance ( $1.1 < y < 2.6$ ). The fluctuations of the target participant numbers influence strongly the hadron production sources in the target hemispheres. They also contribute to the projectile hemisphere, but this contribution is only important in the rapidity interval  $0 < y < 1$ , i.e. close to midrapidity. It turns out that this "correlation length" in rapidity,  $\Delta y \approx 1$ , as seen in Fig. 3.14 and Fig. 3.15, is not large enough to reproduce the data. The large values of  $\omega_i$  and their strong  $N_P^{proj}$ -dependence in the NA49 data (cf. Fig. 3.5) in the projectile rapidity interval,  $1.1 < y < 2.6$ , thus demonstrate a significantly larger amount of mixing in peripheral reactions than generated in simple hadron/string transport approaches.

### 3.3 Multiplicity Fluctuations in Au+Au Collisions at RHIC

The charged multiplicity fluctuations in Au+Au collisions at  $\sqrt{s} = 200$  GeV have been measured recently by the PHENIX Collaboration [93, 94]. This section presents the results based on wounded nucleon model while employing the HSD transport model to define the centrality selection and to calculate the properties of hadron production sources (see [92] for details). This combined picture leads to a good agreement with the PHENIX data and suggests that the measured multiplicity fluctuations result dominantly from participant number fluctuations.

The centrality selection is an important aspect of fluctuation studies in A+A collisions. As it was discussed in the previous section 3.2 the samples of collisions with a fixed number of projectile participants  $N_P^{proj}$  can be selected to minimize the participant number fluctuations at a fixed target experiment. This selection is possible due to a measurement of the number of nucleon spectators from the projectile,  $N_S^{proj}$ , in each individual collision by a calorimeter which covers the projectile fragmentation domain.

In a collider type experiment charged spectators (e.g. protons,  $\alpha$ -particles) turn in magnetic field of the detectors and cannot be measured. Thus another centrality trigger should be used. For multiplicity fluctuations data the PHENIX Collaboration uses the following centrality selection. There are two kinds of detectors which define the centrality of Au+Au collision, Beam-Beam Counters (BBC) and Zero Degree Calorimeters (ZDC). At the c.m. pair energy  $\sqrt{s} =$

200 GeV, the BBC measure the charged particle multiplicity in the pseudorapidity range  $3.0 < |\eta| < 3.9$ , and the ZDC – the number of neutrons with  $|\eta| > 6.0$  [93, 94]. These neutrons are part of the nucleon spectators. Due to technical reasons the neutron spectators can be only detected by the ZDC (not protons and nuclear fragments), but in both hemispheres. The BBC distribution will be used in the HSD calculations to divide Au+Au collision events into 5% centrality samples. HSD does not specify different spectator groups – neutrons, protons, and nuclear fragments such that one can not use the ZDC information. In Fig. 3.16 (left) the HSD results for the BBC distribution and centrality classes in Au+Au collisions at  $\sqrt{s} = 200$  GeV are shown. One finds a good agreement between the HSD shape of the BBC distribution and the PHENIX data [93, 94]. The experimental estimates of  $\langle N_P \rangle$  for different centrality classes are based on the Glauber model. These estimates vary by less than 0.5% depending on the shape of the cut in the ZDC/BBC space or whether the BBC alone is used as a centrality measure [93, 94]. Note, however, that the HSD  $\langle N_P \rangle$  numbers are not exactly equal to the PHENIX values. It is also not obvious that different definitions for the 5% centrality classes give the same values of the scaled variance  $\omega_P$  for the participant number fluctuations.

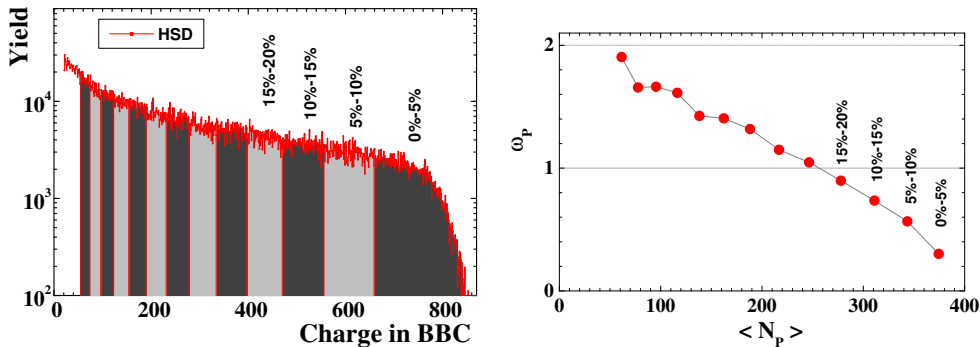


Figure 3.16: HSD model results for Au+Au collisions at  $\sqrt{s} = 200$  GeV. *Left:* Centrality classes defined via the BBC distribution. *Right:* The average number of participants,  $\langle N_P \rangle$ , and the scaled variance of the participant number fluctuations,  $\omega_P$ , calculated for the 5% BBC centrality classes.

Defining the centrality selection via the HSD transport model (which is similar to the BBC in the PHENIX experiment) we calculate the mean number of nucleon participants,  $\langle N_P \rangle$ , and the scaled variance of its fluctuations,  $\omega_P$ , in each 5%



centrality sample. The results are shown in Fig. 3.16, right. The Fig. 3.17 (left) shows the HSD results for the mean number of charged hadrons per nucleon participant,  $n_i = \langle N_i \rangle / \langle N_P \rangle$ , where the index  $i$  stands for “-”, “+”, and “ch”, i.e negatively, positively, and all charged final hadrons. Note that the centrality dependence of  $n_i$  is opposite to that of  $\omega_P$ :  $n_i$  increases with  $\langle N_P \rangle$ , whereas  $\omega_P$  decreases.

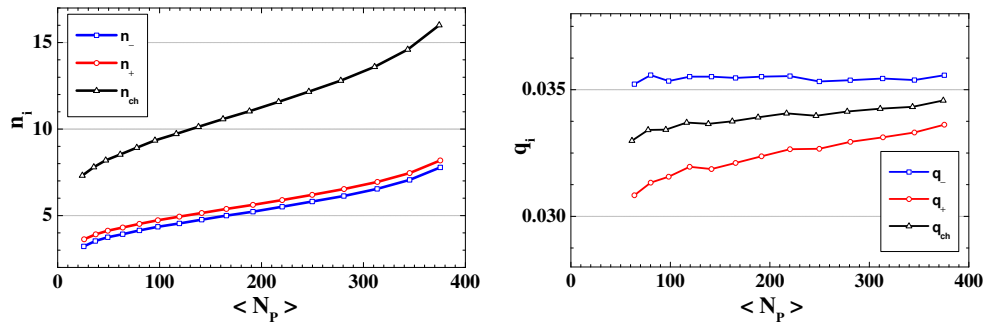


Figure 3.17: HSD results for different BBC centrality classes in Au+Au collisions at  $\sqrt{s} = 200$  GeV. *Left*: The mean number of charged hadrons per participant,  $n_i = \langle N_i \rangle / \langle N_P \rangle$ . *Right*: The fraction of accepted particles,  $q_i = \langle N_i^{acc} \rangle / \langle N_i \rangle$ .

The PHENIX detector accepts charged particles in a small region of the phase space with pseudorapidity  $|\eta| < 0.26$  and azimuthal angle  $\phi < 245^\circ$  and the  $p_T$  range from 0.2 to 2.0 GeV/c [93, 94]. The fraction of the accepted particles  $q_i = \langle N_i^{acc} \rangle / \langle N_i \rangle$  calculated within the HSD model is shown in the r.h.s. of Fig. 3.17. According to the HSD results only  $3 \div 3.5\%$  of charged particles are accepted by the mid-rapidity PHENIX detector.

To estimate the role of the participant number event-by-event fluctuations the wounded nucleon model has been used (see e.g., Refs [96, 91, 103, 98]),

$$\omega_i = \omega_i^* + n_i \omega_P . \quad (3.21)$$

The first term in the r.h.s. of Eq. 3.21 corresponds to the fluctuations of the hadron multiplicity from one source, and the second term,  $n_i \omega_P$ , gives additional fluctuations due to the fluctuations of the number of sources. As usually, it has been assumed that the number of sources is proportional to the number of nucleon participants. The value of  $n_i$  in Eq. 3.21 is then the average number of  $i$ 'th particles per participant,  $n_i = \langle N_i \rangle / \langle N_P \rangle$ . Also it has been assumed that

nucleon-nucleon collisions define the fluctuations  $\omega_i^*$  from a single source. To calculate the fluctuations  $\omega_i^{acc}$  in the PHENIX acceptance the acceptance scaling formula (see e.g., Refs. [96, 91, 103, 98]) is used:

$$\omega_i^{acc} = 1 - q_i + q_i \omega_i , \quad (3.22)$$

where  $q_i$  is the fraction of the accepted  $i$ 'th hadrons by the PHENIX detector. Using Eq. 3.21 for  $\omega_i$  one finds,

$$\omega_i^{acc} = 1 - q_i + q_i \omega_i^* + q_i n_i \omega_P . \quad (3.23)$$

The HSD results for  $\omega_P$  (Fig. 3.16, right),  $n_i$  (Fig. 3.17, left),  $q_i$  (Fig. 3.17, right), together with the HSD nucleon-nucleon values,  $\omega_-^* = 3.0$ ,  $\omega_+^* = 2.7$ , and  $\omega_{ch}^* = 5.7$  at  $\sqrt{s} = 200$  GeV, define completely the results for  $\omega_i^{acc}$  according to Eq. 3.23. We find a surprisingly good agreement of the results given by Eq. 3.23 with the PHENIX data shown in Fig. 3.18. Note that the centrality dependence of  $\omega_i^{acc}$  stems from the product,  $n_i \cdot \omega_P$ , in the last term of the r.h.s. of Eq. 3.23.

### 3.4 Summary of Chapter 3

The centrality dependence of multiplicity fluctuations have been studied for Pb+Pb collisions at 158 AGeV (in line with NA49 data) and Au+Au collisions at  $\sqrt{s} = 200$  GeV (PHENIX data). Different centrality selections have been performed in the analyses in correspondence to experimental situations. For the fix-target experiment NA49 samples of events with fixed numbers of the projectile participants,  $N_P^{proj}$ , have been studied while in collider type experiment PHENIX centrality classes of events have been defined by multiplicity in certain phase space. A decrease of participants fluctuations (and thus volume fluctuations) for more central collisions in both experiments has been obtained.

In section 3.2 the results for the scaled variances of negative, positive, and all charged hadrons in Pb+Pb minimum bias simulations at 158 AGeV have been presented based on HSD transport model. Also the UrQMD results have been shown for the comparison (see [91] for the details).

The samples with  $N_P^{proj} = 20 - 60$  show the large fluctuations of the number of target nucleons,  $N_P^{targ}$ , which participate in inelastic collisions,  $\omega_P^{targ} \geq 2$ .

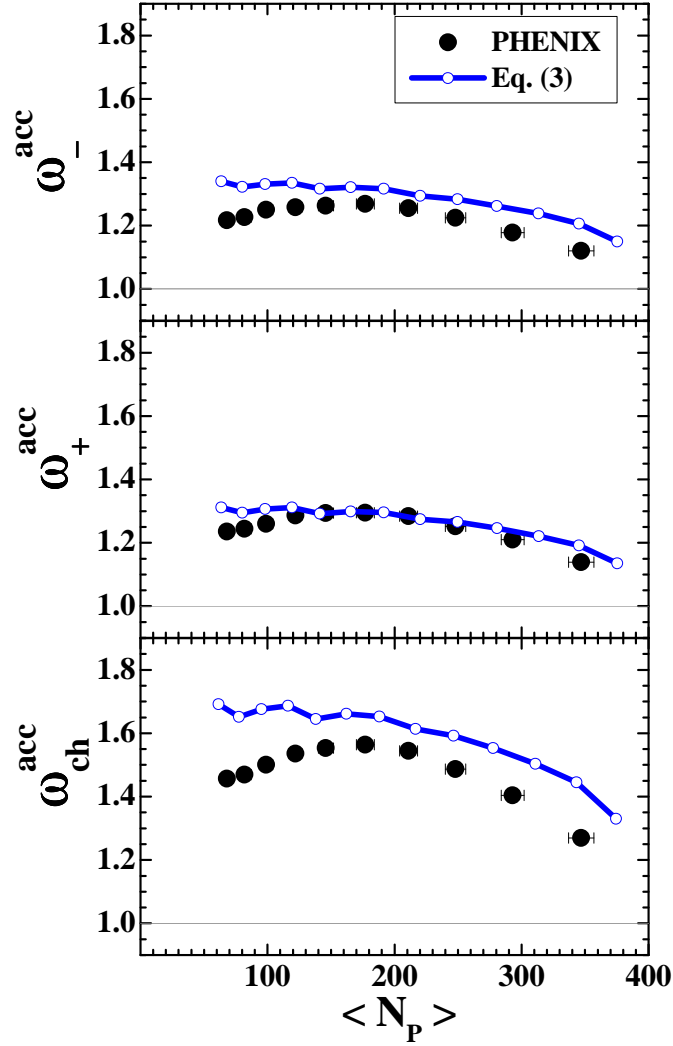


Figure 3.18: The scaled variance of charged particle fluctuations in Au+Au collisions at  $\sqrt{s} = 200$  GeV with the PHENIX acceptance. The circles are the PHENIX data [93, 94] while the open points (connected by the solid line) correspond to Eq. 3.23 with the HSD results for  $\omega_P$ ,  $n_i$ , and  $q_i$ .

The final hadron multiplicity fluctuations exhibit analogous behavior, which explains the large values of the HSD and UrQMD scaled variances  $\omega_i$  in the target hemispheres and in the full  $4\pi$  acceptance. On the other hand, the asymmetry between the projectile and target participants – introduced in the data samples by the trigger condition of fixed  $N_P^{targ}$  – can be used to explore different dynamics of nucleus-nucleus collisions by measuring the final multiplicity fluctuations as a function of rapidity (cf. Fig. 3.15). This analysis reveals that the NA49 data indicate a rather strong mixing of the longitudinal flows of the projectile

and target hadron production sources. This is so not only for central collisions – in line with the HSD and UrQMD approaches [104, 29, 105] – but also for rather peripheral reactions. This sheds new light on the nucleus-nucleus reaction dynamics at top SPS energies for peripheral and mid-peripheral Pb+Pb collisions. It demonstrates a significantly larger amount of mixing than is generated in simple hadron/string transport approaches.

In [section 3.3](#) the results for multiplicity fluctuations in Au+Au collisions at  $\sqrt{s} = 200$  GeV based on the wounded nucleon model (see [92]) are presented in comparison to the preliminary PHENIX data [93, 94]. Assuming that the number of hadron sources are proportional to the number of nucleon participants, the HSD transport model has been used to calculate the scaled variance of participant number fluctuations,  $\omega_P$ , and the number of  $i$ 'th hadrons per nucleon accepted by the mid-rapidity PHENIX detector,  $q_i n_i$ , in different Beam-Beam Counter centrality classes. The HSD model for nucleon-nucleon collisions has been also used to estimate the fluctuations from a single source,  $\omega_i^*$ . It has been found that this such combined model is in a good agreement with the PHENIX data [93, 94]. In different (5%) centrality classes  $\omega_P$  goes down and  $q_i n_i$  goes up with increasing  $\langle N_P \rangle$ . This results in non-monotonic dependence of  $\omega_i^{acc}$  on  $\langle N_P \rangle$  as seen in the PHENIX data.

Thus, one can conclude that both qualitative and quantitative features of the centrality dependence of the fluctuations seen in the present PHENIX data are the consequences of participant number fluctuations. To avoid a dominance of the participant number fluctuations one needs to analyze most central collisions with a much more rigid ( $\leq 1\%$ ) centrality selection.

## Chapter 4

# Baryon Number and Electric Charge Fluctuations in Pb+Pb Collisions at SPS energies

The aim of the present chapter is to study the event-by-event fluctuations of the net baryon number and electric charge in Pb-Pb collisions at 158 AGeV energies within the HSD transport approach [103]. An important role of the fluctuations in the number of target nucleon participants is revealed since they strongly influence all measured fluctuations even in the samples of events with rather rigid centrality trigger.

### 4.1 Net Baryon Number Fluctuations

Let's start with a quantitative discussion by first considering the fluctuations of the net baryon number in different regions of the participant domain in collisions of two identical nuclei. These fluctuations are most closely related to the fluctuations of the number of participant nucleons because of baryon number conservation.

The HSD results for  $\omega_B$  in Pb+Pb at 158 AGeV are presented in Fig. 4.1. In each event the nucleon spectators when counting the number of baryons are subtracted. The net baryon number in the full phase space,  $B \equiv N_B - N_{\bar{B}}$ , equals then to the total number of participants  $N_P = N_P^{targ} + N_P^{proj}$ . At fixed  $N_P^{proj}$  the  $N_P$  number fluctuates due to fluctuations of  $N_P^{targ}$ . These fluctuations correspond

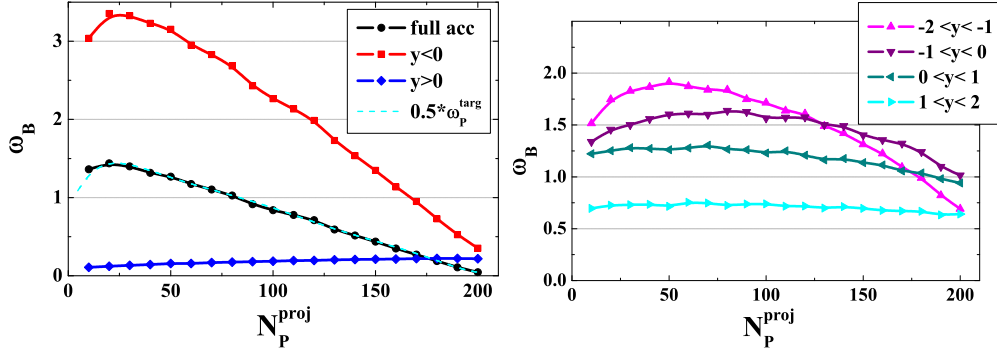


Figure 4.1: The HSD simulations for Pb+Pb collisions at 158 AGeV for fixed values of  $N_P^{proj}$ . *Left:* The baryon number fluctuations in full acceptance,  $\omega_B$ , in projectile hemisphere,  $\omega_B^p$  (lower curve), and in target hemisphere,  $\omega_B^t$  (upper curve). The dashed line,  $0.5 \omega_P^{targ}$ , demonstrates the validity of the relation (Eq. 4.1). *Right:* The scaled variances of the baryon number fluctuations in different rapidity intervals.

to an average value,  $\langle N_P^{targ} \rangle \simeq N_P^{proj}$ , and a scaled variance,  $\omega_P^{targ}$  (see Fig. 3.4). Thus, for the net baryon number fluctuations in the full phase space one finds,

$$\omega_B = \frac{Var(N_P)}{\langle N_P \rangle} \simeq \frac{\langle (N_P^{targ})^2 \rangle - \langle N_P^{targ} \rangle^2}{2\langle N_P^{targ} \rangle} = \frac{1}{2} \omega_P^{targ}. \quad (4.1)$$

A factor 1/2 in the right hand side of Eq. 4.1 appears because only half of the total number of participants fluctuates.

One introduces  $\omega_B^p$  and  $\omega_B^t$ , where the superscripts  $p$  and  $t$  mark quantities measured in the projectile and target momentum hemispheres, respectively. Fig. 4.1 demonstrates that  $\omega_B^t > \omega_B^p$ , both in the whole projectile-target hemispheres and in the symmetric rapidity intervals. On the other hand one observes that  $\omega_B^p \approx \omega_B^t$  in most central collisions. This is because the fluctuations of the target participants become negligible in this case, i.e.  $\omega_P^{targ} \rightarrow 0$  (Fig. 3.4, right). As a consequence the fluctuations of any observable in the symmetric rapidity intervals become identical in most central collisions. Note also that transparency-mixing effects are different at different rapidities. From Fig. 3.4 (right) it follows that  $\omega_B^p$  in the target rapidity interval  $[-2, -1]$  is much larger than  $\omega_B^t$  in the symmetric projectile rapidity interval  $[1, 2]$ . This fact reveals the strong transparency effects. On the other hand, the behavior is different in symmetric rapidity intervals near the midrapidity. From Fig. 3.4 (right) one observes that  $\omega_B^p$  in the target

rapidity interval  $[-1, 0]$  is already much closer to  $\omega_B^t$  in the symmetric projectile rapidity interval  $[0, 1]$ . This gives a rough estimate of the width,  $\Delta y \approx 1$ , for the region in rapidity space where projectile and target nucleons communicate to each others.

As discussed in [subsection 3.2.4](#), the mixing of the projectile and target participants is absent in T- and R-models. Therefore, in T-models, the net baryon number in the projectile hemisphere equals to  $N_p^{proj}$  and does not fluctuate, i.e.  $\omega_B^p(T) = 0$ , whereas the net baryon number in the target hemisphere equals to  $N_p^{targ}$  and fluctuates with  $\omega_B^t(T) = \omega_P^{targ}$ . These relations are reversed in R-models. One introduces now a mixing of baryons between the projectile and target hemispheres. Let  $\alpha$  be the probability for a (projectile) target participant to be detected in the (target) projectile hemisphere. One denotes by  $n^t$  and  $n^p$  the number of baryons which end up in the target and projectile hemisphere, respectively, from the opposite hemisphere. Then the probabilities to detect  $B^t$  baryons in the target hemisphere, and  $B^p$  baryons in the projectile hemisphere, can be written as,

$$\begin{aligned}
P(B^t; N_P^{proj}) &= \\
&\sum_{N_P^{targ}} W(N_P^{targ}; N_P^{proj}) \sum_{n^t=1}^{N_P^{targ}} \sum_{n^p=1}^{N_P^{proj}} \alpha^{n^p} (1-\alpha)^{N_P^{targ}-n^p} \frac{N_P^{targ}!}{n^p!(N_P^{targ}-n^p)!} \\
&\times \alpha^{n^t} (1-\alpha)^{N_P^{proj}-n^t} \frac{N_P^{proj}!}{n^t!(N_P^{proj}-n^t)!} \delta(B^t - N_P^{targ} - n^t + n^p), \quad (4.2)
\end{aligned}$$

$$\begin{aligned}
P(B^p; N_P^{proj}) &= \\
&\sum_{N_P^{targ}} W(N_P^{targ}; N_P^{proj}) \sum_{n^t=1}^{N_P^{targ}} \sum_{n^p=1}^{N_P^{proj}} \alpha^{n^p} (1-\alpha)^{N_P^{targ}-n^p} \frac{N_P^{targ}!}{n^p!(N_P^{targ}-n^p)!} \\
&\times \alpha^{n^t} (1-\alpha)^{N_P^{proj}-n^t} \frac{N_P^{proj}!}{n^t!(N_P^{proj}-n^t)!} \delta(B^p - N_P^{proj} - n^p + n^t), \quad (4.3)
\end{aligned}$$

where  $W(N_P^{targ}; N_P^{proj})$  is the probability distribution of  $N_P^{targ}$  in a sample with fixed value of  $N_P^{proj}$ . From [Eq. 4.2](#) and [Eq. 4.3](#) with a straightforward calculation

one finds:

$$\begin{aligned}\omega_B^t &= (1 - \alpha)^2 \omega_P^{targ} + 2\alpha(1 - \alpha) , \\ \omega_B^p &= \alpha^2 \omega_P^{targ} + 2\alpha(1 - \alpha) .\end{aligned}\quad (4.4)$$

A (complete) mixing of the projectile and target participants is assumed in M-models. Thus each participant nucleon with equal probability,  $\alpha = 1/2$ , can be found either in the target or in projectile hemispheres. In M-models the fluctuations in both projectile and target hemispheres are identical. The limiting cases,  $\alpha = 0$  and  $\alpha = 1$ , of Eq. 4.4 correspond to T- and R-models, respectively. In summary, the scaled variances of the net baryon number fluctuations in the projectile,  $\omega_B^p$ , and target,  $\omega_B^t$ , hemispheres are:

$$\omega_B^p(T) = 0 , \quad \omega_B^t(T) = \omega_P^{targ} , \quad (4.5)$$

$$\omega_B^p(M) = \omega_B^t(M) = \frac{1}{2} + \frac{1}{4} \omega_P^{targ} , \quad (4.6)$$

$$\omega_B^p(R) = \omega_P^{targ} , \quad \omega_B^t(R) = 0 , \quad (4.7)$$

in the T- (Eq. 4.5), M- (Eq. 4.6) and R- (Eq. 4.7) models of the baryon number flow. The different models lead to significantly different predictions for  $\omega_B^p$  and  $\omega_B^t$ .

Fig. 4.2 shows the predictions of T-, M- and R-models (Eq. 4.5-Eq. 4.7) with  $\omega_P^{targ}$  from Fig. 3.4 for Pb+Pb collisions at 158A GeV.

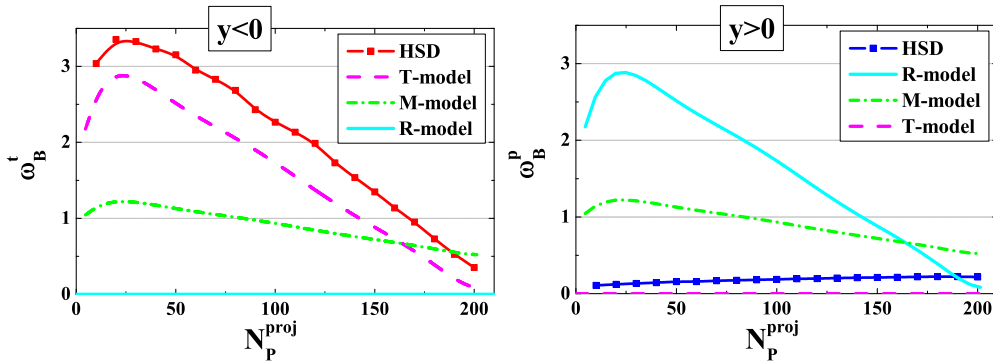


Figure 4.2: The  $\omega_B^t$  (left) and  $\omega_B^p$  (right) of the HSD simulations in comparison to T-, M- and R-models (Eq. 4.5-Eq. 4.7), with  $\omega_P^{targ}$  taken from Fig. 3.4.

From Fig. 4.2 one concludes that the HSD results are close to the T-model



estimates for baryon flow. However, the deviations from the results (Eq. 4.5) are clearly seen:  $\omega_B^p > 0$  and  $\omega_B^t > \omega_P^{targ}$ . One can not fit the HSD values of  $\omega_B^t$  and  $\omega_B^p$  by Eq. 4.4. To make  $\omega_B^p > 0$  one needs  $\alpha > 0$ , but this induces  $\omega_B^t < \omega_P^{targ}$ , i.e. a mixing of baryons between the projectile and target hemispheres creates a non-zero baryon number fluctuations in the projectile hemisphere on the expense of fluctuations in the target hemisphere. Indeed, it follows from Eq. 4.4 that  $\omega_B^p$  increases with  $\alpha$  for all  $\alpha$ , if  $\omega_P^{targ} > 1$ , and for  $\alpha < (2 - \omega_P^{targ})^{-1}$ , if  $\omega_P^{targ} < 1$ . On the other hand,  $\omega_B^t$  increases with  $\alpha$  if  $\alpha < (1 - \omega_P^{targ})(2 - \omega_P^{targ})^{-1}$ . This shows that an increase of  $\omega_B^t$  with  $\alpha$  is only possible for  $\omega_P^{targ} < 1$ . Thus, for  $\omega_P^{targ} > 1$  one finds an increase of  $\omega_B^p$  with  $\alpha$  and a decrease of  $\omega_B^t$  with  $\alpha$  for all physical values of  $\alpha$  from 0 to 1. Therefore, the HSD values of  $\omega_B^t$  (i.e. the fact that  $\omega_B^t > \omega_P^{targ}$ ) can not be explained by Eq. 4.4 with  $\alpha > 0$ .

The numbers of target and projectile participants are defined as  $N_P^{targ} \equiv A - N_S^{targ}$  and  $N_P^{proj} \equiv A - N_S^{proj}$ . The actual event-by-event numbers of baryons in the target and projectile hemispheres,  $N_B^t$  and  $N_B^p$ , may differ from  $N_P^{targ}$  and  $N_P^{proj}$ . This is because a transfer of baryons between the projectile and target hemispheres arises from the production of baryon-antibaryon pairs. The partners of each newly created  $b\bar{b}$ -pair can be detected with non-zero probability in different hemispheres. One introduces  $b^t \equiv N_B^t - N_P^{targ}$  and the number of antibaryons in the target hemisphere,  $\bar{b}^t$ . Similarly,  $b^p \equiv N_B^p - N_P^{proj}$ , while  $\bar{b}^p$  is the number of antibaryons in the projectile hemisphere. One finds:

$$\omega_B^t \equiv \frac{Var(N_P^{targ} + b^t - \bar{b}^t)}{\langle B^t \rangle} = \omega_P^{targ} + \frac{1}{N_P^{proj}} [Var(b^t) + Var(\bar{b}^t) + 2 \Delta(N_P^{targ}, b^t) - 2 \Delta(N_P^{targ}, \bar{b}^t) - 2 \Delta(b^t, \bar{b}^t)], \quad (4.8)$$

$$\omega_B^p \equiv \frac{Var(N_P^{proj} + b^p - \bar{b}^p)}{\langle B^p \rangle} = \frac{1}{N_P^{proj}} \times [Var(b^p) + Var(\bar{b}^p) - 2 \Delta(b^p, \bar{b}^p)], \quad (4.9)$$

where

$$\Delta(N_1, N_2) \equiv \langle N_1 \cdot N_2 \rangle - \langle N_1 \rangle \cdot \langle N_2 \rangle. \quad (4.10)$$

As  $N_P^{proj} = const$  in the sample, it follows that  $\omega_P^{proj} = 0$ ,  $\Delta(N_P^{proj}, b^p) = 0$ ,  $\Delta(N_P^{proj}, \bar{b}^p) = 0$ , these terms are absent in the r.h.s. of Eq. 4.9. Different terms

of Eq. 4.8 and Eq. 4.9 found from the HSD simulations are presented in Fig. 4.3.

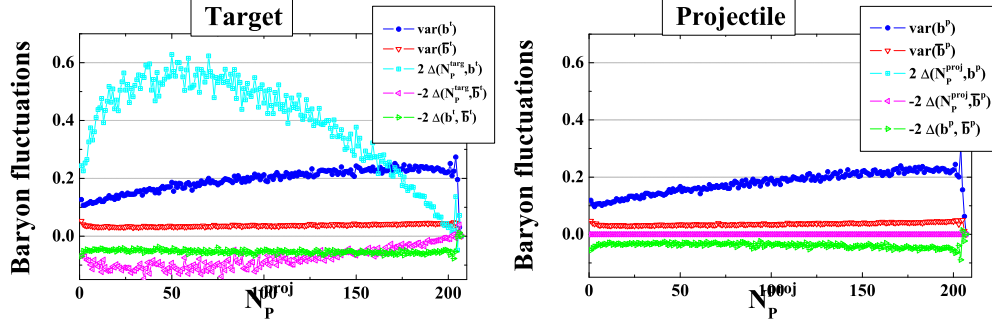


Figure 4.3: Different terms of Eq. 4.8, left, and Eq. 4.9, right, are presented as a function of  $N_P^{proj}$ .

One observes that terms of Eq. 4.8 and Eq. 4.9 expressing the fluctuations of antibaryons,  $Var(\bar{b}^p)/N_P^{proj}$ , and the correlation terms,  $2\Delta(N_P^{targ}, \bar{b}^t)/N_P^{proj}$  and  $-2\Delta(b^t, \bar{b}^t)/N_P^{proj}$ , with antibaryons included, are small. Therefore, one finds,  $\omega_B^p \cong Var(b^p)/N_P^{proj}$ . In the target hemisphere, the  $\omega_P^{targ}$  gives the main contribution to  $\omega_B^t$  in Eq. 4.8. The term  $Var(b^t)/N_P^{proj}$  also contributes to  $\omega_B^t$ , similarly to that,  $Var(b^p)/N_P^{proj}$ , in the projectile hemisphere. However, the main additional term to  $\omega_B^t$  is  $2\Delta(N_P^{targ}, b^t)/N_P^{proj}$ , which is due to (positive) correlations between  $N_P^{targ}$  and  $b^t$ . This implies that in events with large  $N_P^{targ}$  (i.e.  $N_P^{targ} > \langle N_P^{targ} \rangle \cong N_P^{proj}$ ) some additional baryons move from the projectile to the target hemisphere, and when  $N_P^{targ}$  is small (i.e.  $N_P^{targ} < \langle N_P^{targ} \rangle \cong N_P^{proj}$ ) the baryons move in the reverse direction from the target to the projectile hemisphere as shown in Fig. 4.4.

Remind that Eq. 4.4 predicts for  $\omega_B^t$  the opposite behavior: due to a simple mixing of baryons between the target and projectile hemispheres the initially large fluctuations,  $\omega_P^{targ}$ , are transformed into smaller ones,  $\omega_B^t$ . It seems that the origin of this effect is the following: For  $N_P^{targ} > N_P^{proj}$  each projectile nucleon interacts, in average, more often than the target nucleon. The projectile participant loses then a larger part of its energy, and in the rapidity space its position becomes closer to  $y_{c.m.} = 0$  than the position of target participants. This gives to projectile participants more chances to move due to further rescatterings from projectile to target hemisphere, in a comparison with target participants to move in the opposite direction. For  $N_P^{targ} < N_P^{proj}$  there is a reverse situation. This fact was not taken into account in Eq. 4.2 and Eq. 4.3 where it has been assumed that

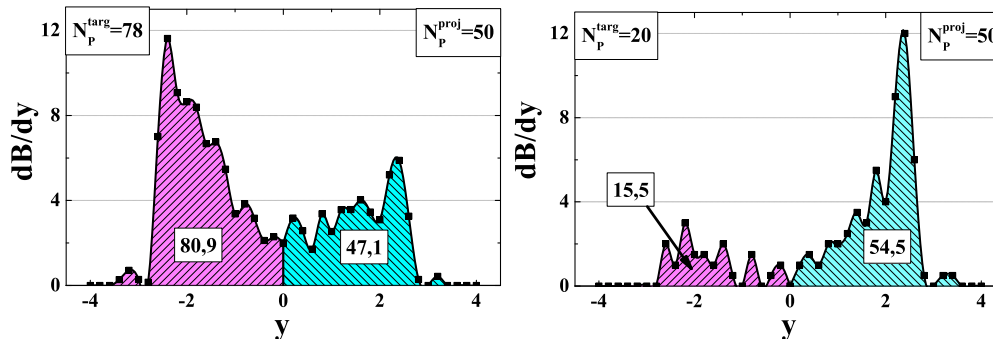


Figure 4.4: The HSD results for Pb+Pb collisions at 158 AGeV for the rapidity distributions of baryon numbers in nonsymmetric samples with  $N_P^{proj} = 50$ ,  $N_P^{targ} = 78$  (left), and  $N_P^{proj} = 50$ ,  $N_P^{targ} = 20$  (right). The numbers in the areas mark the correspondent baryon numbers.

the mixing probability  $\alpha$  is the same for projectile and target participants, and independent of  $N_P^{targ}$ .

## 4.2 Net Electric Charge Fluctuations

The T-, M- and R-models give very different predictions for  $\omega_B^p$  and  $\omega_B^t$  for the samples of events with fixed values of  $N_P^{targ}$ . Additional interesting correlations between the  $B^t$  and  $B^p$  numbers, as those seen in the HSD simulations, can be expected. Unfortunately, it is difficult to test experimentally such correlations since an identification of protons and a measurement of neutrons in a large acceptance in a single event is difficult.

In this section we consider the HSD results for the net electric charge,  $Q$ , fluctuations. As  $Q \cong 0.4B$  in the initial heavy nuclei one can naively expect that  $Q$  fluctuations are quite similar to  $B$  fluctuations. However, there is a principal difference between  $Q$  and  $B$  in relativistic A+A collisions. Fig. 4.5 demonstrates the rapidity distributions of the net baryon number,  $B = N_B - N_{\bar{B}}$  (left), and total number of baryons,  $N_B + N_{\bar{B}}$  (right), for different centralities in Pb+Pb collisions at 158 AGeV. One observes that both quantities are very close to each other; the  $y$ -dependence and absolute values are very close for  $B$  and  $N_B - N_{\bar{B}}$  distributions. This is, of course, because the number of antibaryons is rather small,  $N_{\bar{B}} \ll N_B$ .

Fig. 4.6 shows the same as Fig. 4.5 but for the electric charge  $Q = N_+ -$

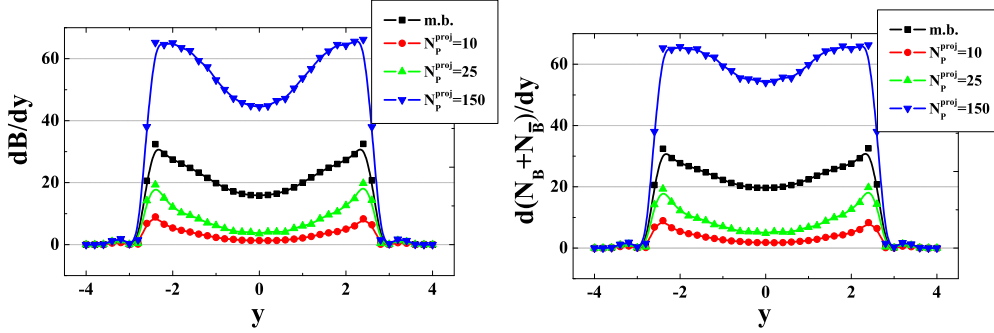


Figure 4.5: The HSD rapidity distributions in Pb+Pb collisions at 158 AGeV for the net baryon number,  $B = N_B - N_{\bar{B}}$  (left), and total number of baryons,  $N_B + N_{\bar{B}}$  (right), at different  $N_P^{proj}$  and in the minimum bias (m.b.) sample.

$N_-$  (left), and total number of charged particles,  $N_{ch} \equiv N_+ + N_-$  (right).

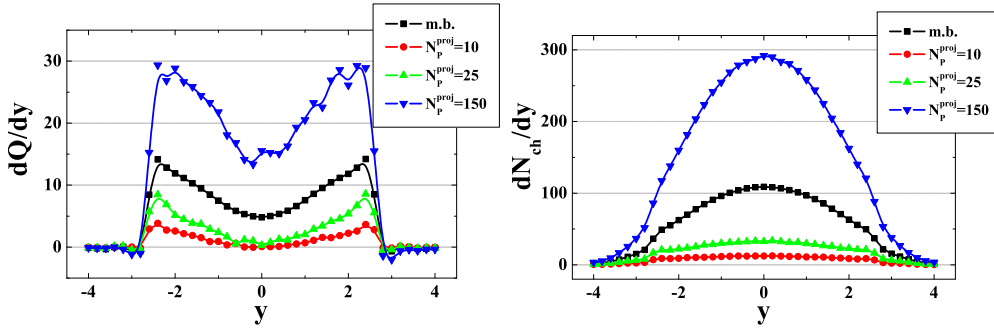


Figure 4.6: The same as in Fig. 4.5 but for the electric charge  $Q = N_+ - N_-$  (left), and total number of charged particles,  $N_{ch} \equiv N_+ + N_-$  (right).

The  $y$ -dependence of  $dQ/dy$  and  $dN_{ch}/dy$  is quite different. Besides, the absolute values of  $N_{ch}$  are about 10 times larger than those of  $Q$ . This implies that  $Q \ll N_+ \approx N_-$ .

In the previous section the scaled variance  $\omega_B$  to quantify the measure of the net baryon fluctuations has been used. It appears to be a useful variable as  $\omega_B$  is straightforwardly connected to  $\omega_P^{targ}$  and due to the relatively small number of antibaryons. Fig. 4.6 tells that  $\omega_Q$  is a bad measure of the electric charge fluctuations in high energy A+A collisions. One observes that  $\omega_Q \equiv Var(Q)/\langle Q \rangle$  is much larger than 1 simply due to the small value of  $\langle Q \rangle$  in a comparison with  $N_+$  and  $N_-$ . If the A+A collision energy increases, it follows,  $\langle Q \rangle \rightarrow 0$ , and thus  $\omega_Q \rightarrow \infty$ . The same will happen with  $\omega_B$ , too, at much larger energies. A useful

measure of the net electric charge fluctuations is the quantity (see, e.g., [106]):

$$X_Q \equiv \frac{Var(Q)}{\langle N_{ch} \rangle}. \quad (4.11)$$

A value of  $X_Q$  can be easily calculated for the Boltzmann ideal gas in the grand canonical ensemble. In this case the number of negative and positive particles fluctuates according to the Poisson distribution (i.e.  $\omega_- = \omega_+ = 1$ ), and the correlation between  $N_+$  and  $N_-$  are absent (i.e.  $\langle N_+ N_- \rangle = \langle N_+ \rangle \langle N_- \rangle$ ), so that  $X_Q = 1$ . On the other hand, the canonical ensemble formulation (i.e. when  $Q = const$  fixed exactly for all microscopic states of the system) leads to  $X_Q = 0$ . Fig. 4.7 shows the results of the HSD simulations for the full acceptance, for the projectile and target hemispheres (left), and also for symmetric rapidity intervals in the c.m.s. (right).

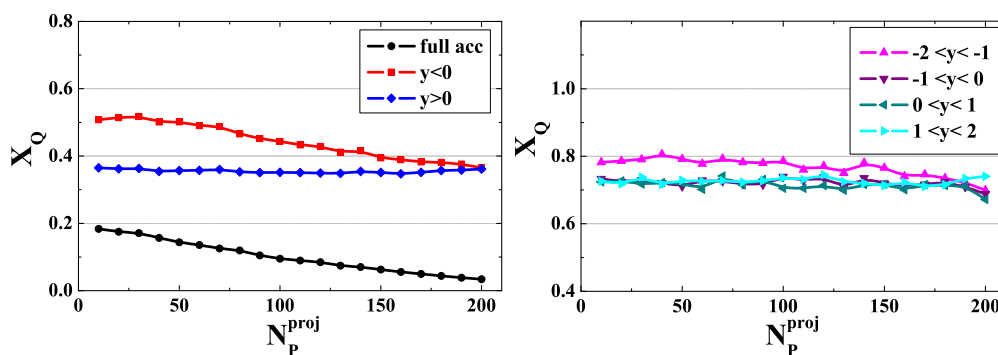


Figure 4.7: *Left*: The HSD simulations in Pb+Pb collisions at 158 AGeV for  $X_Q$  at different values of  $N_P^{proj}$  in the full acceptance (lower curve), for the projectile (middle curve) and target (upper curve) hemispheres. *Right*: The same, but for symmetric rapidity intervals in the c.m.s.

The  $Q$  fluctuation in the full acceptance is due to  $N_P^{targ}$  fluctuations. As  $Q \cong 0.4B$  in colliding (heavy) nuclei, one may expect  $Var(Q) \cong 0.16 Var(B)$ . In addition,  $\langle N_{ch} \rangle \cong 4\langle N_P \rangle$  at 158 AGeV, so that one estimates  $X_Q \cong 0.04 \omega_B$  for the fluctuations in the full phase space. The actual values of  $X_Q$  presented in Fig. 4.7 (left) are about 3 times larger. This is because of  $Q$  fluctuations due to different event-by-event values of proton and neutron participants even in a sample with fixed values of  $N_P^{proj}$  and  $N_P^{targ}$ .

From Fig. 4.7 (right) one sees only a tiny difference between the  $X_Q$  values in the symmetric rapidity intervals in the projectile and target hemispheres, and

slightly stronger effects for the whole projectile and target hemispheres (Fig. 4.7, right). In fact, the fluctuations of  $N_+$  and  $N_-$  are very different in the projectile and target hemispheres, and the scaled variances  $\omega_+^t$  and  $\omega_-^t$  have a very strong  $N_P^{proj}$ -dependence. This is shown on top-left and middle-left panels of Fig. 3.10.

The  $X_Q$  can be presented in two equivalent forms

$$\begin{aligned} X_Q &= \omega_+ \frac{\langle N_+ \rangle}{\langle N_{ch} \rangle} + \omega_- \frac{\langle N_- \rangle}{\langle N_{ch} \rangle} - 2 \frac{\Delta(N_+, N_-)}{\langle N_{ch} \rangle} \\ &= 2 \omega_+ \frac{\langle N_+ \rangle}{\langle N_{ch} \rangle} + 2 \omega_- \frac{\langle N_- \rangle}{\langle N_{ch} \rangle} - \omega_{ch} . \end{aligned} \quad (4.12)$$

Eq. 4.12 is valid for any region of the phase space: full phase space, projectile or target hemisphere, etc. As seen from Fig. 3.10, both  $\omega_+^t$  and  $\omega_-^t$  are large and strongly  $N_P^{proj}$ -dependent. This is not seen in  $X_Q^t$  because of strong correlations between  $N_+^t$  and  $N_-^t$ , i.e. the term  $2 \Delta(N_+, N_-)/\langle N_{ch} \rangle$  compensates  $\omega_+$  and  $\omega_-$  terms in Eq. 4.12. This is also seen on bottom-left of Fig. 3.10.

A cancellation of strong  $N_P^{proj}$ -dependence in the target hemisphere takes place between the sum of  $\omega_+^t$  and  $\omega_-^t$  terms of Eq. 4.12, and the  $\omega_{ch}^t$ -term.

Fig. 4.8 shows a comparison of the HSD results for  $X_Q$  with NA49 data in Pb+Pb collisions at 158 AGeV for the forward rapidity interval  $1.1 < y < 2.6$  inside the projectile hemisphere with additional  $p_T$ -filter imposed.

As an illustration, the HSD results in the symmetric backward rapidity interval  $-2.6 < y < -1.1$  (target hemisphere) are also included. One observes no difference between the  $X_Q$  results for the NA49 acceptance in the projectile and target hemispheres. The HSD values for  $\omega_+$ ,  $\omega_-$ , and  $\omega_{ch}$  are rather different in the projectile and target hemispheres for the NA49 acceptance (see Fig. 3.10). This is not seen in Fig. 4.8 for  $X_Q$ . As explained above a cancellation between  $\omega_+$ ,  $\omega_-$  and  $\omega_{ch}$  terms take place in Eq. 4.12. In fact, NA49 did not perform the  $X_Q$  measurements. The  $X_Q$ -data (solid dots) presented in Fig. 4.8 are obtained from Eq. 4.12 using the NA49 data for  $\omega_+$ ,  $\omega_-$ , and  $\omega_{ch}$  as well as  $\langle N_+ \rangle$ ,  $\langle N_- \rangle$ , and  $\langle N_{ch} \rangle$  [95, 107, 108]. Such a procedure leads, however, to very large errors for  $X_Q$  (which are not indicated in Fig. 4.8) which excludes any conclusion about the (dis)agreement of HSD results with NA49 data.

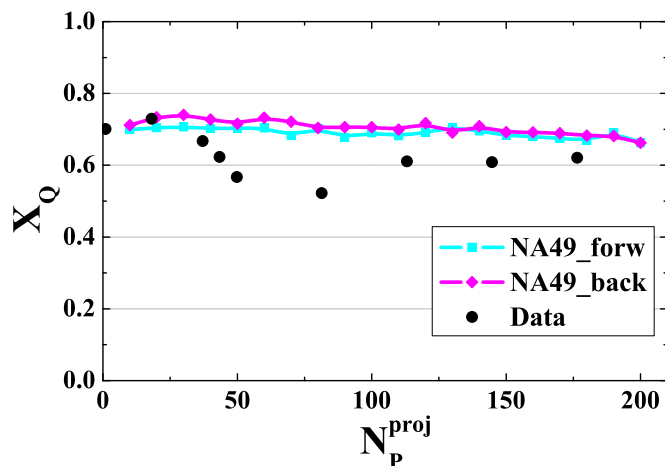


Figure 4.8: The HSD results for  $X_Q$  for Pb+Pb collisions at 158 AGeV for the forward rapidity interval  $1.1 < y < 2.6$  inside the projectile hemisphere. The solid dots are the estimates obtained from Eq. 4.12 using the NA49 experimental data [95, 107, 108] (the error bars are not indicated here). For illustration, the HSD results in the symmetric backward rapidity interval  $-2.6 < y < -1.1$  (target hemisphere) are also presented.

### 4.3 Fluctuations in Most Central Collisions

In this section the baryon number and electric charge fluctuations in the symmetric rapidity interval  $[-y, y]$  in the c.m.s. for the most central Pb+Pb events are considered. The sample of most central events is chosen by restricting the impact parameter to  $b < 2$  fm. It gives about 2% most central Pb+Pb collisions from the whole minimum bias sample. Fig. 4.9 shows the HSD results for electric charge fluctuations in 2% most central Pb+Pb collisions for the symmetric rapidity interval  $\Delta Y = [-y, y]$  in the c.m.s. as the function of  $\Delta y = \Delta Y/2$ .

For  $\Delta Y \rightarrow 0$  one finds  $X_Q \rightarrow 1$ . This can be understood as follows: For  $\Delta Y \rightarrow 0$  the fluctuations of negatively, positively and all charged particles behave as for the Poisson distribution:  $\omega_+ \cong \omega_- \cong \omega_{ch} \cong 1$ . Then from Eq. 4.12 it follows that  $X_Q \cong 1$ , too. From Fig. 4.9 (right) one observes that  $\omega_+$ ,  $\omega_-$ , and  $\omega_{ch}$  all increase with increasing interval  $\Delta Y$ . However,  $X_Q$  decreases with  $\Delta Y$  and – because of global  $Q$  conservation – it goes approximately to zero when all final particles are accepted.

In Fig. 4.10 (left) the HSD results for the scaled variances are presented in full acceptance as functions of  $N_P^{\text{proj}}$ . Fig. 4.10 (right) demonstrates the probability

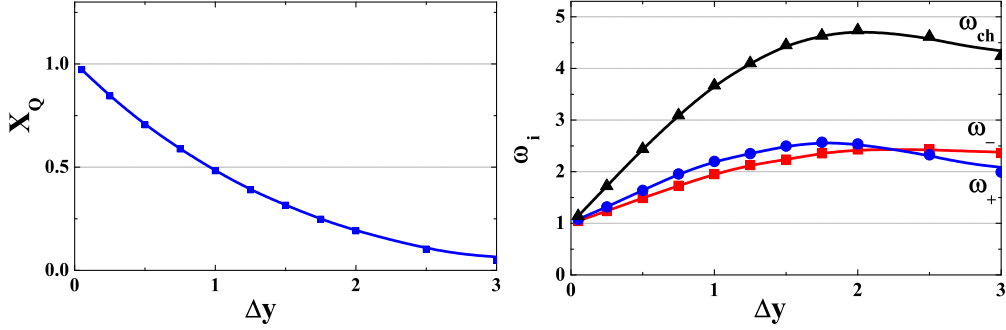


Figure 4.9: The HSD results for electric charge fluctuations in 2% most central Pb+Pb collisions at 158 AGeV in the symmetric rapidity interval,  $\Delta Y = [-y, y]$  as a function of  $\Delta y = \Delta Y/2$  in the c.m.s. A *left* panel shows the behavior of  $X_Q$ , and a *right* one demonstrates separately  $\omega_+$ ,  $\omega_-$ , and  $\omega_{ch}$ .

distribution of events with  $b < 2$  fm over  $N_P^{proj}$ .

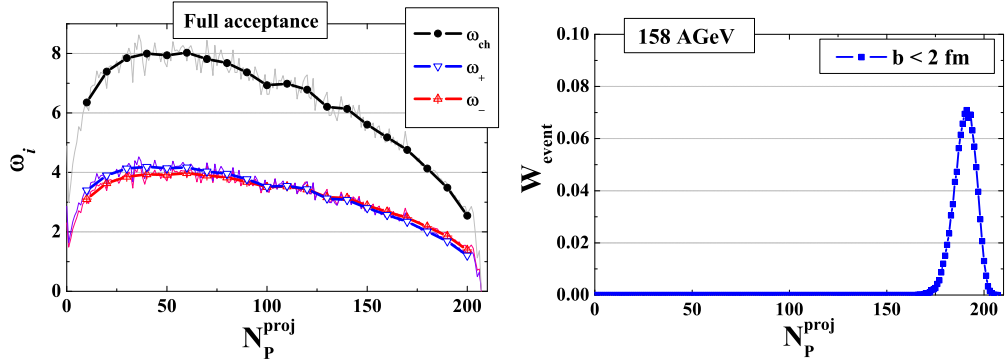


Figure 4.10: The HSD results in Pb+Pb collisions at 158 AGeV. *Left*: The scaled variances  $\omega_+$ ,  $\omega_-$ , and  $\omega_{ch}$  in the full acceptance (like in Fig. 3.5). *Right*: The distributions of events over  $N_P^{proj}$  in most central collisions with  $b < 2$  fm.

One observes that even in the 2% centrality sample the values of  $N_P^{proj}$  are noticeably smaller than the maximum value,  $A = 208$ . As seen from Fig. 4.10 (left) the HSD values of  $\omega_+$ ,  $\omega_-$ , and  $\omega_{ch}$  become then essentially larger than 1 in agreement with those presented in Fig. 4.9.

Fig. 4.11 shows the net baryon number fluctuations in the symmetric rapidity interval  $[-y, y]$  in the c.m.s. as the function of  $\Delta Y$ .



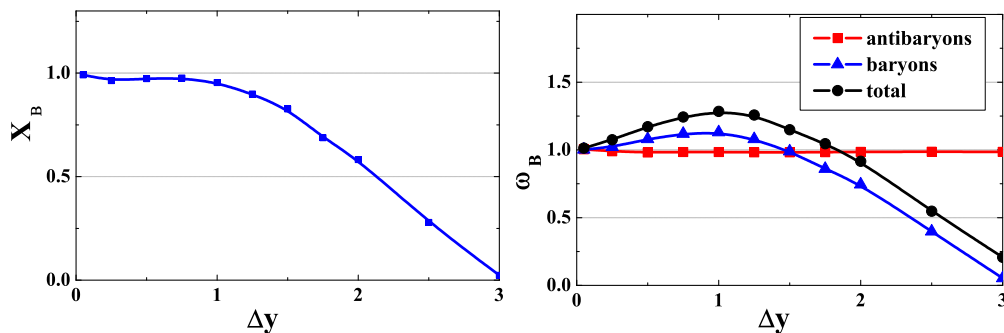


Figure 4.11: The HSD results for net baryon number fluctuations in 2% most central Pb+Pb collisions at 158 AGeV in the symmetric rapidity interval  $\Delta Y = [-y, y]$  as a function of  $\Delta y = \Delta Y/2$  in the c.m.s. The *left* panel shows the behavior of  $X_B$ , and a *right* panel presents separately  $\omega_{N_B}$ ,  $\omega_{N_{\bar{B}}}$ , and  $\omega_{N_B+N_{\bar{B}}}$ .

As a measure of the net baryon number fluctuations one has used the quantity,

$$X_B \equiv \frac{Var(B)}{\langle N_B + N_{\bar{B}} \rangle}. \quad (4.13)$$

As for the electric charge, one finds that  $X_B \rightarrow 1$  at  $\Delta Y \rightarrow 0$  (this is because all  $\omega_{N_B}$ ,  $\omega_{N_{\bar{B}}}$ , and  $\omega_{N_B+N_{\bar{B}}}$  go to 1 in this limit (see Fig. 4.11, left), and  $X_B \rightarrow 0$  at upper limit of  $\Delta Y$  because of global baryon number conservation.

Writing the variance  $Var(B)$  in the form,

$$Var(B) = 2 Var(N_B) + 2 Var(N_{\bar{B}}) - Var(N_B + N_{\bar{B}}), \quad (4.14)$$

one finds

$$X_B = 2 \omega_{N_B} \frac{\langle N_B \rangle}{\langle N_B + N_{\bar{B}} \rangle} + 2 \omega_{N_{\bar{B}}} \frac{\langle N_{\bar{B}} \rangle}{\langle N_B + N_{\bar{B}} \rangle} - \omega_{N_B+N_{\bar{B}}}. \quad (4.15)$$

The behavior of the different terms in Eq. 4.15 is the following: As seen from Fig. 4.11, right,  $\omega_{N_{\bar{B}}} \cong 1$  for all values of  $\Delta Y$ . This is because  $N_{\bar{B}} \ll N_B$ , and baryon number conservation does not affect the fluctuations of antibaryons. Due to the small number of antibaryons in comparison to baryons, one also observes  $\omega_B \cong \omega_{N_B} \cong \omega_{N_B+N_{\bar{B}}}$ .

## 4.4 Electric charge fluctuations: comparison to the data

This section presents the HSD results for the event-by-event electric charge fluctuations as measured by the NA49 Collaboration in central Pb+Pb collisions at 20, 30, 40, 80 and 160 A GeV [109]. The interest in this observable (as a signal of deconfinement) is related to the predicted in Refs.[110, 111] suppression of event-by-event fluctuations of the electric charge in a quark-gluon plasma relative to a hadron gas. However, these predictions were based on the assumption that the initial electric charge fluctuations survive the hadronization phase.

The first experimental measurement of charge fluctuations in central heavy-ion collisions by PHENIX [112] and STAR [113] at RHIC and by the NA49 [109] at SPS showed a quite moderate suppression of the electric charge fluctuations. This observation has been attributed to the fact that the initial fluctuations are distorted by the hadronization. In particular, the observed fluctuations might be related to the final resonance decays.

In this respect it is important to compare the experimental data with the results of microscopic transport models such as HSD where the resonance decays are included by default. The event-by-event electric charge fluctuations are quantified by  $\Phi$  defined as [109, 114]:

$$\Phi_q = \sqrt{\frac{\langle Z^2 \rangle}{\langle N \rangle}} - \sqrt{\overline{z^2}}, \quad (4.16)$$

where

$$z = q - \bar{q}, \quad Z = \sum_{i=1}^N (q_i - \bar{q}). \quad (4.17)$$

Here  $q$  denotes a single particle variable, i.e. electric charge  $q$ ;  $N$  is the number of particles of the event within the acceptance, and over-line and  $\langle \dots \rangle$  denote averaging over a single particle inclusive distribution and over events, respectively. By construction,  $\Phi$  of the system, which is an independent sum of identical sources of particles, is equal to the  $\Phi$  for a single source [114, 115].

In order to remove the sensitivity of the final signal to the trivial global charge

conservation (GCC) the measure  $\Delta\Phi_q$  is defined as the difference:

$$\Delta\Phi_q = \Phi_q - \Phi_{q,\text{GCC}} . \quad (4.18)$$

Here the value of  $\Phi_q$  is given by [116, 117]:

$$\Phi_{q,\text{GCC}} = \sqrt{1 - P} - 1, \quad (4.19)$$

where

$$P = \frac{\langle N_{ch} \rangle}{\langle N_{ch} \rangle_{tot}} \quad (4.20)$$

with  $\langle N_{ch} \rangle$  and  $\langle N_{ch} \rangle_{tot}$  being the mean charged multiplicity in the detector acceptance and in full phase space (excluding spectator nucleons), respectively.

By construction, the value of  $\Delta\Phi_q$  is zero if the particles are correlated by global charge conservation only. It is negative in case of an additional correlation between positively and negatively charged particles, and it is positive if the positive and negative particles are anti-correlated [117].

Fig. 4.12 shows the HSD results for the dependence of  $\Phi_q$  (l.h.s.) and  $\Delta\Phi_q$  (r.h.s.) on the fraction of accepted particles  $\langle N_{ch} \rangle$  and  $\langle N_{ch} \rangle_{tot}$  (calculated for ten different rapidity intervals increasing in size from  $\Delta y = 0.3$  to  $\Delta y = 3$  in equal steps) for central Pb+Pb collisions at 20, 30, 40, 80 and 158 A GeV. The NA49 data [109] are shown as full symbols, whereas the open symbols (connected by lines) reflect the HSD results. The dashed line shows the dependence expected for the case if the only source of particle correlations is the global charge conservation  $\Phi_{q,\text{GCC}}$  (Eq. 4.19).

The data as well as the HSD results for  $\Phi_q$  (Fig. 4.12, l.h.s.) are in a good agreement and show a monotonic decrease with increasing fraction of accepted particles. After subtraction the contribution by global charge conservation (the dashed line in Fig. 4.12), the values of  $\Delta\Phi_q$  vary between 0 and  $-0.05$  which are significantly larger than the values expected for QGP fluctuations ( $-0.5 < \Delta\Phi_q < -0.15$  [117]).

Fig. 4.13 presents the energy dependences of  $\Delta\Phi_q$  for two selected rapidity intervals – the intermediate rapidity interval  $\Delta y = 1.2$  (l.h.s.) and for the largest rapidity interval  $\Delta y = 3$  (r.h.s.). The both, data and HSD results, show the a

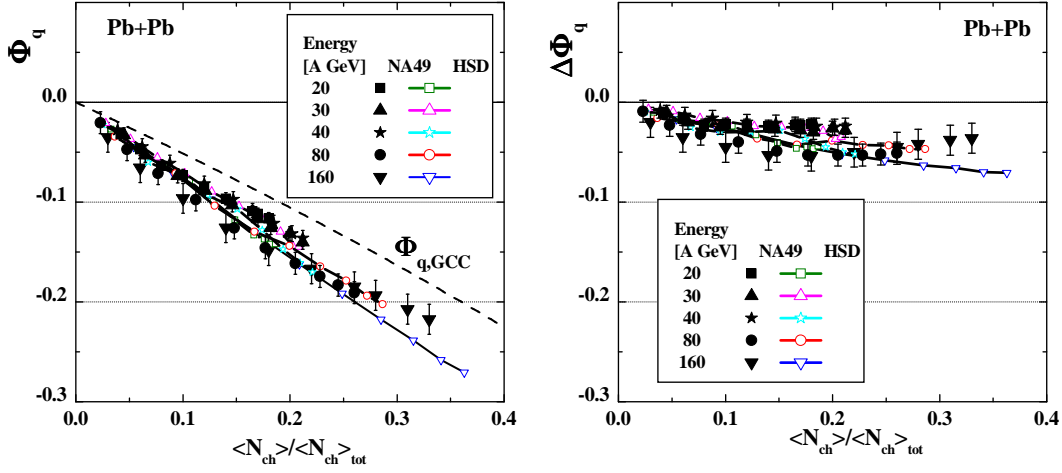


Figure 4.12: The dependence of the  $\Phi_q$  (l.h.s.) and  $\Delta\Phi_q$  (r.h.s.) on the fraction of accepted particles for central Pb+Pb collisions at 20-158 AGeV. The NA49 data [109] are shown as full symbols, whereas the open symbols (connected by lines) stay for the HSD results. The dashed line shows the dependence expected for the case if the only source of particle correlations is the global charge conservation  $\Phi_{q,GCC}$ , Eq. 4.19.

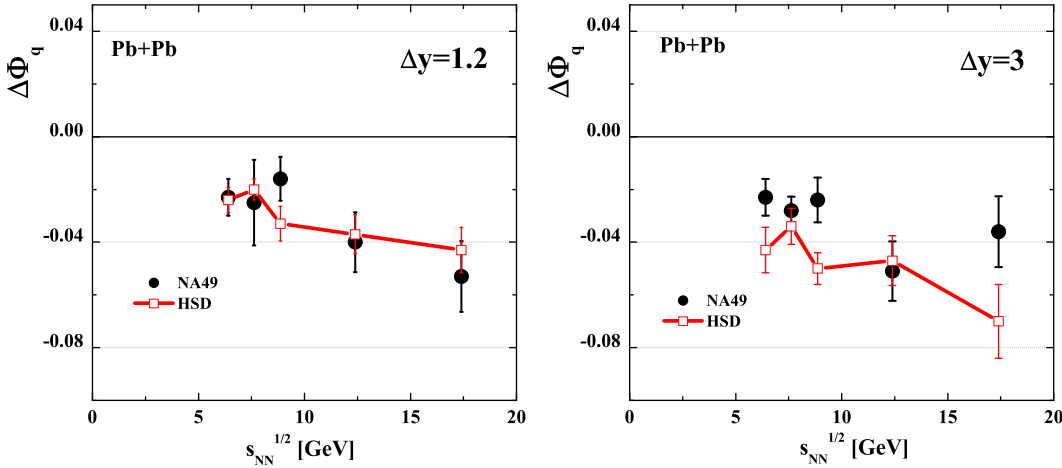


Figure 4.13: The energy dependence of  $\Delta\Phi_q$  measured in central Pb+Pb collisions for a narrow rapidity interval  $\Delta y = 1.2$  (l.h.s.) and a broad rapidity interval  $\Delta y = 3$  (r.h.s.). The NA49 data [109] are shown as full symbols, whereas the the open symbols (connected by lines) reflect the HSD results.

weak decrease of  $\Delta\Phi_q$  with increasing energy.

The fact that the HSD model, that includes no explicit phase transition, describes the experimental data can be considered an independent proof that the event-by-event charge fluctuations are driven by the hadronization phase and dominantly by the resonance decays (which are naturally included in HSD) and no longer sensitive to the initial phase fluctuations from a QGP.

## 4.5 Summary of Chapter 4

The goal of this study was to investigate the sensitivity of event-by-event fluctuations of baryon number and electric charge to the early stage dynamics of hot and dense nuclear matter created in heavy-ion collisions at SPS energies and the influence of the further hadronization and rescattering phase. The study has been based on the microscopic HSD transport model which allows also to investigate (on event-by-event basis) the influence of the experimental acceptance and the set-up on the final observables.

It has been found that the fluctuations in the number of target participants strongly influences the baryon number and charged multiplicity fluctuations. The consequences of this fact depend crucially on the dynamics of the initial flows of the conserved charges and inelastic energy.

For a better quantitative understanding of the HSD results three limiting groups of models for nucleus-nucleus collisions have been discussed: transparency, mixing and reflection. These "pedagogical" considerations indicate that the HSD model shows only a small mixing on initial baryon flow and is closer to the transparency model (cf. [section 3.2](#)). This supports the findings from Ref. [[104](#), [29](#), [105](#), [118](#)] about the influence of the partonic degrees of freedom on the initial phase dynamics which might increase the mixing by additional strong parton-parton interactions. Thus, the measurement of the net baryon number fluctuations helps to quantify the mixing of initial baryon flow.

The first microscopic event-by-event calculations of the charge fluctuations  $\Delta\Phi_q$  within the HSD model show a good agreement with the NA49 data at SPS energies. Thus, this observable is dominated by the final stage dynamics, i.e. the hadronization phase and the resonance decays, and rather insensitive to the initial QGP dynamics.

## Chapter 5

# Excitation Function of the Multiplicity Fluctuations in Central Nucleus-Nucleus Collisions

This Chapter presents the results of HSD study on the excitation function of the multiplicity fluctuations in central nucleus-nucleus collisions. For better understanding of the dynamics effects the  $A+A$  are compared with corresponding  $p+p$ .

Note, that some observables in  $p+p$  and  $A+A$  collisions are rather close to each other. For example, the charged hadron multiplicity per participating nucleon,  $n_{ch} \equiv \langle N_{ch} \rangle / \langle N_P \rangle$ , at SPS energies of  $20 \div 158$  AGeV are not much different in central Pb+Pb and inelastic  $p+p$  collisions [16, 119],  $R_{ch} \equiv (n_{ch})_{AA} / (n_{ch})_{pp} = 1 \div 1.5$ <sup>1</sup>. This explains a vitality of the wounded nucleon model (WNM) [97] which treats the final state in  $A+A$  collision as the result of independent nucleon-nucleon ( $N+N$ ) collisions (see, e.g., Ref. [121] which discusses the recent data [122] on d+Au collisions at the RHIC energies of  $\sqrt{s_{NN}} = 200$  GeV). However, the basic concept of the WNM is in a severe conflict with many other data, e.g., with multi-strange baryon production,  $R_{\Omega} \equiv (n_{\Omega})_{AA} / (n_{\Omega})_{pp} \cong 12.5$  [123] in Pb+Pb at 158 AGeV. The  $R_{\Omega}$  enhancement is expected to be even stronger at smaller

---

<sup>1</sup>Note that  $R_{ch} < 1$  at low collision energies. The change in behavior of  $R_{ch}$  is discussed in Ref. [120].

collision energies. The search for quark-gluon plasma signatures in A+A collisions is usually based on the expectation of a very different behavior of special physical observables in A+A and p+p collisions. Famous examples of QGP signatures are the ‘strangeness enhancement’, ‘ $J/\psi$  suppression’, and ‘jet quenching’. In all these cases one compares a suitably normalized physical quantity in A+A and in p+p reactions at the same collision energy per nucleon.

In general, one can define two groups of hadron observables. The first group includes observables which are rather similar in A+A and p+p collisions, thus, they can be reasonably described within the WNM. The second group consists of A+A observables which are very different from those in p+p collisions. The question arises: are the multiplicity fluctuations in A+A collisions close to those in p+p reactions, or are they very different? The aim of present chapter is to answer this question [124].

## 5.1 p+p collisions

The compilation of proton-proton (p+p) data for  $\langle N_{ch} \rangle$  and  $\omega_{ch}$  are taken from Ref. [96] and presented in Fig. 5.1. The energy dependence can be parameterized by the functions [96]:

$$\langle N_{ch} \rangle \cong -4.2 + 4.69 \left( \frac{\sqrt{s_{NN}}}{GeV} \right)^{0.31}, \quad \omega_{ch} \cong 0.35 \frac{(\langle N_{ch} \rangle - 1)^2}{\langle N_{ch} \rangle}, \quad (5.1)$$

where  $\sqrt{s_{NN}}$  is the center of mass energy. At high collision energies the KNO scaling [125] holds which implies that the multiplicity distribution  $P(N_{ch})$  behaves as

$$\langle N_{ch} \rangle P(N_{ch}) = \psi(N_{ch}/\langle N_{ch} \rangle)$$

(see also Ref. [126, 127]). For  $\langle N_{ch} \rangle \gg 1$  it follows,

$$\langle N_{ch}^k \rangle = C_k \langle N_{ch} \rangle^k.$$

In particular,  $\omega_{ch} \propto \langle N_{ch} \rangle$  [128] as also seen from the parametrization (Eq. 5.1).

The HSD model description of the p+p data (for p+p reaction this is almost equivalent to the Lund-String model [82]) is shown in Fig. 5.1 by the solid lines. It gives a good reproduction of the p+p data for  $\langle N_{ch} \rangle$ , but slightly underestimates

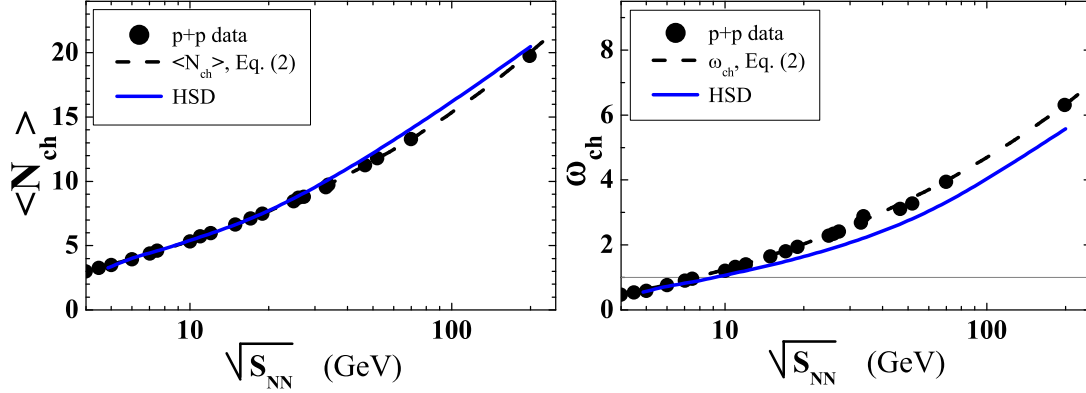


Figure 5.1: The multiplicity (*left*) and scaled variance (*right*) of all charged hadrons in  $p+p$  inelastic collisions as functions of collision energy. The dashed lines correspond to the parametrization (Eq. 5.1) from Ref. [96]. The solid lines are the HSD results.

$\omega_{ch}$  at high collision energies. For negatively and positively charged hadrons the average multiplicities and scaled variances in  $p+p$  collisions can be presented in terms of the corresponding quantities for all charged particles,

$$\langle N_{\pm} \rangle = \frac{1}{2} (\langle N_{ch} \rangle \pm 2) , \quad \omega_{\pm} = \frac{1}{2} \omega_{ch} \frac{\langle N_{ch} \rangle}{\langle N_{ch} \rangle \pm 2} . \quad (5.2)$$

## 5.2 N+N collisions

To compare central collisions of heavy nuclei and N+N collisions within the HSD model one constructs the multiplicities and scaled variances of N+N using the HSD results for  $p+p$ ,  $p+n$  and  $n+n$  collisions (as in subsection 3.2.3):

$$\langle N_i^{NN} \rangle = \alpha_{pp} \langle N_i^{pp} \rangle + \alpha_{pn} \langle N_i^{pn} \rangle + \alpha_{nn} \langle N_i^{nn} \rangle , \quad (5.3)$$

$$\omega_i^{NN} = \frac{1}{\langle N_i^{NN} \rangle} [\alpha_{pp} \omega_i^{pp} \langle N_i^{pp} \rangle + \alpha_{pn} \omega_i^{pn} \langle N_i^{pn} \rangle + \alpha_{nn} \omega_i^{nn} \langle N_i^{nn} \rangle] , \quad (5.4)$$

where  $\alpha_{pp} = Z^2/A^2 \cong 0.16$ ,  $\alpha_{pn} = 2Z(A-Z)/A^2 \cong 0.48$ ,  $\alpha_{nn} = (A-Z)^2/A^2 \cong 0.36$  are the probabilities of proton-proton, proton-neutron, and neutron-neutron collisions in Pb+Pb ( $A=208$ ,  $Z=82$ ) or Au+Au ( $A=197$ ,  $Z=79$ ) reactions. The results are presented in Fig. 5.2. A small difference between  $p+p$  and N+N collisions is only seen at SPS energies (shown separately in the left upper corners)



and gradually disappears at RHIC energies.

### 5.3 Central A+A collisions

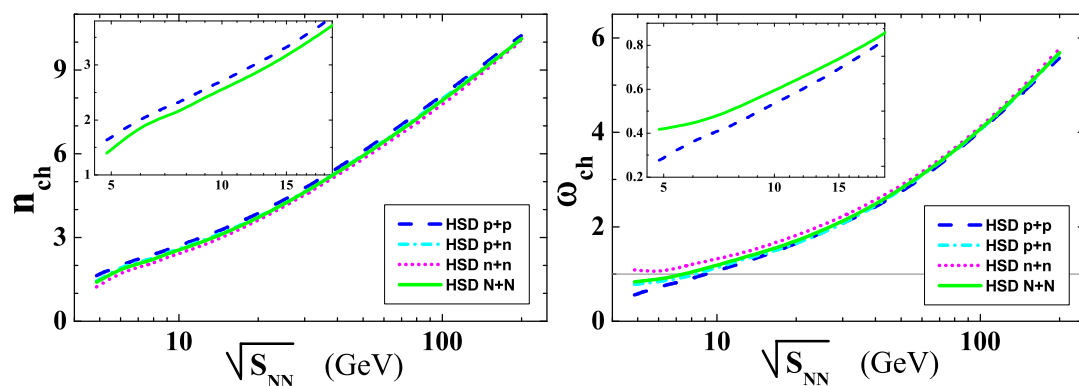


Figure 5.2: The HSD results for  $n_{ch}$  (left) and  $\omega_{ch}$  (right) in p+p (dashed line), p+n (dashed-dotted line), n+n (dotted line), and N+N (solid line) collisions.

In Fig. 5.3 the HSD model results are shown for the multiplicities per participating nucleons,  $n_i = \langle N_i \rangle / \langle N_P \rangle$ , and for the scaled variances,  $\omega_i$ , in central collisions (zero impact parameter,  $b = 0$ ) of Pb+Pb at  $E_{lab} = 10, 20, 30, 40, 80, 158$  AGeV and Au+Au at  $\sqrt{s_{NN}} = 62, 130, 200$  GeV. From Fig. 5.3 one concludes that the HSD results for the scaled variances in central A+A collisions are close to those in N+N collisions. For the SPS energy region all scaled variances,  $\omega_{\pm}$  and  $\omega_{ch}$ , in central A+A collisions are slightly below the N+N results. The reversed situation is observed for RHIC energies. Thus, the HSD results for multiplicity fluctuations are rather similar to those of the WNM. For the samples with a fixed number of nucleon participants,  $N_P^{proj} = N_P^{targ} = const$ , in Pb+Pb collisions at 158 AGeV, HSD shows fluctuations of the final hadrons close to those in N+N collisions at the same energy. This happens to be also valid for most central collisions ( $b = 0$ ) considered in the present study. The participant number fluctuations are found to be rather small for collisions with  $b = 0$ . For example, in Pb+Pb collisions with  $b = 0$  at 158 AGeV the mean number of participants is  $\langle N_P \rangle \cong 392$ , and the scaled variance is  $\omega_P \cong 0.055$ . The additional fluctuations,  $\Delta\omega_i$ , of  $i$ th hadrons due to participant number fluctuations can be estimated as

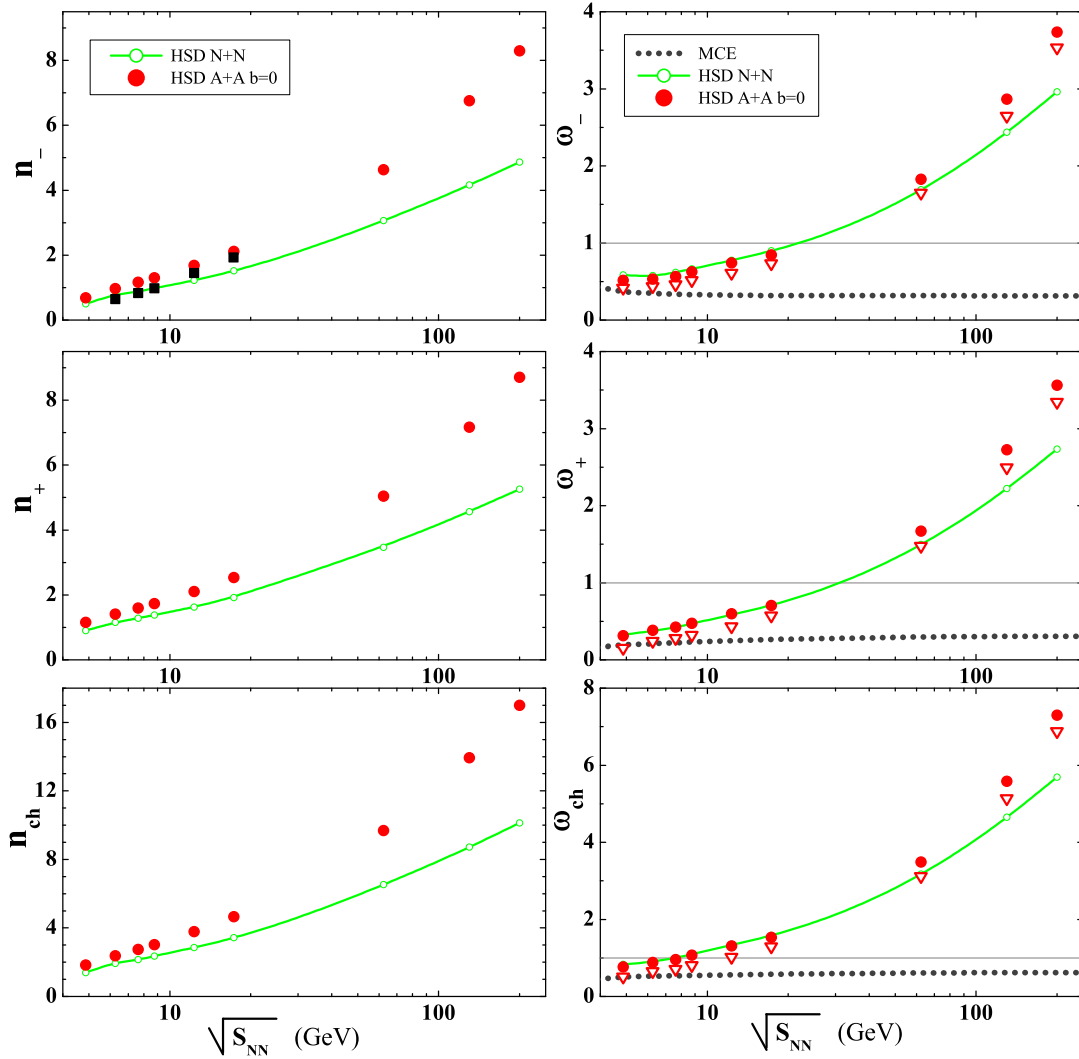


Figure 5.3: The multiplicities per participant,  $n_i$  (*left*), and scaled variances,  $\omega_i$  (*right*). The solid lines are the HSD results for N+N collisions according to Eq. 5.3. The full circles are the HSD results for central A+A collisions for zero impact parameter,  $b = 0$ . The full squares for  $n_-$  are the NA49 data [16, 119] for  $(\langle\pi^- \rangle + \langle K^- \rangle) / \langle N_P \rangle$  in the samples of 7% most central Pb+Pb collisions. The HSD results for  $\omega_i$  after the subtraction of the contributions  $\Delta\omega_i$  (Eq. 5.5) are shown by open triangles. The dotted lines are the MCE HG model results for  $\omega_i$  [129]. The HG parameters correspond to the chemical freeze-out conditions found from fitting the hadron yields.

(see subsection 3.2.3),

$$\Delta\omega_i = n_i \omega_P . \quad (5.5)$$

The HSD results for  $\omega_i$  after subtraction of the contributions  $\Delta\omega_i$  (Eq. 5.5) are shown in Fig. 5.3 by open triangles. The contributions to  $\omega_i$  due to participant number fluctuations estimated by Eq. 5.5 are small, and they do not explain the (positive) difference,  $\omega_i(\text{AA}) - \omega_i(\text{NN})$  seen in Fig. 5.3 at  $\sqrt{s_{NN}} = 200$  GeV.

On the other hand in the statistical model the scaled variances  $\omega_i = 1$  for the ideal Boltzmann gas in the grand canonical ensemble (GCE). The deviations of  $\omega_i$  from unity in the hadron-resonance gas (HG) model stem from Bose and Fermi statistics, resonance decays, and exactly enforced conservation laws within the canonical ensemble (CE) or micro-canonical ensemble (MCE) [129, 101, 130]. Note that the statistical model gives no predictions for the energy dependence of hadron multiplicities. All yields are proportional to the system volume  $V$  which is a free model parameter fitted to the multiplicity data at each collision energy. However, the statistical model does predict the scaled variances as  $\omega_i$  to become independent of the system volume for large systems. In Fig. 5.3 the scaled variances  $\omega_i$  calculated within the MCE HG model along the chemical freeze-out line (see Ref. [129] for details) are presented by the dotted lines:  $\omega_i$  reach their asymptotic values at RHIC energies,  $\omega_{\pm}(\text{MCE}) \cong 0.3$  and  $\omega_{ch}(\text{MCE}) \cong 0.6$ . The corresponding results in the GCE and CE are the following:  $\omega_{\pm}(\text{GCE}) \cong 1.2$  and  $\omega_{ch}(\text{GCE}) \cong 1.6$ ,  $\omega_{\pm}(\text{CE}) \cong 0.8$  and  $\omega_{ch}(\text{CE}) \cong 1.6$ . The HSD results for  $\omega_i$  in central A+A collisions are very different. They remain close to the corresponding values in p+p collisions and, thus, increase with collision energy as  $\omega_i \propto n_i$ . One observes no indication for ‘thermalization’ of fluctuations in the HSD results. This is especially seen for RHIC energies:  $\omega_i(\text{HSD})/\omega_i(\text{MCE}) \geq 10$  at  $\sqrt{s_{NN}} = 200$  GeV.

## 5.4 Comparison to the data

The fluctuations of the number of nucleon participants correspond to volume fluctuations, hence, they translate directly to the final multiplicity fluctuations. To avoid these ‘trivial’ fluctuations, one has to select a sample of very central,  $\leq 1\%$ , collisions. Such a rigid centrality selection has been recently done for the NA49 data [131] by fixing the number of projectile participants,  $N_P^{proj} \cong A$ .

The HG model was compared with the NA49 data [131] for the sample of 1% most central collisions at the SPS energies,  $20 \div 158$  AGeV in Ref. [129]. It was

found that the MCE results for  $\omega_{\pm}$  are very close to the data, they are shown by the dashed lines in Fig. 5.4. The NA49 acceptance probabilities for positively and negatively charged hadrons are approximately equal, and their numerical values are:  $q = 0.038, 0.063, 0.085, 0.131, 0.163$ , at the SPS energies of 20, 30, 40, 80, 158 AGeV, respectively. In the statistical model the scaled variances  $\omega_{\pm}^{acc}$  for the accepted particles are calculated from  $\omega_{\pm}$  in the full space according to the acceptance scaling formulae (see Ref. [129] for details):

$$\omega_{\pm}^{acc} = 1 - q + q \omega_{\pm} . \quad (5.6)$$

Note that the energy dependence of  $\omega_{\pm}^{acc}$  seen in Fig. 5.4 is strongly influenced by an increase with energy of the acceptance parameter  $q$ : only about 4% of the hadrons are detected at 20 AGeV and 16% at 158 AGeV.

The comparison of the HSD results for central Pb+Pb collisions (zero impact parameter,  $b = 0$ ) with the preliminary NA49 data of 1% most central collisions, selected by the number of projectile spectators, is presented in Fig. 5.4. It demonstrates a good agreement of the HSD results with the preliminary NA49 data. There are also no essential differences between the MCE HG model and the HSD transport model results. Several comments are needed at this point: The HSD results within the NA49 acceptance demonstrate that the acceptance scaling formulae (Eq. 5.6) is violated. The straightforward calculations (full circles in Fig. 5.4) lead to smaller values of  $\omega_{\pm}^{acc}$  than those obtained with the acceptance scaling formulae (Eq. 5.6) (open circles in Fig. 5.4). This difference may lead to a 10% effect in  $\omega_{\pm}^{acc}$  for the NA49 acceptance conditions. Thus, the MCE results for  $\omega_{\pm}^{acc}$  may also be about 10% smaller than those obtained from Eq. 5.6 and shown in the upper panel of Fig. 5.4. The lower panel of Fig. 5.4 demonstrates that the MCE and HSD results for  $\omega_{\pm}$  at the lowest SPS energy 20 AGeV are ‘occasionally’ rather close to each other. They both are also close to  $\omega_{\pm}$  in  $p+p$  collisions (cf. Fig. 5.2 and Fig. 5.3). The HSD scaled variances  $\omega_i$  increase with collision energy. In contrast, the MCE  $\omega_i$  values remain approximately constant. The ratio of the HSD to MCE values of  $\omega_{\pm}$  reaches about the factor of 2 at the highest SPS energy 158 AGeV. It becomes a factor of 10 at the top RHIC energy  $\sqrt{s_{NN}} = 200$  GeV. However, the rigid centrality selection is absent for the available RHIC fluctuation data. Due to this reason the participant number fluctuations give a dominant contribution to  $\omega_i$ . On the other hand, for the SPS

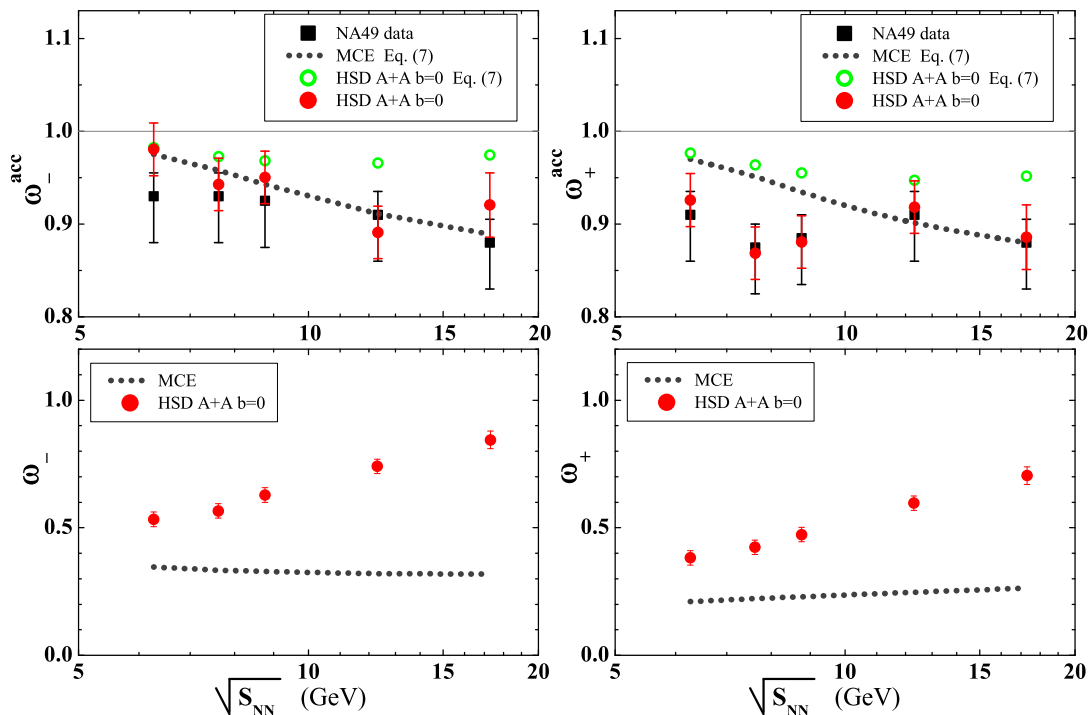


Figure 5.4: *Upper panel.* The scaled variances  $\omega_{\pm}^{acc}$  for central Pb+Pb collisions. The squares with error bars are the NA49 data for 1% most central collisions [131]. The dotted lines show the MCE HG model results calculated from full  $4\pi$  scaled variances using Eq. 5.6. The full circles present the HSD results in Pb+Pb collisions for  $b = 0$  with the NA49 experimental acceptance conditions, while the open circles are obtained from the  $4\pi$  HSD scaled variances using Eq. 5.6. *Lower panel.* The MCE HG (dotted line) and HSD (full circles) results for the  $4\pi$  scaled variances  $\omega_{\pm}$  (the same as in Fig. 5.3 are shown for SPS energies.

data the small values of the acceptance,  $q = 0.04 \div 0.16$ , and 10% possible ambiguities coming from Eq. 5.6 almost mask the difference between the HSD and MCE results (Fig. 5.4, upper panel).

## 5.5 Summary of Chapter 5

The particle number fluctuations in central A+A collisions from 10 to 21300 AGeV have been studied within the HSD transport model. HSD predicts that the scaled variances  $\omega_i$  in central A+A collisions remain close to the corresponding values in p+p collisions and increase with collision energy as the multiplicity per participating nucleon, i.e.  $\omega_i \propto n_i$ . The scaled variances  $\omega_i$  calculated within the

statistical HG model along the chemical freeze-out line show a rather different behavior:  $\omega_i$  approach finite values at high collision energy. At the top RHIC energy  $\sqrt{s_{NN}} = 200$  GeV the HSD values for  $\omega_i$ (HSD) are already about 10 times larger than the corresponding MCE HG values for  $\omega_i$ (MCE).

Thus, the HSD and HG scaled variances  $\omega_i$  show a different energy dependence and are very different numerically at high energies. However, a comparison with preliminary NA49 data of very central,  $\leq 1\%$ , Pb+Pb collisions at the SPS energy range does not distinguish between the HSD and MCE HG results. This happens because of two reasons: First, the MCE HG and HSD results for  $\omega_i$  at SPS energies are not too much different from each other and from  $\omega_i$  in  $p+p$  collisions. Second, small experimental values of the acceptance,  $q = 0.04 \div 0.16$ , and 10% possible ambiguities coming from the acceptance scaling relation (Eq. 5.6) make the difference between the HSD and MCE HG results almost invisible. New measurements of  $\omega_i$  for samples of very central A+A collisions with large acceptance at both SPS and RHIC energies are needed to allow for a proper determination of the underlying dynamics.

## Chapter 6

# Multiplicity Fluctuations in Nucleus-Nucleus Collisions: Dependence on Energy and Atomic Number

An ambitious experimental program for the search of the QCD critical point has been started by the NA61 Collaboration at the SPS [8, 132]. The program includes a variation in the atomic mass number  $A$  of the colliding nuclei as well as an energy scan (see Fig. 6.1 taken from [133]). This allows to scan the phase diagram in the plane of temperature  $T$  and baryon chemical potential  $\mu_B$  near the critical point as argued in Ref. [8, 132]. One expects to ‘locate’ the position of the critical point by studying its ‘fluctuation signals’. High statistics multiplicity fluctuation data will be taken for p+p, C+C, S+S, In+In, and Pb+Pb collisions at bombarding energies of  $E_{lab}=10, 20, 30, 40, 80,$  and 158 AGeV.

The aim of the chapter is to study the same energy and system size dependence of event-by-event multiplicity fluctuations within the HSD microscopic transport approach. The UrQMD calculations have been performed by Benjamin Lungwitz [134] and are used here for comparison and completeness of the picture. Our study thus is in full correspondence to the experimental program of the NA61 Collaboration [8, 132].

The QCD critical point is expected to be experimentally seen as a non-monotonic dependence of the multiplicity fluctuations, i.e. a specific combination

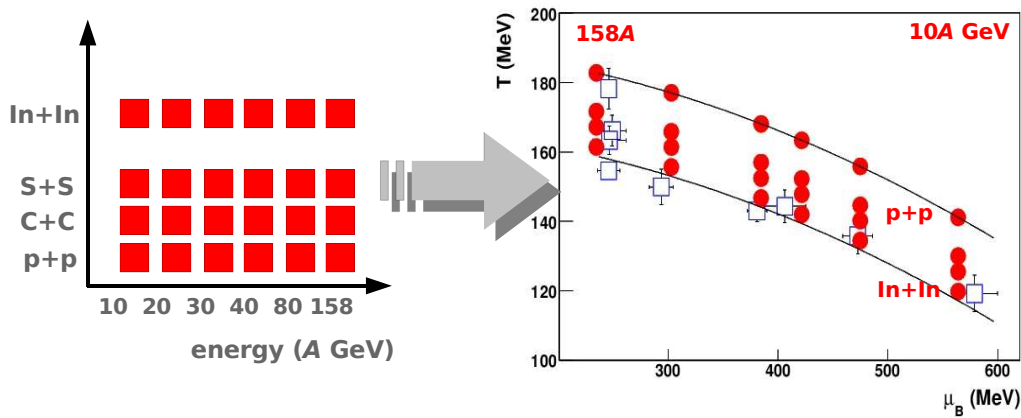


Figure 6.1: Left: The data sets on central A+A collisions planned to be registered by NA61 in a search for the critical point of strongly interacting matter and a study of the properties of the onset of deconfinement. Right: Hypothetical positions of the chemical freeze-out points of the reactions (In+In, S+S, C+C and p+p from bottom to top at 158A, 80A, 40A, 30A, 20A and 10A GeV from left to right) to be studied by NA61 in the (temperature)-(baryon-chemical potential) plane are shown by full dots. The open squares show the existing NA49 data.

of atomic mass number  $A$  and bombarding energy  $E_{lab}$  could move the chemical freeze-out of the system close to the critical point and show a ‘spike’ in the multiplicity fluctuations. Since HSD and UrQMD do not include explicitly a phase transition from a hadronic to a partonic phase, a clear suggestion for the location of the critical point can not be made – it is beyond the scope of such hadron-string models. However, this study might be helpful in the interpretation of the upcoming experimental data since it will allow to subtract simple dynamical and geometrical effects from the expected QGP signal. The deviations of the future experimental data from the HSD and UrQMD predictions may be considered as an indication for the critical point signals.

Theoretical estimates give about 10% increase of the multiplicity fluctuations due to the critical point [135, 42, 136]. It is large enough to be observed experimentally within the statistics of NA61 [8, 132]. To achieve this goal, it is necessary to have a control on other possible sources of fluctuations. One of such sources is the fluctuation of the number of nucleon participants. It has been shown in Chapter 3 that these fluctuations give a dominant contribution to hadron multiplicity fluctuations in A+A collisions. On the other hand one can suppress the participant number fluctuations by selecting most central A+A



collisions (see Ref. [91, 98] for details). That's why the NA61 Collaboration plans to measure central collisions of light and intermediate ions instead of peripheral Pb+Pb collisions. It is important to stress, that the conditions for the centrality selection in the measurement of fluctuations are much more stringent than those for mean multiplicity measurements.

## 6.1 Multiplicity fluctuations in proton-proton collisions

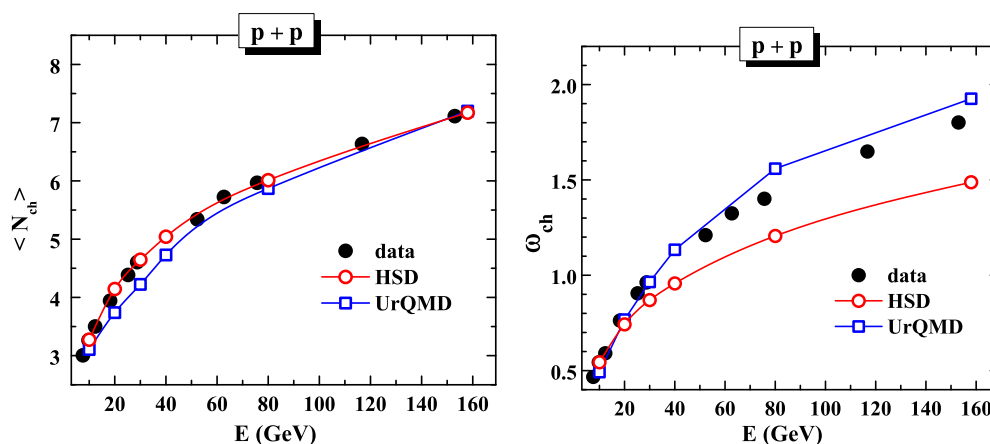


Figure 6.2: The average multiplicity (*left*) and scaled variance (*right*) of charged hadrons in p+p inelastic collisions. The open circles and squares (connected by solid lines) show the results of HSD and UrQMD, respectively, whereas the full circles present the experimental data from Ref. [96].

Fig. 6.2 shows the HSD and UrQMD results for inelastic p+p collisions in comparison to the experimental data taken from Ref. [96]. Both models give a good reproduction of the p+p data for  $\langle N_{ch} \rangle$ , but slightly (over) underestimate  $\omega_{ch}$  at high collision energies. The differences between the HSD and UrQMD model results for  $\omega_{ch}$  can be attributed to different realizations of the string fragmentation model, in particular, differences in the fragmentation functions and the fragmentation scheme, i.e. fragmentation via heavy baryonic and mesonic resonances in UrQMD and direct light hadron production by string fragmentation in HSD.

For negative and positive charged hadrons the average multiplicities and scaled

variances in p+p collisions can be presented in terms of the corresponding quantities for all charged particles,

$$\langle N_{\pm} \rangle = \frac{1}{2} (\langle N_{ch} \rangle \pm 2) , \quad \omega_{\pm} = \frac{1}{2} \omega_{ch} \frac{\langle N_{ch} \rangle}{\langle N_{ch} \rangle \pm 2} . \quad (6.1)$$

Note, that the energy dependence of the measured charged multiplicity and fluctuations for p+p collisions can be parametrized by [Eq. 5.1](#).

## 6.2 Participant number fluctuations

To minimize the event-by-event fluctuations of the number of nucleon participants in measuring the multiplicity fluctuations the NA49 Collaboration has been trying to fix  $N_P^{proj}$  in Pb+Pb collisions. Samples of collisions with a fixed number of projectile spectators,  $N_S^{proj} = const$  (and thus a fixed number of projectile participants,  $N_P^{proj}$ ), have been selected according to the criteria  $|y - y_{beam(target)}| \leq 0.32$ . This selection is possible in fixed target experiments at the SPS, where  $N_S^{proj}$  is measured by a Zero Degree Veto Calorimeter covering the projectile fragmentation domain. A similar centrality selection is expected to be implemented in the future NA61 experiment. However, even in samples with  $N_P^{proj} = const$  the number of target participants will fluctuate considerably. Hence, an asymmetry between projectile and target participants is introduced, i.e.  $N_P^{proj}$  is constant by constraint, whereas  $N_P^{targ}$  fluctuates independently (the consequences of this asymmetry have been discussed in Ref. [\[98\]](#)).

In each sample with  $N_P^{proj} = const$  the number of target participants fluctuates around its mean value with the scaled variance  $\omega_P^{targ}$ . The mean value equals to  $\langle N_P^{targ} \rangle \cong N_P^{proj}$ , if  $N_P^{proj}$  is not too close to its limiting values,  $N_P^{proj} = 1$  and  $N_P^{proj} = A$ . The scaled variance of target participants  $\omega_P^{targ}$  as a function of fixed number of projectile participants  $N_P^{proj}$  has been obtained from HSD and UrQMD in [Chapter 3](#) for Pb+Pb collisions at 158 AGeV.

[Fig. 6.3](#) presents the HSD scaled variances  $\omega_P^{targ}$  for C+C, O+O, Ne+Ne, S+S, In+In, and Pb+Pb collisions at 158 AGeV as a function of  $N_P^{proj}$ . The fluctuations of  $N_P^{targ}$  are quite strong for peripheral reactions (small  $N_P^{proj}$ ) and negligible for the most central collisions (large  $N_P^{proj}$ ). A vanishing of  $\omega_P^{targ} \cong 0$  at  $N_P^{proj} \cong A$  does not, however, show up in collisions of light nuclei (from C to S). Even for the maximal values of  $N_P^{proj} = A$  the fluctuations  $\omega_P^{targ}$  do not vanish and

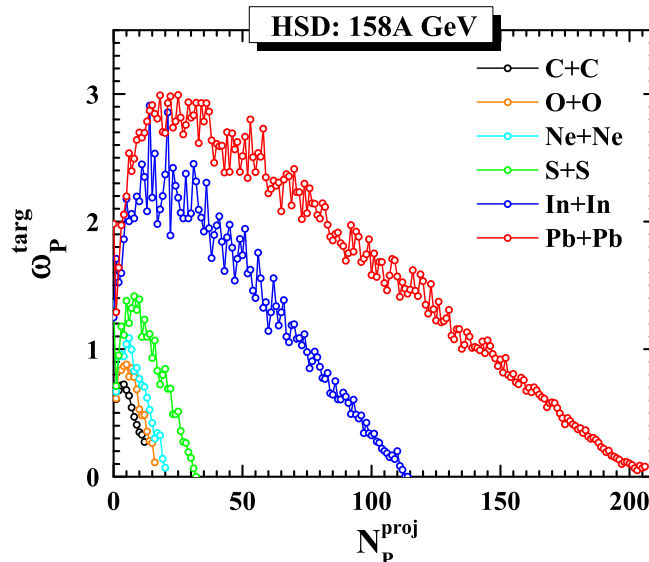


Figure 6.3: The scaled variance  $\omega_P^{targ}$  for the fluctuations of the number of target participants,  $N_P^{targ}$ . The HSD simulations of  $\omega_P^{targ}$  as a function of  $N_P^{proj}$  are shown for different colliding nuclei, In+In, S+S, Ne+Ne, O+O and C+C at  $E_{lab}=158$  AGeV.

increase with decreasing atomic mass number  $A$ . For example in C+C collisions for  $N_P^{proj} = A = 12$  the number of participants from the target still fluctuates and the scaled variance amounts to  $\omega_P^{targ} \cong 0.25$ .

The temperature  $T$  and baryon chemical potential  $\mu_B$  at the hadron chemical freeze-out demonstrate the dependence on both the collision energy and system size [137]. Thus, changing the number of participating nucleons one may scan the  $T - \mu_B$  plane. Some combination of  $N_P$  and  $E_{lab}$  might move the chemical freeze-out point close the QCD critical point. One could then expect an increase of multiplicity fluctuations in comparison to their ‘background values’.

Why does one need central collisions of light and intermediate ions instead of studying peripheral Pb+Pb collisions for a search of the critical point? Fig. 6.3 explains this issue. At fixed  $N_P^{proj}$  the average total number of participants,  $N_P \equiv N_P^{proj} + N_P^{targ}$ , is equal to  $\langle N_P \rangle \cong 2N_P^{proj}$ , and, thus, it fluctuates as  $\omega_P = 0.5\omega_P^{targ}$ . Then, for example, the value of  $N_P^{proj} \cong 30$  corresponds to almost zero participant number fluctuations,  $\omega_P \cong 0$ , in S+S collisions while  $\omega_P$  becomes large and is close to 1 and 1.5 for In+In and Pb+Pb, respectively. Even if  $N_P^{proj}$  is fixed exactly, the sample of the peripheral collision events in the heavy-ion

case contains large fluctuations of the participant number: this would ‘mask’ the critical point signals. As also seen in [Fig. 6.3 \(right\)](#), the picture becomes actually more complicated if the atomic mass number  $A$  is too small. In this case, the number of participants from a target starts to fluctuate significantly even for the largest and fixed value of  $N_P^{proj} = A$ .

## 6.3 Multiplicity fluctuations at zero impact parameter

### 6.3.1 Centrality Selection in A+A Collisions by Impact Parameter

The importance of a selection of the most central collisions for studies of hadron multiplicity fluctuations has been stressed in our previous chapters. Due to its convenience in theoretical studies (e.g., in hydrodynamical models) one commonly uses the condition on impact parameter  $b$ , for the selection of the ‘most central’ collisions in model calculations. However, the number of participant even at  $b = 0$  is not strictly fixed and fluctuates according to some distributions (cf. [Fig. 4.10](#)). It should be stressed again that the conditions  $b < b_{max}$  can not be fixed experimentally since the impact parameter itself can not be measured in a straightforward way. Actually, in experiments one accounts for the 1%, 2% etc. most central events selected by the measurement of spectators in the Veto calorimeter, which corresponds to the event class with the largest  $N_P^{proj}$ . As it will be demonstrated below the multiplicity fluctuations are very sensitive to the centrality selection criteria. In particular, the transport model results for  $b = 0$  and for 1% events with the largest  $N_P^{proj}$  are rather different (see below).

Let’s start with the  $b = 0$  centrality selection criterium. Recall that the charged multiplicity fluctuations are closely related to the fluctuations of the number of participants (cf. [Chapter 3](#)). Therefore, it is useful to estimate the average number of participants,  $\langle N_P \rangle$ , and the scaled variances of its fluctuations,  $\omega_P$ , in  $A + A$  collision events which satisfy the  $b = 0$  condition. The left panel in [Fig. 6.4](#) shows the ratio,  $\langle N_P \rangle / 2A$ , in  $A + A$  collisions with  $b = 0$  for different nuclei at collision energies  $E_{lab} = 10$  and 158 AGeV. Both transport models (HSD and UrQMD) show a monotonous increase of  $\langle N_P \rangle / 2A$  with collision energy for

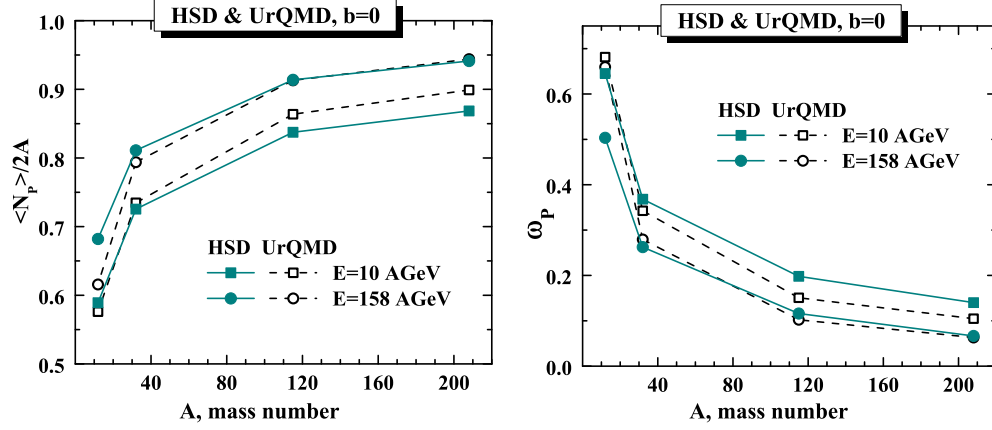


Figure 6.4: *Left:* Mean  $\langle N_P \rangle$ , divided by the maximum number of participants  $2A$  in events with  $b = 0$  for different nuclei at collision energies  $E_{lab}=10$  and 158 AGeV. *Right:* The scaled variance  $\omega_P$  in events with  $b = 0$  for different nuclei at collision energies  $E_{lab}=10$  and 158 AGeV.

all nuclei in the energy range  $10 \div 158$  AGeV (Fig. 6.4, left). Correspondingly, the fluctuations of the number of participants  $\omega_P$  for all nuclei become smaller with increasing collision energy (Fig. 6.4, right). As seen from Fig. 6.4 (left) about 90% of all nucleons are participants for Pb+Pb collisions with  $b = 0$ . This number becomes essentially smaller, about 60-70%, for C+C collisions. One can therefore expect that participant number fluctuations at  $b = 0$  are small for heavy nuclei but strongly increase for light systems. This is demonstrated in Fig. 6.4 (right):  $\omega_P$  is about  $0.1 \div 0.2$  in Pb+Pb and In+In but becomes much larger,  $0.5 \div 0.7$ , in C+C collisions.

One can conclude that the condition  $b = 0$  corresponds to ‘most central’  $A + A$  collisions only for nuclei with large atomic mass number (In and Pb). In this case the average number of participants is close to its maximum value and its fluctuations are rather small. However, in the studies of event-by-event multiplicity fluctuations in the collisions of light nuclei (C and S) the criterium  $b = 0$  is far from selecting the ‘most central’  $A + A$  collisions.

### 6.3.2 HSD and UrQMD Results for the Multiplicity Fluctuations for $b=0$

Results of HSD and UrQMD transport model calculations for the scaled variance of negative,  $\omega_-$ , positive,  $\omega_+$ , and all charged,  $\omega_{ch}$ , hadrons are shown in [Fig. 6.5](#) and [Fig. 6.6](#) at different collision energies,  $E_{lab} = 10, 20, 30, 40, 80, 158$  AGeV, and for different colliding nuclei, C+C, S+S, In+In, Pb+Pb. The transport model results correspond to collision events for zero impact parameter,  $b = 0$ . To make the picture more complete, the transport model results for inelastic p+p collisions are shown too, for reference. Note that the proton spectators are not accounted for in the calculation of  $N_+$  and  $N_{ch}$ . Thus, proton spectators do not contribute to  $\omega_+$  and  $\omega_{ch}$ .

One sees a monotonic dependence of the multiplicity fluctuations on both  $E_{lab}$  and  $A$ : the scaled variances  $\omega_-$ ,  $\omega_+$ , and  $\omega_{ch}$  increase with  $E_{lab}$  and decrease with  $A$ . The results for p+p collisions are different from those for light ions. Note that within HSD and UrQMD a detailed comparison of the multiplicity fluctuations in nucleon-nucleon inelastic collisions and  $b = 0$  heavy-ion collisions (Pb+Pb and Au+Au), including the energy dependence up to  $\sqrt{s_{NN}} = 200$  GeV, has been presented in [Chapter 5](#) and in Refs. [[124](#), [138](#)].

[Fig. 6.5](#) corresponds to the full  $4\pi$  acceptance, i.e. all particles are accepted without any cuts in phase space. In actual experiments the detectors accept charged hadrons in limited regions of momentum space. [Fig. 6.6](#) shows the HSD and UrQMD results for multiplicity fluctuations in the projectile hemisphere (i.e. positive rapidities,  $y > 0$  in the c.m. frame). This corresponds to the maximal possible acceptance, up to 50% of all charged particles, by the optimized detectors of the NA61 Collaboration [[8](#), [132](#)]. One observes from [Fig. 6.6](#) that the energy and system size dependencies of the multiplicity fluctuations in the projectile hemisphere ( $y > 0$ ) become less pronounced than in full  $4\pi$  acceptance. Note also that the centrality selection criterium  $b = 0$  keeps the symmetry between the projectile and target hemispheres. Thus, the results for a  $y < 0$  acceptance are identical to those for  $y > 0$  presented in [Fig. 6.6](#).

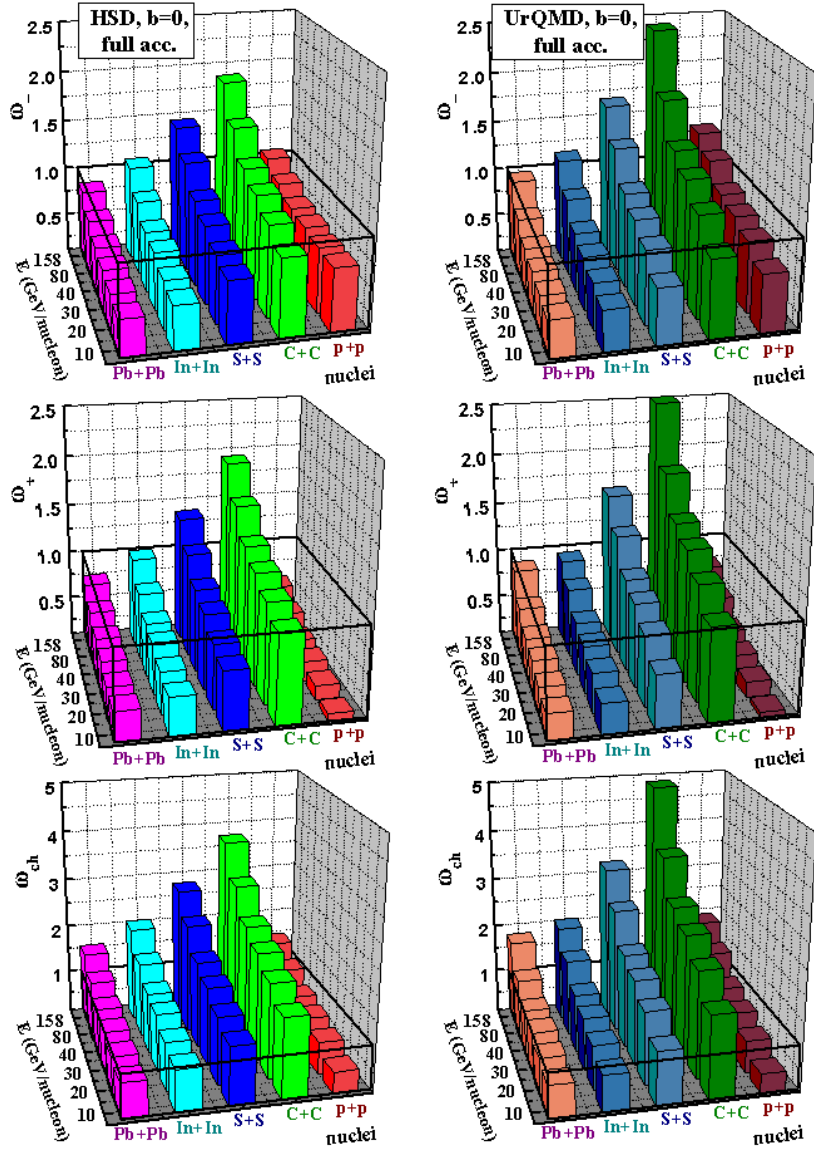


Figure 6.5: The results of HSD (*left*) and UrQMD (*right*) simulations for  $\omega_-$  (top panel),  $\omega_+$  (middle panel), and  $\omega_{ch}$  (lower panel) in p+p and central C+C, S+S, In+In, Pb+Pb collisions at  $E_{lab} = 10, 20, 30, 40, 80, 158$  AGeV. The condition  $b = 0$  is used here as a criterium for centrality selection. There are no cuts in acceptance.

### 6.3.3 Comparison to the Independent Source Model

The multiplicity fluctuations in elementary nucleon-nucleon collisions and fluctuations of the number of nucleon participants are presented in the right panels



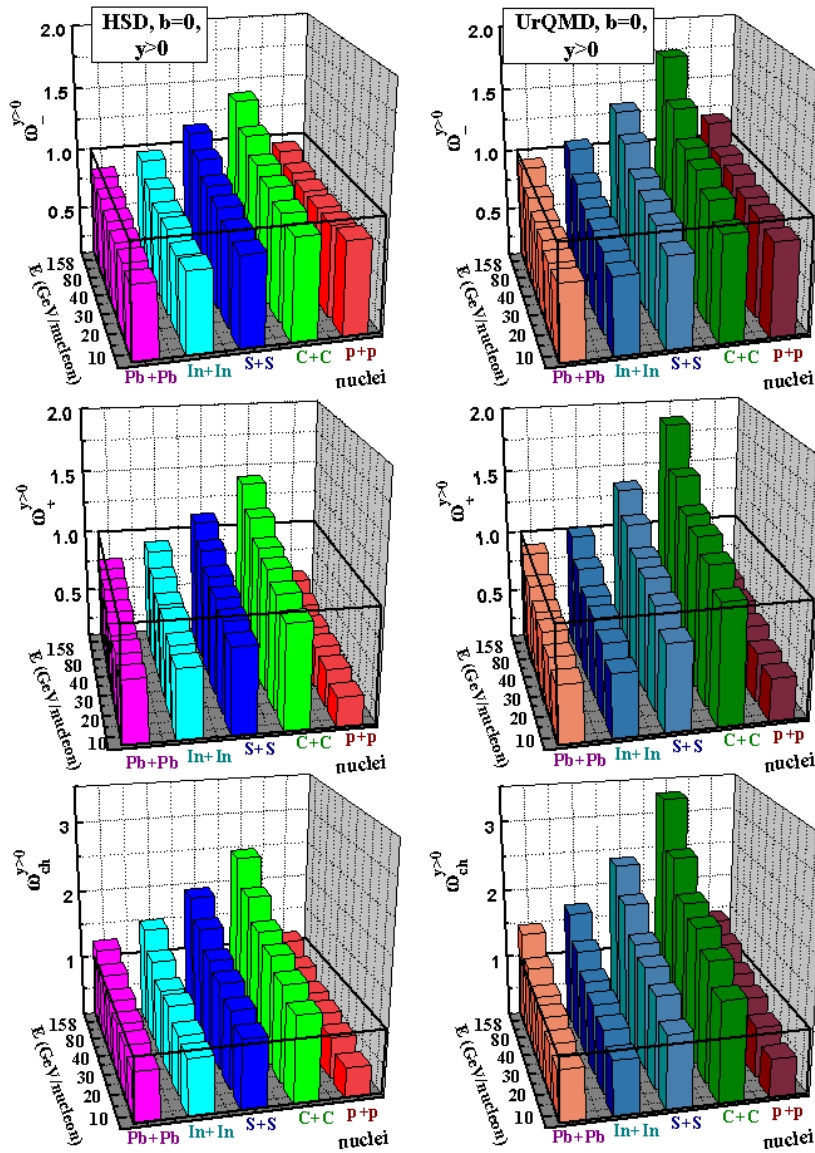


Figure 6.6: The same as in Fig. 6.5, but only hadrons with positive c.m. rapidities,  $y > 0$  (projectile hemisphere), are accepted.

of Fig. 6.2 and Fig. 6.4, respectively. Their combination explains the main features of hadron multiplicity fluctuations in  $A + A$  collisions shown in Fig. 6.5 and Fig. 6.6, in particular, the dependence on collision energy and atomic mass number. They also are responsible for the larger values of  $\omega_i$  in the UrQMD simulations in comparison to those from HSD. To illustrate this the wounded nuclear model, WNM (see subsection 3.2.3) is considered.



The multiplicity fluctuations in  $A + A$  collisions can be then written according to the WNM as:

$$\omega_i = \omega_i^* + n_i \omega_P, \quad (6.2)$$

where  $\omega_i^*$  denotes the fluctuations of the hadron multiplicity from one source and the term  $n_i \omega_P$  gives additional fluctuations due to the fluctuations of the number of sources. One usually assumes that the number of sources is proportional to the number of nucleon participants. The value of  $n_i$  in Eq. 6.2 then is the average number of  $i$ 'th particles per participant,  $n_i = \langle N_i \rangle / \langle N_P \rangle$ , and  $\omega_P$  equals the scaled variance for the number of nucleon participants. Nucleon-nucleon collisions, which are the weighted combinations of p+p, p+n, and n+n reactions, define the fluctuations  $\omega_i^*$  from a single source (see details in Refs. [91, 124]).

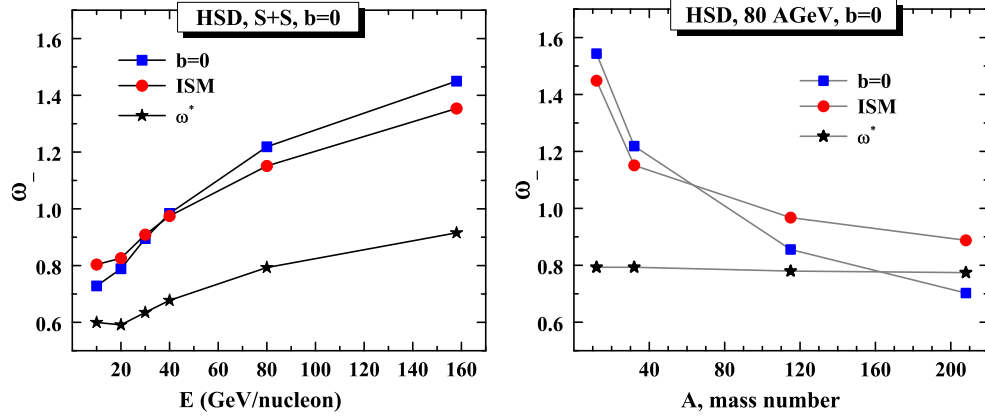


Figure 6.7: The *left* panel illustrates the energy dependence of  $\omega_-$  in S+S collisions at  $b = 0$  in the full  $4\pi$  acceptance, the *right* panel – the  $\omega_-$  dependence on atomic mass number at  $E_{lab}=80$  AGeV. The HSD results are shown by the squares while the circles correspond to Eq. 6.2 of the wounded nuclear model. The stars show the first term,  $\omega_-^*$ , in the *right*. of Eq. 6.2 – scaled variance for negative hadrons in nucleon-nucleon collisions, where the values of  $\omega_-^*$ ,  $n_i$ , and  $\omega_P$  are calculated within HSD.

In Fig. 6.7 the HSD results for  $\omega_i$  in  $A + A$  collisions at  $b = 0$  are compared to the WNM – Eq. 6.2. One concludes that the transport model results for the multiplicity fluctuations are in qualitative agreement with Eq. 6.2 of the independent source model. Both  $n_i$  and  $\omega_i^*$  increase strongly with collision energy as seen from Fig. 6.2. This explains, due to Eq. 6.2, the monotonous increase with energy of

the scaled variances  $\omega_i$  in  $A + A$  collisions at  $b = 0$  seen in Fig. 6.5 and Fig. 6.6. Note that  $\omega_P$  at  $b = 0$  decreases with collision energy as shown in Fig. 6.4, *right*. This, however, does not compensate a strong increase of both  $n_i$  and  $\omega_i^*$ . The atomic mass number dependence of the scaled variances  $\omega_i$  in  $A + A$  collisions with  $b = 0$  follows from the A-dependence of  $\omega_P$ . Fig. 6.4 (*right*) demonstrates a strong increase of  $\omega_P$  for light nuclei. This, due to Eq. 6.2, is transformed to the corresponding behavior of  $\omega_i$  seen in Fig. 6.5 and Fig. 6.6.

## 6.4 Multiplicity fluctuations in 1% most central collisions

In this section the centrality selection procedure by fixing the number of projectile participants  $N_P^{proj}$  is considered. This corresponds to the real situation of  $A + A$  collisions in fixed target experiments. As a first step one simulates in HSD and UrQMD the minimal bias events - which correspond to an all impact parameter sample - and calculate the event distribution over the number of participants  $N_{part}$ . Then, one selects 1% most central collisions which correspond to the largest values of  $N_P^{proj}$ . In such a sample of A+A collisions events with largest  $N_P^{proj}$  from different impact parameters can contribute. After that one calculates the values of  $\omega_P$  in these samples. Note, that even for a fixed number of  $N_P^{proj}$  the number of target participants  $N_P^{targ}$  fluctuates. Thus, the total number of participants  $N_P = N_P^{targ} + N_P^{proj}$  fluctuates, too. In our 1% sample, both  $N_P^{targ}$  and  $N_P^{proj}$  fluctuate. Besides there are correlations between  $N_P^{targ}$  and  $N_P^{proj}$ .

Fig. 6.8 shows the ratio  $\langle N_P \rangle / 2A$  and the scaled variance,  $\omega_P$ , for 1% most central collisions selected by the largest values of  $N_P^{proj}$ . These results are compared with those for the  $b = 0$  centrality selection. For heavy nuclei, like In and Pb, one finds no essential differences between these two criteria of centrality selection. However, the 1% centrality trigger defined by the largest values of  $N_P^{proj}$  looks much more rigid for light ions (S and C). In this case the ratio  $\langle N_P \rangle / 2A$  is larger, and  $\omega_P$  is essentially smaller than for the criterion  $b = 0$ . As a result the 1% centrality trigger by the largest values of  $N_P^{proj}$  leads to a rather weak A-dependence of  $\omega_P$ .

Some comments are appropriate at this point. Let's define the centrality  $c(N)$  as a percentage of events with a multiplicity larger than  $N$  (this can be

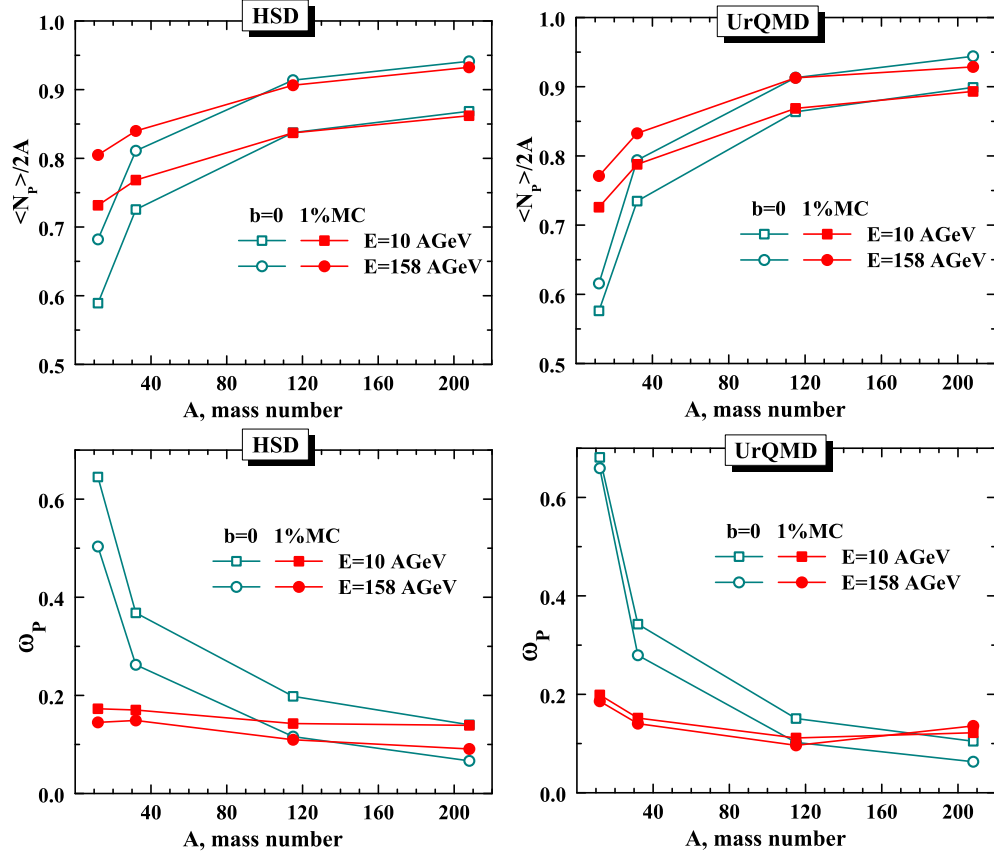


Figure 6.8: The HSD (*left*) and UrQMD (*right*) results for the ratio  $\langle N_P \rangle / 2A$  (the upper panel) and the scaled variance of the participant number fluctuations,  $\omega_P$  (the lower panel), for the 1% most central collisions selected by the largest values of  $N_P^{proj}$  (full symbols), for different nuclei at collision energies  $E_{lab}=10$  and 158 AGeV. The open symbols present the results of Fig. 6.4 (*right*) for  $b=0$ .

the number of produced hadrons, number of participants, etc.). It was argued in Ref. [139] that a selection of  $c(N)$  of most central  $A+A$  collisions is equivalent to restricting the impact parameter,  $b < b(N)$ , with,

$$b(N) = \sqrt{\frac{\sigma_{inel}}{\pi} c(N)}, \quad (6.3)$$

where  $\sigma_{inel}$  is the total inelastic  $A+A$  cross section. Thus, the centrality criterion by the multiplicity  $N$  is equivalent to the geometrical criterion by the impact parameter  $b$ . Moreover, the result (Eq. 6.3) does not depend on the specific observable  $N$  used to define the  $c$ -percentage of most central  $A+A$  collisions. Eq. 6.3

should remain the same for any observable  $N$  which is a monotonic function of  $b$ . Therefore, the relation (Eq. 6.3) reduces any centrality selection to the geometrical one. This result was obtained in Ref. [139] by neglecting the fluctuations of multiplicity  $N$  at a given value of  $b$ . This is valid if  $c$  is not too small and the colliding nuclei are not too light. In the sample of A+A events with 1% of largest  $N_P^{proj}$ , the relation (Eq. 6.3) can not be applied for S+S and C+C collisions.

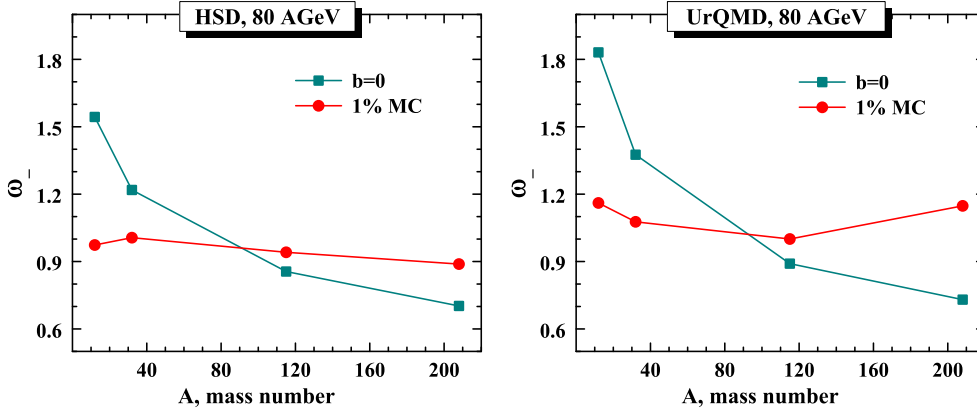


Figure 6.9: The dependence of  $\omega_-$  on atomic mass number at  $E_{lab}=80$  AGeV for the HSD (left) and UrQMD (left) simulations. The squares correspond to  $b = 0$ , and circles to 1% largest  $N_P^{proj}$ .

Fig. 6.9 shows a comparison of the A-dependence of  $\omega_-$  in the transport models for two different samples of the collision events: for  $b = 0$  and for the 1% of events with largest  $N_P^{proj}$  values. One can see that the multiplicity fluctuations are rather different in these two samples. Moreover, these differences are in the opposite directions for heavy nuclei and for light nuclei. For light nuclei,  $\omega_-$  is essentially smaller in the 1% sample with largest  $N_P^{proj}$  values, whereas for heavy nuclei the smaller fluctuations correspond to  $b = 0$  events. Note that in the 1% sample with largest  $N_P^{proj}$  values the A-dependence of multiplicity fluctuations becomes much weaker. In this case a strong increase of the multiplicity fluctuations for light nuclei, seen for  $b = 0$ , disappears.

For the 1% most central A+A collision events - selected by the largest values of  $N_P^{proj}$  - the HSD multiplicity fluctuations are shown in Fig. 6.10 and Fig. 6.12 and the corresponding UrQMD results are shown in Fig. 6.11 and Fig. 6.13. The results from both models are also presented in Table 6.1. The model uncertainties are shown as errorbars in Fig. 6.10 and Fig. 6.11. For light nuclei (S

and C) the multiplicity fluctuations in the samples of 1% most central collisions are smaller than in the  $b = 0$  selection and the atomic mass number dependencies become less pronounced (compare Fig. 6.10 and Fig. 6.11 with Fig. 6.5). This is because the participant number fluctuations  $\omega_P$  have now essentially smaller A-dependence, as seen in Fig. 6.8.

Fig. 6.5 shows that both HSD and UrQMD predict a monotonic dependence of the charge particle multiplicity with energy. So, the hadronic ‘background’ for the NA61 experiments is expected to be a smooth monotonic function of beam energy.

Besides of differences in the realization of the string fragmentation model in HSD and UrQMD 1.3 mentioned above (cf. Fig. 3.4), additional deviations can be attributed to different initializations of the nuclei in both models. Indeed, the event-by-event observables show a higher sensitivity to the initial nucleon density distribution than the standard single particle observables [140]. A pilot study using UrQMD shows different  $\omega$  when applying different initialization shapes. Due to this effects a systematic error of 20% is attributed to  $\omega$ . Such a sensitivity of the A-dependence of  $\omega_{ch}$  to the details of the models indicates a necessity for further studies of the initializations of the nuclei in transport model approaches. This becomes important for the theoretical interpretation of future experimental data on event-by-event fluctuations.

Note that the wounded nuclear model and Eq. 6.2 work for the multiplicity fluctuations simulated by the transport models in full  $4\pi$  acceptance but not for the acceptance in a specific rapidity region. The results for inelastic p+p collisions are identical in the projectile and target hemispheres. This is not the case in the sample of 1% most central  $A + A$  collisions selected by  $N_P^{proj}$ . The total number of nucleons participating in  $A + A$  collisions fluctuates. These fluctuations are not symmetric in forward-backward hemispheres: in the selected 1% sample the number of target participants  $N_P^{targ}$  fluctuates essentially stronger than that of  $N_P^{proj}$ . The consequences of the asymmetry in an event selection depend on the dynamics of A+A collision (see Ref. [98] for details). The HSD and UrQMD results in Fig. 6.12 and Fig. 6.13 clearly demonstrate larger values for all scaled variances,  $\omega_-$ ,  $\omega_+$ , and  $\omega_{ch}$ , for  $y < 0$  acceptance than those for  $y > 0$  one. This is due to stronger target participant fluctuations,  $\omega_P^{targ} > \omega_P^{proj}$ .

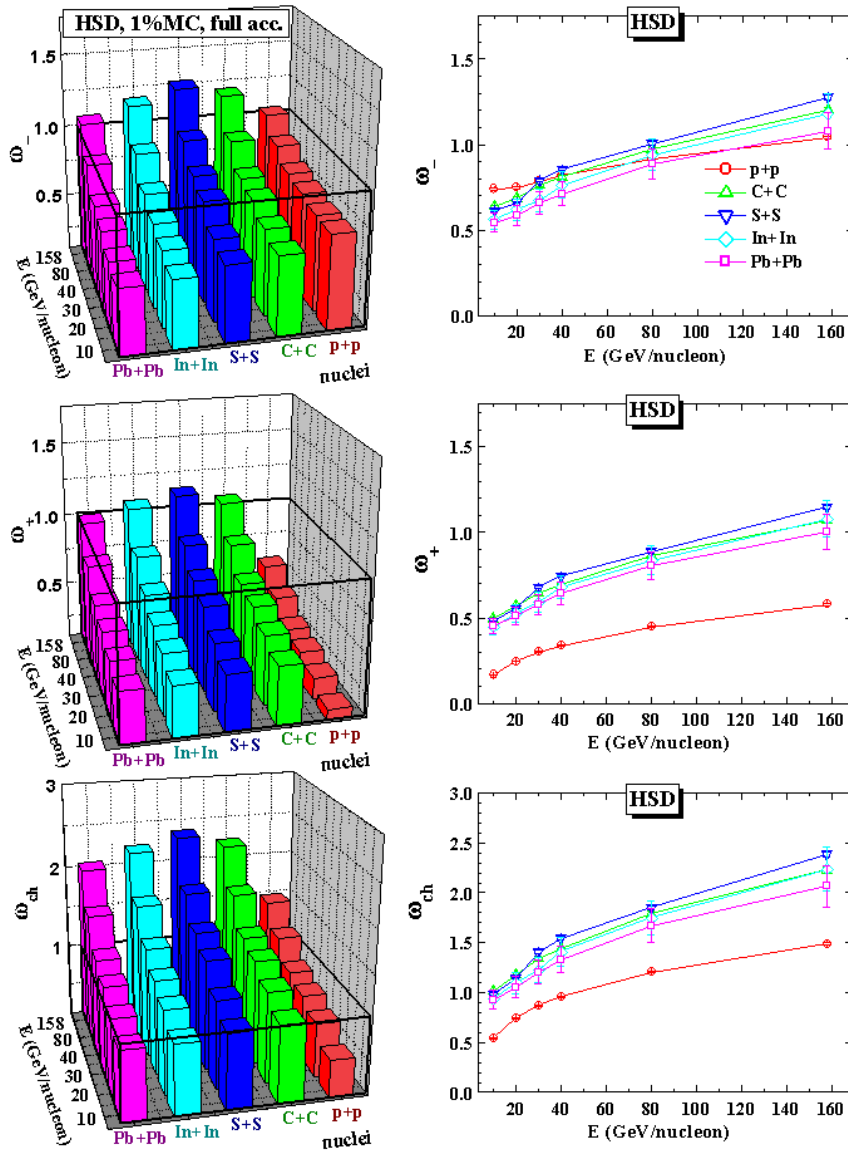


Figure 6.10: The HSD results for  $\omega_-$  (upper panel),  $\omega_+$  (middle panel), and  $\omega_{ch}$  (lower panel) in  $A + A$  and  $p+p$  collisions for the full  $4\pi$  acceptance in 3D (*left*) and 2D (*right*) projection. The 1% most central C+C, S+S, In+In, and Pb+Pb collisions are selected by choosing the largest values of  $N_P^{proj}$  at different collision energies  $E_{lab}=10, 20, 30, 40, 80, 158$  AGeV. The errorbars indicate the estimated uncertainties in the model calculations. The HSD results from inelastic  $p+p$  collisions are the same as in Fig. 6.5.

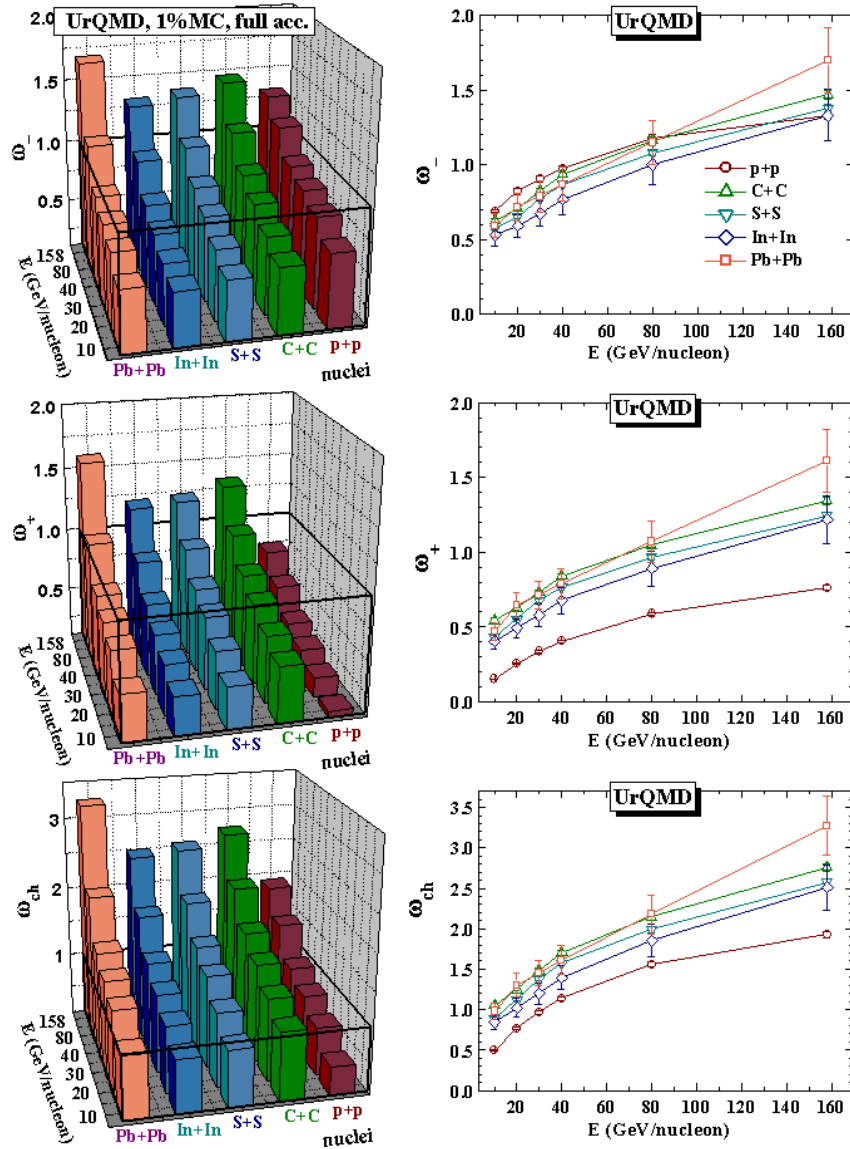


Figure 6.11: The same as in Fig. 6.10, but for the UrQMD.

## 6.5 Summary of Chapter 6

The event-by-event multiplicity fluctuations in nucleus-nucleus collisions have been studied for different energies and system sizes within the HSD transport approach. For comparison the corresponding results from the UrQMD v1.3 model have been presented also. This study is in full correspondence to the future experimental program of the NA61 Collaboration at the SPS. The central C+C,

		HSD: full acc.			HSD: $y > 0$		
		-	+	ch	-	+	ch
p+p	10	0.74	0.17	0.54	0.85	0.33	0.53
	20	0.75	0.25	0.74	0.83	0.39	0.68
	30	0.79	0.30	0.87	0.83	0.42	0.77
	40	0.82	0.34	0.96	0.84	0.44	0.82
	80	0.92	0.45	1.21	0.88	0.49	0.96
	158	1.04	0.58	1.49	0.94	0.58	1.16
C+C	10	0.64	0.50	1.02	0.73	0.53	0.77
	20	0.69	0.57	1.18	0.73	0.56	0.86
	30	0.76	0.64	1.34	0.74	0.58	0.91
	40	0.81	0.69	1.44	0.74	0.62	0.97
	80	0.97	0.86	1.79	0.82	0.69	1.16
	158	1.20	1.07	2.23	0.94	0.78	1.39
S+S	10	0.61	0.48	0.99	0.72	0.52	0.76
	20	0.66	0.55	1.14	0.70	0.56	0.83
	30	0.79	0.68	1.41	0.76	0.59	0.94
	40	0.86	0.75	1.54	0.80	0.62	1.01
	80	1.01	0.89	1.85	0.83	0.70	1.17
	158	1.28	1.15	2.39	0.96	0.79	1.41
In+In	10	0.56	0.45	0.94	0.71	0.54	0.77
	20	0.62	0.53	1.10	0.68	0.56	0.82
	30	0.67	0.59	1.22	0.69	0.60	0.87
	40	0.76	0.68	1.41	0.74	0.63	0.98
	80	0.94	0.84	1.75	0.80	0.70	1.13
	158	1.18	1.08	2.24	0.93	0.80	1.38
Pb+Pb	10	0.54	0.45	0.93	0.68	0.56	0.76
	20	0.58	0.51	1.05	0.69	0.59	0.82
	30	0.66	0.58	1.20	0.69	0.63	0.90
	40	0.71	0.64	1.33	0.75	0.64	0.98
	80	0.89	0.80	1.67	0.77	0.71	1.11
	158	1.08	1.00	2.07	0.93	0.80	1.34

Table 6.1: The HSD scaled variances  $\omega_-$ ,  $\omega_+$ , and  $\omega_{ch}$  for the 1% of most central collisions selected by largest values of  $N_P^{proj}$ . The numbers correspond to those presented in Fig. 6.10 and Fig. 6.12.

S+S, In+In, and Pb+Pb nuclear collisions from  $E_{lab} = 10, 20, 30, 40, 80, 158$  AGeV have been investigated. The influence of participant number fluctu-



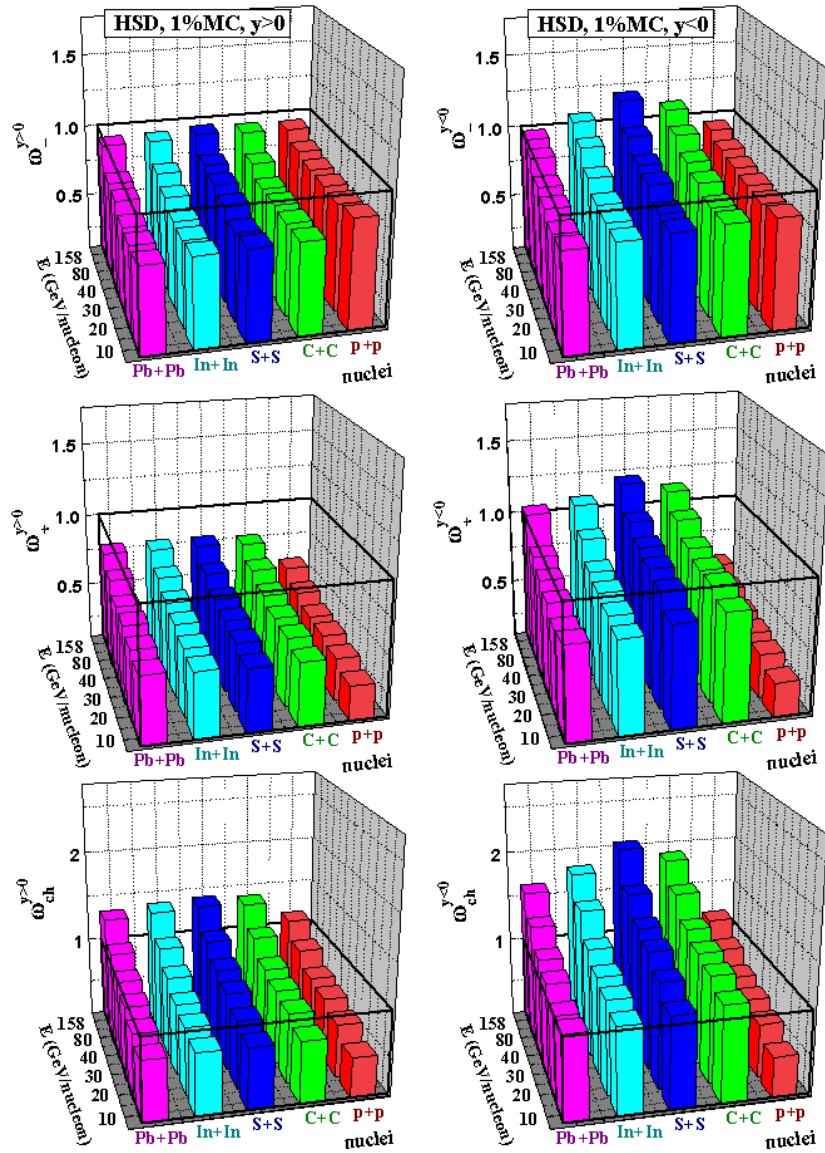


Figure 6.12: The same as in Fig. 6.10, but for final hadrons accepted in the projectile hemisphere,  $y > 0$  (left), and in the target hemisphere,  $y < 0$  (right). The HSD results in inelastic p+p collisions are the same as in Fig. 6.6.

ations on hadron multiplicity fluctuations has been emphasized and studied in detail. To make these ‘trivial’ fluctuations smaller, one has to consider the most central collisions. Indeed, one needs to make a very rigid selection – 1% or smaller – of the ‘most central’ collision events. In addition, one wants to compare the event-by-event fluctuations in these ‘most central’ collisions for heavy and for

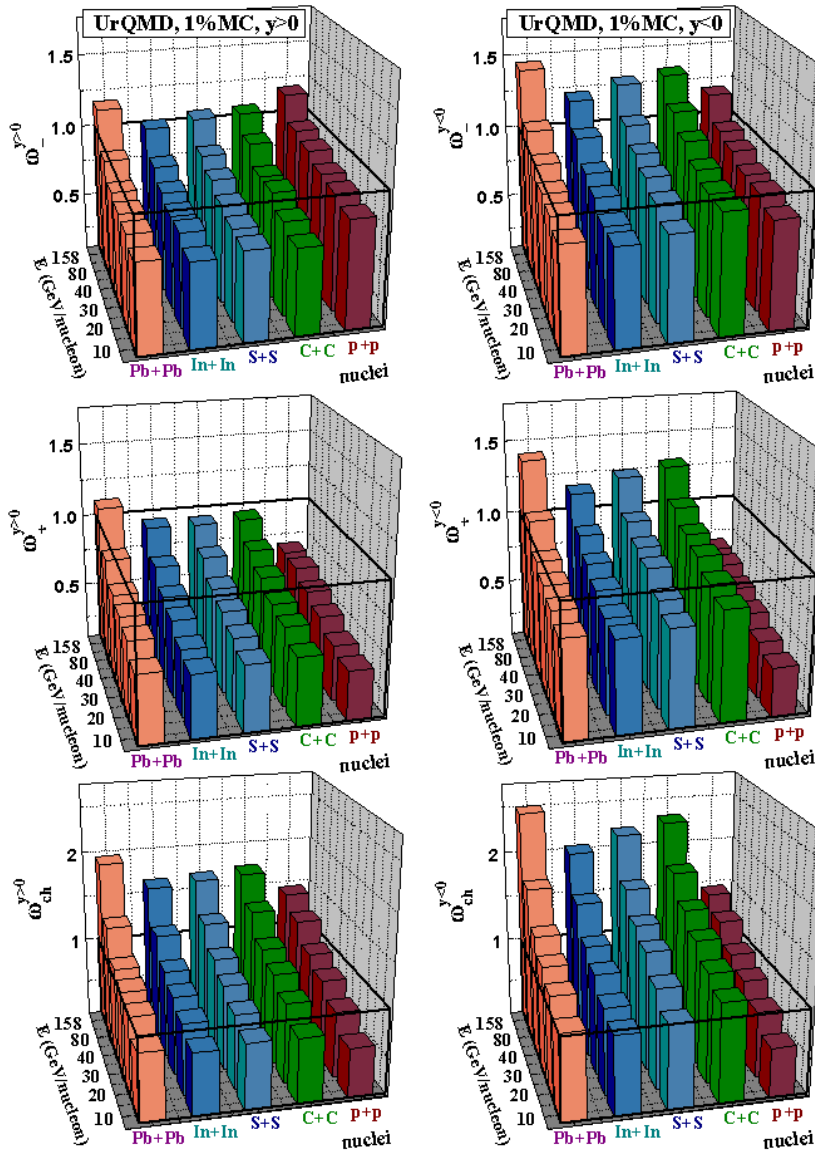


Figure 6.13: The same as in Fig. 6.12, but for the UrQMD.

light nuclei. Under these new requirements different centrality selections are not equivalent to each other. As a consequence, there is no universal geometrical selection by the impact parameter. This is a new and serious problem for theoretical models (e.g., for hydrodynamical models) in a precision description of the event-by-event fluctuation data. The above statements have been illustrated by the  $b = 0$  selection criterium considered in this work. For light nuclei even these ‘absolutely central’ geometrical collisions lead to rather large fluctuations of the

number of participants, essentially larger than in the 1% most central collisions selected by the largest values of the projectile participants  $N_P^{proj}$ .

Furthermore, the number of projectile participants has been used to define the centrality selection. This is the most promising way of the centrality selection in fixed target experiments. It also corresponds to the experimental plans of the NA61 collaboration. The 1% most central collisions has been defined by selecting the largest values of the projectile participants  $N_P^{proj}$ . The multiplicity fluctuations calculated in these samples show a much weaker dependence on the atomic mass number  $A$  than for the criterium  $b = 0$ . A monotonic energy dependence for the multiplicity fluctuations is obtained in both the HSD and UrQMD transport models. The two models demonstrate a similar qualitative behavior of the particle number fluctuations. However, the UrQMD 1.3 results for the scaled variances  $\omega_-$ ,  $\omega_+$ , and  $\omega_{ch}$  are systematically larger than those obtained within HSD. This is mainly due to the corresponding inequalities for the scaled variances  $\omega_{ch}$  (see Fig. 6.2, right) for p+p collisions in these models. This study has demonstrated a sensitivity of the multiplicity fluctuations to some specific details of the transport models. Nevertheless, the present HSD and UrQMD results for the scaled variances provide a general trend of their dependencies on  $A$  and  $E_{lab}$  and also indicate quantitatively the systematic uncertainties.

It has to be stressed again, that HSD and UrQMD do not include explicitly a phase transition to the QGP. The expected enhanced fluctuations - attributed to the critical point and phase transition - can be observed experimentally on top of a monotonic and smooth 'hadronic background'. The most promising signature of the QCD critical point would be an observation of a non-monotonic dependence of the scaled variances with bombarding energy  $E_{lab}$  for central A+A collisions with fixed atomic mass number. In the fixed target SPS experiments the centrality selection in A+A collisions is defined by the number of the projectile participants. The measurements of  $\omega_-$ ,  $\omega_+$ , and  $\omega_{ch}$  are then preferable in the forward hemispheres. In this case the remaining small fluctuations of the number of target participants in the 1% most central collisions become even less important, as they contribute mainly to the particle fluctuations in the backward hemisphere. These findings should be helpful for the optimal choice of collision systems and collision energies for the experimental search of the QCD critical point.

## Chapter 7

# Ratio Fluctuations in Nucleus-Nucleus Collisions: Statistical and Transport Models

Several hadronic observables in central Pb+Pb collisions show qualitative changes in their energy dependence. The ratio of average  $\langle K^+ \rangle$  to  $\langle \pi^+ \rangle$  yields exhibits a non-monotonic behavior in the low-energy SPS range close to  $\sqrt{s_{NN}} \approx 7.6$  GeV [141]. In the same energy range, the slopes of the hadron transverse momentum distributions show an approximately constant value after a rapid rise at lower energies [142]. These features are not observed in elementary interactions and appear to be unique characteristics of heavy-ion collisions. The data are consistent with the expected signals of the onset of a phase transition in heavy-ion collisions at low SPS energies [141, 120].

The measurement of the fluctuations in the kaon to pion ratio by the NA49 Collaboration [143] was the first event-by-event measurement in nucleus-nucleus collisions. It was suggested that this ratio might allow to distinguish events with enhanced strangeness production attributed to the QGP phase. Nowadays, the excitation function for this observable is available in a wide range of energies: from the NA49 collaboration [144] in Pb+Pb collisions at the CERN SPS and from the STAR collaboration [145, 146] in Au+Au collisions at RHIC. Results from NA49 show an enhancement of fluctuations in the kaon to pion multiplicity ratio for low energies which may be a signal of a deconfinement phase transition. On the other hand there is no enhancement for the proton to pion ratio fluctuations.

First statistical model estimates of the  $K/\pi$  fluctuations have been reported in Refs. [147, 148]. A further statistical model analysis has been presented in Fig. 7.1 and Ref. [149]. One should mention again the complexity of applying experimental acceptance cuts to the statistical model results. The lower panel of Fig. 7.1 shows  $K/\pi$  fluctuations only in full acceptance with and without correlation between kaons and pions (full and empty symbols). Chemical equilibrium has been tested using the parameter  $\gamma_q$ . The equilibrium case ( $\gamma_q = 1$ , boxes in the figure) under-estimates the  $K/\pi$  fluctuations at all energies, while the non-equilibrium case (when  $\gamma_q$  is fitted, triangles) describes the higher energies SPS and RHIC acceptably. It, however, considerably under-estimates the data at lower SPS energies. The results from the transport model UrQMD have been presented in Ref. [150] for the SPS energy range. It also fails to explain the rise of  $K/\pi$  fluctuations for low SPS energies (cf. section 7.4).

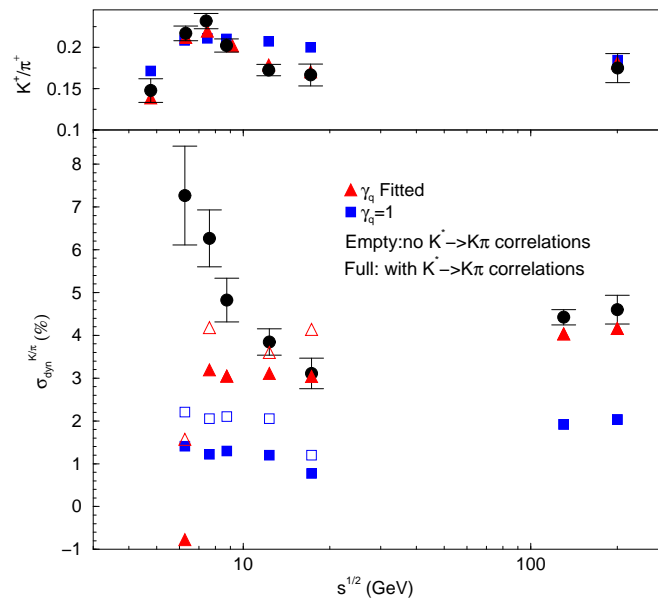


Figure 7.1: The excitation function of the  $K/\pi$  ratio (top panel) and ratio fluctuations (low panel) within statistical model calculations. The figure is taken from Ref. [149].

This chapter presents the results of a systematic study of  $K/\pi$ ,  $K/p$  and  $p/\pi$  ratio fluctuations based on the HSD transport model in comparison to statistical model results in different ensembles [151, 152]. The statistical model calculations have been performed by M. Hauer and shown here for completeness and relative

comparison.

## 7.1 Measures of Particle Ratio Fluctuations

### 7.1.1 Notations and Approximations

Let's introduce some notations. The deviation  $\Delta N_A$  from the average number  $\langle N_A \rangle$  of the particle species  $A$  is defined by  $N_A = \langle N_A \rangle + \Delta N_A$ , while the covariance for species  $A$  and  $B$  is:

$$\Delta(N_A, N_B) \equiv \langle \Delta N_A \Delta N_B \rangle = \langle N_A N_B \rangle - \langle N_A \rangle \langle N_B \rangle, \quad (7.1)$$

the scaled variance

$$\omega_A \equiv \frac{\Delta(N_A, N_A)}{\langle N_A \rangle} = \frac{\langle (\Delta N_A)^2 \rangle}{\langle N_A \rangle} = \frac{\langle N_A^2 \rangle - \langle N_A \rangle^2}{\langle N_A \rangle}, \quad (7.2)$$

and the correlation coefficient

$$\rho_{AB} \equiv \frac{\langle \Delta N_A \Delta N_B \rangle}{[\langle (\Delta N_A)^2 \rangle \langle (\Delta N_B)^2 \rangle]^{1/2}}. \quad (7.3)$$

The fluctuations of the ratio  $R_{AB} \equiv N_A/N_B$  will be characterised by [147, 148]

$$\sigma^2 \equiv \frac{\langle (\Delta R_{AB})^2 \rangle}{\langle R_{AB} \rangle^2}. \quad (7.4)$$

Using the expansion,

$$\frac{N_A}{N_B} = \frac{\langle N_A \rangle + \Delta N_A}{\langle N_B \rangle + \Delta N_B} = \frac{\langle N_A \rangle + \Delta N_A}{\langle N_B \rangle} \times \left[ 1 - \frac{\Delta N_B}{\langle N_B \rangle} + \left( \frac{\Delta N_B}{\langle N_B \rangle} \right)^2 - \dots \right], \quad (7.5)$$

one finds to second order in  $\Delta N_A/\langle N_A \rangle$  and  $\Delta N_B/\langle N_B \rangle$  the average value and fluctuations of the  $A$  to  $B$  ratio:

$$\langle R_{AB} \rangle \cong \frac{\langle N_A \rangle}{\langle N_B \rangle} \left[ 1 + \frac{\omega_B}{\langle N_B \rangle} - \frac{\Delta(N_A, N_B)}{\langle N_A \rangle \langle N_B \rangle} \right], \quad (7.6)$$

$$\begin{aligned} \sigma^2 &\cong \frac{\Delta(N_A, N_A)}{\langle N_A \rangle^2} + \frac{\Delta(N_B, N_B)}{\langle N_B \rangle^2} - 2 \frac{\Delta(N_A, N_B)}{\langle N_A \rangle \langle N_B \rangle} \\ &= \frac{\omega_A}{\langle N_A \rangle} + \frac{\omega_B}{\langle N_B \rangle} - 2\rho_{AB} \left[ \frac{\omega_A \omega_B}{\langle N_A \rangle \langle N_B \rangle} \right]^{1/2}. \end{aligned} \quad (7.7)$$

If species  $A$  and  $B$  fluctuate independently according to the Poisson distributions (this takes place, for example, in the GCE for an ideal Boltzmann gas) one finds,  $\omega_A = \omega_B = 1$  and  $\rho_{AB} = 0$ . [Eq. 7.7](#) then reads

$$\sigma^2 = \frac{1}{\langle N_A \rangle} + \frac{1}{\langle N_B \rangle}. \quad (7.8)$$

In a thermal gas, the average multiplicities are proportional to the system volume  $V$ . [Eq. 7.8](#) demonstrates then a simple dependence  $\sigma^2 \propto 1/V$  on the system volume.

A few examples concerning to [Eq. 7.7](#) are appropriate here. When  $\langle N_B \rangle \gg \langle N_A \rangle$ , e.g.,  $A = K^+ + K^-$  and  $B = \pi^+ + \pi^-$ , the  $\sigma^2$  ([Eq. 7.7](#)) is dominated by the less abundant particles and the resonances decaying into it. When  $\langle N_A \rangle \cong \langle N_B \rangle$ , e.g.,  $A = \pi^+$  and  $B = \pi^-$ , the correlation term in [Eq. 7.7](#) may become especially important. A resonance decaying always into a  $\pi^+\pi^-$ -pair does not contribute to  $\sigma^2$  ([Eq. 7.7](#)), but contributes to  $\pi^+$  and  $\pi^-$  average multiplicities. This leads [[148](#)] to a suppression of  $\sigma^2$  ([Eq. 7.7](#)) in comparison to its value given by [Eq. 7.8](#). For example, if all  $\pi^+$  and  $\pi^-$  particles come by pairs from decay of resonances, one finds the correlation coefficient  $\rho_{\pi^+\pi^-} = 1$  in [Eq. 7.7](#), and thus  $\sigma^2 = 0$ . In this case, the numbers of  $\pi^+$  and  $\pi^-$  fluctuate as the number of resonances, but the ratio  $\pi^+/\pi^-$  does not fluctuate!

### 7.1.2 Mixed Events Procedure

The experimental data for  $N_A/N_B$  fluctuations are usually presented in terms of the so called dynamical fluctuations [153]<sup>1</sup>

$$\sigma_{dyn} \equiv \text{sign}(\sigma^2 - \sigma_{mix}^2) |\sigma^2 - \sigma_{mix}^2|^{1/2}, \quad (7.9)$$

where  $\sigma^2$  is defined by Eq. 7.7, and  $\sigma_{mix}^2$  corresponds to the following *mixed events* procedure<sup>2</sup>. One takes a large number of nucleus-nucleus collision events, and measures the numbers of  $N_A$  and  $N_B$  in each event. Then all  $A$  and  $B$  particles from all events are combined into one *set*. A construction of *mixed events* is done like the following: One fixes a random number  $N = N_A + N_B$  according to the experimental probability distribution  $P(N)$ , takes randomly  $N$  particles ( $A$  and/or  $B$ ) from the *whole set*, fixes the values of  $N_A$  and  $N_B$ , and returns these  $N$  particles into the *set*. This is the mixed event number one. Then one constructs event number 2, number 3, etc.

Note that the number of events is much larger than the number of hadrons,  $N$ , in any single event. Therefore, the probabilities  $p_A$  and  $p_B = 1 - p_A$  to take the  $A$  and  $B$  species from the whole *set* can be considered as constant values during the event construction. Another consequence of a large number of events is the fact that all  $A$  and  $B$  particles in any constructed *mixed event* most probably belong to different *physical events* of nucleus-nucleus collisions. Therefore, the correlations between  $N_B$  and  $N_A$  numbers in a physical event are expected to be destroyed in a mixed event. This is the main purpose of the mixed events construction. For any function  $f$  of  $N_A$  and  $N_B$  the mixed events averaging is then defined as,

$$\begin{aligned} \langle f(N_A, N_B) \rangle_{mix} &= \sum_N P(N) \sum_{N_A, N_B} f(N_A, N_B) \times \\ &\delta(N - N_A - N_B) \frac{(N_A + N_B)!}{N_A! N_B!} p_A^{N_A} p_B^{N_B}. \end{aligned} \quad (7.10)$$

The straightforward calculation of mixed averages (Eq. 7.10) can be simplified by

<sup>1</sup>Other dynamical measures,  $\Phi$  [114, 154] and  $F$  [148], can be also used.

<sup>2</sup>The idealized mixed events procedure appropriate for model analysis is described here. The real experimental mixed events procedure is more complicated and includes experimental uncertainties, such as particle identification etc.



introducing the generating function  $Z(x, y)$ ,

$$\begin{aligned} Z(x, y) &\equiv \sum_N P(N) \sum_{N_A, N_B} \delta(N - N_A - N_B) \frac{(N_A + N_B)!}{N_A! N_B!} (xp_A)^{N_A} (yp_B)^{N_B} \\ &= \sum_N P(N) (xp_A + yp_B)^N . \end{aligned} \quad (7.11)$$

The averages (Eq. 7.10) are then expressed as  $x$ - and  $y$ -derivatives of  $Z(x, y)$  at  $x = y = 1$ . One finds:

$$\begin{aligned} \langle N_A \rangle_{mix} &= \left( \frac{\partial Z}{\partial x} \right)_{x=y=1} = p_A \langle N \rangle , \\ \langle N_B \rangle_{mix} &= \left( \frac{\partial Z}{\partial y} \right)_{x=y=1} = p_B \langle N \rangle , \end{aligned} \quad (7.12)$$

$$\langle N_A(N_A - 1) \rangle_{mix} = \left( \frac{\partial^2 Z}{\partial^2 x} \right)_{x=y=1} = p_A^2 \langle N(N - 1) \rangle , \quad (7.13)$$

$$\langle N_B(N_B - 1) \rangle_{mix} = \left( \frac{\partial^2 Z}{\partial^2 y} \right)_{x=y=1} = p_B^2 \langle N(N - 1) \rangle , \quad (7.14)$$

$$\begin{aligned} \langle N_A N_B \rangle_{mix} - \langle N_A \rangle_{mix} \langle N_B \rangle_{mix} &= \left( \frac{\partial^2 Z}{\partial x \partial y} \right)_{x=y=1} \\ &= p_A p_B \omega_N \langle N \rangle , \end{aligned} \quad (7.15)$$

where

$$\begin{aligned} \langle N \rangle &\equiv \sum_N N P(N) , \\ \langle N^2 \rangle &\equiv \sum_N N^2 P(N) , \\ \omega_N &\equiv \frac{\langle N^2 \rangle - \langle N \rangle^2}{\langle N \rangle} . \end{aligned} \quad (7.16)$$

Calculating the  $N_A/N_B$  fluctuations for mixed events according to Eq. 7.7 one

gets:

$$\begin{aligned}
\sigma_{mix}^2 &\equiv \frac{\Delta_{mix}(N_A, N_A)}{\langle N_A \rangle^2} + \frac{\Delta_{mix}(N_B, N_B)}{\langle N_B \rangle^2} - 2 \frac{\Delta_{mix}(N_A, N_B)}{\langle N_A \rangle \langle N_B \rangle} \\
&= \left[ \frac{1}{\langle N_A \rangle} + \frac{\omega_N - 1}{\langle N \rangle} \right] + \left[ \frac{1}{\langle N_B \rangle} + \frac{\omega_N - 1}{\langle N \rangle} \right] - 2 \frac{\omega_N - 1}{\langle N \rangle} \\
&= \frac{1}{\langle N_A \rangle} + \frac{1}{\langle N_B \rangle} .
\end{aligned} \tag{7.17}$$

A comparison of the final result in Eq. 7.17 with Eq. 7.8 shows that the mixed event procedure gives the same  $\sigma^2$  for  $N_A/N_B$  fluctuations as in the GCE formulation for an ideal Boltzmann gas, i.e.  $\omega_A = \omega_B = 1$  and  $\rho_{AB} = 0$ . If  $\omega_N = 1$  (e.g., for the Poisson distribution  $P(N)$ ), one indeed finds  $\omega_A^{mix} = \omega_B^{mix} = 1$  and  $\rho_{AB}^{mix} = 0$ . Otherwise, if  $\omega_N \neq 1$ , the mixed events procedure leads to  $\omega_A^{mix} \neq 1$ ,  $\omega_B^{mix} \neq 1$ , and to non-zero  $N_A N_B$  correlations, as seen from the second line of Eq. 7.17. However, the final result for  $\sigma_{mix}^2$  (Eq. 7.17) is still the same simple. It does not depend on the specific form of  $P(N)$ . Non-trivial ( $\omega_{A,B}^{mix} \neq 1$ ) fluctuations of  $N_A$  and  $N_B$  as well as non-zero  $\rho_{AB}^{mix}$  correlations may exist in the mixed events procedure, but they are canceled out exactly in  $\sigma_{mix}^2$ .

## 7.2 Fluctuations of Ratios in Statistical Models

### 7.2.1 Quantum Statistics and Resonance Decays

The occupation numbers,  $n_{\mathbf{p},j}$ , of single quantum states (with fixed projection of particle spin) labeled by the momentum vector  $\mathbf{p}$  are equal to  $n_{\mathbf{p},j} = 0, 1, \dots, \infty$  for bosons and  $n_{\mathbf{p},j} = 0, 1$  for fermions. Their average values are

$$\langle n_{\mathbf{p},j} \rangle = \frac{1}{\exp[(\epsilon_{\mathbf{p}j} - \mu_j)/T] - \alpha_j} , \tag{7.18}$$

and their fluctuations read

$$\begin{aligned}
\langle (\Delta n_{\mathbf{p},j})^2 \rangle_{gce} &\equiv \langle (n_{\mathbf{p},j} - \langle n_{\mathbf{p},j} \rangle)^2 \rangle_{gce} \\
&= \langle n_{\mathbf{p},j} \rangle (1 + \alpha_j \langle n_{\mathbf{p},j} \rangle) \equiv v_{\mathbf{p},j}^2 ,
\end{aligned} \tag{7.19}$$

where  $T$  is the system temperature,  $m_j$  is the mass of a particle  $j$  and  $\epsilon_{\mathbf{p}j} = \sqrt{\mathbf{p}^2 + m_j^2}$  is the single particle energy. A value of  $\alpha_j$  depends on quantum statistics, it is  $+1$  for bosons and  $-1$  for fermions, while  $\alpha_j = 0$  gives the Boltzmann approximation. The chemical potential  $\mu_j$  of a species  $j$  equals to:  $\mu_j = q_j \mu_Q + b_j \mu_B + s_j \mu_S$ , where  $q_j$ ,  $b_j$ ,  $s_j$  are the particle electric charge, baryon number, and strangeness, respectively, while  $\mu_Q$ ,  $\mu_B$ ,  $\mu_S$  are the corresponding chemical potentials which regulate the average values of these global conserved charges in the GCE.

In the equilibrium hadron-resonance gas the mean number of primary particles (or resonances) are calculated as:

$$\langle N_j^* \rangle \equiv \sum_{\mathbf{p}} \langle n_{\mathbf{p},j} \rangle = \frac{g_j V}{2\pi^2} \int_0^\infty p^2 dp \langle n_{\mathbf{p},j} \rangle, \quad (7.20)$$

where  $V$  is the system volume and  $g_j$  is the degeneracy factor of a particle of species  $j$  (the number of spin states). In the thermodynamic limit,  $V \rightarrow \infty$ , the sum over the momentum states can be substituted by a momentum integral.

It is convenient to introduce a microscopic correlator,  $\langle \Delta n_{\mathbf{p},j} \Delta n_{\mathbf{k},i} \rangle$ , which in the GCE has a simple form:

$$\langle \Delta n_{\mathbf{p},j} \Delta n_{\mathbf{k},i} \rangle_{gce} = v_{\mathbf{p},j}^2 \delta_{ij} \delta_{\mathbf{p}\mathbf{k}}. \quad (7.21)$$

Hence there are no correlations between different particle species,  $i \neq j$ , and/or between different momentum states,  $\mathbf{p} \neq \mathbf{k}$ . Only the Bose enhancement,  $v_{\mathbf{p},j}^2 > \langle n_{\mathbf{p},j} \rangle$  for  $\alpha_j = 1$ , and the Fermi suppression,  $v_{\mathbf{p},j}^2 < \langle n_{\mathbf{p},j} \rangle$  for  $\alpha_j = -1$ , exist for fluctuations of primary particles in the GCE. The correlator (Eq. 7.1) can be presented in terms of microscopic correlators (Eq. 7.21):

$$\langle \Delta N_j^* \Delta N_i^* \rangle_{gce} = \sum_{\mathbf{p}, \mathbf{k}} \langle \Delta n_{\mathbf{p},j} \Delta n_{\mathbf{k},i} \rangle_{gce} = \delta_{ij} \sum_{\mathbf{p}} v_{\mathbf{p},j}^2. \quad (7.22)$$

In the case of  $i = j$  the above equation gives the variance of primordial particles (before resonance decays) in the GCE.

For the hadron resonance gas – formed in relativistic A+A collisions – the corrections due to quantum statistics (Bose enhancement and Fermi suppression)

are small<sup>3</sup>. For the pion gas at  $T = 160$  MeV, one finds  $\omega_\pi \cong 1.1$ , instead of  $\omega = 1$  for Boltzmann particles. The quantum statistics effects are even smaller for heavier particles like kaons and almost negligible for resonances.

The average final (after resonance decays) multiplicities  $\langle N_i \rangle$  are equal to:

$$\langle N_i \rangle = \langle N_i^* \rangle + \sum_R \langle N_R \rangle \langle n_i \rangle_R . \quad (7.23)$$

In [Eq. 7.23](#),  $N_i^*$  denotes the number of stable primary hadrons of species  $i$ , the summation  $\sum_R$  runs over all types of resonances  $R$ , and  $\langle n_i \rangle_R \equiv \sum_r b_r^R n_{i,r}^R$  is the average over resonance decay channels. The parameters  $b_r^R$  are the branching ratios of the  $r$ -th branches,  $n_{i,r}^R$  is the number of particles of species  $i$  produced in resonance  $R$  decays via a decay mode  $r$ . The index  $r$  runs over all decay channels of a resonance  $R$  with the requirement  $\sum_r b_r^R = 1$ . In the GCE the correlator ([Eq. 7.1](#)) after resonance decays can be calculated as [\[148\]](#):

$$\begin{aligned} \langle \Delta N_A \Delta N_B \rangle_{gce} &= \langle \Delta N_A^* \Delta N_B^* \rangle_{gce} \\ &+ \sum_R [\langle \Delta N_R^2 \rangle \langle n_A \rangle_R \langle n_B \rangle_R + \langle N_R \rangle \langle \Delta n_A \Delta n_B \rangle_R] , \end{aligned} \quad (7.24)$$

where  $\langle \Delta n_A \Delta n_B \rangle_R \equiv \sum_r b_r^R n_{A,r}^R n_{B,r}^R - \langle n_A \rangle_R \langle n_B \rangle_R$ .

## 7.2.2 Global Conservation Laws

In the MCE, the energy and conserved charges are fixed exactly for each microscopic state of the system. This leads to two modifications in comparison with the GCE. First, additional terms appear for the primordial microscopic correlators in the MCE. They reflect the (anti)correlations between different particles,  $i \neq j$ , and different momentum levels,  $\mathbf{p} \neq \mathbf{k}$ , due to charge and energy conser-

---

<sup>3</sup>Possible strong Bose effects are discussed in Ref. [\[155, 156\]](#)

vation in the MCE [129],

$$\begin{aligned}
\langle \Delta n_{\mathbf{p},j} \Delta n_{\mathbf{k},i} \rangle_{mce} &= v_{\mathbf{p},j}^2 \delta_{ij} \delta_{\mathbf{p}\mathbf{k}} - \frac{v_{\mathbf{p},j}^2 v_{\mathbf{k},i}^2}{|A|} [ q_i q_j M_{qq} + b_i b_j M_{bb} + s_i s_j M_{ss} \\
&+ (q_i s_j + q_j s_i) M_{qs} - (q_i b_j + q_j b_i) M_{qb} - (b_i s_j + b_j s_i) M_{bs} \\
&+ \epsilon_{\mathbf{p}j} \epsilon_{\mathbf{k}i} M_{\epsilon\epsilon} - (q_i \epsilon_{\mathbf{p}j} + q_j \epsilon_{\mathbf{k}i}) M_{q\epsilon} + (b_i \epsilon_{\mathbf{p}j} + b_j \epsilon_{\mathbf{k}i}) M_{b\epsilon} \\
&- (s_i \epsilon_{\mathbf{p}j} + s_j \epsilon_{\mathbf{k}i}) M_{s\epsilon} ], \tag{7.25}
\end{aligned}$$

where  $|A|$  is the determinant and  $M_{ij}$  are the minors of the following matrix,

$$A = \begin{pmatrix} \Delta(q^2) & \Delta(bq) & \Delta(sq) & \Delta(\epsilon q) \\ \Delta(qb) & \Delta(b^2) & \Delta(sb) & \Delta(\epsilon b) \\ \Delta(qs) & \Delta(bs) & \Delta(s^2) & \Delta(\epsilon s) \\ \Delta(q\epsilon) & \Delta(b\epsilon) & \Delta(s\epsilon) & \Delta(\epsilon^2) \end{pmatrix}, \tag{7.26}$$

with the elements,  $\Delta(q^2) \equiv \sum_{\mathbf{p},j} q_j^2 v_{\mathbf{p},j}^2$ ,  $\Delta(qb) \equiv \sum_{\mathbf{p},j} q_j b_j v_{\mathbf{p},j}^2$ ,  $\Delta(q\epsilon) \equiv \sum_{\mathbf{p},j} q_j \epsilon_{\mathbf{p}j} v_{\mathbf{p},j}^2$ , etc. The sum,  $\sum_{\mathbf{p},j}$ , means integration over momentum  $\mathbf{p}$ , and the summation over all hadron-resonance species  $j$  contained in the model. The first term in the r.h.s. of Eq. 7.25 corresponds to the microscopic correlator (Eq. 7.21) in the GCE. Note that the presence of the terms containing a single particle energy,  $\epsilon_{\mathbf{p}j} = \sqrt{\mathbf{p}^2 + m_j^2}$ , in Eq. 7.25 is a consequence of energy conservation. In the CE only charges are conserved, thus the terms containing  $\epsilon_{\mathbf{p}j}$  in Eq. 7.25 are absent. The  $A$  in Eq. 7.26 becomes then a  $3 \times 3$  matrix (see Ref. [130]). An important property of the microscopic correlator method is that the particle number fluctuations and the correlations in the MCE or CE, although being different from those in the GCE, are expressed by quantities calculated within the GCE. The microscopic correlator (Eq. 7.25) can be used to calculate the primordial particle (or resonances) correlator in the MCE (or in the CE):

$$\langle \Delta N_i \Delta N_j \rangle_{mce} = \sum_{\mathbf{p},\mathbf{k}} \langle \Delta n_{\mathbf{p},i} \Delta n_{\mathbf{k},j} \rangle_{mce}. \tag{7.27}$$

A second feature of the MCE (or CE) is the modification of the resonance decay contribution to the fluctuations in comparison to the GCE (Eq. 7.24). In

the MCE (or CE) it reads[130, 129]:

$$\begin{aligned}
\langle \Delta N_A \Delta N_B \rangle_{mce} &= \langle \Delta N_A^* \Delta N_B^* \rangle_{mce} \\
&+ \sum_R \langle N_R \rangle \langle \Delta n_A \Delta n_B \rangle_R \\
&+ \sum_R \langle \Delta N_A^* \Delta N_R \rangle_{mce} \langle n_B \rangle_R \\
&+ \sum_R \langle \Delta N_B^* \Delta N_R \rangle_{mce} \langle n_A \rangle_R \\
&+ \sum_{R,R'} \langle \Delta N_R \Delta N_{R'} \rangle_{mce} \langle n_A \rangle_R \langle n_B \rangle_{R'} . \quad (7.28)
\end{aligned}$$

Additional terms in Eq. 7.28 compared to Eq. 7.24 are due to correlations (for primordial particles) induced by energy and charge conservations in the MCE. The Eq. 7.28 has the same form in the CE [130] and MCE [129], the difference between these two ensembles appears because of different microscopic correlators (Eq. 7.25). The microscopic correlators of the MCE together with Eq. 7.27 should be used to calculate the correlators  $\langle \Delta N_A^* \Delta N_B^* \rangle_{mce}$ ,  $\langle \Delta N_A^* \Delta N_R \rangle_{mce}$ ,  $\langle \Delta N_A^* \Delta N_R \rangle_{mce}$ ,  $\langle \Delta N_B^* \Delta N_R \rangle_{mce}$ , and  $\langle \Delta N_R \Delta N_{R'} \rangle_{mce}$  entering in Eq. 7.28. The correlators (Eq. 7.28) define finally the scaled variances  $\omega_A$  and  $\omega_B$  (Eq. 7.2), and correlations  $\rho_{AB}$  (Eq. 7.3) between  $N_A$  and  $N_B$  numbers. Together with the average multiplicities  $\langle N_A \rangle$  and  $\langle N_B \rangle$  they define completely the fluctuations  $\sigma^2$  (Eq. 7.7) in the particle  $A$  and  $B$  number ratio.

### 7.3 Statistical and HSD model results

This section presents the results of HSD transport model and the hadron-resonance gas statistical model (SM) for the multiplicity fluctuations of pions, kaons, protons and their ratios in central nucleus-nucleus collisions. To carry out the SM calculations one has to fix the chemical freeze-out parameters. The dependence of  $\mu_B$  on the collision energy is parameterized as in Ref [157]:  $\mu_B(\sqrt{s_{NN}}) = 1.308 \text{ GeV} \cdot (1 + 0.273 \sqrt{s_{NN}})^{-1}$ , where the c.m. nucleon-nucleon collision energy,  $\sqrt{s_{NN}}$ , is taken in units of GeV. The system is assumed to be net strangeness free, i.e.  $S = 0$ , and to have the charge to baryon ratio of the initial colliding nuclei, i.e.  $Q/B = 0.4$ . These two conditions define the system strange,  $\mu_S$ , and electric,  $\mu_Q$ , chemical potentials. For the chemical freeze-out

condition we chose the average energy per particle,  $\langle E \rangle / \langle N \rangle = 1$  GeV [20]. Finally, the strangeness saturation factor,  $\gamma_S$ , is parametrized as in Ref. [137]:  $\gamma_S = 1 - 0.396 \exp(-1.23 T/\mu_B)$ . This determines all parameters of the model. An extended version of the THERMUS framework [158] is used for the SM calculations (for more details see Ref. [129]).

### 7.3.1 Results for $\omega_A$ and $\rho_{AB}$

According to Eq. 7.7 the fluctuation of the  $K = K^+ + K^-$  to  $\pi = \pi^+ + \pi^-$  ratio is given by

$$\sigma^2 = \frac{\omega_K}{\langle N_K \rangle} + \frac{\omega_\pi}{\langle N_\pi \rangle} - 2\rho_{K\pi} \left[ \frac{\omega_K \omega_\pi}{\langle N_K \rangle \langle N_\pi \rangle} \right]^{1/2}. \quad (7.29)$$

The same is valid for  $K/p$  and  $p/\pi$  fluctuations.

$\sqrt{s_{NN}}$ [ GeV ]	HSD full acceptance								
	$\langle N_\pi \rangle$	$\langle N_K \rangle$	$\langle N_p \rangle$	$\omega_\pi$	$\omega_K$	$\omega_p$	$\rho_{K\pi}$	$\rho_{p\pi}$	$\rho_{Kp}$
6.27	612.03	43.329	181.83	0.961	1.107	0.506	-0.091	0.048	-0.137
7.62	732.11	60.801	180.03	1.077	1.141	0.526	-0.063	0.025	-0.128
8.77	823.71	75.133	179.43	1.159	1.168	0.546	-0.033	0.016	-0.129
12.3	1072.3	116.44	180.81	1.378	1.250	0.596	0.046	-0.006	-0.126
17.3	1364.6	165.52	186.97	1.619	1.348	0.641	0.126	-0.010	-0.118
62.4	2933.9	449.29	240.53	3.006	1.891	0.863	0.412	0.074	-0.029
130	4304.2	692.59	307.31	4.538	2.378	1.020	0.557	0.177	0.067
200	5204.0	861.77	352.91	5.838	2.765	1.122	0.634	0.251	0.135

Table 7.1: The HSD results for the average multiplicities  $\langle N_\pi \rangle$ ,  $\langle N_K \rangle$ ,  $\langle N_p \rangle$  and values of  $\omega_\pi$ ,  $\omega_K$ ,  $\omega_p$ , and  $\rho_{K\pi}$ ,  $\rho_{Kp}$ ,  $\rho_{p\pi}$  for central (impact parameter  $b = 0$ ) Pb+Pb (Au+Au) collisions at different c.m. energies  $\sqrt{s_{NN}}$ .

The values of  $\omega_\pi$ ,  $\omega_K$ ,  $\omega_p$  and  $\rho_{K\pi}$ ,  $\rho_{Kp}$ ,  $\rho_{p\pi}$  for the HSD simulations of Pb+Pb (Au+Au) central (with impact parameter  $b = 0$ ) collisions are presented in Table 7.1. Both the SM and HSD results are shown in Fig. 7.2 and Fig. 7.3. Let us first comment the SM results. In the SM the scaled variances  $\omega_A$  and correlation parameter  $\rho_{AB}$  approach finite values in the thermodynamic limit of large volumes. These limiting values are presented in Fig. 7.2 and Fig. 7.3. For central Pb+Pb and Au+Au collisions the corresponding volumes in the SM are large enough. Finite volume corrections are expected on the level of a few percent. The finite volume effects for the scaled variances and correlation parameters in

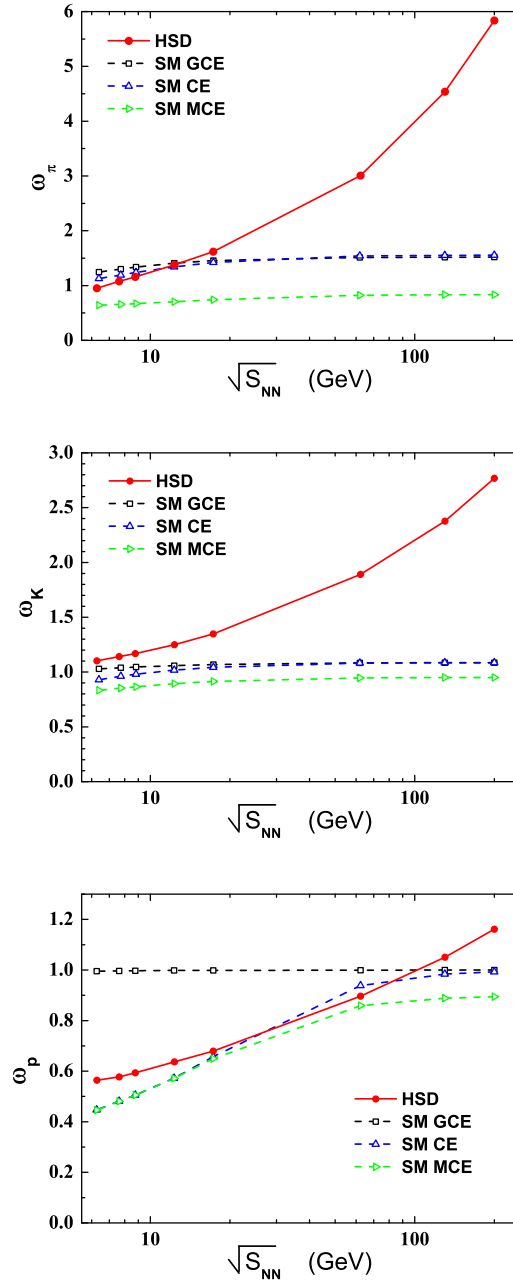


Figure 7.2: The SM results in the GCE, CE, and MCE ensembles and the HSD results (impact parameter  $b = 0$ ) are presented for the scaled variances  $\omega_\pi$ ,  $\omega_K$ ,  $\omega_p$  for Pb+Pb (Au+Au) collisions at different c.m. energies  $\sqrt{s_{NN}}$ .

the CE and MCE are, however, difficult to calculate (see Ref. [159]) and they will not be considered here.



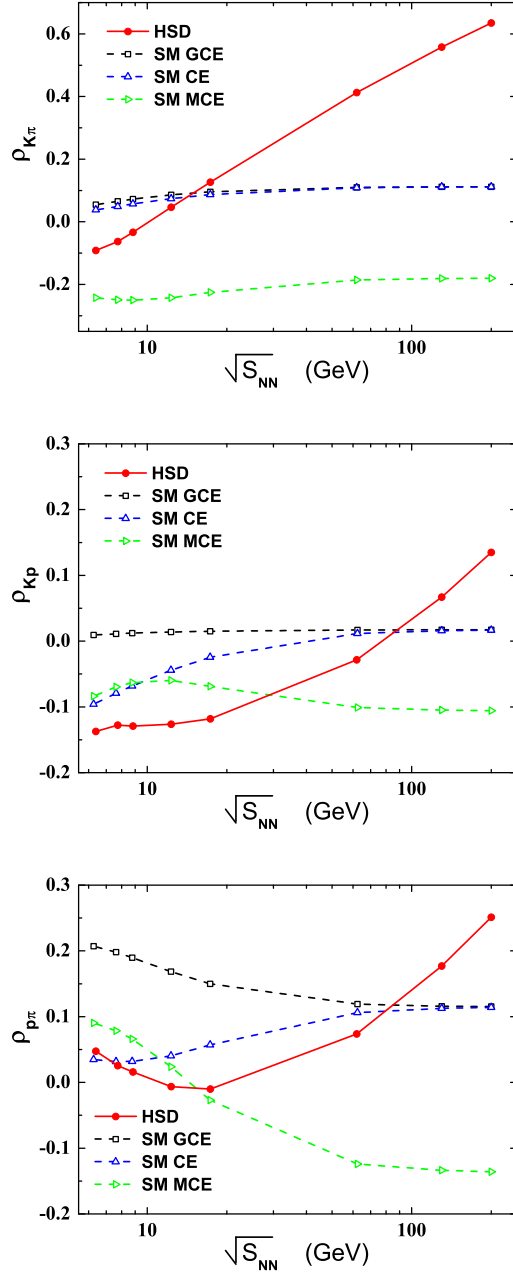


Figure 7.3: The SM results in the GCE, CE, and MCE ensembles and the HSD results (impact parameter  $b = 0$ ) are presented for the correlation parameters  $\rho_{K\pi}$ ,  $\rho_{Kp}$ ,  $\rho_{p\pi}$  for Pb+Pb (Au+Au) collisions at different c.m. energies  $\sqrt{s_{NN}}$

The  $\pi$ - $K$  correlations  $\rho_{K\pi}$  are due to resonances having simultaneously  $K$  and  $\pi$  mesons in their decay products. In the hadron-resonance gas within the GCE

ensemble, these quantum statistics and resonance decay effects are responsible for deviations of  $\omega_K$  and  $\omega_\pi$  from 1, and of  $\rho_{K\pi}$  from 0. The most important effect of an exact charge conservation in the CE ensemble is a suppression of the kaon number fluctuation. This happens mainly due to exact strangeness conservation and is reflected in smaller CE values of  $\omega_K$  at low collision energies in comparison to those from the GCE ensemble. The MCE values of  $\omega_K$  and  $\omega_\pi$  are further suppressed in comparison those from the CE ensemble. This is due to exact energy conservation. The effect is stronger for pions than for kaons since pions carry a larger part of the total energy. An important feature of the MCE is the anticorrelation between  $N_\pi$  and  $N_K$ , i.e. negative values of  $\rho_{K\pi}$ . This is also a consequence of energy conservation for each microscopic state of the system in the MCE [129]. The presented results demonstrate that global conservation laws are rather important for the values of  $\omega_\pi$ ,  $\omega_K$ , and  $\rho_{K\pi}$ . In particular, the exact energy conservation strongly suppresses the fluctuations in the pion and kaon numbers and leads to  $\omega_K < 1$  and  $\omega_\pi < 1$  in the MCE ensemble, instead of  $\omega_K > 1$  and  $\omega_\pi > 1$  in the GCE and CE ensembles. The exact energy conservation changes also the  $\pi$ - $K$  correlation into an anticorrelation: instead of  $\rho_{K\pi} > 0$  in the GCE and CE ensembles one finds  $\rho_{K\pi} < 0$  in the MCE. The effects of global conservation laws and resonance decays are also seen for  $\rho_{Kp}$ ,  $\rho_{p\pi}$  and  $\omega_p$ .

As seen from Fig. Fig. 7.2 and Fig. 7.3 the HSD results for  $\omega_A$  and  $\rho_{AB}$  (denoted by the solid lines) are close to the CE and MCE results for low SPS energies. One may conclude that the influence of conservation laws is more stringent at low collision energies. The HSD values for  $\omega_A$  and  $\rho_{AB}$  increase, however, at high collision energies and a sizeable deviation of the HSD results from those in the MCE SM is observed with increasing energies for  $\sqrt{s_{NN}} > 200$  GeV. Similar behaviour has been observed earlier in Ref. [124] for the scaled variance of all charged hadrons.

A strong deviation of HSD from the SM with increasing energies is a consequence of non-equilibrium dynamics in the hadron-string model which is driven by the formation of heavy strings and their decay. Indeed, future experimental data on multiplicity fluctuations and correlations allow to shed more light on the equilibration pattern achieved in heavy-ion collisions.

We point out again that important aspects of the event-by-event fluctuations in nucleus-nucleus collisions are the dependence on the centrality selection and experimental acceptance. We accordingly discuss the role of these effects using

HSD results for the scaled variance  $\omega_\pi$  of the pion number fluctuations. In Fig. 7.4 the scaled variance  $\omega_\pi$  (calculated within HSD) for the full acceptance and for the experimental acceptance are shown in nucleus-nucleus collisions for zero impact parameter  $b = 0$  (see the next Section for details of the experimental acceptance). Introducing the probability  $q$  of pion experimental acceptance as the ratio of an average accepted to the total multiplicities,  $q = \langle N_\pi^{acc} \rangle / \langle N_\pi^{tot} \rangle$ , one finds:

$$\omega_\pi^{acc} = 1 - q + q \omega_\pi^{full} . \quad (7.30)$$

Eq. 7.30 connects the scaled variance  $\omega_\pi^{full}$  in the full  $4\pi$  space with  $\omega_\pi^{acc}$  defined for the experimental acceptance. The acceptance scaling (Eq. 7.30) assumes (see, e.g. Ref. [101]) an absence of particle correlations in momentum space. Fig. 7.4 demonstrates that the acceptance scaling (Eq. 7.30) underestimates the scaled variance  $\omega_\pi^{acc}$  at RHIC energies.

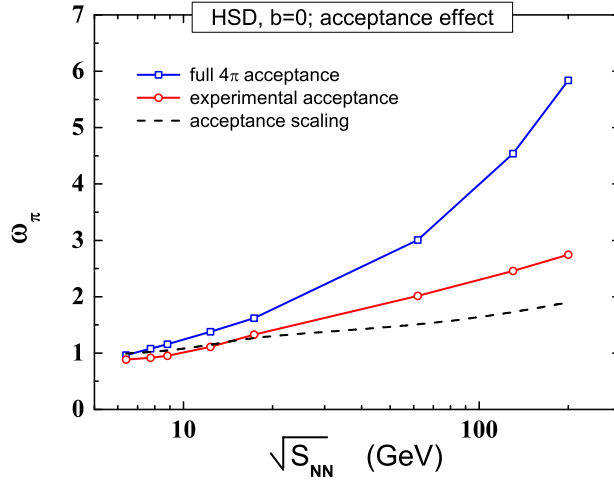


Figure 7.4: (Color online) The HSD results for  $\omega_\pi$  are presented for Pb+Pb (Au+Au) collisions with zero impact parameter ( $b = 0$ ) at different c.m. energies  $\sqrt{s_{NN}}$ . The upper solid line corresponds to the full  $4\pi$ -acceptance and the middle one to the experimental acceptance. The lower dashed line corresponds to the acceptance scaling (Eq. 7.30).

The samples of collision events selected experimentally are 3.5% of most central collision events in Pb+Pb collisions at the SPS energies and 5% in Au+Au collisions at RHIC energies. Fig. 7.5 presents the HSD results for  $\omega_\pi$  in these

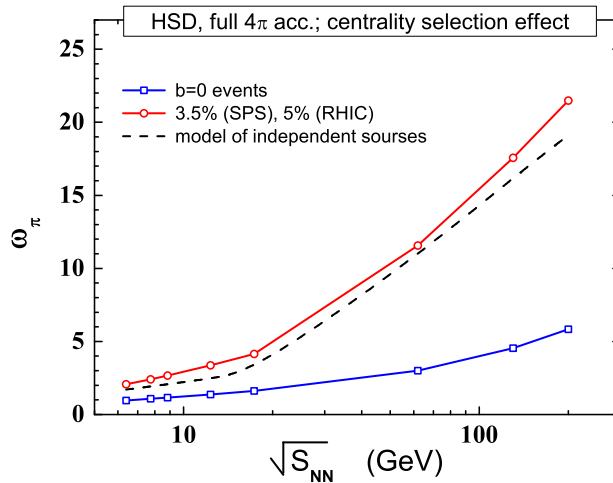


Figure 7.5: (Color online) The HSD results for  $\omega_\pi$  for Pb+Pb (Au+Au) collisions at different c.m. energies  $\sqrt{s_{NN}}$  within the full  $4\pi$ -acceptance. The lower solid line corresponds to zero impact parameter ( $b = 0$ ) and the upper one to the experimentally selected samples of collision events. The dashed line reflects the model of independent sources (Eq. 7.31).

samples of the most central events and their comparison with the HSD results at zero impact parameter. One finds much larger values of  $\omega_\pi$  in the centrality selected samples than for  $b = 0$ . The effect is especially strong at RHIC energies. This can be qualitatively understood within the model of independent sources:

$$\omega_\pi = \omega_\pi^s + n_\pi \omega_P, \quad (7.31)$$

where  $\omega_\pi^s$  is the scaled variance for pions produced by one source,  $\omega_P$  is the scaled variance for the fluctuations of nucleon participants, and  $n_\pi$  is the average pion multiplicity per participating nucleon which increases monotonously with collision energy. Collisions with zero impact parameter correspond to  $\omega_P \cong 0$ . Thus,  $\omega_\pi^s$  can be approximately taken as  $\omega_\pi$  at  $b = 0$ . The HSD results correspond approximately to  $\omega_P \cong 0.5$  for the 3.5% most central Pb+Pb collisions at SPS energies and  $\omega_P \cong 1$  for the 5% most central Au+Au collisions at RHIC energies. Please note that we used the restrictions on impact parameter  $b$  in the HSD calculations to form the samples of most central events. The results of the model of independent sources (Eq. 7.31) for  $\omega_\pi$  are shown by the dashed line in Fig. 7.5

and are close to the actual values of the HSD simulations for  $\omega_\pi$ .

### 7.3.2 $\sigma$ , $\sigma_{mix}$ , and $\sigma_{dyn}$ for $K/\pi$ ratio fluctuations

The fluctuation in the kaon to pion ratio is dominated by the fluctuations of kaons alone since the average multiplicity of kaons is about 10 times smaller than that of pions. Thus, the 1-st term in the r.h.s. of Eq. 7.29 gives the dominant contribution, and the 2-nd and 3-rd terms give only small corrections. The model calculations of Eq. 7.29 require, in addition to  $\omega_K$ ,  $\omega_\pi$ , and  $\rho_{K\pi}$  values, the knowledge of the average multiplicities  $\langle N_K \rangle$  and  $\langle N_\pi \rangle$ . For the HSD simulations (impact parameter  $b = 0$  in Pb+Pb collisions at SPS energies and Au+Au collisions at RHIC) the corresponding average multiplicities are presented in Table 7.1. To fix average multiplicities in the SM one needs to choose the system volume. For each collision energy the volume of the statistical system has been fixed in a way to obtain the same kaon average multiplicity in the SM as in the HSD calculations:  $\langle N_K \rangle_{stat} = \langle N_K \rangle_{HSD}$ . Recall that average multiplicities of kaons and pions are the same in all statistical ensembles. The SM volume in central Pb+PB (Au+Au) collisions is large enough and all statistical ensembles are thermodynamically equivalent for the average pion and kaon multiplicities, since these multiplicities are much larger than 1.

In Fig. 7.6 the values of  $\sigma$  (in percent) – calculated according to Eq. 7.29 and Eq. 7.17 – are presented, in the *left* and *right* panel, respectively, for the SM in different ensembles as well as for the HSD simulations. The first conclusion from Fig. 7.6 (*left*) is that all results for  $\sigma$  in the different models are rather similar. One observes a monotonic decrease of  $\sigma$  with collision energy. This is just because of an increase of the kaon and pion average multiplicities with collision energy. The mixed event fluctuations  $\sigma_{mix}$  in the model analysis are fully defined by these average multiplicities according to Eq. 7.17. The values of  $\sigma_{mix}$  are therefore the same in the different statistical ensembles. They are also very close to the HSD values because the statistical system volume has been defined to obtain the same kaon average multiplicities in the statistical model as in HSD at each collision energy. As seen from Fig. 7.6 (*right*) the requirement of  $\langle N_K \rangle_{stat} = \langle N_K \rangle_{HSD}$  leads to almost equal values of  $\sigma_{mix}$  in both HSD and the SM.

Differences between the statistical ensembles as well as between the statistical and HSD results become visible for other measures of  $K/\pi$  fluctuations, such as

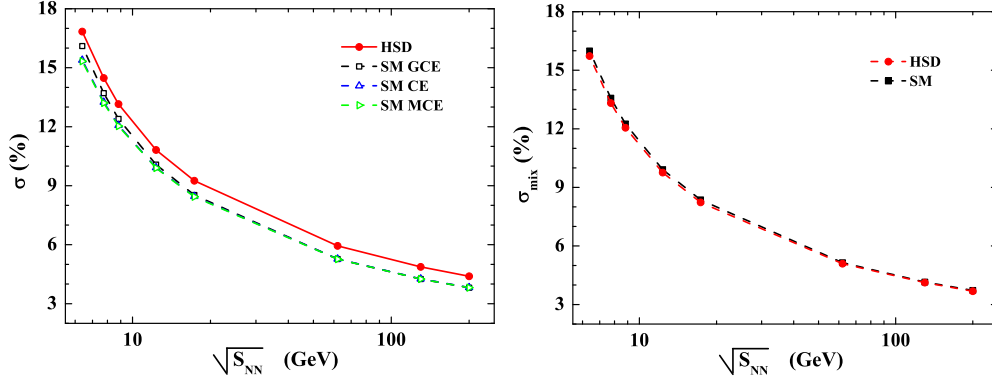


Figure 7.6: *Left*: The SM results in the GCE, CE, and MCE ensembles as well as the HSD results (impact parameter  $b = 0$ ) are presented for  $\sigma \cdot 100\%$  defined by Eq. 7.29 for Pb+Pb (Au+Au) collisions at different c.m. energies  $\sqrt{s_{NN}}$ . *Right*: The same as in the *left* panel, but for  $\sigma_{mix} \cdot 100\%$  in mixed events defined by Eq. 7.17,  $\sigma_{mix}^2 = 1/\langle N_K \rangle + 1/\langle N_\pi \rangle$ .

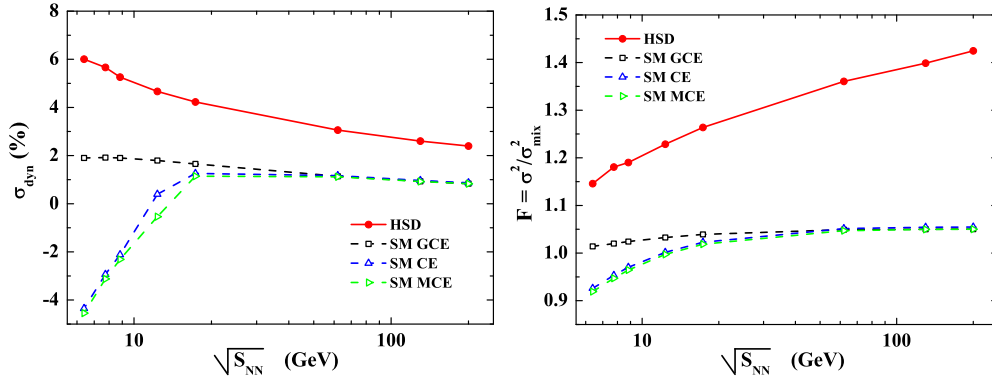


Figure 7.7: *Left*: The results for the  $K/\pi$  fluctuations at different c.m. energies  $\sqrt{s_{NN}}$  in the GCE, CE, and MCE ensembles as well as from HSD (impact parameter  $b = 0$ ) are presented for  $\sigma_{dyn} \cdot 100\%$  defined by Eq. 7.9). *Right*: The same as in the *left* panel but for  $F = \sigma^2 / \sigma_{mix}^2$ .

$\sigma_{dyn}$  defined by Eq. 7.9 and  $F = \sigma^2 / \sigma_{mix}^2$ . They are shown in Fig. 7.7, *left* and *right*, respectively. At small collision energies the CE and MCE results in Fig. 7.7 demonstrate negative values of  $\sigma_{dyn}$ , respectively  $F < 1$ . When the collision energy increases,  $\sigma_{dyn}$  in the CE and MCE ensembles becomes positive, i.e.  $F > 1$ . Moreover, the different statistical ensembles approach to the same values of  $\sigma_{dyn}$  and  $F$  at high collision energy. In the statistical model the values of  $\sigma$  and  $\sigma_{mix}$  approach to zero at high collision energies due to an increase of

the average multiplicities. The same trivial limit should be also valid for  $\sigma_{dyn}$  in the SM. In contrast, the measure  $F$  shows a non-trivial behavior at high energies: the SM gives  $F \cong 1.05$  in high energy limit. The HSD result for  $F$  demonstrates a monotonic increase with collision energy. An interesting feature of the SM is the approximately equal values of  $\sigma$  (and, thus,  $\sigma_{dyn}$  and  $F$ ) in the CE and MCE ensembles. From Fig. 7.2 and Fig. 7.3 one observes that both  $\omega_K$ ,  $\omega_\pi$  and  $\rho_{K\pi}$  are rather different in the CE and MCE. Thus, as discussed above, an exact energy conservation influences the particle scaled variances and correlations. These changes are, however, canceled out in the fluctuations of the kaon to pion ratio.

### 7.3.3 Volume Fluctuations

It has been mentioned in the literature (see, e.g., [147]) that the particle number ratio is independent of volume fluctuations since both multiplicities are proportional to the volume. In fact, the *average multiplicities*  $\langle N_K \rangle$  and  $\langle N_\pi \rangle$ , but not  $N_K$  and  $N_\pi$ , are proportional to the system volume. Let us consider the problem in the SM assuming the presence of volume fluctuations at fixed values of  $T$  and  $\mu_B$ . This assumption corresponds approximately to volume fluctuations in nucleus-nucleus collisions from different impact parameters in each collision event. Under these assumptions the SM values remain the same for any volume (if only this volume is large enough and the finite size corrections can be neglected). However, the average hadron multiplicities are proportional to the volume. Therefore, the SM result for  $\sigma^2$  reads,  $\sigma^2 = \sigma_0^2 V_0/V$ , where  $V_0$  is the average system volume, and  $\sigma_0^2$  is calculated for the average multiplicities corresponding to this average volume  $V_0$ . Expanding  $V_0/V = V_0/(V_0 + \delta V)$  in a series of  $\delta V/V_0$ , one finds to second order in  $\delta V/V_0$ ,

$$\sigma^2 \cong \sigma_0^2 \left[ 1 + \frac{\langle (\delta V)^2 \rangle}{V_0^2} \right], \quad (7.32)$$

where

$$\langle (\delta V)^2 \rangle = \int dV (V - V_0)^2 W(V) \quad (7.33)$$

corresponds to averaging over the volume distribution function  $W(V)$  which describes the volume fluctuations. As clearly seen from Eq. 7.32 the volume fluctuations influence, of course, the  $K/\pi$  particle number fluctuations and make them larger. Comparing the  $K/\pi$  particle number fluctuations in, e.g., 1% of most central nucleus-nucleus collisions with those in, e.g., 10% one should take into account two effects. First, in the 10% sample the average volume  $V_0$  is smaller than that in 1% sample and, thus,  $\sigma_0^2$  in Eq. 7.32 is larger. Second, the volume fluctuations (Eq. 7.33) in the 10% sample is larger, and this gives an additional contribution to  $\sigma^2$  according to Eq. 7.32.

One may also consider volume fluctuations at fixed energy and conserved charges (see, e.g., Ref. [160]). In this case the connection between the average multiplicity and the volume becomes more complicated. The volume fluctuation within the MCE ensemble can strongly affect the fluctuations in the particle number ratios. This possibility will be discussed in more detail in a forthcoming study.

## 7.4 Excitation function for the ratio fluctuations: Comparison with data

A comparison of the SM results for fluctuations in different ensembles with the data looks problematic at present; the same is true for most other theoretical models. This is because of difficulties in implementing the experimental acceptance and centrality selection which, however, can be taken into account in the transport approach. In order to compare the HSD calculations with the measured data, the experimental cuts are applied for the simulated set of HSD events. In Fig. 7.8 the HSD results of  $\sigma_{dyn}$  for the  $K/\pi$ ,  $p/\pi$  and  $K/p$  ratios are shown in comparison with the experimental data by the NA49 Collaboration at the SPS [144] and the preliminary data of the STAR Collaboration at RHIC [145, 146, 161, 162]. The available results of UrQMD calculations (from Refs. [144, 150, 163]) are also shown by the dashed lines.

For the SPS energies we use the NA49 acceptance tables from Ref. [144]. For the RHIC energies we use the following cuts: in pseudorapidity,  $|\eta| < 1$ , and in transverse momentum,  $0.2 < p_T < 0.6$  GeV/c for kaons and pions and  $0.4 < p_T < 1$  GeV/c for protons [145, 146, 161, 162]. We note also, that HSD results



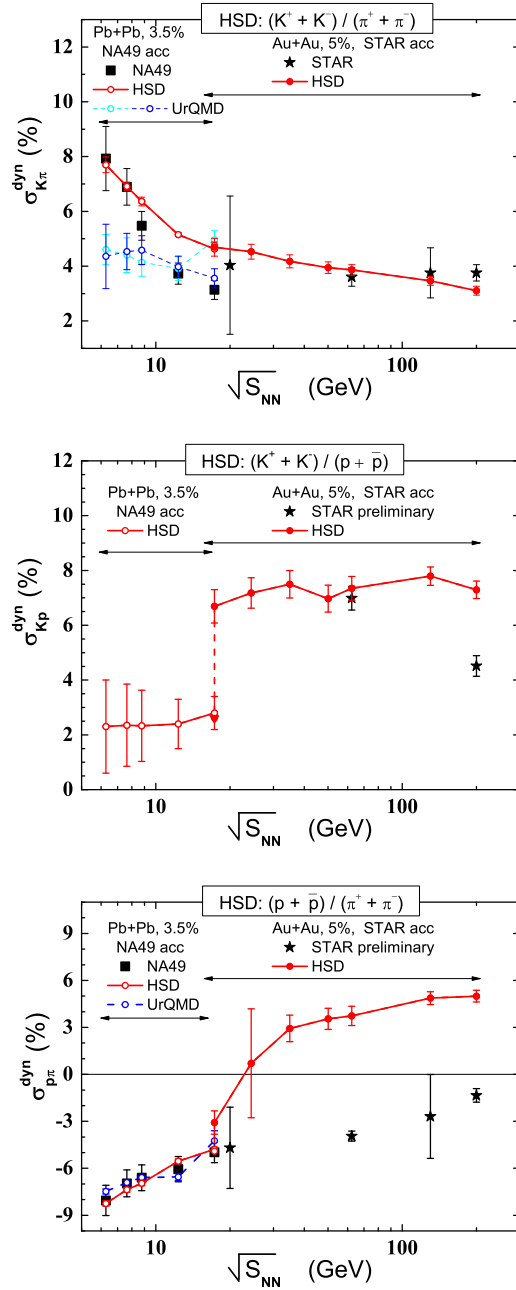


Figure 7.8: The HSD results for the excitation function in  $\sigma_{dyn}$  for the  $K/\pi$ ,  $K/p$ ,  $p/\pi$  within the experimental acceptance (solid line) in comparison to the experimental data measured by the NA49 Collaboration at SPS [144] and by the STAR Collaboration at RHIC [145, 146, 161, 162]. The UrQMD calculations are shown by dotted lines.

presented in Fig. 7.8 correspond to the centrality selection as in the experiment: the NA49 data correspond to the 3.5% most central collisions selected via veto calorimeter, whereas in the STAR experiment the 5% most central events with the highest multiplicities in the pseudorapidity range  $|\eta| < 0.5$  have been selected.

One sees that the UrQMD model gives practically a constant  $\sigma_{dyn}^{K\pi}$ , which is by about 40% smaller than the results from HSD at the lowest SPS energy. This difference between the two transport models may be probably attributed to different realizations of the string and resonance dynamics in HSD and UrQMD: in UrQMD the strings decay first to heavy baryonic and mesonic resonances which only later on decay to ‘light’ hadrons such as kaons and pions. In HSD the strings dominantly decay directly to ‘light’ hadrons (from the pseudoscalar meson octet) or the vector mesons  $\rho$ ,  $\omega$  and  $K^*$  (or the baryon octet and decouplet in case of baryon number  $\pm 1$ ). Such a ‘non-equilibrated’ string dynamics may lead to stronger fluctuations of the  $K/\pi$  ratio. Note that all differences between SM and transport models, as well as between different versions of the transport models, become clearly seen at the smallest bombarding energies. This is only because of using  $\sigma_{dyn}$  as a measure of the  $K/\pi$  ratio fluctuations. If one uses  $F = \sigma^2/\sigma_{mix}^2$  as a measure of the  $K/\pi$  fluctuations the conclusion will be opposite: as Fig. 7.7 (right) demonstrates the difference between the SM and HSD predictions measured in  $F$  would increase with collision energy.

At the SPS energies the HSD simulations lead to negative values of  $\sigma_{dyn}$  for the proton to pion ratio. This is in agreement with the NA49 data in Pb+Pb collisions. On the other hand HSD gives large positive values of  $\sigma_{dyn}^{p\pi}$  at RHIC energies which strongly overestimate the preliminary STAR data for Au+Au collisions [161]. For  $\sigma_{dyn}^{Kp}$  only preliminary STAR data in Au+Au collisions are available [162] which demonstrate a qualitative agreement with the HSD results (Fig. 7.8). The HSD results for  $\sigma_{dyn}^{Kp}$  show a weak energy dependence in both SPS and RHIC energy regions. A peculiar feature is, however, a strong ‘jump’ between the SPS and RHIC values, seen in the middle panel of Fig. 7.8, in the HSD calculations which is caused by the different acceptances in the SPS and RHIC measurements.

The influence of the experimental acceptance is clearly seen at 160 A GeV where a switch from the NA49 to the STAR acceptance leads to the jump in  $\sigma_{dyn}^{Kp}$  by 3% - middle panel of Fig. 7.8. On the other hand, our calculations for Pb+Pb (3.5% central) and for Au+Au (5% central) collisions - performed within the

NA49 acceptance for both cases at 160 A GeV - shows a very weak sensitivity of  $\sigma_{dyn}^{Kp}$  on the actual choice of the collision system and centrality – cf. the coincident open circle and triangle at 160 A GeV in the middle panel of Fig. 7.8.

## 7.5 Summary of Chapter 7

The event-by-event multiplicity fluctuations of pions, kaons, protons as well as their correlations and ratio fluctuations in central Au+Au (or Pb+Pb) collisions from low SPS up to top RHIC energies have been studied within the HSD transport approach and in the statistical hadron-resonance gas model for different statistical ensembles – the grand canonical ensemble (GCE), canonical ensemble (CE), and micro-canonical ensemble (MCE). The substantial differences in the HSD and statistical model results for the scaled variances  $\omega_A$  (Fig. 7.2) and the correlation parameters  $\rho_{AB}$  (Fig. 7.3) has been obtained. The HSD results at SPS energies are close to those in the CE and MCE statistical model. This indicates a dominant role of resonance decays and global conservation laws for low energy nucleus-nucleus collisions. On the other hand, substantial differences in HSD and statistical model results have been observed at RHIC energies which can be attributed to non-equilibrium dynamical effects in the HSD simulations. These quantities may serve as good observables to probe the amount of equilibration achieved in central nucleus-nucleus collisions.

On the other hand, it has been found that the observable  $\sigma_{dyn}$ , which characterizes ratio fluctuations, appears to be rather sensitive to the details of the model at low collision energies. The CE and MCE results in Fig. 7.7 demonstrate negative values of  $\sigma_{dyn}^{K\pi}$ , while the GCE gives approximately a constant positive value of  $\sigma_{dyn}^{K\pi}$ . The HSD results correspond to larger values of  $\sigma_{dyn}^{K\pi}$  than those in the GCE statistical model. They even show an increase at the lowest SPS energies.

It has been found that the HSD model can qualitatively reproduce the measured excitation function for the  $K/\pi$  ratio fluctuations in central Au+Au (or Pb+Pb) collisions from low SPS up to top RHIC energies. Accounting for the experimental acceptance as well as the centrality selection has a relatively small influence on  $\sigma_{dyn}$  and does not change the shape of the  $\sigma_{dyn}$  excitation function.

The HSD results for  $\sigma_{dyn}^{p\pi}$  appear to be close to the NA49 data at the SPS.

The data for  $\sigma_{dyn}^{Kp}$  in Pb+Pb collisions at the SPS energies will be available soon and allow for further insight. A comparison of the HSD results with preliminary STAR data in Au+Au collisions at RHIC energies are not fully conclusive:  $\sigma_{dyn}$  from HSD calculations is approximately in agreement with data [162] for the kaon to proton ratio, but overestimate the experimental results [161] for the proton to pion ratio. New data on event-by-event fluctuations in Au+Au at RHIC energies will help to clarify the situation.

## Chapter 8

# Forward-backward correlations in nucleus-nucleus collisions: baseline contributions from geometrical fluctuations

Correlations of particles between different regions of rapidity have for a long time been considered to be a signature of new physics. A shortening in the correlation length in rapidity has been thought to signal a transition to a quark-gluon plasma [164, 165]. Conversely, the appearance of long-range correlations has been associated with the onset of the percolation limit, also linked to the QCD phase transition [166, 167]. Recently, the correlations across a large distance in rapidity have also been suggested to arise from a color glass condensate [168, 169]. The observation of such correlations in A+A collisions at RHIC energies by the STAR Collaboration [170, 171] has therefore elicited a lot of theoretical interest.

The purpose of this Chapter is to identify some *baseline* contributions to the experimentally observed correlations, contributions that do not depend on new physics [172]. Two models that incorporate event-by-event fluctuations in initial conditions have been used to illustrate the effect of these contributions: the HSD transport model and a ‘toy’ wounded nucleon model. The HSD results are an essential element of the thesis, whereas the results of the ‘toy’ wounded nucleon model, obtained by M. Hauer, are presented for comparison. Based on such a comparison one can argue that a study of the dependence of correlations on the

centrality bin definition as well as the bin size may distinguish between ‘trivial’ correlations and correlations arising from ‘new physics’.

## 8.1 Definition of Observables

The statistical properties of a particular sample of events can be characterized by a set of moments or cumulants of some observable. These properties depend upon a set of criteria which are used to select this sample. Applied to the context of heavy-ion collisions this translates to the construction of centrality bins of collision events from minimum-bias data. The charged hadron multiplicities  $N_A$  and  $N_B$  will be considered in two symmetric intervals  $\Delta\eta$  of pseudo-rapidity. After construction of the centrality bins, one can calculate the moments of a resulting distribution  $P_c^{\eta_{gap}}(N_A, N_B; \Delta\eta)$ :

$$\langle N_A^k \cdot N_B^l \rangle_c^{\eta_{gap}} \equiv \sum_{N_A, N_B} N_A^k N_B^l P_c^{\eta_{gap}}(N_A, N_B; \Delta\eta) . \quad (8.1)$$

In [Eq. 8.1](#) the subscript  $c$  denotes a particular centrality bin, while the superscript  $\eta_{gap}$  denotes the separation of two symmetric intervals  $\Delta\eta$  in pseudo-rapidity space where particle multiplicities  $N_A$  and  $N_B$  are measured. The correlation coefficient<sup>1</sup> is defined by

$$\rho \equiv \frac{\langle \Delta N_A \cdot \Delta N_B \rangle_c^{\eta_{gap}}}{\sqrt{\langle (\Delta N_A)^2 \rangle_c^{\eta_{gap}} \langle (\Delta N_B)^2 \rangle_c^{\eta_{gap}}}} \quad (8.2)$$

and measures how strongly multiplicities  $N_A$  and  $N_B$  – in a given centrality bin  $c$  for pseudo-rapidity separation  $\eta_{gap}$  – are correlated. In [Eq. 8.2](#),  $\Delta N \equiv N - \langle N \rangle_c^{\eta_{gap}}$  and  $\langle (\Delta N_A)^2 \rangle_c^{\eta_{gap}} = \langle (\Delta N_B)^2 \rangle_c^{\eta_{gap}}$  for symmetric intervals.

The recent preliminary data on the forward-backward correlation coefficient ([Eq. 8.2](#)) of charged particles by the STAR Collaboration [[170](#), [171](#)] exhibit two striking features: a) an approximate independence on the width of the pseudo-rapidity gap  $\eta_{gap}$ , b) a strong increase of  $\rho$  with centrality.

---

<sup>1</sup> A different notation from Refs. [[170](#), [171](#)] is used denoting the correlation coefficient as  $\rho$  and reserve the letter  $b$  for the impact parameter.

## 8.2 Glauber Monte Carlo Model

The PHOBOS Glauber Monte Carlo code [173] coupled to a ‘toy’ wounded nucleon model is used here, referred to as GMC. The aim of this model is to emphasize two crucial aspects: 1) an averaging over different system sizes within one centrality bin introduces correlations; 2) the strength of these correlations depend on the criteria used for the centrality definition and on the size of the centrality bins.

Employing the Glauber code the distribution of the number of participating nucleons,  $N_P$ , is modeled in each nucleus-nucleus collision for given impact parameter  $b$  (cf. Fig. 8.1, left). This is done for Au+Au with standard Wood-Saxon profile and the nucleon-nucleon cross section of  $\sigma_{NN} = 42$  mb. The ‘event’ construction proceeds then in a two-step process. Firstly, the total number of charged particles is randomly generated:

$$N_{ch} = \sum_{i=1}^{N_P} n_{ch}^i, \quad (8.3)$$

where the number of charged particles  $n_{ch}^i$  per participating nucleon are generated by independently sampling a Poisson distribution with given mean value  $\bar{n}_{ch} = 10$ . Secondly, these charged particles are randomly distributed according to a Gaussian in pseudo-rapidity space:

$$\frac{dN_{ch}}{d\eta} \propto \exp\left(-\frac{\eta^2}{2\sigma_\eta}\right), \quad (8.4)$$

where  $\sigma_\eta = 3$  defines the width of the pseudo-rapidity distribution. Hence, in each single event there are no correlations between the momenta of any two particles. Note that numerical values of  $\bar{n}_{ch}$  and  $\sigma_\eta$  are fixed in a way to have a rough correspondence with the data on charged particle production at  $\sqrt{s} = 200$  GeV.

Fig. 8.1 (left) shows the GMC event distribution in the  $(b, N_P)$ -plane. For each of these events we randomly generate the number of charge particles  $N_{ch}$  and their  $\eta$ -distribution according to Eq. 8.3 and Eq. 8.4, respectively. The construction of centrality classes can now be done in several ways. The following criteria are chosen: via impact parameter  $b$ , via the number of participating (wounded) nucleons  $N_P$ , and via the charged particle multiplicity  $N_{ch}^{ref}$  in the midrapidity

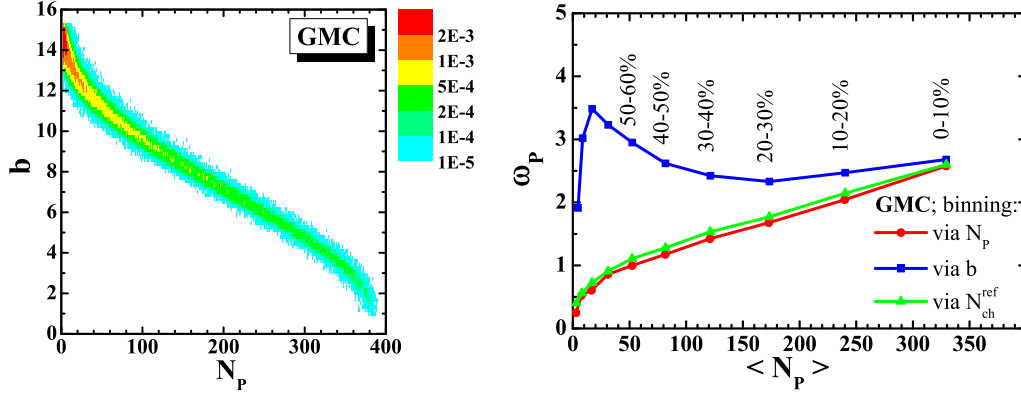


Figure 8.1: *Left*: The histogram shows the distribution of events with a fixed number of participating nucleons  $N_P$  and fixed impact parameter  $b$  in Au+Au collisions at  $\sqrt{s} = 200$  GeV. *Right*: The scaled variance  $\omega_P$  of the distribution of participating nucleons in 10% bins as defined via  $b$ ,  $N_P$ , and  $N_{ch}^{ref}$ .

window  $|\eta| < 1$ .

In the case of choosing the number of participating nucleons  $N_P$  for centrality definition, one takes vertical cuts in Fig. 8.1 (*left*), while choosing the impact parameter  $b$ , one takes horizontal cuts. Hence, depending on the centrality definition, one may assign a particular event (characterized by  $N_P$  and  $b$ ) to two different centrality bins.

Fig. 8.1 (*right*) shows the resulting scaled variance  $\omega_P$ ,

$$\omega_P \equiv \frac{\langle (\Delta N_P)^2 \rangle_c}{\langle N_P \rangle_c}, \quad (8.5)$$

of the underlying distribution of the number of participating nucleons  $N_P$  in each centrality bin. Using the centrality selection via impact parameter  $b$ , which is only the theoretically available trigger, one generally obtains a rather wide distribution of participating nucleons in each bin. The lines for centrality selections via  $N_{ch}^{ref}$  and via  $N_P$  are similar due to the event construction by Eq. 8.3 and Eq. 8.4. An interesting feature of the GMC model is that  $\omega_P$  increases with centrality for the selection via  $N_P$ . This conclusion of the GMC model seems to have a rather general origin.

The sensitivity of the forward-backward correlation signal as a function of the separation  $\eta_{gap}$  of two narrow intervals ( $\Delta\eta = 0.2$ ) on the centrality definition is



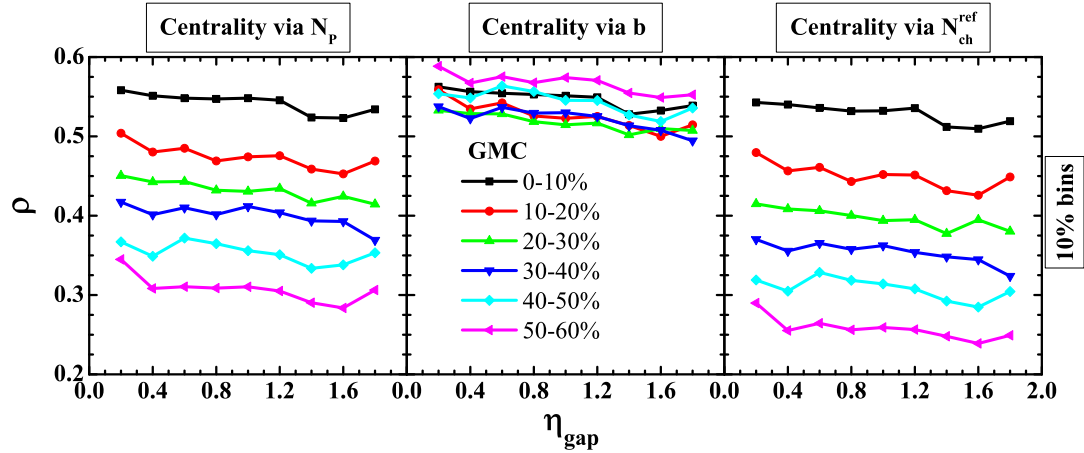


Figure 8.2: The forward-backward correlation coefficient  $\rho$  for 10% centrality classes defined via  $N_P$  (*left*), via the impact parameter  $b$  (*middle*), and via the multiplicity in the central rapidity region  $N_{ch}^{ref}$  (*right*).

investigated now. This is done for the 10% centrality defined via  $N_P$ , via  $b$ , and via  $N_{ch}^{ref}$ . The results are shown in Fig. 8.2. In the GMC one can identify the number of participating nucleons  $N_P$  with the system size, and  $\omega_P$  as the measure for system size fluctuations. Having a large system – as measured by  $N_P$  – implies a large number of charged particles  $N_{ch}$ . In GMC they are distributed independently in pseudo-rapidity space. Conversely, an event with small  $N_P$  contains only few charged particles. By grouping the collision events into 10% centrality bins one finds rather large  $N_P$ -fluctuations in one specific bin. The averaging over different states in the centrality bin introduces correlations between any two regions of pseudo-rapidity. Small systems will have few particles ‘on the left’ and few particles ‘on the right’ with respect to midrapidity. Large systems will have many particles ‘on the left’ and many particles ‘on the right’. But this just means a non-zero forward-backward correlation. From the definition (Eq. 8.2) one finds a positive correlation coefficient  $\rho$  due to averaging over system sizes.

Note that centrality selections via  $N_P$  and via  $N_{ch}$  give essentially the same results for  $\rho$  in the GMC (cf. *left* and *right* panels of Fig. 8.2). Using the impact parameter  $b$  for the centrality definition generates centrality bins with almost constant  $\rho$  as seen in Fig. 8.2 (*middle*). This is due to a rather flat dependence of  $\omega_P$  on the centrality defined via  $b$  as shown in Fig. 8.1 (*right*). In the GMC model the apparent ordering of  $\rho$  values with respect to centrality bins originates

from the width of the underlying distribution in the number of wounded nucleons in each bin, i.e. from the values of  $\omega_P$ .

The measured and apparently strong forward-backward correlations can be accounted for by a ‘toy’ model such as the GMC, provided it produces particles over the whole rapidity range and includes strong enough event-by-event fluctuations of  $N_P$ . The next section will show that an introduction of dynamics and hadron re-interactions within HSD does not alter these conclusions significantly.

### 8.3 HSD Transport Model Simulations

A physically more reasonable scenario which, however, also does not include any ‘new physics’ (such as color glass condensate, quark-gluon plasma, etc.) can be obtained in the Hadron-String-Dynamics (HSD) transport approach (see [Chapter 2](#) for the details).

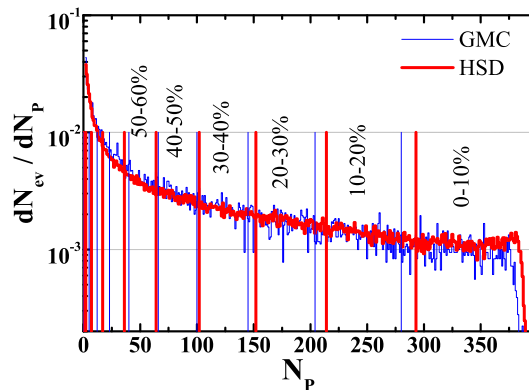


Figure 8.3: The HSD and GMC distributions of events over  $N_P$ . The vertical lines indicate 10% centrality bins.

As before within the GMC, the HSD events are generated according to a uniform distribution,  $N_{ev}(b) \sim b$ . The resulting distribution of events in the  $(N_P, b)$ -plane is similar to the GMC result depicted in [Fig. 8.1 \(left\)](#).

[Fig. 8.3](#) shows the distribution of events with fixed  $N_P$  for both models. The vertical lines indicate 10% centrality bins as defined by the  $N_P$  distribution. Note, that the peripheral part of the distribution determines also the centrality binning and the real bin widths. This is crucial for most central collisions where the number of events is small. Slight uncertainties in the peripheral ‘tail’ of the

distribution leads to large errors in the sizes of most central bins and hence to large changes in results for fluctuations and correlations.

In contrast to the STAR data, the charged particle reference multiplicity  $N_{ch}^{ref}$  in the same pseudo-rapidity range  $|\eta| < 1$  for all values of  $\eta_{gap}$  is used in the HSD simulations. This procedure introduces a systematic bias, since the pseudo-rapidity regions for the measured multiplicity in a small  $\Delta\eta$  window (signal) and for the reference multiplicity partially overlap. This bias, however, is small and does not affect any of the conclusions.

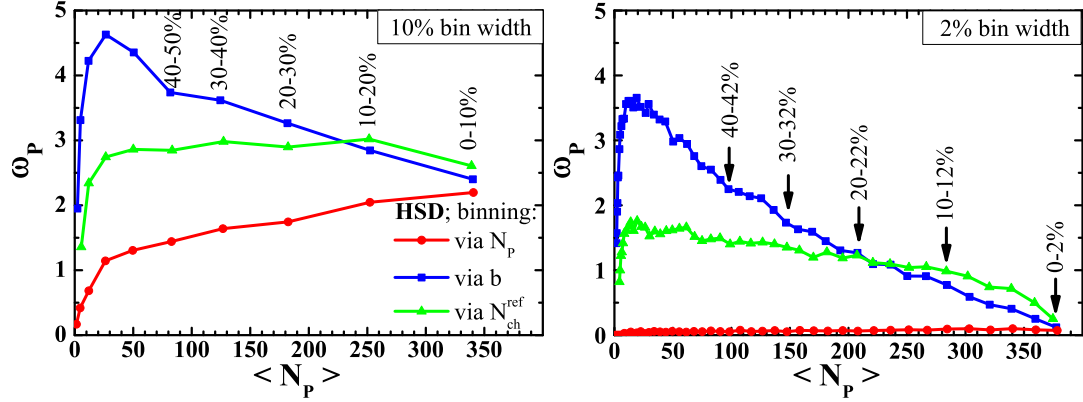


Figure 8.4: The HSD results for the fluctuations  $\omega_{part}$  as a function of the mean value  $\langle N_P \rangle$  of the participating nucleons within bins as defined via  $b$ ,  $N_P$ , and  $N_{ch}^{ref}$ . The *left* panel corresponds to a 10% and the *right* to a 2% bin width.

Fig. 8.4 shows the scaled variance of the underlying  $N_P$  distribution for 10% (*left*) and 2% (*right*) centrality bins defined via different centrality triggers within HSD. The results for 10% bins can be compared with the scaled variance  $\omega_P$  in the GMC model in Fig. 8.1 (*right*). Fluctuations of the number of participants, as well as their average values, are similar in both HSD and GMC models when the centrality bins are defined via  $N_P$ . These quantities are completely defined by the  $N_P$  distribution, which is similar in both models (Fig. 8.3). Binning via the impact parameter  $b$  in HSD, as well as in GMC, gives decreasing fluctuations in the participant number with increasing collision centrality. The results for 10% bins defined via the reference multiplicity are rather different in the GMC and HSD models. In GMC the charged multiplicity distribution is implemented according to Eq. 8.3 and Eq. 8.4. Hence, the results obtained by binning via the reference multiplicity follow the line obtained by binning via  $N_P$ . In contrast to

the GMC, in the HSD simulations the average number of charged particles  $\bar{n}_{ch}$  per participating nucleon is not a constant, but increases with  $N_P$ . Additionally, the shape of rapidity distribution is also different in different centrality bins. These two effects lead to different values of  $\omega_P$  in the centrality bins defined via  $N_{ch}^{ref}$  in the GMC and HSD models.

One comment is appropriate here. It was argued in Ref. [139] that any centrality selection in nucleus-nucleus collisions is equivalent to the geometrical one via impact parameter  $b$ . This result was obtained in Ref. [139] by neglecting the fluctuations at a given value of  $b$ . Thus, different centrality selection criterions give indeed the same *average* values of physical observables. However, they may lead to rather different fluctuations of these observables in the corresponding centrality bins, cf. equal values of  $\langle N_P \rangle$  and different values of  $\omega_P$  for different centrality selections presented in Fig. 8.4.

When considering smaller centrality bins (2% in Fig. 8.4, *right*) the fluctuations in the participant number become smaller and more strongly dependent on the definition of the binning.

Fig. 8.5 summarizes the dependence of forward-backward correlation coefficient  $\rho$  as a function of  $\eta_{gap}$  on the bin size and centrality definition within the HSD model. The dependence of  $\rho$  on  $\eta_{gap}$  is almost flat, reflecting a boost-invariant distribution of particles created by string breaking in the HSD. The *right top* panel of Fig. 8.5 demonstrates also a comparison of the HSD results with the STAR data [170, 171]. One observes that the HSD results exceed systematically the STAR data. However, the main qualitative features of the STAR data – an approximate independence of the width of the pseudo-rapidity gap  $\eta_{gap}$  and a strong increase of  $\rho$  with centrality – are fully reproduced by the HSD simulations.

The correlation coefficient  $\rho$  largely follows the trend of the participant number fluctuations  $\omega_P$  as a function of centrality. The actual results, however, strongly depend on the way of defining the centrality bins. For instance, choosing smaller centrality bins leads to weaker forward-backward correlations, a less pronounced centrality dependence, and a stronger dependence on the bin definition. The physical origin for this is demonstrated in Fig. 8.6. As the bin size becomes comparable to the width of the correlation band between  $N_P$  and  $N_{ch}^{ref}$ , the systematic deviations of different centrality selections become dominant: the same centrality bins defined by  $N_P$  and by  $N_{ch}^{ref}$  contain different events and may give

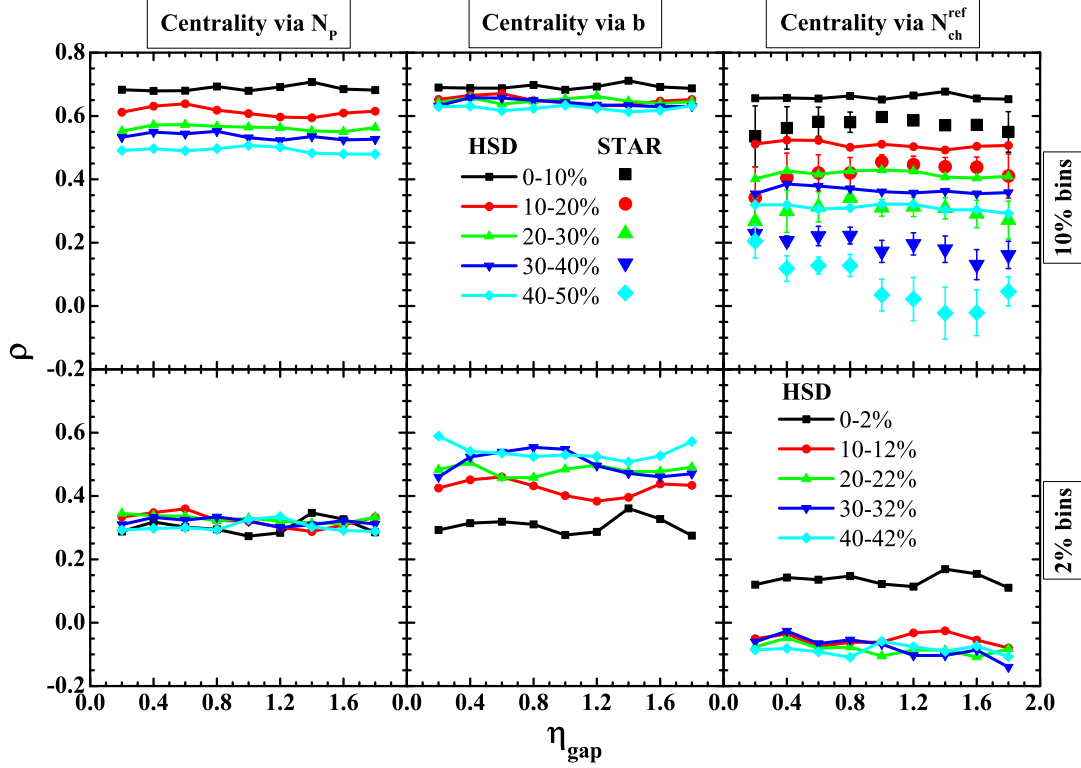


Figure 8.5: The HSD results for the forward-backward correlation coefficient  $\rho$  for 10% (*top*) and 2% (*bottom*) centrality classes defined via  $N_P$  (*left*), via impact parameter  $b$  (*center*), and via the reference multiplicity  $N_{ch}^{ref}$  (*right*). The symbols in the *top right* panel present the STAR data in Au+Au collisions at  $\sqrt{s} = 200$  GeV [170, 171].

rather different values for the forward-backward correlation coefficient  $\rho$ .

It should be underlined that these properties are specific to the *geometric* nature of the correlations analyzed here. If the observed fluctuations are of *dynamical* origin (for example, arising from the quantum fluctuations of coherent fields created in the first  $fm/c$  of the system's lifetime as in Refs. [168, 169]), there are no evident reasons why they should strongly depend on the centrality bin definitions and bin sizes. Thus, the experimental analysis for different bin sizes and centrality definitions – as performed here – may serve as a diagnostic tool for an origin of the observed correlations. A strong specific dependence of the correlations on bin size and centrality definition would signify their geometrical origin!

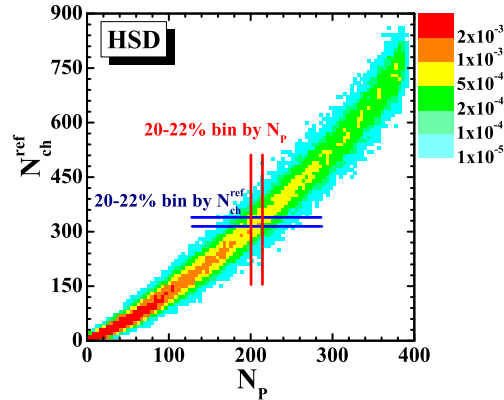


Figure 8.6: The histogram shows the distribution of HSD events with fixed number of participating nucleons  $N_P$  and fixed reference charge particle multiplicity  $N_{ch}^{ref}$ . The same centrality class (20-22% as an example) defined in various ways contains different events.

## 8.4 Summary of Chapter 8

In conclusion this Chapter presents a study of the system size event-by-event fluctuations causing the rapidity forward-backward correlations in relativistic heavy-ion collisions. The analysis has been based on two independent models – the microscopic HSD transport approach and a ‘toy’ wounded nucleon model realized as a Glauber Monte Carlo event generator. It has been shown that strong forward-backward correlations arise due to an averaging over many different events that belong to one 10% centrality bin. In contrast to average multiplicities, the resulting fluctuations and correlations depend strongly on the specific centrality trigger. For example, the centrality selection via impact parameter  $b$  used in most theoretical calculations and via  $N_{ch}^{ref}$  used experimentally lead to rather different values of  $\omega_P$  and  $\rho$  and their dependence on centrality.

In the HSD model the  $N_P$  distribution is similar to that in the GMC. It includes also the fluctuations in the number of strings and the fluctuations in the number of hadrons from individual string fragmentation. The HSD simulations reveal strong forward-backward correlations and reproduce the main qualitative features of the STAR data in A+A collisions at RHIC energies [168, 169].

The forward-backward correlations can be studied experimentally for smaller size centrality bins defined by  $N_{ch}^{ref}$ . When the size of the bins decreases, the

---

contribution of ‘geometrical’ fluctuations should lead to weaker forward-backward correlations and to a less pronounced centrality dependence. Note, that the ‘geometrical’ fluctuations discussed here are in fact present in all dynamical models of nucleus-nucleus collisions. Thus, they should be carefully accounted before any discussion of new physical effects is addressed. A future experimental analysis – in the direction examined here – should clarify whether the observed correlations by the STAR Collaboration at RHIC contain really additional contributions from ‘new physics’.

## Chapter 9

# Summary and Discussion

It has been argued in the introduction ([Chapter 1](#)) that fluctuations may be considered as a probe for the phase transition and the critical point in the phase diagram. The current thesis has been devoted to a systematic study of fluctuations and correlations in heavy-ion collisions within the HSD transport approach reviewed in [Chapter 2](#). This is a powerful tool to study nucleus-nucleus collisions and allows to completely simulate experimental collisions on an event-by-event basis. Thus, the transport model has been used to study fluctuations and correlations including the influence of experimental acceptance as well as centrality, system size and collision energy. The comparison to experimental data can separate the effects induced by a phase transition since there is no phase transition in the HSD version used here.

The centrality dependence of multiplicity fluctuations has been studied in [Chapter 3](#). Different centrality selections have been performed in the analysis in correspondence to the experimental situation. For the fix-target experiment NA49 events with fixed numbers of the projectile participants,  $N_P^{proj}$ , have been studied while in the collider experiment PHENIX centrality classes of events have been defined by the multiplicity in certain phase space region. A decrease of participant fluctuations (and thus volume fluctuations) in more central collisions for both experiments has been obtained.

The HSD transport model results for the scaled variances of negative, positive, and all charged hadrons in Pb+Pb minimum bias simulations at 158 AGeV have been presented in [Chapter 4](#). Large fluctuations of the target participants (obtained in HSD for semi-peripheral collisions) may lead to the nontrivial be-



havior in the multiplicity fluctuations seen in the data. As it has been shown in [Chapter 4](#) the fluctuations in the number of target participants also strongly influence the baryon number and charged multiplicity fluctuations. The asymmetry between the projectile and target participants – introduced in the data samples by the trigger condition – can be used to explore different dynamics of nucleus-nucleus collisions by measuring the final multiplicity fluctuations as a function of rapidity. This analysis reveals that the NA49 data indicate a rather strong mixing of the longitudinal flows of the projectile and target hadron production sources. The HSD model shows only a small mixing in the initial baryon flow. The higher level of mixing – seen in the data – may be explained by additional strong parton-parton interactions.

The results for multiplicity fluctuations in Au+Au collisions at  $\sqrt{s} = 200$  GeV – based on the wounded nucleon model – have been also presented and compared to the preliminary PHENIX data. The HSD transport model has been used to calculate the scaled variance of participant number fluctuations and the number of hadrons per nucleon in different centrality classes. This combined picture – both qualitative and quantitative – reproduces the experimental results. One can conclude that the centrality dependence of the fluctuations seen in the present PHENIX data are the consequences of participant number fluctuations. To avoid a dominance of the participant number fluctuations one needs to analyze most central collisions with a much more rigid centrality selection!

The HSD model calculations for the charge fluctuations  $\Delta\Phi_q$  show a good agreement with the NA49 data at SPS energies. Thus, this observable is dominated by the final stage dynamics, i.e. the hadronization phase and the resonance decays, and rather insensitive to the initial QGP dynamics.

The excitation function of multiplicity fluctuations in central A+A collisions has been studied in [Chapter 5](#). HSD predicts an increase of the scaled variances of multiplicities with collision energy. The scaled variances – calculated within the statistical HG model along the chemical freeze-out line – approach finite values at high collision energy. At the top RHIC energy  $\sqrt{s_{NN}} = 200$  GeV the HSD values for the multiplicity fluctuations are already about 10 times larger than the corresponding values from the statistical model. However, a comparison with preliminary NA49 data of very central,  $\leq 1\%$ , Pb+Pb collisions in the SPS energy range does not distinguish between the HSD and statistical HG results because both results are not too much different from each other and because the

small experimental acceptance makes the difference almost invisible. New measurements of multiplicity fluctuations for samples of very central A+A collisions with large acceptance at both SPS and RHIC energies are needed to allow for a proper determination of the underlying dynamics.

**Chapter 6** has been devoted to transport model calculations of multiplicity fluctuations in nucleus-nucleus collisions as a function of colliding energy and system size. This study is in full correspondence to the experimental program of the NA61 Collaboration at the SPS. Central C+C, S+S, In+In, and Pb+Pb nuclear collisions at  $E_{lab} = 10, 20, 30, 40, 80, 158$  AGeV have been investigated. The influence of participant number fluctuations on hadron multiplicity fluctuations has been emphasized and studied in detail. It has been argued again that to make these ‘trivial’ fluctuations smaller, one has to consider the most central collisions. It has been also determined that different centrality selections are not equivalent to each other. This statement has been illustrated by the  $b = 0$  selection criterium. For light nuclei even these ‘absolutely central’ geometrical collisions lead to rather large fluctuations in the number of participants, essentially larger than in the 1% most central collisions selected by the largest values of the projectile participants  $N_P^{proj}$ .

It has to be stressed again, that the HSD (as well as the UrQMD) transport approach do not include explicitly a phase transition to the QGP. The expected enhanced fluctuations - attributed to the critical point and phase transition - can be observed experimentally on top of a monotonic and smooth ‘hadronic background’. These findings should be helpful for the optimal choice of collision systems and collision energies for the experimental search of the QCD critical point.

The event-by-event multiplicity fluctuations of pions, kaons, protons and their ratio fluctuations in central Pb+Pb (Au+Au) collisions from low SPS up to top RHIC energies have been studied within the HSD transport approach and within the statistical hadron-resonance gas model in **Chapter 7**. The grand canonical ensemble (GCE), canonical ensemble (CE), and micro-canonical ensemble (MCE) have been used to quantify the effects of conservation laws in the statistical model. Substantial differences in the HSD and statistical model results for the scaled variances  $\omega_A$  and the correlation parameters  $\rho_{AB}$  have been obtained. The HSD results at SPS energies are close to those in the CE and MCE statistical model. This indicates a dominant role of resonance decays and global conservation laws at

low energy nucleus-nucleus collisions. On the other hand, substantial differences in the HSD and statistical model results have been observed at RHIC energies which can be attributed to non-equilibrium dynamical effects in the HSD simulations. These quantities may serve as good observables to probe the amount of equilibration achieved in central nucleus-nucleus collisions! On the other hand the observable  $\sigma_{dyn}$ , which is used for ratio fluctuations, appears to be rather sensitive to the details of the model at low collision energies.

The HSD model can qualitatively reproduce the measured excitation function for the  $K/\pi$  ratio fluctuations  $\sigma_{dyn}^{K\pi}$  in central A+A collisions from low SPS up to top RHIC energies. Accounting for the experimental acceptance as well as the centrality selection has a relatively small influence on  $\sigma_{dyn}^{K\pi}$  and does not change the shape of the excitation function.

The HSD results for  $\sigma_{dyn}^{p\pi}$  appear to be close to the NA49 data but overestimate the STAR results. On the other hand  $\sigma_{dyn}^{Kp}$  from HSD calculations are in agreement with STAR data and, furthermore, show an essential sensitivity to the experimental acceptance. New data on event-by-event fluctuations will help to clarify the situation and allow for further insight.

**Chapter 8** has presented a study of the system size event-by-event fluctuations causing rapidity forward-backward correlations in relativistic heavy-ion collisions. The HSD simulations reveal strong forward-backward correlations and reproduce the main qualitative features of the STAR data in A+A collisions at RHIC energies. It has been shown that strong forward-backward correlations arise due to an averaging over many different events that belong to one 10% centrality bin. In contrast to average multiplicities, the resulting fluctuations and correlations depend strongly on the specific centrality trigger. For example, the centrality selection via impact parameter  $b$  and via the reference multiplicity  $N_{ch}^{ref}$  lead to rather different participant fluctuations and forward-backward correlations as well as their dependence on centrality.

The forward-backward correlations can be studied experimentally for smaller size centrality bins. With decreasing the size of the bins, the contribution of ‘geometrical’ fluctuations should lead to weaker forward-backward correlations and to a less pronounced centrality dependence.

A strong influence of geometrical fluctuations on fluctuations and correlations of observed quantities has been found in this work. The HSD transport approach has been used to quantify these influences. It has been found that in order to

decrease volume fluctuations – which is connected to participant number fluctuations – one should consider most central collisions or very narrow centrality bins. Note, that the ‘geometrical’ fluctuations discussed here are in fact present in all dynamical models of nucleus-nucleus collisions.

This study is expected to be helpful for both experimentalists and theorists to understand the importance of volume fluctuations which should be carefully accounted before any discussion of new physical effects is addressed.

# Appendix A:

## String Model

The Monte Carlo simulation program FRITIOF [174, 175, 82] which determine the outcome of high-energy photon-nucleon and hadron-hadron interactions in our model uses the Lund formalism to describe the breakup of the strings into hadrons in form of the JETSET package. This Appendix serves as a brief introduction into the basic ideas of the Lund model [174, 176]. The description of the Lund string model follows in part [177] using its illustrations.

Since the mediators of the color force, i.e. the gluons, themselves carry color charges they are subject to strong self interactions. If the sources are separated more than  $\approx 0.3$  fm these strong color interactions confine the field lines to a narrow flux tube with constant energy density  $k$  per unit length. This leads to the linear increase of the quark potential at large distances which is seen for example in charmonium and bottonium spectroscopy, i.e. the energy levels of bound  $c\bar{c}$  pairs.

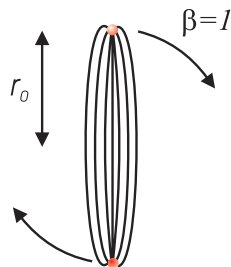


Figure 9.1: Simple string model for hadron. Neglecting the masses of the quarks the angular momentum of the hadron is given by the orbital angular momentum of the flux tube.

If one considers a hadron as two massless quarks which are connected by a string as in Fig. 9.1 the angular momentum of this object is equal to the total

orbital momentum of the flux tube. Assume that the ends of the tube rotate with the velocity of light. Then the local velocity at radius  $r$  will be

$$\beta(r) = \frac{r}{r_0} \quad (9.1)$$

where  $r_0$  is half the length of the string. The total mass is then

$$M = \int_0^{r_0} \frac{k dr}{\sqrt{1 - \beta(r)^2}} = kr_0\pi, \quad (9.2)$$

and the orbital momentum of the hadron is given as

$$J = 2 \int_0^{r_0} \frac{kr\beta dr}{\sqrt{1 - \beta(r)^2}} = \frac{kr_0^2\pi}{2}. \quad (9.3)$$

Eliminating  $r_0$  between these equations yields the linear relation between the angular momentum and mass of a hadron:

$$J = \alpha' M^2 + const \quad (9.4)$$

with  $\alpha' = (2\pi k)^{-1}$ . The string tension  $k$  can be estimated via the typical hadronic mass  $1 \text{ GeV}$  and the hadronic diameter which is known from electron scattering to be about  $1 \text{ fm}$ . The linear energy density then yields  $k = 1 \text{ GeV fm}^{-1}$  and  $\alpha' \approx 0.8 \text{ GeV}^{-2}$  which has to be compared to  $\alpha'_R \approx 0.9 \text{ GeV}^{-2}$  of the Regge trajectories. Despite of its simplicity the string model yields an astonishing good estimate for the Regge slope  $\alpha'_R$ .

Thus, the Regge spectrum of hadrons can be explained by assuming that the quark and antiquark (diquark) are connected by a color field which is compressed into a flux tube that contains a constant amount of energy per unit length. This constant force field leads to a linearly rising potential which is also seen in charmonium and bottomium spectroscopy as well as lattice QCD results. Phenomenologically, the string tension is known to be  $k \approx 1 \text{ GeV/fm} \approx 0.2 \text{ GeV}^2$ .

A simple model which describes hadrons as a charge and an anticharge connected by a massless relativistic string that plays the role of the constant force field may be introduced. The momentum of the state is located in the endpoint particles and its total energy can be decomposed into the potential energy in the force field and the kinetic energy of the endpoint particles.

Then the equation of motion of a relativistic particle under the influence of a constant force  $-k$  is

$$\frac{dp}{dt} = -k \quad (9.5)$$

and gives us

$$\begin{aligned} p(t) &= k(t_0 - t) \\ E(x) &= k(x_0 - x) \end{aligned} \quad (9.6)$$

Thus, the equation for the trajectory of a free particle with mass  $m$  and energy  $E$  is

$$m^2 = E^2 - p^2 = k^2[(x_0 - x)^2 - (t_0 - t)^2] \quad (9.7)$$

One sees that the particle moves on a hyperbola in space time which is centered at  $(t_0, x_0)$  and has the size parameter  $m/k$ . A massless particle ( $m = 0$ ) would move on the lightcones. At the turning point  $(t_0, x_0)$  it would have vanishing momentum and energy and would change its velocity immediately from  $+c$  to  $-c$ .

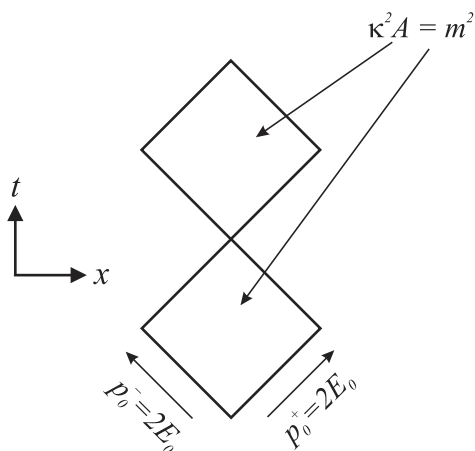


Figure 9.2: Space-time diagram of a yoyo hadron with mass  $m$  at rest.

A meson is treated as a system of two massless particles, a quark and an antiquark, which interact with each other by an attractive constant force. Replacing the antiquark by a diquark one ends up with a model for a baryon. The space-time picture of such a yoyo hadron at rest is depicted in [Fig. 9.2](#). If the two

constituents of the hadron move apart with the same energy  $E_0$  from a common origin but in opposite direction, the total momentum of the system vanishes and its total energy

$$E_{tot} = 2E_0 \quad (9.8)$$

equals the hadron mass  $m$ . The two particles then move along the two different lightcones and lose energy and momentum per unit length and time to the force field according to Eq. 9.6. At time  $t_0 = E_0/k$  they turn around and after that they head towards each other and now gain energy and momentum from the force field. The period of the motion is  $T = 4t_0$ .

Another general property of the massless relativistic string model is the so-called area law: The total area  $A$  spanned by the force field in space-time during one period is related to the squared mass of the system. For the yoyo hadron at rest this area is given by the sum of the two squares with diagonal  $2t_0 = E_{tot}/k$  (cf. Fig. 9.2):

$$k^2 A = k^2 2 \frac{t_0^2}{2} = E_{tot}^2 = m^2. \quad (9.9)$$

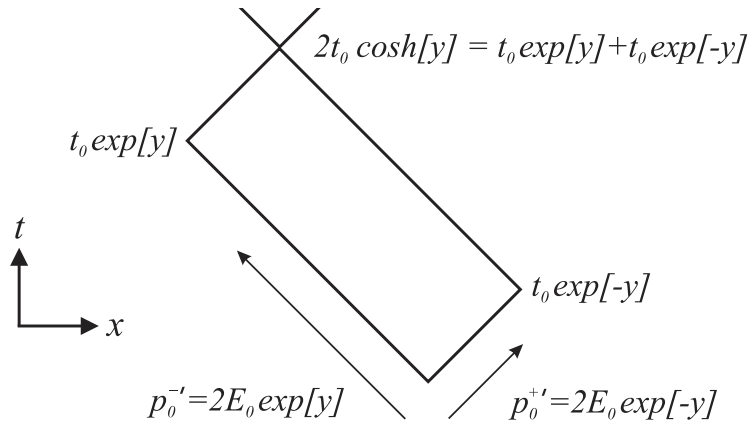


Figure 9.3: Yoyo hadron that moves with rapidity  $y$  along the negative  $x$ -direction.

Fig. 9.3 now shows a yoyo hadron that moves with rapidity  $y$  along the negative  $x$ -direction. Boosting from the rest frame of the yoyo hadron to the moving



system one gets the new meeting time  $2t_0 \cosh(y)$ . The period of the moving hadron is therefore time dilated  $T' = 4t_0 \cosh(y) > T$ .

The space-time area covered by the force field is two times the size of the shown rectangle (cf. Fig. 9.3), i.e.

$$A' = 4t_0^2 = \frac{m^2}{k^2} = A . \quad (9.10)$$

The strings that are formed after a high-energy collision have an invariant mass that is in general larger than that of stable hadrons or low lying excited states. Therefore, they decay into lower mass fragments due to the creation of new quark-antiquark pairs out of the vacuum along the force field (see Fig. 9.4). At each vertex where a new  $q\bar{q}$  pair is produced one has to require local conservation of energy, momentum and internal quantum numbers, e.g. charge, strangeness, etc. As a consequence the newly created  $q$  and  $\bar{q}$  have zero momenta and start to separate because of the two attached string pieces. During the separation they gain energy and momentum by eating up the force field between them and the other string end.

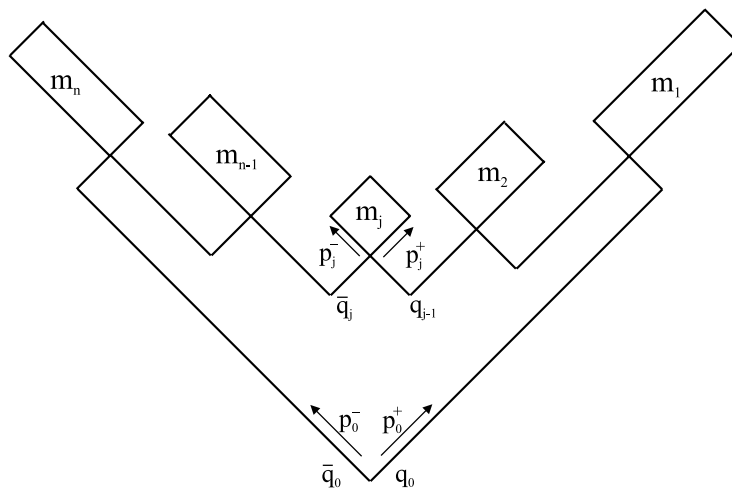


Figure 9.4: Fragmentation of a string into several hadrons.

The fragmentation process is uniquely determined by the set of Lorentz-invariant scaling variables  $\{z_i\}$  and therefore only depends on the fragmentation function  $f(z)$ . The requirement that taking the fragmentation steps along the negative and positive lightcone should lead to the same result in the limit  $n \rightarrow \infty$

restricts the fragmentation function to the following functional form

$$f(z) = N \frac{(1-z)^a}{z} \exp\left(-b \frac{m^2}{z}\right) \quad (9.11)$$

which is called Lund fragmentation function. Here  $a$  and  $b$  are parameters which have to be fitted to experiment while  $N$  is a normalization constant and  $m$  denotes the mass of the produced hadron. The parameters determine the behavior of  $f(z)$  as  $z$  approaches 0 or 1. The factor  $(1/z) \exp(-bm^2/z)$  peaks at  $z = bm^2$  (for  $bm^2 < 1$ ) and rapidly vanishes for smaller  $z$ . The factor  $(1-z)^a$  vanishes as  $z \rightarrow 1$ . One sees that as long as the mass  $m$  of the produced hadron is small compared to  $1/\sqrt{b} \approx 1.0 - 1.7 \text{ GeV}$  it is very unlikely that the fragment carries a large fraction of the available string energy. The average fraction

$$\langle z \rangle = \int_0^1 dz z f(z) \quad (9.12)$$

that the hadron takes from the (positive) lightcone momentum of the (remainder) string lies between 0.18 (for  $m = 0.14 \text{ GeV} \approx m_\pi$ ) and 0.5 (for  $m = 1 \text{ GeV} \approx m_N$ ). The ultimate number of string fragments depends on the invariant mass of the initial string.

A set of independently chosen random numbers  $\{z_i\}$  can solve the problem of fragmenting a high energetic string. However, it is very unlikely that the iteration process ends at the turning point of the  $\bar{q}_0$  which is required by energy and momentum conservation. There are some ways to cure this problem [178] but which show up to be unsuitable for Monte Carlo implementation. In the JETSET package the following way was chosen: Fragmentation happens randomly at both ends of the string, until the remaining invariant mass drops below a certain threshold. In the final step the kinematics of two hadrons are chosen simultaneously and energy and momentum conservation is guaranteed. The choice of some parameters, e.g. the threshold invariant mass, ensure that the  $z$  distribution of the final particles agrees with the default distribution (Eq. 9.11).

The fact that the string nevertheless fragments into onshell hadrons cannot be understood in purely classical terms. It can be argued on a quantum mechanical level that all breakup configurations that give unphysical masses simply cannot be projected onto a physical state. Note that in the nuclear medium the interactions with the surrounding nucleons may modify the masses of the fragments compared

to the situation in vacuum.

Up to now we have neglected the transverse momenta  $p_T$  and the masses  $\mu$  of the quarks. The  $q$  and the  $\bar{q}$  that are created in the string fragmentation have transverse momentum  $p_T(q) = -p_T(\bar{q})$  and instead of the hadron mass  $m$  the transverse mass

$$m_T = \sqrt{m^2 + p_T^2} \quad (9.13)$$

enters [Eq. 9.11](#). Furthermore, if the quarks have a finite mass they do not move on the lightcones anymore but their trajectories in space-time will be the hyperbolae. The asymptotes of such a yoyo mode are again rectangles, cf. left-hand side of [Fig. 9.5](#), but in contrast to the situation of massless constituents the oscillation time now also depends on the constituent mass  $\mu$ . However, this only influences the internal motion of the hadron after the production and is of no importance for the fragmentation process itself. Note, however, that the constituent masses  $\mu$  might influence the hadron-formation times, i.e. the times when the world lines of the quark and antiquark of a yoyo hadron cross. By interpreting the straight lines of the previous fragmentation diagrams as the asymptotes for the hyperbolic world lines of massive quarks, the fragmentation model can be developed in exactly the same way as before [[176](#)].

There is nevertheless a physical difference between the production of massless and massive quarks (see right-hand side of [Fig. 9.5](#)). Because of local energy conservation a real massive  $q\bar{q}$  pair cannot be created at one single space-time point. This is only possible for virtual quark pairs which then tunnel to real quark pairs. The connected tunneling probability has been calculated in Ref. [[179](#)] and leads to an additional suppression of heavy quark production in the string fragmentation. Consider a newly created virtual  $q\bar{q}$  pair at time  $t = 0$ . Due to local energy conservation the energy of the quark (or antiquark) must be zero:

$$t = 0 : \quad E_q^2 = E_{\bar{q}}^2 = 0 = p_L^2 + p_T^2 + \mu^2 , \quad (9.14)$$

where  $p_T$  denotes the transverse momentum of the quark ( $p_T(\bar{q}) = -p_T(q)$ ) and  $\mu$  its constituent mass. They therefore both have (imaginary) longitudinal mo-

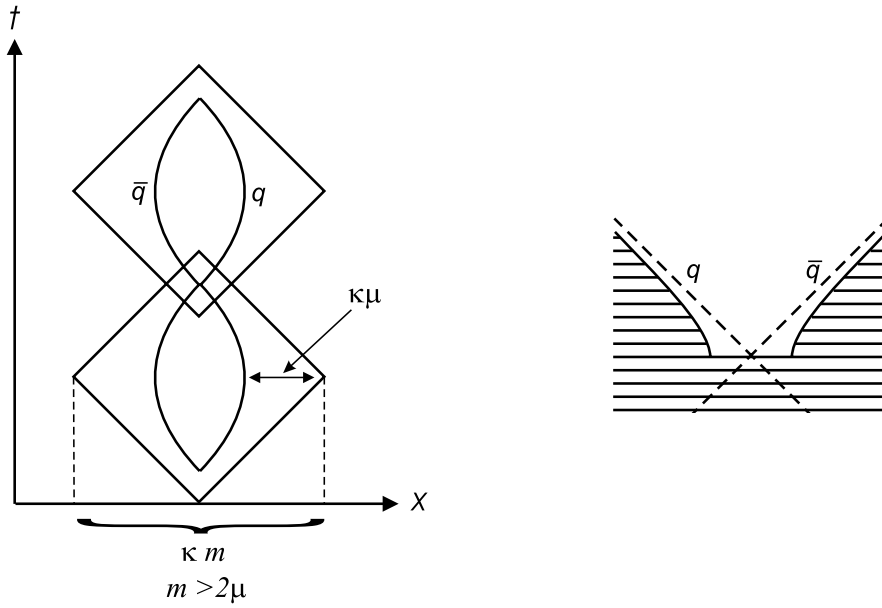


Figure 9.5: *Left:* Motion of a massive  $q$  and  $\bar{q}$  in a yoyo hadron. *Right:* A pair of massive quarks is created in the force field and moves apart on different branches of the same hyperbola.

menta:

$$t = 0 : \quad p_L = \pm i\mu_T = \pm i\sqrt{p_T^2 + \mu^2} . \quad (9.15)$$

At time  $t > 0$  the quark and antiquark have separated a distance  $2r$  and thereby gained the energy  $2kr$  from the flux tube:

$$\begin{aligned} t > 0 : \quad E_q + E_{\bar{q}} &= 2\sqrt{p_L^2(r) + \mu_T^2} = 2Kr \\ \Rightarrow p_L(r) &= \pm i\sqrt{\mu_T^2 - (kr)^2} . \end{aligned} \quad (9.16)$$

The quarks have tunneled to real quarks when  $p_L(r) = 0$ , i.e. when  $r = \mu_T/k$ . Hence, the tunneling probability is given as:

$$P = |e^{-S}|^2 \quad \text{with} \quad S = 2 \int_0^{\mu_T/k} |p_L(r)| dr = \frac{\pi\mu_T^2}{2k} . \quad (9.17)$$

**Eq. 9.17** leads to a Gaussian distribution of transverse momentum and suppresses high  $p_T$ . Furthermore, the production of quarks with large constituent mass  $\mu$

is strongly reduced by the tunneling probability. This leads to a suppression of strange and charm particle production in the string fragmentation. Since the tunneling amplitude is very sensitive to the size of the constituent quark masses which are not well-defined quantities, one usually extracts the suppression factors from experiment. As it has been mentioned before, one experimentally observes that strangeness production in  $pp$  collisions is suppressed by about a factor of 0.3. If one inserts the constituent mass [180] of the light quark flavors  $u$  and  $d$  ( $\mu_u \approx \mu_d \approx 0.325 \text{ GeV}$ ) into Eq. 9.17, one ends up with a realistic value for the constituent strange quark mass of  $\mu_s \approx 0.425 \text{ GeV}$  for this suppression factor. Furthermore, a constituent charm quark mass  $\mu_c \approx 1.3 \text{ GeV}$  leads to a relative suppression

$$P(u\bar{u}, d\bar{d}) : P(s\bar{s}) : P(c\bar{c}) \approx 1 : 0.3 : 10^{-11} . \quad (9.18)$$

This means that  $c\bar{c}$  pair creation essentially never occurs during a soft hadronization process but only in hard processes like  $q\bar{q} \rightarrow c\bar{c}$  or  $g\bar{g} \rightarrow c\bar{c}$ . The tunneling probability also suppresses the production of antibaryons via diquark-antidiquark creation in the string fragmentation. Assuming a mass of about  $0.5 \text{ GeV}$  for the diquark leads to a suppression factor of about 0.1 compared to  $u\bar{u}$  or  $d\bar{d}$  creation. However, there are other possibilities for baryon creation in a fragmentation process as it has been mentioned before. Note that the above suppression factors are extracted from experiments using elementary targets and projectiles, i.e. they correspond to the string tension and quark masses in vacuum. If the string fragmentation takes place inside (a dense) nuclear medium, the quark masses as well as the value of  $k$  might change and could lead to different tunneling amplitudes.

## Bibliography

- [1] Z. Fodor and S. D. Katz, *JHEP* **03**, 014 (2002), hep-lat/0106002.
- [2] Z. Fodor, S. D. Katz, and K. K. Szabo, *Phys. Lett.* **B568**, 73 (2003), hep-lat/0208078.
- [3] M. Cheng *et al.*, *Phys. Rev.* **D79**, 074505 (2009), 0811.1006.
- [4] NA38, M. C. Abreu *et al.*, *Phys. Lett.* **B449**, 128 (1999).
- [5] NA49, J. Bachler *et al.*, *Nucl. Phys.* **A661**, 45 (1999).
- [6] NA50, B. Alessandro *et al.*, *Eur. Phys. J.* **C39**, 335 (2005), hep-ex/0412036.
- [7] NA60, R. Arnaldi *et al.*, *J. Phys.* **G32**, S51 (2006), nucl-ex/0609039.
- [8] NA49-future, M. Gazdzicki *et al.*, *A new sps programme Vol. CPOD2006*, p. 016, 2006, nucl-ex/0612007.
- [9] BRAHMS, I. Arsene *et al.*, *Nucl. Phys.* **A757**, 1 (2005), nucl-ex/0410020.
- [10] B. B. Back *et al.*, *Nucl. Phys.* **A757**, 28 (2005), nucl-ex/0410022.
- [11] STAR, J. Adams *et al.*, *Nucl. Phys.* **A757**, 102 (2005), nucl-ex/0501009.
- [12] PHENIX, K. Adcox *et al.*, *Nucl. Phys.* **A757**, 184 (2005), nucl-ex/0410003.
- [13] ALICE, K. Aamodt *et al.*, *JINST* **0803**, S08002 (2008).
- [14] K. Peters, *AIP Conf. Proc.* **814**, 33 (2006).
- [15] A. N. Sissakian, A. S. Sorin, and V. D. Toneev, (2006), nucl-th/0608032.
- [16] The NA49, S. V. Afanasiev *et al.*, *Phys. Rev.* **C66**, 054902 (2002), nucl-ex/0205002.

- 
- [17] The NA49, C. Alt *et al.*, J. Phys. **G30**, S119 (2004), nucl-ex/0305017.
- [18] V. Toneev, PoS **CPOD07**, 057 (2007), 0709.1459.
- [19] P. Braun-Munzinger, K. Redlich, and J. Stachel, (2003), nucl-th/0304013.
- [20] J. Cleymans and K. Redlich, Phys. Rev. Lett. **81**, 5284 (1998), nucl-th/9808030.
- [21] J. Cleymans and K. Redlich, Phys. Rev. **C60**, 054908 (1999), nucl-th/9903063.
- [22] A. Andronic, P. Braun-Munzinger, and J. Stachel, Nucl. Phys. **A772**, 167 (2006), nucl-th/0511071.
- [23] Z. Fodor and S. D. Katz, JHEP **04**, 050 (2004), hep-lat/0402006.
- [24] F. Karsch, J. Phys. **G30**, S887 (2004), hep-lat/0403016.
- [25] R. Anishetty, P. Koehler, and L. D. McLerran, Phys. Rev. **D22**, 2793 (1980).
- [26] S. Date, M. Gyulassy, and H. Sumiyoshi, Phys. Rev. **D32**, 619 (1985).
- [27] L. V. Bravina *et al.*, Phys. Rev. **C60**, 024904 (1999), hep-ph/9906548.
- [28] L. V. Bravina *et al.*, Nucl. Phys. **A698**, 383 (2002), nucl-th/0104023.
- [29] E. L. Bratkovskaya *et al.*, Phys. Rev. **C69**, 054907 (2004), nucl-th/0402026.
- [30] E. V. Shuryak, Nucl. Phys. **A661**, 119 (1999), hep-ph/9906443.
- [31] R. Rapp, Nucl. Phys. **A782**, 275 (2007), nucl-th/0608022.
- [32] T. Matsui and H. Satz, Phys. Lett. **B178**, 416 (1986).
- [33] A. Mocsy and P. Petreczky, Phys. Rev. **D77**, 014501 (2008), 0705.2559.
- [34] R. Rapp and H. van Hees, (2008), 0803.0901.
- [35] A. Andronic, P. Braun-Munzinger, K. Redlich, and J. Stachel, J. Phys. **G35**, 104155 (2008), 0805.4781.

- 
- [36] L. Landau and L. Lifshitz, *Statistical Physics* (Pergamon Press, New York, 1980).
- [37] F. Karsch and E. Laermann, (2003), hep-lat/0305025.
- [38] C. R. Allton *et al.*, Phys. Rev. **D68**, 014507 (2003), hep-lat/0305007.
- [39] G. F. Smoot *et al.*, Astrophys. J. **396**, L1 (1992).
- [40] WMAP, D. N. Spergel *et al.*, Astrophys. J. Suppl. **170**, 377 (2007), astro-ph/0603449.
- [41] M. Gazdzicki, M. I. Gorenstein, and S. Mrowczynski, Phys. Lett. **B585**, 115 (2004), hep-ph/0304052.
- [42] M. A. Stephanov, K. Rajagopal, and E. V. Shuryak, Phys. Rev. **D60**, 114028 (1999), hep-ph/9903292.
- [43] J. S. Schwinger, J. Math. Phys. **2**, 407 (1961).
- [44] P. M. Bakshi and K. T. Mahanthappa, J. Math. Phys. **4**, 12 (1963).
- [45] L. V. Keldysh, Zh. Eksp. Teor. Fiz. **47**, 1515 (1964).
- [46] R. A. Craig, J. Math. Phys. **9**, 605 (1965).
- [47] L. P. Kadanoff and G. Baym, *Quantum statistical mechanics* (Benjamin, New York, 1962).
- [48] W. Cassing, Eur. Phys. J. ST **168**, 3 (2009), 0808.0715.
- [49] J. Berges and J. Cox, Phys. Lett. **B517**, 369 (2001), hep-ph/0006160.
- [50] S. Juchem, W. Cassing, and C. Greiner, Phys. Rev. **D69**, 025006 (2004), hep-ph/0307353.
- [51] W. Cassing and S. Juchem, Nucl. Phys. **A665**, 377 (2000), nucl-th/9903070.
- [52] W. Cassing and S. Juchem, Nucl. Phys. **A672**, 417 (2000), nucl-th/9910052.
- [53] C. Greiner and S. Leupold, Annals Phys. **270**, 328 (1998), hep-ph/9802312.
- [54] W. Botermans and R. Malfliet, Phys. Rept. **198**, 115 (1990).



- 
- [55] S. Leupold, Nucl. Phys. **A672**, 475 (2000), nucl-th/9909080.
- [56] S. Leupold, Nucl. Phys. **A695**, 377 (2001), nucl-th/0008036.
- [57] Y. B. Ivanov, J. Knoll, and D. N. Voskresensky, Nucl. Phys. **A672**, 313 (2000), nucl-th/9905028.
- [58] Y. B. Ivanov, J. Knoll, and D. N. Voskresensky, Phys. Atom. Nucl. **66**, 1902 (2003), nucl-th/0303006.
- [59] W. Cassing, V. Metag, U. Mosel, and K. Niita, Phys. Rept. **188**, 363 (1990).
- [60] W. Cassing and U. Mosel, Prog. Part. Nucl. Phys. **25**, 235 (1990).
- [61] W. Cassing and E. L. Bratkovskaya, Phys. Rept. **308**, 65 (1999).
- [62] W. Cassing, E. L. Bratkovskaya, and A. Sibirtsev, Nucl. Phys. **A691**, 753 (2001), nucl-th/0010071.
- [63] S. A. Bass *et al.*, Prog. Part. Nucl. Phys. **41**, 255 (1998), nucl-th/9803035.
- [64] M. Bleicher *et al.*, J. Phys. **G25**, 1859 (1999), hep-ph/9909407.
- [65] H. Stoecker and W. Greiner, Phys. Rept. **137**, 277 (1986).
- [66] G. F. Bertsch and S. Das Gupta, Phys. Rept. **160**, 189 (1988).
- [67] A. Faessler, Prog. Part. Nucl. Phys. **30**, 229 (1993).
- [68] W. Cassing, E. L. Bratkovskaya, U. Mosel, S. Teis, and A. Sibirtsev, Nucl. Phys. **A614**, 415 (1997), nucl-th/9609050.
- [69] T. Falter, W. Cassing, K. Gallmeister, and U. Mosel, Phys. Lett. **B594**, 61 (2004), nucl-th/0303011.
- [70] C. M. Ko and G.-Q. Li, J. Phys. **G22**, 1673 (1996), nucl-th/9611027.
- [71] J. Aichelin, Phys. Rept. **202**, 233 (1991).
- [72] B.-A. Li and C. M. Ko, Phys. Rev. **C52**, 2037 (1995), nucl-th/9505016.
- [73] W. Ehehalt and W. Cassing, Nucl. Phys. **A602**, 449 (1996).

- 
- [74] W. Cassing and S. Wang, *Z. Phys.* **A337**, 1 (1990).
- [75] K. Weber *et al.*, *Nucl. Phys.* **A539**, 713 (1992).
- [76] W. Cassing, *Nucl. Phys.* **A700**, 618 (2002), nucl-th/0105069.
- [77] W. Cassing, E. L. Bratkovskaya, and S. Juchem, *Nucl. Phys.* **A674**, 249 (2000), nucl-th/0001024.
- [78] S. Hama, B. C. Clark, E. D. Cooper, H. S. Sherif, and R. L. Mercer, *Phys. Rev.* **C41**, 2737 (1990).
- [79] R. Malfliet, *Prog. Part. Nucl. Phys.* **21**, 207 (1988).
- [80] Particle Data Group, L. Montanet *et al.*, *Phys. Rev.* **D50**, 1173 (1994).
- [81] B. Nilsson-Almqvist and E. Stenlund, *Comput. Phys. Commun.* **43**, 387 (1987).
- [82] B. Andersson, G. Gustafson, and H. Pi, *Z. Phys.* **C57**, 485 (1993).
- [83] H.-U. Bengtsson and T. Sjostrand, *Comput. Phys. Commun.* **46**, 43 (1987).
- [84] J. Geiss, W. Cassing, and C. Greiner, *Nucl. Phys.* **A644**, 107 (1998), nucl-th/9805012.
- [85] E. L. Bratkovskaya and W. Cassing, *Nucl. Phys.* **A807**, 214 (2008), 0712.0635.
- [86] H. Sorge, *Phys. Rev.* **C52**, 3291 (1995), nucl-th/9509007.
- [87] H. Sorge, *Phys. Lett.* **B344**, 35 (1995).
- [88] K. Werner and J. Aichelin, *Phys. Lett.* **B308**, 372 (1993).
- [89] W. Cassing and E. L. Bratkovskaya, *Phys. Rev.* **C78**, 034919 (2008), 0808.0022.
- [90] T. Kodama, S. B. Duarte, K. C. Chung, R. Donangelo, and R. A. M. S. Nazareth, *Phys. Rev.* **C29**, 2146 (1984).
- [91] V. P. Konchakovski *et al.*, *Phys. Rev.* **C73**, 034902 (2006), nucl-th/0511083.

- 
- [92] V. P. Konchakovski, M. I. Gorenstein, and E. L. Bratkovskaya, Phys. Rev. **C76**, 031901 (2007), 0704.1831.
- [93] PHENIX, S. S. Adler *et al.*, Phys. Rev. **C71**, 034908 (2005), nucl-ex/0409015.
- [94] J. T. Mitchell, J. Phys. Conf. Ser. **27**, 88 (2005), nucl-ex/0511033.
- [95] NA49, M. Rybczynski *et al.*, J. Phys. Conf. Ser. **5**, 74 (2005), nucl-ex/0409009.
- [96] H. Heiselberg, Phys. Rept. **351**, 161 (2001), nucl-th/0003046.
- [97] A. Bialas, M. Bleszynski, and W. Czyz, Nucl. Phys. **B111**, 461 (1976).
- [98] M. Gazdzicki and M. I. Gorenstein, Phys. Lett. **B640**, 155 (2006), hep-ph/0511058.
- [99] U. Katscher *et al.*, Z. Phys. **A346**, 209 (1993).
- [100] Y. B. Ivanov, V. N. Russkikh, and V. D. Toneev, Phys. Rev. **C73**, 044904 (2006), nucl-th/0503088.
- [101] V. V. Begun, M. Gazdzicki, M. I. Gorenstein, and O. S. Zozulya, Phys. Rev. **C70**, 034901 (2004), nucl-th/0404056.
- [102] FOPI, B. Hong, Phys. Rev. **C66**, 034901 (2002).
- [103] V. P. Konchakovski, M. I. Gorenstein, E. L. Bratkovskaya, and H. Stoecker, Phys. Rev. **C74**, 064911 (2006), nucl-th/0606047.
- [104] H. Weber, E. L. Bratkovskaya, W. Cassing, and H. Stoecker, Phys. Rev. **C67**, 014904 (2003), nucl-th/0209079.
- [105] E. L. Bratkovskaya *et al.*, Prog. Part. Nucl. Phys. **53**, 225 (2004), nucl-th/0312048.
- [106] S. Jeon and V. Koch, (2003), hep-ph/0304012.
- [107] NA49, T. Anticic *et al.*, Phys. Rev. **C70**, 034902 (2004), hep-ex/0311009.
- [108] NA49, P. Dinkelaker, J. Phys. **G31**, S1131 (2005).

- 
- [109] NA49, C. Alt *et al.*, Phys. Rev. **C70**, 064903 (2004), nucl-ex/0406013.
- [110] S. Jeon and V. Koch, Phys. Rev. Lett. **85**, 2076 (2000), hep-ph/0003168.
- [111] M. Asakawa, U. W. Heinz, and B. Muller, Phys. Rev. Lett. **85**, 2072 (2000), hep-ph/0003169.
- [112] PHENIX, K. Adcox *et al.*, Phys. Rev. Lett. **89**, 082301 (2002), nucl-ex/0203014.
- [113] STAR, J. Adams *et al.*, Phys. Rev. **C68**, 044905 (2003), nucl-ex/0307007.
- [114] M. Gazdzicki and S. Mrowczynski, Z. Phys. **C54**, 127 (1992).
- [115] M. Gazdzicki, Eur. Phys. J. **C8**, 131 (1999), nucl-th/9712050.
- [116] S. Mrowczynski, Phys. Rev. **C66**, 024904 (2002), nucl-th/0112007.
- [117] J. Zaraneek, Phys. Rev. **C66**, 024905 (2002), hep-ph/0111228.
- [118] E. L. Bratkovskaya, W. Cassing, and H. Stoecker, Phys. Rev. **C67**, 054905 (2003), nucl-th/0301083.
- [119] NA49, T. Anticic *et al.*, Phys. Rev. **C69**, 024902 (2004).
- [120] M. Gazdzicki and M. I. Gorenstein, Acta Phys. Polon. **B30**, 2705 (1999), hep-ph/9803462.
- [121] A. Bialas and W. Czyz, Acta Phys. Polon. **B36**, 905 (2005), hep-ph/0410265.
- [122] PHOBOS, B. B. Back *et al.*, Phys. Rev. **C72**, 031901 (2005), nucl-ex/0409021.
- [123] NA49, C. Alt *et al.*, Phys. Rev. Lett. **94**, 192301 (2005), nucl-ex/0409004.
- [124] V. P. Konchakovski, M. I. Gorenstein, and E. L. Bratkovskaya, Phys. Lett. **B651**, 114 (2007), nucl-th/0703052.
- [125] Z. Koba, H. B. Nielsen, and P. Olesen, Nucl. Phys. **B40**, 317 (1972).
- [126] A. I. Golokhvastov, Sov. J. Nucl. Phys. **27**, 430 (1978).

- 
- [127] M. Gazdzicki, R. Szwed, G. Wrochna, and A. K. Wroblewski, *Mod. Phys. Lett.* **A6**, 981 (1991).
- [128] A. Wroblewski, *Acta Phys. Polon.* **B4**, 857 (1973).
- [129] V. V. Begun *et al.*, *Phys. Rev.* **C76**, 024902 (2007), nucl-th/0611075.
- [130] V. V. Begun, M. I. Gorenstein, M. Hauer, V. P. Konchakovski, and O. S. Zozulya, *Phys. Rev.* **C74**, 044903 (2006), nucl-th/0606036.
- [131] NA49, B. Lungwitz *et al.*, Energy dependence of multiplicity fluctuations in heavy ion collisions Vol. CFRNC2006, p. 024, 2006, nucl-ex/0610046.
- [132] NA61, A. Laszlo *et al.*, *PoS CPOD07*, 054 (2007), 0709.1867.
- [133] M. Gazdzicki, *Eur. Phys. J. ST* **155**, 37 (2008), 0801.4919.
- [134] V. P. Konchakovski, B. Lungwitz, M. I. Gorenstein, and E. L. Bratkovskaya, *Phys. Rev.* **C78**, 024906 (2008), 0712.2044.
- [135] M. A. Stephanov, K. Rajagopal, and E. V. Shuryak, *Phys. Rev. Lett.* **81**, 4816 (1998), hep-ph/9806219.
- [136] M. Stephanov, *Acta Phys. Polon.* **B35**, 2939 (2004).
- [137] F. Becattini, J. Manninen, and M. Gazdzicki, *Phys. Rev.* **C73**, 044905 (2006), hep-ph/0511092.
- [138] B. Lungwitz and M. Bleicher, *Phys. Rev.* **C76**, 044904 (2007), 0707.1788.
- [139] W. Broniowski and W. Florkowski, *Phys. Rev.* **C65**, 024905 (2002), nucl-th/0110020.
- [140] B. M. Tavares, H. J. Drescher, and T. Kodama, *Braz. J. Phys.* **37**, 41 (2007), hep-ph/0702224.
- [141] NA49, C. Alt *et al.*, *Phys. Rev.* **C77**, 024903 (2008), 0710.0118.
- [142] NA49, M. Gazdzicki *et al.*, *J. Phys.* **G30**, S701 (2004), nucl-ex/0403023.
- [143] NA49, S. V. Afanasev *et al.*, *Phys. Rev. Lett.* **86**, 1965 (2001), hep-ex/0009053.

- 
- [144] NA49, C. Alt *et al.*, (2008), 0808.1237.
- [145] STAR, S. Das, J. Phys. **G32**, S541 (2006).
- [146] B. I. Abelev, (2009), 0901.1795.
- [147] G. Baym and H. Heiselberg, Phys. Lett. **B469**, 7 (1999), nucl-th/9905022.
- [148] S. Jeon and V. Koch, Phys. Rev. Lett. **83**, 5435 (1999), nucl-th/9906074.
- [149] G. Torrieri, Int. J. Mod. Phys. **E16**, 1783 (2007), nucl-th/0702062.
- [150] NA49, C. Roland *et al.*, J. Phys. **G30**, S1381 (2004), nucl-ex/0403035.
- [151] M. I. Gorenstein, M. Hauer, V. P. Konchakovski, and E. L. Bratkovskaya, Phys. Rev. **C79**, 024907 (2009), 0811.3089.
- [152] V. P. Konchakovski, M. Hauer, M. I. Gorenstein, and E. L. Bratkovskaya, (2009), 0906.3229.
- [153] S. A. Voloshin, V. Koch, and H. G. Ritter, Phys. Rev. **C60**, 024901 (1999), nucl-th/9903060.
- [154] S. Mrowczynski, Phys. Lett. **B430**, 9 (1998), nucl-th/9712030.
- [155] V. V. Begun and M. I. Gorenstein, Phys. Rev. **C73**, 054904 (2006), nucl-th/0510022.
- [156] V. V. Begun and M. I. Gorenstein, Phys. Rev. **C77**, 064903 (2008), 0802.3349.
- [157] J. Cleymans, H. Oeschler, K. Redlich, and S. Wheaton, Phys. Rev. **C73**, 034905 (2006), hep-ph/0511094.
- [158] S. Wheaton, J. Cleymans, and M. Hauer, Comput. Phys. Commun. **180**, 84 (2009), hep-ph/0407174.
- [159] M. Hauer, V. V. Begun, and M. I. Gorenstein, Multiplicity distributions in canonical and microcanonical statistical ensembles, 2007, 0706.3290.
- [160] V. V. Begun, M. Gazdzicki, and M. I. Gorenstein, Phys. Rev. **C78**, 024904 (2008), 0804.0075.

- 
- [161] G. Westfall,  $p/\pi$  fluctuations in au-au collisions in star, in *poster at Quark Matter 2009*.
- [162] J. Tian, Event-by-event  $p/k$  fluctuations from a+a collisions at rhic, in *poster at Quark Matter 2009*.
- [163] D. Kresan and V. Friese, PoS **CFRNC2006**, 017 (2006).
- [164] A. Bialas and R. B. Peschanski, Nucl. Phys. **B273**, 703 (1986).
- [165] S. Jeon, L. Shi, and M. Bleicher, Phys. Rev. **C73**, 014905 (2006), nucl-th/0506025.
- [166] N. Armesto, M. A. Braun, E. G. Ferreira, and C. Pajares, Phys. Rev. Lett. **77**, 3736 (1996), hep-ph/9607239.
- [167] M. A. Braun and C. Pajares, Phys. Rev. Lett. **85**, 4864 (2000), hep-ph/0007201.
- [168] N. Armesto, L. McLerran, and C. Pajares, Nucl. Phys. **A781**, 201 (2007), hep-ph/0607345.
- [169] T. Lappi and L. McLerran, Nucl. Phys. **A772**, 200 (2006), hep-ph/0602189.
- [170] STAR, T. J. Tarnowsky, PoS **CPOD07**, 019 (2007), 0711.1175.
- [171] T. Tarnowsky, R. Scharenberg, and B. Srivastava, Int. J. Mod. Phys. **E16**, 1859 (2007), nucl-ex/0702055.
- [172] V. P. Konchakovski, M. Hauer, G. Torrieri, M. I. Gorenstein, and E. L. Bratkovskaya, Phys. Rev. **C79**, 034910 (2009), 0812.3967.
- [173] B. Alver, M. Baker, C. Loizides, and P. Steinberg, (2008), 0805.4411.
- [174] B. Andersson, G. Gustafson, G. Ingelman, and T. Sjostrand, Phys. Rept. **97**, 31 (1983).
- [175] H. Pi, Comput. Phys. Commun. **71**, 173 (1992).
- [176] B. Andersson, Camb. Monogr. Part. Phys. Nucl. Phys. Cosmol. **7**, 1 (1997).
- [177] T. Falter, *Nuclear reactions of high energy protons, photons, and leptons*, PhD thesis, Uni. Giessen, 2004.

- [178] P. Eden, JHEP **05**, 029 (2000), hep-ph/0004132.
- [179] N. K. Glendenning and T. Matsui, Phys. Rev. **D28**, 2890 (1983).
- [180] T. Sjostrand, L. Lonnblad, and S. Mrenna, (2001), hep-ph/0108264.



## Acknowledgments

I would like to express my gratitude to my friends and colleagues, without whom the existence of the thesis in your hands would be impossible. First of all, I am grateful to my supervisor PD Dr. E. Bratkovskaya. Her support and help as well as contribution to the thesis hardly can be overestimated. It is a pleasure and I am very happy to work with her. I am extremely grateful to Prof. M. Gorenstein, whose ideas and scientific intuition provided a groundwork for the dissertation. I am also thankful to Prof. M. Gazdzicki for his contribution to this work, reliable suggestions and for a careful reading of the thesis. I am grateful to Dr. O. Linnyk for the encyclopedic erudition and for the answers of my numerous questions. Thanks to MSc. M. Hauer for his extraordinary ideas in physics and in life. Thanks to Dr. V. Begun for his sober and practical life views. I also appreciate working with my various co-authors Prof. H. Stoecker, JProf. M. Bleicher, Dr. G. Torrieri, Dr. B. Lungwitz and Dr. S. Haussler.

I am very glad to be a member of the H-QM School which has provided excellent possibilities for the education and for the start of a scientific career. Futhermore, I thank all of the participants of the School for the warm and friendly atmosphere during my study. Especially, I am grateful to Dr. H. Büsching for the perfect organization of scientific process and leisure time in the School.

Finally, let me thank my family for the support, which I feel every day of my life and for being always close to me, despite the spatial distance.



# Volodymyr Konchakovski

Helmholtz Research School  
University of Frankfurt

☎ +49-1577-1570152

☎ +49-69-798-47605

✉ [voka@fias.uni-frankfurt.de](mailto:voka@fias.uni-frankfurt.de)



## General information

Date of birth May 15, 1984  
Place of birth Korosten, Ukraine  
Nationality Ukrainian  
Sex male  
Address Frankfurt Institute for Advanced Studies  
Ruth-Moufang-Str. 1  
60438 Frankfurt am Main, Germany

## Field of scientific interests

Relativistic nuclear physics, heavy-ion physics, correlations and fluctuations in relativistic nuclear collisions, critical point and onset of deconfinement, hadron properties in dense nuclear matter.

## Education

2006–present **Ph.D student**, *Helmholtz Research School*, University of Frankfurt, Germany.  
2005–2006 **Engineer**, *Bogolyubov Institute for Theoretical Physics*, Kiev, Ukraine.  
2001–2006 **Student**, *Department of Physics*, *National Taras Shevchenko University of Kyiv*, Ukraine.  
1998–2001 **Pupil**, *Ukrainian Lyceum of Physics and Mathematics*, Kiev, Ukraine.  
1991–1998 **Pupil**, *Secondary school #9*, Korosten, Ukraine.

## Grades

October 2009 (planned) **PhD**, *Institut für Theoretische Physik*, University of Frankfurt, Germany.  
Adviser — PD Dr. E. L. Bratkovskaya (ITP). Title – ‘*Fluctuations and Correlations in Nucleus-Nucleus Collisions within Transport Approaches*’  
2006 **MS**, *Department of Physics*, *National Taras Shevchenko University of Kyiv*, Ukraine.  
Adviser — Prof. A. I. Gorenstein (BITP, Kiev, Ukraine). Title – ‘*Multiplicity Fluctuations in High Energy Nucleus-Nucleus Collisions from Microscopic Transport Approaches*’  
2005 **Bachelor**, *Department of Physics*, *National Taras Shevchenko University of Kyiv*, Ukraine, *cum laude*.  
Adviser — Prof. A. I. Gorenstein (BITP, Kiev, Ukraine). Title – ‘*Statistical Multiplicity Fluctuation within Hadron Gas with Exact Conservation Laws*’  
2001 **School Certificate**, *Ukrainian Lyceum of Physics and Mathematics*, Kiev, Ukraine.

## Participation in Conferences

- June 2009 **International Workshops on 'Critical Point and Onset of Deconfinement'**, BNL, Upton, USA, Talk: *'Fluctuations and correlations from microscopic transport theory'*.
- March 2009 **21nd International Conference on Ultra-Relativistic Nucleus Nucleus Collisions 'Quark Matter 2009'**, Knoxville, USA, Poster: *'Fluctuations and Correlations in Nucleus-Nucleus Collisions: Statistical and Transport Models'*.
- November 2008 **International Symposium on Heavy Ion Physics**, GSI Darmstadt, Germany.
- September 2008 **International Conference 'New Trends in High Energy Physics'**, Yalta, Ukraine, Talk: *'HSD transport model as a tool for studying fluctuations in nucleus-nucleus collisions'*.
- February 2008 **20th International Conference on Ultra-Relativistic Nucleus Nucleus Collisions 'Quark Matter 2008'**, Jaipur, India, Poster: *'Event-by-event Fluctuations in Relativistic Nuclear Collisions within Microscopic Transport Approach – HSD'*.
- September 2007 **International Conference 'New Trends in High Energy Physics'**, Yalta, Ukraine, Talk: *'Multiplicity fluctuations in nucleus-nucleus collisions: centrality and energy dependence'*.
- July 2007 **International Workshops on 'Critical Point and Onset of Deconfinement'**, GSI Darmstadt, Germany, Talk: *'Dynamical Study of Fluctuations in Relativistic Nuclear Collisions'*.
- August 2006 **International School of Subnuclear Physics**, Erice, Italy, Talk: *'Multiplicity Fluctuations in High Energy Nucleus-Nucleus Collisions from Microscopic Transport Approaches'*.
- July 2006 **International Workshops on 'Correlations and Fluctuations in Relativistic Nuclear Collisions'**, Florence, Italy, Talk: *'Fluctuations in high energy nucleus-nucleus collisions from microscopic transport approaches'*.
- February 2006 **Winter School on Theoretical Physics**, Dubna, Russia.
- February 2005 **Winter School on Theoretical Physics**, Dubna, Russia.

## Publications

- [14] V.P. Konchakovski, M. Hauer, M.I. Gorenstein and E.L. Bratkovskaya. *Particle Number Fluctuations and Correlations in Nucleus-Nucleus Collisions*. Submitted to Phys. Rev. C, 2008
- [13] V.P. Konchakovski, M. Hauer, G. Torrieri, M.I. Gorenstein and E.L. Bratkovskaya. *Forward-backward correlations in nucleus-nucleus collisions: baseline contributions from geometrical fluctuations*. Phys. Rev., C79:034910,2009.
- [12] M.I. Gorenstein, M. Hauer, V.P. Konchakovski, and E.L. Bratkovskaya. *Fluctuations of the  $k/\pi$  Ratio in Nucleus-Nucleus Collisions: Statistical and Transport Models*. Phys. Rev., C79:024907, 2009.
- [11] V.P. Konchakovski, B. Lungwitz, M.I. Gorenstein, and E.L. Bratkovskaya. *Multiplicity Fluctuations in Nucleus-Nucleus Collisions: Dependence on Energy and Atomic Number*. Phys. Rev., C78:024906, 2008.
- [10] M. Hauer, V.V. Begun, M. Gazdzicki, M.I. Gorenstein, V.P. Konchakovski and B. Lungwitz. *Multiplicity Fluctuations in Relativistic Nuclear Collisions*. J. Phys., G35:044064, 2008.
- [9] V.P. Konchakovski. *Dynamical Study of Fluctuations in Relativistic Nuclear Collisions*. PoS, CPOD07:021, 2007.
- [8] V.P. Konchakovski, M.I. Gorenstein, and E.L. Bratkovskaya. *Multiplicity Fluctuations in Proton-Proton and Nucleus-Nucleus Collisions*. Phys. Lett., B651:114–118, 2007.
- [7] V.P. Konchakovski, M.I. Gorenstein, and E.L. Bratkovskaya. *Multiplicity Fluctuations in Au+Au Collisions at RHIC*. Phys. Rev., C76:031901, 2007.
- [6] V.P. Konchakovski. *Multiplicity Fluctuations in Nucleus-Nucleus Collisions: Centrality and Energy Dependence*. "Yalta 2007, New trends in high-energy physics" 207-213, 2007.
- [5] V.V. Begun, M. Gazdzicki, M.I. Gorenstein, M. Hauer, V.P. Konchakovski and B. Lungwitz. *Multiplicity Fluctuations in Relativistic Nuclear Collisions: Statistical Model versus Experimental Data*. Phys. Rev., C76:024902, 2007.
- [4] V.P. Konchakovski. *Fluctuations in High Energy Nucleus-Nucleus Collisions from Microscopic Transport Approaches*. PoS, CFRNC2006:010, 2006.
- [3] V.P. Konchakovski, M.I. Gorenstein, E.L. Bratkovskaya, and H. Stoecker. *Baryon Number and Electric Charge Fluctuations in Pb+Pb Collisions at SPS Energies*. Phys. Rev., C74:064911, 2006.
- [2] V.V. Begun, M.I. Gorenstein, M. Hauer, V.P. Konchakovski, and O.S. Zozulya. *Multiplicity Fluctuations in Hadron-Resonance Gas*. Phys. Rev., C74:044903, 2006.
- [1] V.P. Konchakovski, S. Haussler, M.I. Gorenstein, E.L. Bratkovskaya, M. Bleicher and H. Stoecker. *Particle Number Fluctuations in High Energy Nucleus-Nucleus Collisions from Microscopic Transport Approaches*. Phys. Rev., C73:034902, 2006.